

**APPLIED
COMPUTATIONAL
ELECTROMAGNETICS
SOCIETY
JOURNAL**

November 2015
Vol. 30 No. 11
ISSN 1054-4887

The ACES Journal is abstracted in INSPEC, in Engineering Index, DTIC, Science Citation Index Expanded, the Research Alert, and to Current Contents/Engineering, Computing & Technology.

The illustrations on the front cover have been obtained from the research groups at the Department of Electrical Engineering, The University of Mississippi.

THE APPLIED COMPUTATIONAL ELECTROMAGNETICS SOCIETY

<http://aces-society.org>

EDITOR-IN-CHIEF

Atef Elsherbeni

Colorado School of Mines, EECS Dept.
Golden, CO 80401, USA

ASSOCIATE EDITORS-IN-CHIEF

Sami Barmada

University of Pisa, EE Dept.
Pisa, Italy, 56126

Mohammed Hadi

Kuwait University, EE Dept.
Safat, Kuwait

Paolo Mezzanotte

University of Perugia
I-06125 Perugia, Italy

Yasushi Kanai

Niigata Inst. of Technology
Kashiwazaki, Japan

Alistair Duffy

De Montfort University
Leicester, UK

Antonio Musolino

University of Pisa
56126 Pisa, Italy

Ozlem Kilic

Catholic University of America
Washington DC, 20064, USA

Mohamed Bakr

McMaster University, ECE Dept.
Hamilton, ON, L8S 4K1, Canada

Marco Arjona López

La Laguna Institute of Technology
Coahuila 27266, Mexico

Fan Yang

Tsinghua University, EE Dept.
Beijing 100084, China

Abdul Arkadan

Rafik Hariri University
Chouf 2010, Lebanon

EDITORIAL ASSISTANTS

Matthew J. Inman

University of Mississippi, EE Dept.
University, MS 38677, USA

Shanell Lopez

Colorado School of Mines, EECS Dept.
Golden, CO 80401, USA

EMERITUS EDITORS-IN-CHIEF

Duncan C. Baker

EE Dept. U. of Pretoria
0002 Pretoria, South Africa

Ahmed Kishk

University of Mississippi, EE Dept.
University, MS 38677, USA

Allen Glisson

University of Mississippi, EE Dept.
University, MS 38677, USA

Robert M. Bevensee

Box 812
Alamo, CA 94507-0516, USA

David E. Stein

USAF Scientific Advisory Board
Washington, DC 20330, USA

EMERITUS ASSOCIATE EDITORS-IN-CHIEF

Mohamed Abouzahra

MIT Lincoln Laboratory
Lexington, MA, USA

Erdem Topsakal

Mississippi State University, EE Dept.
Mississippi State, MS 39762, USA

Levent Gurel

Bilkent University
Ankara, Turkey

Alexander Yakovlev

University of Mississippi, EE Dept.
University, MS 38677, USA

EMERITUS EDITORIAL ASSISTANTS

Khaled ElMaghoub

University of Mississippi, EE Dept.
University, MS 38677, USA

Christina Bonnington

University of Mississippi, EE Dept.
University, MS 38677, USA

Anne Graham

University of Mississippi, EE Dept.
University, MS 38677, USA

Mohamed Al Sharkawy

Arab Academy for Science and Technology, ECE Dept.
Alexandria, Egypt

NOVEMBER 2015 REVIEWERS

Areeb Ahmed

Md Rezwaul Ahsan

Hany Atallah

Mehmet Belen

Toni Björninen

Lahcene Boukelkoul

Ahmed Boutejdar

Umut Bulus

Vedula Chakravarthy

Mihir Dam

Yasin Damgaci

Martins Ezuma

He Huang

Ming Jin

Sung Kim

Ali Lalbakhsh

Qian Li

Hong Liao

Wen-Jiao Liao

Zhiwei Liu

Ladislau Matekovits

Laercio Mendonca

Andrew Peterson

Mohammad Ranjbar Nikkhah

C. J. Reddy

P. Sampath

Adriana Savin

Abhishek Sharma

Yuhao Wang

Haogang Wang

Gaobiao Xiao

Hua Zeng

Jing Zhao

Huapeng Zhao

THE APPLIED COMPUTATIONAL ELECTROMAGNETICS SOCIETY
JOURNAL

Vol. 30 No. 11

November 2015

TABLE OF CONTENTS

| | |
|--|------|
| “Method of Moments Analysis of Electromagnetic Transmission Through an Arbitrarily Shaped 3D Cavity in a Thick Conducting Plane” Ahmet B. Olcen, Taha Imeci, Mesut Gokten, Josph R. Mautz, and Ercument Arvas | 1137 |
| “A VSIE Solution for EM Scattering Using the Multilevel Complex Source Beam Method” Zhenhong Fan, Yanlong Hu, Dazhi Ding, and Rushan Chen | 1146 |
| “Fast EM Scattering Analysis for the Hard Targets in a Layered Medium by Using the Hierarchical Vector Basis Functions” Liping Zha, Rushan Chen, and Ting Su | 1154 |
| “Waveguide Microwave Imaging: Solids Volume Fraction of Particulate Materials” Alexander V. Brovko, Ethan K. Murphy, and Vadim V. Yakovlev | 1161 |
| “Size Reduced Array Antenna with Enhanced Directivity” Sheikh S. I. Mitu and Farooq Sultan | 1168 |
| “Wide Bandwidth Endfire Antenna with Log-Period Directors” Yuanhua Sun, Guangjun Wen, Haiyan Jin, Ping Wang, Yongjun Huang, and Jian Li | 1173 |
| “A Simple Electromagnetically Fed Circularly-Polarized Circular Microstrip Antenna” Mursyidul I. Sabran, Sharul K. A. Rahim, Ping J. Soh, Chee Y. Leow, and Guy A. E. Vandenbosch | 1180 |
| “The Effect on a Human Heart Model from Dipole Antenna, with and without Shield on SAR and Temperature Increase” Seyed I. Zoonori, Seyed V. Makki, and Abdorreza Torabi | 1188 |
| “Optimized Polygonal Slit Rectangular Patch Antenna with Defective Ground Structure for Wireless Applications” Sanjeeva Reddy B. Rama and Damera Vakula | 1194 |
| “Theoretical Approach for the Design of a New Wideband Ku-band Printed Antenna” Amal Harrabi, Tchanguiz Razban, Yann Mahé, Lotfi Osman, and Ali Gharsallah | 1200 |
| “Two Element Dielectric Resonator Antenna with Beam Switching” M. Kamran Saleem, Majeed A. S. Alkanhal, and Abdel F. Sheta | 1209 |

| | |
|---|------|
| “A Transparent UWB Antenna with a 5 to 6 GHz Band Notch Using Two Split Ring Resonators” Mohd S. A. Rani, Sharul K. A. Rahim, Ping J. Soh, Bashir M. Saad, Mursyidul I. Sabran, and Mohd F. M. Yusoff | 1215 |
| “Transient Current Distribution and Force Analysis of Three Phase Enclosure Type GIB Based on Field-Circuit Coupling FEM Method” Xiangyu Guan, Bing Kang, Naiqiu Shu, Qiangqiang Yan, and Zipin Li | 1223 |
| “Highly Efficient Technique for the Full-Wave Analysis of Circular Waveguide Filters Including Off-Centered Irises” Ángel A. San-Blas and José M. Roca | 1232 |
| “Effect of Plasma on Electromagnetic Wave Propagation and THz Communications for Reentry Flight” Ling Zheng, Qing Zhao, and Xiaojun Xing | 1241 |

Method of Moments Analysis of Electromagnetic Transmission Through an Arbitrarily Shaped 3D Cavity in a Thick Conducting Plane

A. Burak Olcen¹, S. Taha Imeci², Mesut Gokten³, J. R. Mautz¹, and Ercument Arvas⁴

¹Department of Electrical Engineering
Syracuse University, Syracuse, NY 13244, USA
abolcen@yahoo.com, jrmautz@syr.edu

²Department of Electrical and Electronics Engineering
Istanbul Commerce University, Istanbul, Turkey
timeci@ticaret.edu.tr

³Tubitak Space Technologies Research Institute
Ankara, Turkey
mesut.gokten@tubitak.gov.tr

⁴Department of Electrical and Electronics Engineering
Istanbul Medipol University, Istanbul, Turkey
ercumentarvas@gmail.com

Abstract — The method of moments (MOM) with surface equivalence principle is used to numerically solve the problem of electromagnetic scattering from and transmission through an arbitrarily shaped 3D cavity in a thick conducting plane is considered. The conducting walls of the cavity inside the ground plane are of arbitrary shape. The apertures at both ends of the cavity are also of arbitrary shape. An equivalent surface magnetic current placed on the top aperture produces the scattered field in the region where the impressed sources are. The total field inside the cavity is produced by two surface equivalent magnetic currents on the apertures and an equivalent surface electric current residing on the walls of the cavity as well as on both apertures. The transmitted field on the opposite side of the impressed sources is computed by an equivalent surface magnetic current residing on the bottom aperture. Computed results are compared with results in the literature obtained by using other methods. Very good agreement is observed.

Index Terms — Apertures, equivalence principle, moment methods.

I. INTRODUCTION

The coupling of electromagnetic energy through apertures is an important problem in electromagnetic engineering. Bethe [1] offered solutions for coupling through a small circular aperture in a conducting plane wall of zero thickness, utilizing electric and magnetic

dipole moments. His solution, the so-called aperture polarizability method, has been used extensively as a basis for future research on aperture coupled systems. Arvas [2] computed polarizabilities of arbitrary shaped small apertures.

A major breakthrough in dealing with aperture problems came in 1976 when Harrington and Mautz [3] expressed aperture characteristics as admittance matrices, which depend only on the region being considered, being independent of the other region. The aperture coupling is then expressible as the sum of the two independent aperture admittance matrices. The numeric solution is carried out with the method of moments formulated by Harrington [4]. Auckland solved the problem of electromagnetic transmission through a slit in a thick conducting plane, when the cross-section of the slit is rectangular [5] and when it is arbitrarily shaped [6]. Park and Eom published a paper in which they use the aforementioned method to solve for the electromagnetic transmission through circular apertures in a thick conducting plane [7]. Imeci computed transmission through an arbitrary shaped aperture in a conducting plane separating air and a chiral medium [8]. A similar problem was solved by Jin and Volakis [9] using the finite element method. The purpose of this work is to solve this problem using MOM and surface equivalence principle. For homogeneous structures of arbitrary shape, surface meshing is usually simpler than volume meshing. In such cases the method of moments with surface equivalence principle can be simpler than finite

element method. To the best of our knowledge the present work is the first that solves the problem using the method of moments and surface equivalence principle.

II. DEFINITION OF THE PROBLEM

The general problem considered here is shown in Fig. 1. The ground plane of thickness d is assumed to be a perfect electric conductor (PEC) of infinite size in x and y directions. Arbitrarily shaped apertures exist on each side of the thick ground plane. These apertures are connected with an arbitrarily shaped cavity. The regions above and below the ground plane as well as inside the cavity are linear, homogeneous, isotropic dielectric mediums. These regions are named regions a , b , and c from the top to the bottom. In general, each region has a different electric permittivity (ϵ) and magnetic permeability (μ) than the others. The top region, region a , also contains impressed sources (\vec{J}^i, \vec{M}^i) far away. These sources excite a time harmonic plane wave which illuminates the ground plane on the top side. The electric and magnetic fields in each region are unknown and they are going to be calculated by applying the equivalence principle, image theory and the method of moments.

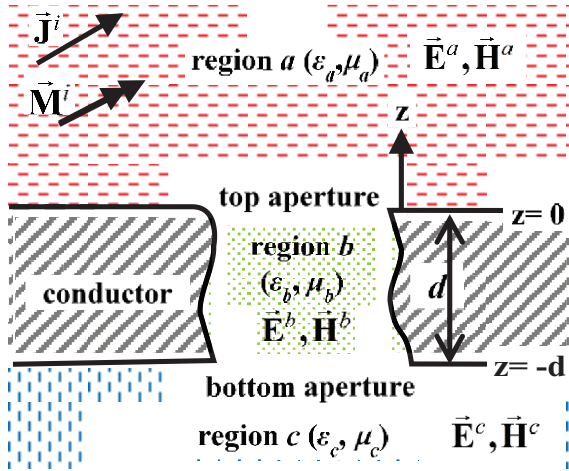


Fig. 1. Cross section view of the problem.

The equivalent problem for the top region is shown in Fig. 2. The impressed sources (\vec{J}^i, \vec{M}^i) and the material (ϵ_a, μ_a) are kept the same as those in the original problem. The top aperture surface of Fig. 1 is now covered by a patch of PEC in Fig. 2. Hence, the whole $z=0$ plane in Fig. 2 is a PEC. Below this plane, the fields are set to be null fields. The tangential electric field in region a of Fig. 1 is zero just above the $z=0$ plane except over the top aperture region. The electric field in the top aperture region is $\vec{E}^a|_{z=0} = \vec{E}^a|_{z=0^+}$ in Fig. 1. By placing an equivalent magnetic surface current:

$$\vec{M}_1 = \vec{E}^a|_{z=0^+} \times \vec{n}_a = \vec{E}^a|_{z=0^+} \times \vec{z}, \quad (1)$$

over this newly placed patch of PEC in Fig. 2, we guarantee that the tangential electric field just above this current in Fig. 2 is the same as the tangential electric field at the same points of Fig. 1. In (1), \vec{z} is the unit vector in the z -direction and $z=0^+$ indicates the limit as z approaches zero from the above. Then the fields in Fig. 2, produced by the impressed sources (\vec{J}^i, \vec{M}^i) and the equivalent magnetic surface current \vec{M}_1 (residing just above the PEC patch), are identical to (\vec{E}^a, \vec{H}^a) in Fig. 1. That is,

$$\vec{E}^a = \vec{E}^a(\vec{J}^i, \vec{M}^i) + \vec{E}^a(\vec{M}_1), \quad (2)$$

$$\vec{H}^a = \vec{H}^a(\vec{J}^i, \vec{M}^i) + \vec{H}^a(\vec{M}_1). \quad (3)$$

The problem in Fig. 2 is a radiation problem of current sources over an infinite ground plane in a half-space filled with homogeneous dielectric medium. This type of problem can be solved by using image theory [10]. The ground plane is removed and the equivalent magnetic surface current is doubled. Impressed sources also have their images taken. The fields produced by these five sources, as they radiate in an unbounded homogeneous medium (ϵ_a, μ_a) are the same as the fields of region a in Fig. 1. That is,

$$\vec{E}^a = \vec{E}^a(\vec{J}^i, \vec{M}^i) + \vec{E}^a(\vec{J}^{i, \text{img}}, \vec{M}^{i, \text{img}}) + \vec{E}^a(2\vec{M}_1), \quad (4)$$

$$\vec{H}^a = \vec{H}^a(\vec{J}^i, \vec{M}^i) + \vec{H}^a(\vec{J}^{i, \text{img}}, \vec{M}^{i, \text{img}}) + \vec{H}^a(2\vec{M}_1). \quad (5)$$

Equivalence for region b is shown in Fig. 3.

Lastly, the equivalent problem for the bottom region is set up. This is very similar to the top region equivalent problem with the major difference being not having impressed sources in the bottom region problem. The final form of the integral equations is obtained:

$$\begin{aligned} -2\vec{H}_{\text{tan}}^a(\vec{M}_1) - \vec{H}_{\text{tan}}^b(\vec{M}_1) - \vec{H}_{\text{tan}}^b(\vec{M}_2) + \vec{H}_{\text{tan}}^b(\vec{J}) &= 2\vec{H}_{\text{tan}}^{\text{inc}} \\ &\text{across top aperture,} \\ -\vec{H}_{\text{tan}}^b(\vec{M}_1) - \vec{H}_{\text{tan}}^b(\vec{M}_2) - 2\vec{H}_{\text{tan}}^c(\vec{M}_2) + \vec{H}_{\text{tan}}^c(\vec{J}) &= 0 \\ &\text{across bottom aperture,} \\ \vec{E}_{\text{tan}}^b(\vec{M}_1) + \vec{E}_{\text{tan}}^b(\vec{M}_2) - \vec{E}_{\text{tan}}^b(\vec{J}) &= 0 \text{ on } S_c, \end{aligned} \quad (6)$$

where \vec{H}^{inc} is the magnetic field of (\vec{J}, \vec{M}_i) in unbounded homogeneous medium. These three equations are going to be used to solve for the three unknowns, \vec{M}_1 , \vec{M}_2 and \vec{J} by the help of the method of moments.

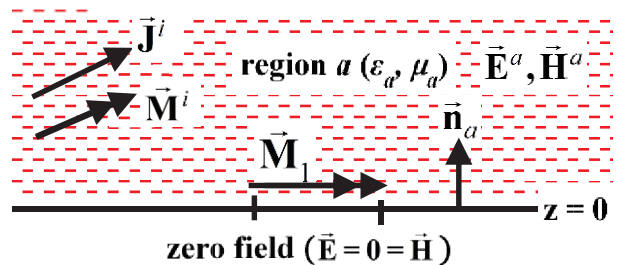


Fig. 2. The equivalent problem for region a .

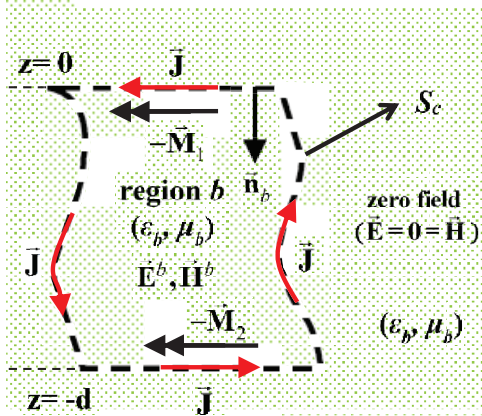


Fig. 3. The equivalence for cavity region.

III. NUMERICAL RESULTS

The problem that is going to be analyzed is a thick conductor with square apertures on the top and the bottom. This problem is previously solved in [9] using the finite element method. The sides of the apertures are $l=w=0.4\lambda$ and the conductor thickness is $d=0.25\lambda$. The triangular meshing is done in such a way that the triangles are more refined on the edges and on x and y axes on apertures. The top aperture is excited with a plane wave on normal incidence with polarization given as $\vec{E}^{inc} = \vec{x}e^{jkz}$. The electric fields on the apertures computed in [9] are in very good agreement with the electric fields in Fig. 4 calculated using the MoM formulation in this research.

Next, the backscattering cross section (RCS) and the transmission coefficient T of the structure are compared. The backscattering cross section is defined as [9]:

$$\sigma(\theta, \phi) = \lim_{r \rightarrow \infty} 4\pi r^2 \frac{|\vec{H}^s(\vec{r})|^2}{|\vec{H}^{inc}|^2}, \quad (7)$$

where $\vec{H}^s(\vec{r})$ is the far zone scattered field, which is the scattered field in the backward direction minus the field scattered that would exist if the entire $z = 0$ plane was perfectly conducting. The transmission coefficient is defined as:

$$T = \frac{P_{trans}}{P_{inc}} = \frac{\text{Re} \left(\iint_{bot.aper.} (\vec{E}_c^* \times \vec{H}_c) \cdot \vec{n}_c ds \right)}{\eta_a |\vec{H}^{inc}|^2 A_1 \cos \theta^{inc}}, \quad (8)$$

where P_{inc} is the time average incident power that would be intercepted by the top aperture if all space was free space, P_{trans} is the time average power transmitted to region c through the bottom aperture, η_a is the impedance of region a , and A_1 is the area of the top aperture. RCS and transmission coefficient plots computed by [9] and those in Fig. 5 computed by the MoM

formulation are very close to each other for square apertures on top and bottom in a thick conductor.

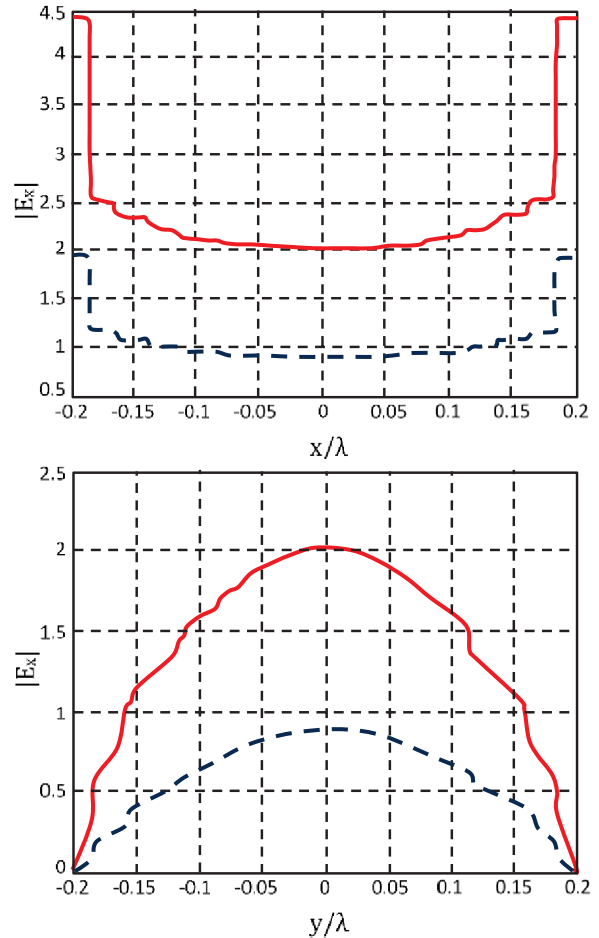
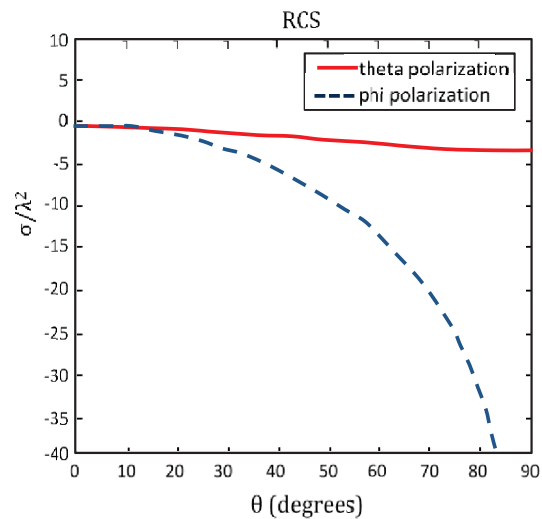


Fig. 4. (a) Electric field at the upper (solid line) and lower (dashed line) apertures, along x -axis, and (b) electric field at the upper (solid line) and lower (dashed line) apertures, along y -axis.



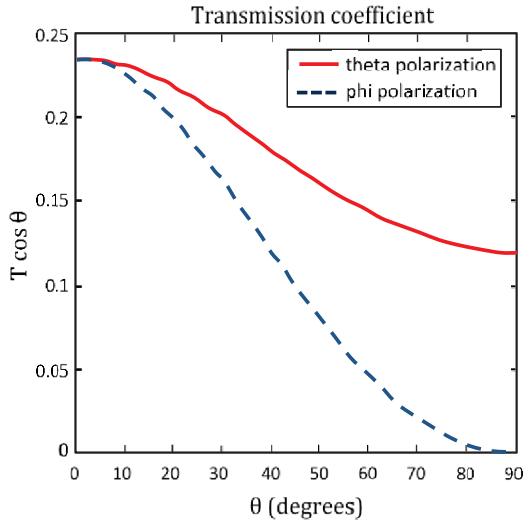


Fig. 5. (a) Backscatter RCS, and (b) transmission coefficient.

A. Cross aperture

A cross aperture on top and bottom is analyzed next. The cavity walls inside the conductor are the sides of a 0.5λ by 0.5λ square prism and the top and bottom walls are cross-shaped apertures. The geometry of mesh is shown in Fig. 6.

RCS and transmission coefficient plots given in Fig. 7 and Fig. 8 are very close to those given by [9].

PROBLEM GEOMETRY $A = B = 0.5\lambda$, $w = 0.125\lambda$, $d = 0.25\lambda$

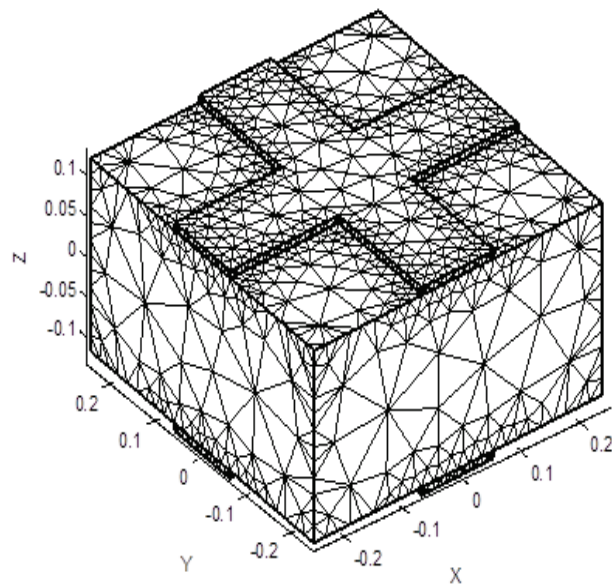


Fig. 6. Meshing of the cross aperture problem.

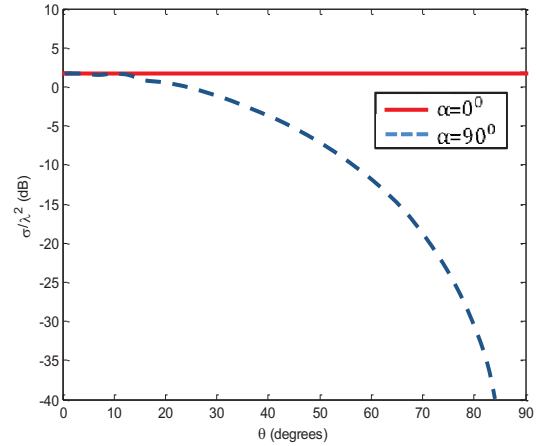


Fig. 7. Backscatter RCS as a function of incidence angle in the $\phi = 0^\circ$ plane; $\vec{E}^{inc}(\vec{r}) = (\vec{\theta}^{inc} \cos \alpha + \vec{\phi}^{inc} \sin \alpha)e^{-j\vec{k}^{inc} \cdot \vec{r}}$.

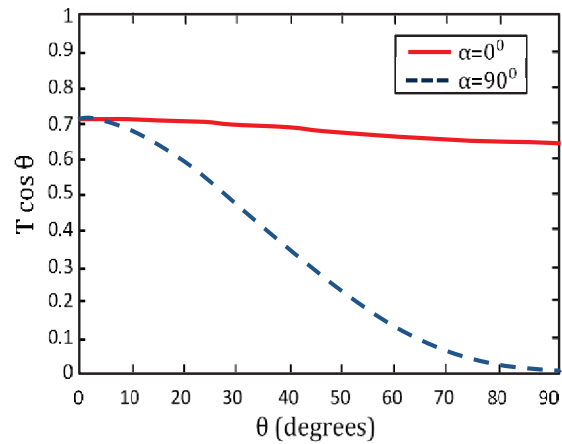


Fig. 8. Transmission coefficient plots of the structure in Fig. 6 as a function of incidence angle in the $\phi = 0^\circ$ plane; $\vec{E}^{inc}(\vec{r}) = (\vec{\theta}^{inc} \cos \alpha + \vec{\phi}^{inc} \sin \alpha)e^{-j\vec{k}^{inc} \cdot \vec{r}}$.

B. Circular aperture

A cylindrical cavity with small circular apertures whose centers are on the z -axis is analyzed. The geometry of meshing is shown in Fig. 9. The radii of the small apertures are $r=0.05\lambda$. The radius of the cylindrical cavity is $R=0.5\lambda$. The thickness of the conductor is $d=0.6\lambda$. The flanges covering the cylindrical cavity and forming small circular apertures on top and bottom have a thickness of 0.01λ . All regions are filled with (ϵ_0, μ_0) .

The incident field is $\vec{E}^{inc} = \vec{y}e^{jkz}$. The magnetic currents on the top and bottom apertures along x and y axes are in Fig. 10 and Fig. 11.

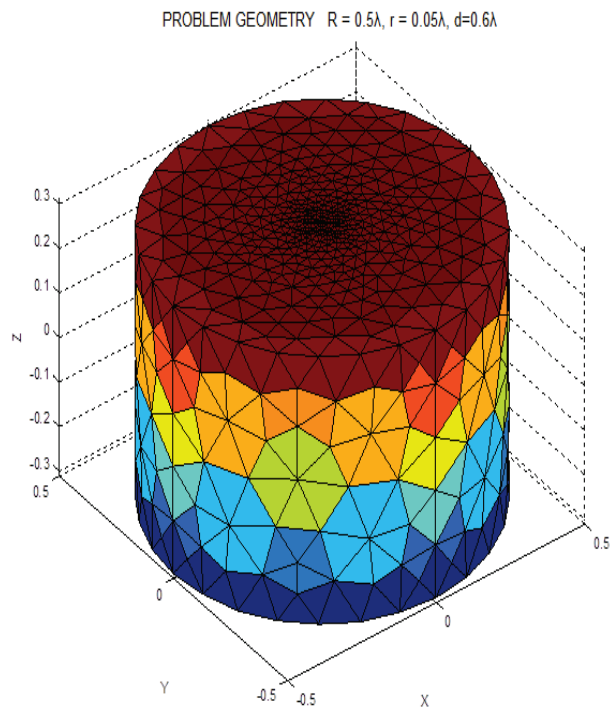


Fig. 9. The geometry of meshing of circular shape aperture.

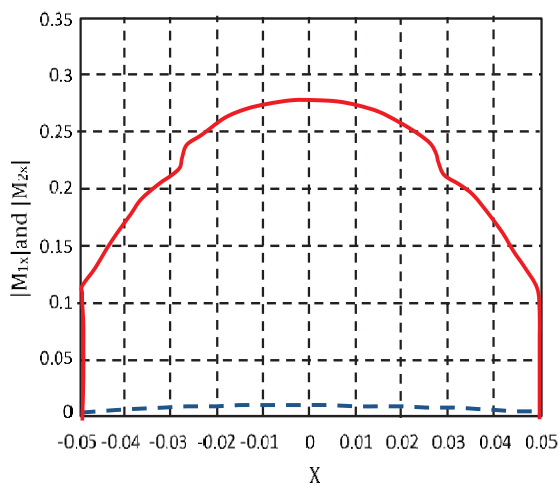


Fig. 10. Magnetic current on top aperture (solid line) and on bottom aperture (dashed line) along the x-axis for the problem.

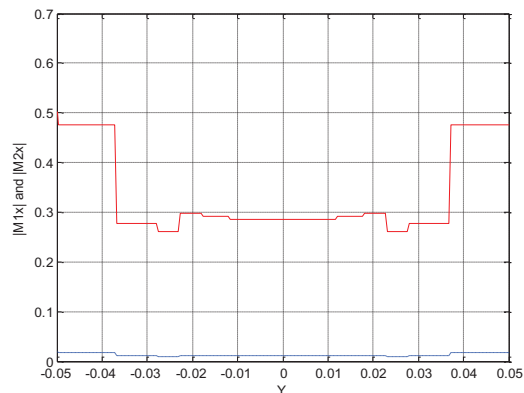


Fig. 11. Magnetic current on top aperture (solid line) and on bottom aperture (dashed line) along the y-axis for the problem.

C. Effect of conductor thickness

Square apertures with varying conductor thicknesses are analyzed to understand the effect of thickness on transmission of the plane wave through the cavity. The problem geometries and corresponding magnetic current plots for the top and bottom apertures are given in Fig. 12 through Fig. 17.

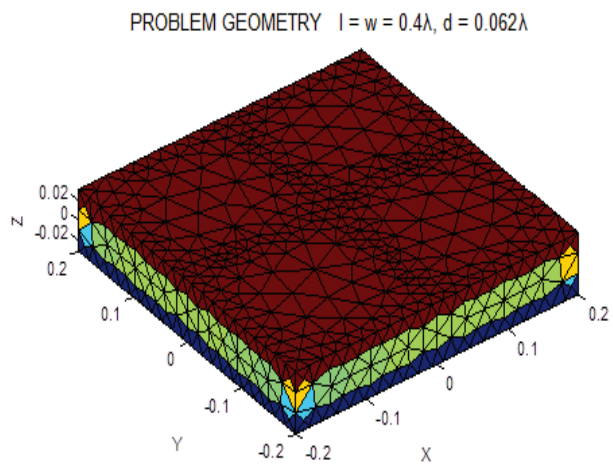


Fig. 12. Triangular meshing of the problem with square apertures (0.4λ -by- 0.4λ) on top and bottom; conductor thickness $d=0.062\lambda$, $\epsilon_a = \epsilon_b = \epsilon_c = \epsilon_0$, $\mu_a = \mu_b = \mu_c = \mu_0$, $\vec{E}^{inc} = \vec{y}e^{jkz}$.

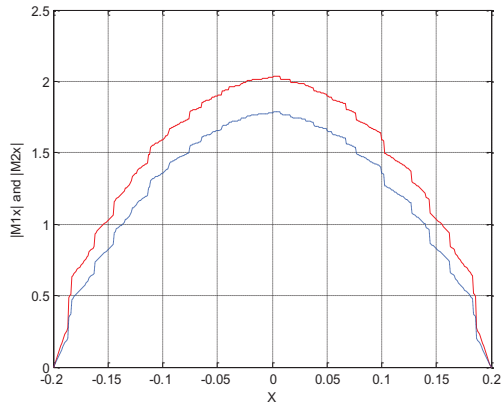


Fig. 13. Magnetic current on top aperture (solid line) and on bottom aperture (dashed line) along the x -axis for the problem in Fig. 12.

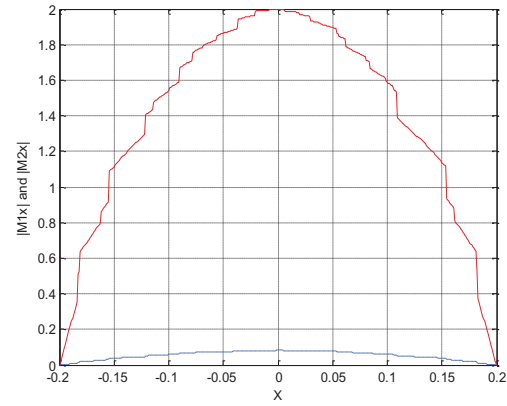


Fig. 16. Magnetic current on top aperture (solid line) and on bottom aperture (dashed line) along the x -axis for the problem in Fig. 15.

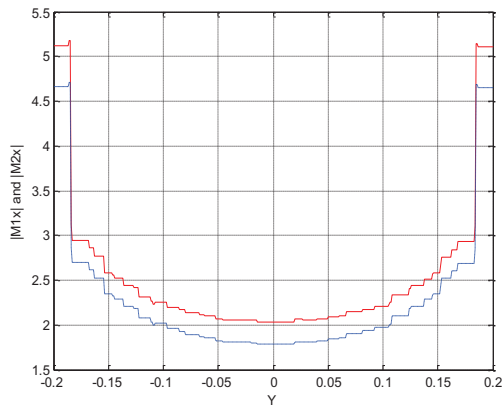


Fig. 14. Magnetic current on top aperture (solid line) and on bottom aperture (dashed line) along the y -axis for the problem in Fig. 12.

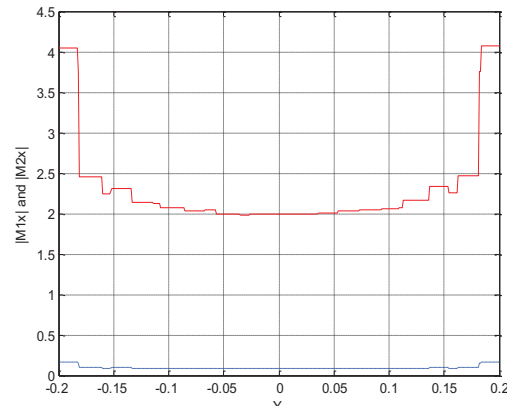


Fig. 17. Magnetic current on top aperture (solid line) and on bottom aperture (dashed line) along the y -axis for the problem in Fig. 15.

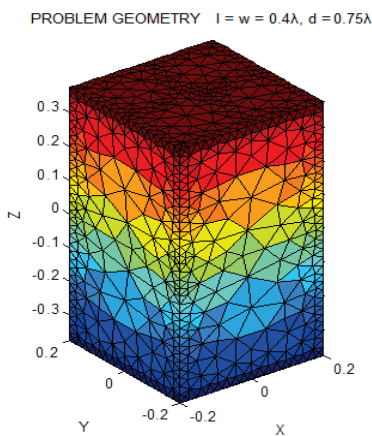


Fig. 15. Triangular meshing of the problem with square apertures (0.4λ -by- 0.4λ) on top and bottom; conductor thickness $d=0.75\lambda$, $\epsilon_a = \epsilon_b = \epsilon_c = \epsilon_0$, $\mu_a = \mu_b = \mu_c = \mu_0$, $\vec{E}^{inc} = \vec{y}e^{jkz}$.

As seen from the magnetic current plots, increasing the conductor thickness reduces the magnetic current on the bottom aperture and therefore reduces the tangential electric field on the bottom aperture. Reduction of the tangential electric field on bottom aperture is generally accompanied by reduction of the transmission coefficient.

The effect of meshing on convergence and many more numerical results are available in [11].

D. Results for circular aperture with a conic cavity

To prove the versatility of the method, a conic cavity in a thick conductor ($d=0.5\lambda$) with circular apertures on top and bottom with radii of $R=0.25\lambda$ and $r=0.125\lambda$ respectively is analyzed. The problem geometry is shown in Fig. 18. The top and bottom magnetic currents along x and y axes are given in Fig. 19 and Fig. 20. RCS and transmission coefficients plots are shown in Fig. 21 and Fig. 22.

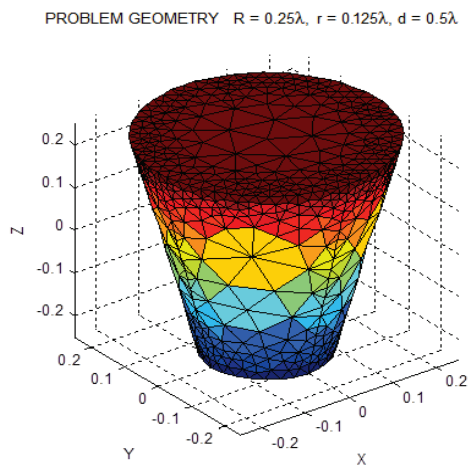


Fig. 18. Circular apertures with a conic cavity, $\vec{E}^{inc} = \vec{y}e^{jkz}$.

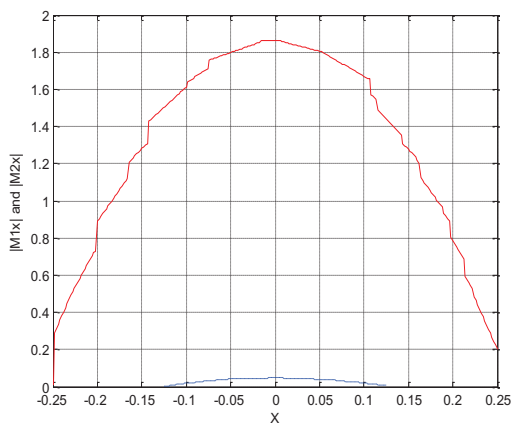


Fig. 19. Magnetic current on top aperture (solid line) and on bottom aperture (dashed line) along the x -axis for the problem in Fig. 18.

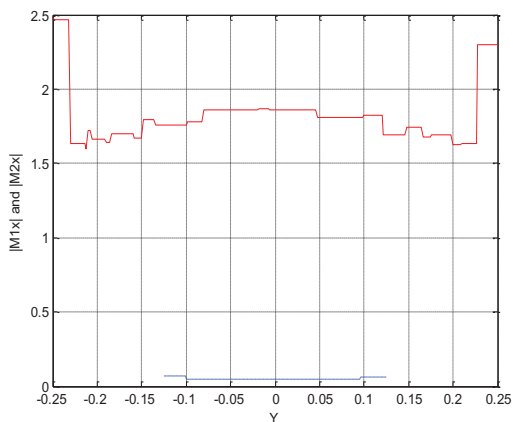


Fig. 20. Magnetic current on top aperture (solid line) and on bottom aperture (dashed line) along the y -axis for the problem in Fig. 18.

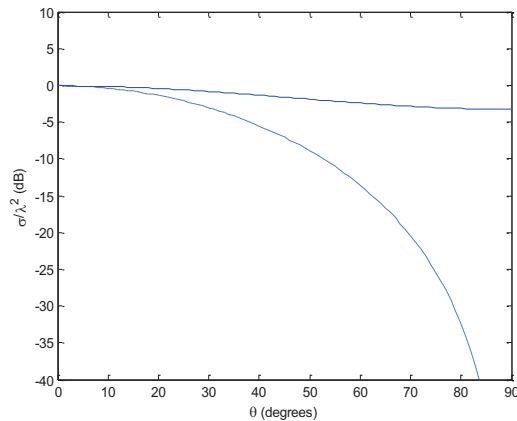


Fig. 21. Backscatter RCS of the structure in Fig. 18 as a function of incidence angle in the $\phi = 0^\circ$ plane; solid line: \vec{E}^{inc} is phi polarized; dashed line: \vec{E}^{inc} is theta polarized.

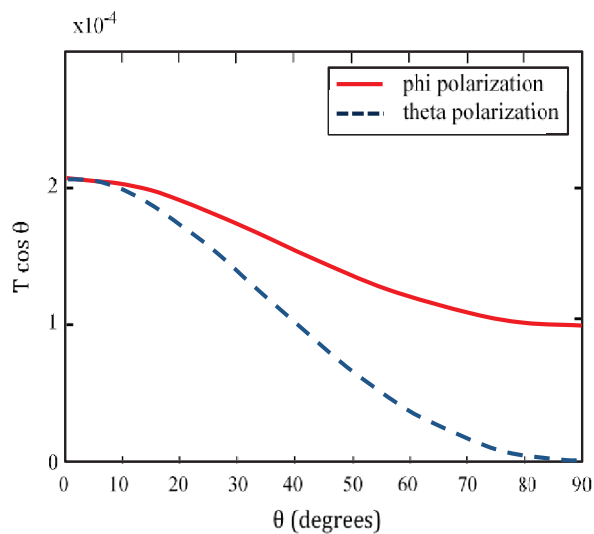


Fig. 22. Transmission coefficient plots of the structure in Fig. 18 as a function of incidence angle in the $\phi = 0^\circ$ plane; solid line: \vec{E}^{inc} is phi polarized; dashed line: \vec{E}^{inc} is theta polarized.

IV. CONCLUSION

A simple moment solution is given to numerically analyze the problem of electromagnetic scattering from and transmission through an arbitrarily shaped aperture in a thick perfectly conducting ground plane. Computed results for square, cross and circular apertures are presented. Results for circular aperture with a conic cavity are also presented. The above computed results cannot be predicted by a simple theory. However, the results show that the fields on the shadow side of the aperture are much smaller than those on the lit side even when the thickness of the ground plane is small.

The method of moments formulation introduced in this paper can give the same results as the numerical methods that use volumetric meshing such as FEM. Since for homogeneous bodies MoM with only surface meshing is possible, it can give results faster than FEM, especially when problems with large volumes are to be solved.

It is known that, numerical results obtained by MOM and surface equivalence formulation may give erroneous results due to some spurious internal resonances [12]. Such spurious results were avoided by monitoring the condition number of the moment matrix and the stability of the computed results as the size, frequency or the number of triangular patches were changed slightly.

REFERENCES

- [1] H. A. Bethe, "Theory of diffraction by small holes," *Phys. Rev.*, vol. 66, pp. 163-182, Oct. 1944.
- [2] E. Arvas and R. F. Harrington, "Computation of the magnetic polarizability of conducting disks and the electric polarizability of apertures," *IEEE Trans. Antennas Propag.*, vol. AP-31, no. 5, pp. 719-725, Sep. 1983.
- [3] R. F. Harrington and J. R. Mautz, "A generalized network formulation for aperture problems," *IEEE Trans. Antennas Propag.*, vol. AP-24, no. 6, pp. 870-873, Nov. 1976.
- [4] R. F. Harrington, *Field Computation by Moment Methods*, Macmillan, New York, 1968.
- [5] D. T. Auckland and R. F. Harrington, "Electromagnetic transmission through a filled slit in a conducting plane of finite thickness, TE case," *IEEE Trans. Microwave Theory Tech.*, vol. MTT-26, pp. 499-505, July 1978.
- [6] D. T. Auckland and R. F. Harrington, "A nonmodal formulation for electromagnetic transmission through a filled slot of arbitrary cross section in a thick conducting screen," *IEEE Trans. Microwave Theory Tech.*, vol. MTT-28, pp. 548-555, June 1980.
- [7] B. Park and H. J. Eom, "Electromagnetic transmission through multiple circular apertures in a thick conducting plane," *IEEE Trans. Antennas Propag.*, vol. 52, no. 4, pp. 1049-1055, 2004.
- [8] Ş. T. İmeci, F. Altunkılıç, J. R. Mautz, and E. Arvas, "Transmission through an arbitrarily shaped aperture in a conducting plane separating air and a chiral medium," *ACES Journal*, vol. 25, no. 7, pp. 587-599, July 2010.
- [9] J. M. Jin and J. L. Volakis, "Electromagnetic scattering by and transmission through a three-dimensional slot in a thick conducting plane," *IEEE Trans. Antennas Propag.*, vol. 39, no. 4, pp. 543-550, 1991.

- [10] R. F. Harrington, *Time-Harmonic Electromagnetic Fields*, McGraw-Hill, New York, 1961.
- [11] A. B. Olcen, *Method of Moments Analysis of an Aperture in a Thick Ground Plane*, Ph.D. Dissertation, Syracuse University, Syracuse, New York, 2012.
- [12] E. Arvas and J. R. Mautz, "On the non-uniqueness of the surface EFIE applied to multiple conducting and/or dielectric bodies," *AEU*, vol. 42, no. 6, pp. 364-369, Nov./Dec. 1988.



A. Burak Olcen received his B.Sc. in Electronics and Communication Engineering from Istanbul Technical University, Istanbul, Turkey in 1999, and his M.Sc. and Ph.D. from Syracuse University, New York, USA in 2002 and 2012 respectively. He worked for PPC as an RF Design Engineer between 2000 and 2007 in Syracuse, New York. He is currently the General Manager of RFMTEK, a research company in Bursa, Turkey. His research interests include electromagnetic theory, antennas, satellite and wireless communication. He has 12 US patents in RF/microwave field.



Ş. Taha İmeci received the B.Sc. degree in Electronics and Communications Engineering from Yildiz Technical University, Istanbul, Turkey in 1993, and the M.S.E.E. and Ph.D. degrees from Syracuse University, Syracuse, NY in 2001 and 2007, respectively.

He was with Anaren Microwave Inc., East Syracuse, NY from 2000 to 2002, Herley Farmingdale, New York from 2002 to 2003, PPC, Syracuse, NY from 2003 to 2005, and Sonnet Software Inc., Liverpool, NY from 2006 to 2007. His current research areas are microstrip patch antennas and electromagnetic theory.



Mesut Gokten was born in Tokat, Turkey in 1975. He graduated from Istanbul Technical University Electronics and Communications Engineering Dept. in 1997. He received his M.S.E.E. (with honors) and Ph.D. degrees from Syracuse University Electrical Engineering Dept. in 2003 and 2007, respectively and served as a Teaching and Research Assistant from August 2000 to

May 2005 at the same department. He was with Dielectric Laboratories, Inc. of Cazenovia, NY from May 2005 to August 2006. From August 2006 to March 2014, he was a Senior Researcher at the R&D and Satellite Dept. at Turksat AS, Ankara, Turkey. Currently, he is the Deputy Director at Tubitak Space Technologies Research Institute. His research is focused on computational electromagnetics, design and implementation of microwave devices and systems for satellite communications.

Joseph R. Mautz was born in Syracuse, NY in 1939. He received the B.S., M.S. and Ph.D. degrees in Electrical Engineering from Syracuse University, Syracuse, NY in 1961, 1965, and 1969 respectively.

Until July 1993, he was a Research Associate in the Department of Electrical and Computer Engineering of Syracuse University working on radiation and scattering problems. He is presently an Adjunct Professor in the Electrical Engineering and Computer Science Department at the same University. His primary fields of interest are electromagnetic theory and applied mathematics. He is a Member of the Applied Computational Electromagnetics Society (ACES).



Ercument Arvas received the B.S. and M.S. degrees from the Middle East Technical University, Ankara, Turkey in 1976 and 1979, respectively, and the Ph.D. degree from Syracuse University, Syracuse, NY in 1983, all in Electrical Engineering.

From 1984 to 1987, he was with the Electrical Engineering Department, Rochester Institute of Technology, Rochester, NY. He was with the EE Department of Syracuse University between 1987 and 2014. He is currently a Professor in the EE Department of Istanbul Medipol University. His research and teaching interests are in electromagnetic scattering and microwave devices.

Arvas is a Member of the Applied Computational Electromagnetics Society (ACES), and Fellow of IEEE and Electromagnetics Academy.

A VSIE Solution for EM Scattering Using the Multilevel Complex Source Beam Method

Z. H. Fan, Y. L. Hu, D. Z. Ding, and R. S. Chen

Department of Communication Engineering
Nanjing University of Science and Technology, Nanjing, 210094, China
eerschen@njjust.edu.cn

Abstract — Multilevel complex source beam (CSB) method is introduced to accelerate the volume-surface integral equation (VSIE) for the analysis of electromagnetic scattering from the composite structures comprising conductor and dielectric material. The field generated by each basis function or testing function is expressed by use of the equivalent point source defined over the complex sphere. The far interactions between basis functions and testing functions are replaced by the interactions between complex point sources, which can be calculated efficiently by taking advantage of the directionality of the complex point sources. The translation invariance property of Green's function is exploited to further improve efficiency. In numerical examples, the number of CSBs and truncation angle are given for each level, and the computational efficiency of the proposed method is validated by comparison with the conventional VSIE method.

Index Terms — Electromagnetic scattering, multilevel complex source beam, volume-surface integral equation.

I. INTRODUCTION

A lot of attention has been paid to the electromagnetic scattering from the composite structures comprising conductor and dielectric material for its wide range of applications. Two kinds of integral equations have been investigated to deal with composite objects. The surface integral equation (SIE) methods, represented by Poggio-Miller-Chang-Harrington-Wu-Tsai (PMCHWT) [1]-[2] integral equation, Müller integral equation [3], electric/magnetic current combined-field integral equation (JMCFIE) [4]-[5] etc., are effective for homogeneous or piecewise homogeneous composite objects, but they are unable to tackle the inhomogeneous materials. Although it requires more number of unknowns than SIE, the volume-surface integral equation (VSIE) method is more powerful since it can handle inhomogeneous dielectric material [6]-[7]. Meanwhile, VSIE uses only the free-space Green's function, which makes programming easier than SIE. This work aims to investigate a novel fast algorithm to speed up the analysis of the VSIE.

When analyzing the integral equation by the method of moments (MoM), the number of unknowns N increases with the electrical size of the scatterers, which prevents directly solving the large structure due to the storage complexity of $O(N^2)$ and the time complexity of $O(N^3)$. During the past several decades, many fast algorithms were proposed to analyze the electrically large scatterers, including the multilevel fast multipole method (MLFMM) [8]-[10], the adaptive integral method (AIM) [11], the adaptive cross approximation (ACA) [12]-[14], etc. Recently, complex source beam (CSB) method and its multilevel version [15]-[18] were proposed to speed up the analysis of perfect electric conductor (PEC) scattering problems. In this method, each basis function is expressed by complex point sources by invoking the extended equivalence theorem [15]. The equivalent point source locates at a complex point, which is obtained by introducing an imaginary spatial displacement to the real position vector. The field generated by complex point source, which is called as complex source beam, has intrinsically the directionality. The directionality of CSB is exploited to accelerate the calculation by replacing the interactions between the basis functions and testing functions belonging to far groups with the interactions between complex point sources. As compared with MLFMM, one advantage of multilevel CSB (MLCSB) is that it requires a lower memory to calculate the interactions between the well separated groups since they are calculated partly with MLCSB rather than globally with MLFMM. The other advantage lies in that MLCSB is free from a particular decomposition of the Green's function. Therefore it is applicable to radiation and scattering problems in inhomogeneous space, for which MLFMM is inconvenient.

In this paper, the solution of VSIE is accelerated by MLCSB for the analysis of the scattering from composite object. The complex point sources are first exploited to express the volume Schaubert-Wilton-Glisson (SWG) basis function [19]. The choices for the number and truncation angle of complex point sources are discussed

in detail. The computational efficiency is illustrated by comparison with the conventional VSIE.

This paper is organized as follows. In Section II, the basic theory and formulations of VSIE method accelerated by MLCSB are presented. Several numerical results are given to demonstrate the validity of the proposed method in Section III. Conclusions are summarized in Section IV.

II. THEORY AND FORMULATIONS

A. Volume-surface electric field integral equations

We aim to obtain the scattering electric field \vec{E}^s from an arbitrarily shaped composite structure under an incident plane wave \vec{E}^i as shown in Fig. 1. The symbol S denotes the surface of PEC parts of the composite structures, and V denotes the volume of dielectric parts. For dielectric media, the permittivity $\epsilon(\vec{r})$ is a function of spatial position and the permeability is μ_0 . ϵ_0 and μ_0 denotes the permittivity and permeability of free space.

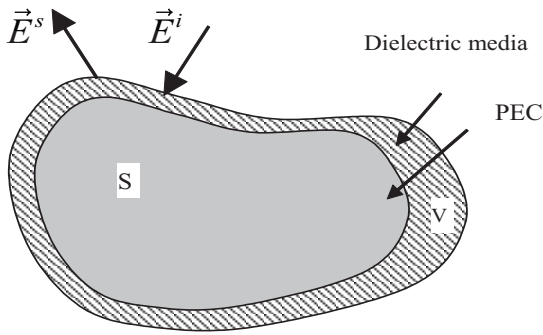


Fig. 1. Geometry of composite structure.

The VSIE [6]-[7] is built by enforcing both the consistency condition of electric field in dielectric V and the boundary condition for the electric field on the PEC surface S:

$$\vec{E}^i = \frac{\vec{D}(\vec{r})}{\epsilon(\vec{r})} + j\omega\mu_0 \int_V \vec{G}(\vec{r}, \vec{r}') \cdot \vec{J}_v(\vec{r}') d\vec{r}' + j\omega\mu_0 \int_S \vec{G}(\vec{r}, \vec{r}') \cdot \vec{J}_s(\vec{r}') d\vec{r}' \quad (\vec{r} \in V), \quad (1)$$

$$\vec{E}_{tan}^i = \left[\begin{array}{l} j\omega\mu_0 \int_V \vec{G}(\vec{r}, \vec{r}') \cdot \vec{J}_v(\vec{r}') d\vec{r}' \\ + j\omega\mu_0 \int_S \vec{G}(\vec{r}, \vec{r}') \cdot \vec{J}_s(\vec{r}') d\vec{r}' \end{array} \right]_{tan} \quad (\vec{r} \in S). \quad (2)$$

In equations (1) and (2), j denotes the imaginary unit, \vec{J}_v and \vec{J}_s are the electric current densities in the V and on the S, respectively. \vec{D} is the electric flux density, and $\vec{J}_v(\vec{r}) = j\omega K(\vec{r})\vec{D}(\vec{r})$, $K(\vec{r}) = [\epsilon(\vec{r}) - \epsilon_0]/\epsilon(\vec{r})$, ω is angular frequency. The subscript tan denotes taking the

tangential components of corresponding vector. $\vec{G}(\vec{r}, \vec{r}')$ is the three dimensional dyadic Green's function in free space:

$$\vec{G}(\vec{r}, \vec{r}') = (\vec{I} + \frac{1}{k^2} \nabla \nabla) \frac{e^{-jk|\vec{r}-\vec{r}'|}}{4\pi|\vec{r}-\vec{r}'|}, \quad (3)$$

where \vec{I} is the unit dyadic and k is the wavenumber in free space.

In the implementation of method of moments for solving the VSIE, \vec{D} is expanded by the SWG basis functions, and \vec{J}_s is expanded by the Rao-Wilton-Glisson (RWG) [20] basis functions. By use of the Galerkin's testing, equations (1) and (2) can be converted to the following matrix equation:

$$\begin{bmatrix} Z^{DD} & Z^{MD} \\ Z^{DM} & Z^{MM} \end{bmatrix} \begin{bmatrix} D^V \\ I^S \end{bmatrix} = \begin{bmatrix} v^V \\ v^S \end{bmatrix}, \quad (4)$$

where vectors D^V and I^S represent the coefficients of the basis functions which expanding \vec{D} and \vec{J}_s , respectively. v^V and v^S relate to incident field for dielectric and PEC parts, respectively.

B. Multilevel complex source beam method

MLCSB method is applied to accelerate the matrix-vector multiplication required by the iterative solver for solving equation (4). To implement the MLCSB scheme, octree grouping is utilized. Based on the extended equivalence theorem introduced in [15], a set of equivalence point sources are constructed for each basis function to generate the same electromagnetic fields in the interesting region. The point sources are distributed at a sphere with complex radius, which are constructed by extending the real coordinates of points on the sphere enclosing the grouping box into complex coordinates. The field generated by the point sources locating at the complex positions, or complex point sources, has directionality, in contrast to the isotropic field generated by real point sources. The directionality depends on the imaginary coordinates of point sources and can be exploited to develop fast algorithms.

The equivalence complex point sources are distributed at the surface of the complex sphere which locating at the angle of $[(n-1)\Delta\theta, (m-1)\Delta\varphi_n]$ with $n=1, \dots, N_\theta+1$ and $m=1, \dots, N_{\varphi_n}+1$, as shown in Fig. 2. Here $\Delta\theta=180^\circ/N_\theta$ is the angle interval of CSBs along the θ direction. N_θ is the number of CSBs along the θ direction. $\Delta\varphi_n=360^\circ/N_{\varphi_n}$ is the angle interval of CSBs along the φ direction which varying with the θ component of the position vector of points. $N_{\varphi_n} = \text{Int}[2(n+1)\sin(n-1)\Delta\theta]$ is the number of CSBs in the φ direction [18].

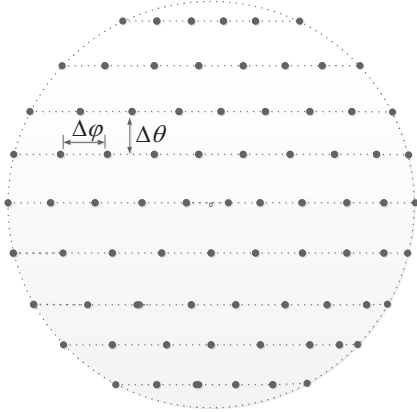


Fig. 2. The distribution of CSBs.

For PEC part, the interactions of observation RWG function $\vec{f}^S(\vec{r})$ and source RWG function $\vec{f}^S(\vec{r}')$ are represented by the CSBs as follows [16],[18]:

$$\int_{S_n} \vec{G}(\vec{r}, \vec{r}') \cdot \vec{f}_n^S(\vec{r}') ds' = \sum_{p=1}^P \vec{G}(\vec{r}, \vec{r}'_p) \cdot \vec{w}_{np}, \quad (5)$$

$$\begin{aligned} \int_{S_m} \vec{f}_m^S(\vec{r}) \cdot \sum_{p=1}^P \vec{G}(\vec{r}, \vec{r}'_p) \cdot \vec{w}_{np} ds \\ = \sum_{q=1}^Q \vec{w}_{mq} \cdot \sum_{p=1}^P \vec{G}(\vec{r}_q, \vec{r}'_p) \cdot \vec{w}_{np}. \end{aligned} \quad (6)$$

Similarly, for dielectric part, the interactions of observation SWG function $\vec{f}^V(\vec{r})$ and source SWG function $\vec{f}^V(\vec{r}')$ can be represented by the CSBs:

$$\int_{V_n} j\omega K(\vec{r}') \vec{G}(\vec{r}, \vec{r}') \cdot \vec{f}_n^V(\vec{r}') dv' = \sum_{p=1}^P \vec{G}(\vec{r}, \vec{r}'_p) \cdot \vec{u}_{np}, \quad (7)$$

$$\begin{aligned} \int_{V_m} \vec{f}_m^V(\vec{r}) \cdot \sum_{p=1}^P \vec{G}(\vec{r}, \vec{r}'_p) \cdot \vec{u}_{np} dv \\ = \sum_{q=1}^Q \vec{\eta}_{mq} \cdot \sum_{p=1}^P \vec{G}(\vec{r}_q, \vec{r}'_p) \cdot \vec{u}_{np}, \end{aligned} \quad (8)$$

P and Q are the numbers of CSBs for the basis and testing functions, respectively. They are set to the same value in this work, although they can have different values. $\vec{r}'_p = \vec{r}'_{np} - jb_0 \hat{r}'_{np}$, \vec{r}'_{np} is the location vector of the p -th CSB for the n -th basis function. \hat{r}'_{np} is a unit vector that from the center of these CSBs to the p -th CSB. b_0 determines the beam waist of the CSB. \vec{w}_{np} is the vector beam weight of the p -th CSB for the n -th RWG function $\vec{f}_n^S(\vec{r}')$, and \vec{u}_{np} is the vector beam weight of the p -th CSB for the n -th source SWG function along with its corresponding permittivity $j\omega K(\vec{r}') \vec{f}_n^V(\vec{r}')$, which distinguishes from the definition of \vec{w}_{np} . $\vec{\eta}_{mq}$ is

the vector beam weight of the q -th CSB for the m -th observation SWG basis function. In the implementation, the expressions of impedance matrices for far field parts in (4) can be replaced by the interactions between CSBs, and listed as follows:

$$Z_{nn}^{DD} = j\omega\mu_0 \sum_{q=1}^Q \vec{\eta}_{mq} \cdot \sum_{p=1}^P \vec{G}(\vec{r}_q, \vec{r}'_p) \cdot \vec{u}_{np}, \quad (9)$$

$$Z_{nn}^{DM} = j\omega\mu_0 \sum_{q=1}^Q \vec{w}_{mq} \cdot \sum_{p=1}^P \vec{G}(\vec{r}_q, \vec{r}'_p) \cdot \vec{u}_{np}, \quad (10)$$

$$Z_{nn}^{MD} = j\omega\mu_0 \sum_{q=1}^Q \vec{\eta}_{mq} \cdot \sum_{p=1}^P \vec{G}(\vec{r}_q, \vec{r}'_p) \cdot \vec{w}_{np}, \quad (11)$$

$$Z_{nn}^{MM} = j\omega\mu_0 \sum_{q=1}^Q \vec{w}_{mq} \cdot \sum_{p=1}^P \vec{G}(\vec{r}_q, \vec{r}'_p) \cdot \vec{w}_{np}. \quad (12)$$

Now, the matrix equations can be decomposed into near and far field parts:

$$\left\{ [Z_{Near}] + \begin{bmatrix} \eta Tu & \eta Tw \\ wTu & wTw \end{bmatrix} \right\} \cdot \begin{bmatrix} D \\ I \end{bmatrix} = \begin{bmatrix} v^V \\ v^S \end{bmatrix}, \quad (13)$$

T is the transfer matrix and denotes the interactions between the beams for the well separated groups [16],[18]. To compute the interactions between two well separated groups M and N with acceptable accuracy [18], only the interactions of the CSBs within the truncation angle $\pm\theta$, are required due to their radiation directionality, as shown in Fig. 3. The MLCSB method is realized with the octree grouping technique similar to MLFMM [8]. In the finest level, the interactions of self group and near-field groups are computed by the method of moments directly while the interactions of the well separated groups are computed by the CSB method in corresponding levels.

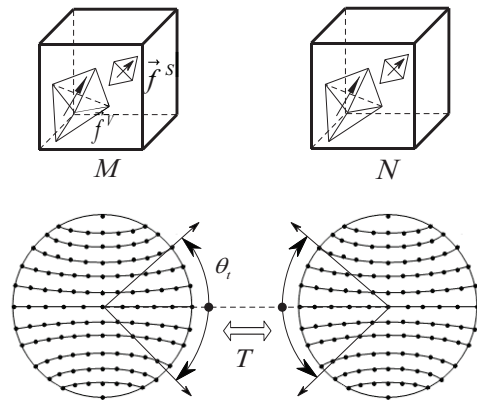


Fig. 3. The interactions between two far field groups by CSBs within $\pm\theta$.

The translation invariance property of Green's function is utilized to further improve the efficiency. The number of different interactions between the given group and all its far-field groups at the same level is

$7^2 \cdot 3^2 = 40$ for two-dimension models, and is $7^3 \cdot 3^3 = 316$ for three-dimension models. Moreover, using the symmetry property of the Green's function, only 12 transfer matrices need to be computed and stored for two-dimension problems as shown in Fig. 4, and 56 transfer matrices for three-dimension problems [18].

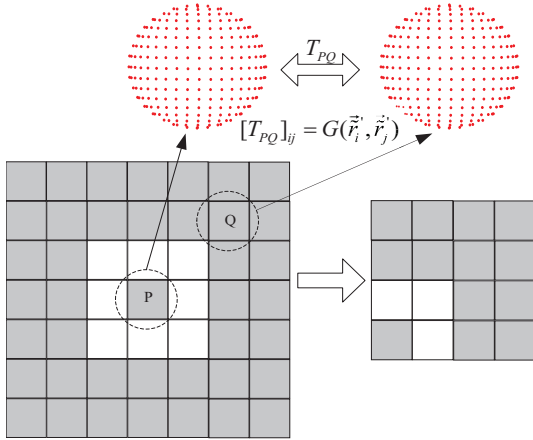


Fig. 4. Interactions between group P and its far field groups.

III. NUMERICAL RESULTS

In this section, two numerical examples are presented to validate the accuracy and efficiency of the proposed MLCSB accelerated VSIE method. All calculations are performed on the personal computer with 2.67 GHz central processing unit (CPU) and 8 GB random access memory (RAM).

Firstly, consider the electromagnetic scattering from a PEC sphere with the radius 0.15 m, coated with a dielectric layer with the thickness 0.03 m and relative permittivity $\epsilon_r = 2$. The incident plane wave operates at the frequency of 1 GHz, and it propagates along z direction with vertical polarization. In our analysis, the number of total unknown is 16905, in which 14491 for dielectric part and 2214 for PEC part. The $\Delta\theta$ value of CSBs is 30° , and the truncation angle θ_t is 160° . The values of bistatic RCS normalized to square wavelength obtained from the MLCSB accelerated VSIE, the Mie series and software FEKO are shown in Fig. 5 and they are in good agreement. The storage requirement and computational time are listed in Table 1. It can be observed that the CSB accelerated VSIE method requires about 62.6% storage and 73.7% time cost less than the conventional VSIE method.

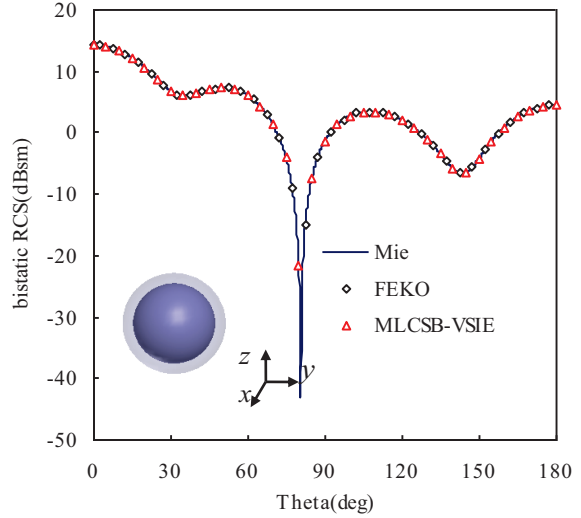


Fig. 5. The bistatic RCS of coated sphere ($\phi = 0$), obtained from proposed method, Mie series and software FEKO.

Table 1: Computational efficiency comparison (number of unknowns: 16905)

| | CPU Time (s) | Memory (GB) |
|------------|--------------|-------------|
| VSIE | 1495 | 2.3 |
| MLCSB-VSIE | 392 | 0.86 |

In order to investigate the choices of $\Delta\theta$ and θ_t for each level of MLCSB, the scattering from coated cuboids with four different sizes are computed as the second example. The size of the grouping box at the finest level is kept to 0.18 wavelength. The number of unknowns and the adopted number of level increase as the size of the structure increases. The structures are all illuminated by a vertical polarization plane wave along z direction and the frequency is 300 MHz. Some structural and computational parameters are listed in Table 2. All the structures are coated by a dielectric layer with relative permittivity of $\epsilon_r = 2$ and thickness of 0.05 m.

Table 2: Parameters of the coated cuboids

| | Dimension of PEC Part (unit: m) | Number of Unknowns | Number of Levels |
|---------|---------------------------------|--------------------|------------------|
| Model 1 | 0.6*0.3*0.3 | 8794 | 1 |
| Model 2 | 1.2*0.3*0.3 | 15128 | 2 |
| Model 3 | 2.4*0.3*0.3 | 27913 | 3 |
| Model 4 | 4.8*0.3*0.3 | 53454 | 4 |

Here, the relative root mean square (RRMS) error is exploited to compare the accuracy of the methods, and which is defined as:

$$\sqrt{\frac{1}{n} \sum_{i=1}^n |a_i - b_i|^2 / |b_i|^2}, \quad (14)$$

where a_i and b_i are the bistatic RCS values (unit: m^2) of the proposed method and conventional VSIE method, respectively, and n denotes the number of observation points. To determine the appropriate values of $\Delta\theta$ and θ_i for each level, we first fix θ_i as 180° to prevent the truncating error and check the RCS accuracy with different $\Delta\theta$. When analyzing the proper $\Delta\theta$ for a higher level, the values of $\Delta\theta$ for the lower levels are chosen as the maximum $\Delta\theta$ value satisfying the RRMS error less than 0.01 for the corresponding low level models. The RRMS error curves for different $\Delta\theta$ at different levels are shown in Fig. 6. From Fig. 6, we can find that the $\Delta\theta$ values can be chosen as $30^\circ, 22.5^\circ, 20^\circ, 15^\circ$ from level 1 to level 4 to ensure the RRMS error less than 0.01. Then we fix $\Delta\theta$ to the values for corresponding levels, and check the RCS accuracy with different θ_i for each level. The RRMS error curves for different θ_i are shown in Fig. 7, and it can be concluded that the θ_i values can be chosen as $160^\circ, 140^\circ, 100^\circ$ and 80° from level 1 to 4, respectively, to ensure the RRMS error less than 0.01. The bistatic RCS curves of model 3 calculated with the above $\Delta\theta$ and θ_i are shown in Fig. 8. Good agreement is observed between MLCBSB accelerated VSIE method and the conventional method. The memory requirement and total CPU time for two methods are given in Fig. 9. It can be observed that the MLCBSB accelerated VSIE method requires about much less storage and time less than the conventional VSIE does.

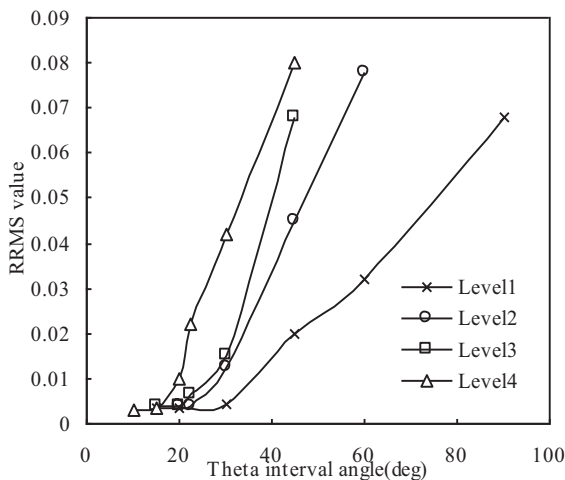


Fig. 6. The RRMS values of bistatic RCS for different theta angle interval with different levels.

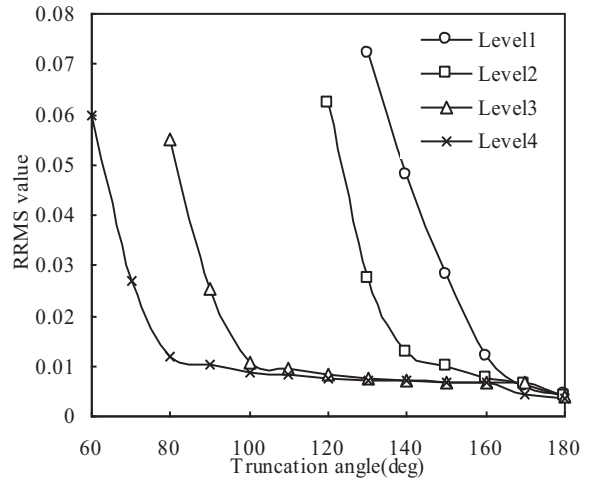


Fig. 7. The RRMS values of bistatic RCS for different truncation angle with different levels.

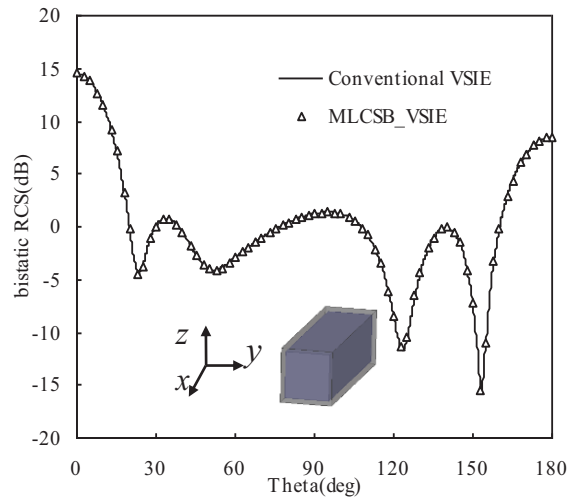
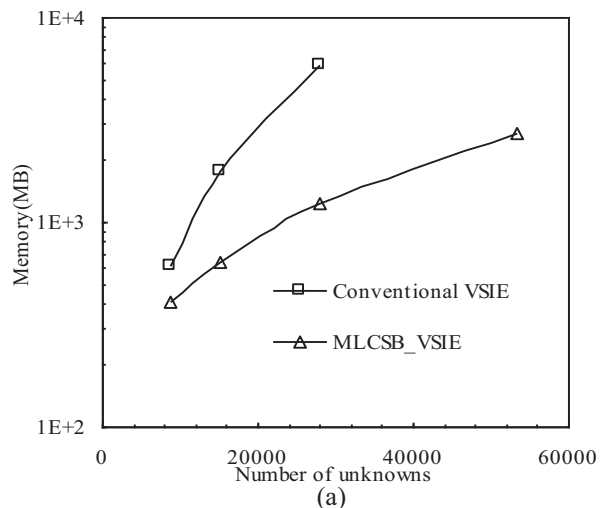


Fig. 8. The bistatic RCS of model 3 ($\phi=0$).



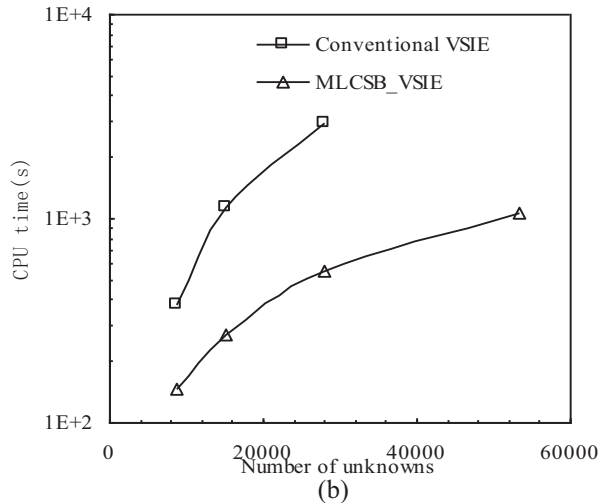


Fig. 9. The comparisons of consumption for different models with different number of unknowns: (a) memory and (b) CPU time.

IV. CONCLUSION

In this paper, the MLCSB accelerated VSIE method is utilized to efficiently analyze the electromagnetic scattering from composite structures comprising PEC and dielectric material. The parameter values of MLCSB method are discussed in detail. The comparisons of memory consumption and CPU time with conventional VSIE are given. From the numerical results, the accuracy and efficiency of the proposed scheme are demonstrated.

REFERENCES

- [1] P. L. Huddleston, L. N. Medgyesi-Mitschang, and J. M. Putnam, "Combined field integral equation formulation for scattering by dielectrically coated conducting bodies," *IEEE Trans. Antennas Propag.*, vol. 34, no. 4, pp. 510-520, Apr. 1986.
- [2] K. C. Donopudi, J.-M. Jin, and W. C. Chew, "A higher order multilevel fast multipole algorithm for scattering from mixed conducting/dielectric bodies," *IEEE Trans. Antennas Propag.*, vol. 51, no. 10, pp. 2814-2821, Oct. 2003.
- [3] P. Ylä-Oijala and M. Taskinen, "Well-conditioned Muller formulation for electromagnetic scattering by dielectric objects," *IEEE Trans. Antennas Propag.*, vol. 53, no. 10, pp. 3316-3323, 2005.
- [4] P. Ylä-Oijala and M. Taskinen, "Application of combined field integral equation for electromagnetic scattering by dielectric and composite objects," *IEEE Trans. Antennas Propag.*, vol. 53, no. 3, pp. 1168-1173, 2005.
- [5] P. Ylä-Oijala, M. Taskinen, and J. Sarvas, "Multilayered media Green's functions for MPIE with general electric and magnetic sources by the Hertz potential approach," *Progress In Electromagnetics Research*, vol. 33, pp. 141-165, 2001.
- [6] C. C. Lu and W. C. Chew, "A coupled surface-volume integral equation approach for the calculation of electromagnetic scattering from composite metallic and material targets," *IEEE Trans. Antennas Propag.*, vol. 48, pp. 1866-1868, 2000.
- [7] C. Luo and C. C. Lu, "Electromagnetic scattering computation using a hybrid surface and volume integral equation formulation," *Applied Computational Electromagnetics Society (ACES) Journal*, vol. 22, no. 3, pp. 340-349, 2007.
- [8] J. M. Song and W. C. Chew, "Fast multipole method solution using parametric geometry," *Microwave and Optical Technology Letters*, vol. 7, no. 16, pp. 760-765, 1994.
- [9] J. M. Song, C. C. Lu, and W. C. Chew, "Multilevel fast multipole algorithm for electromagnetic scattering by large complex objects," *IEEE Trans. Antennas Propag.*, vol. 45, pp. 1488-1493, 1997.
- [10] D. Z. Ding, S. F. Tao, and R. S. Chen, "Fast analysis of finite and curved frequency-selective surfaces using the VSIE with MLFMA," *International Journal of Numerical Modelling: Electronic Networks, Devices and Fields*, vol. 24, no. 5, pp. 425-436, 2011.
- [11] E. Bleszynski, M. Bleszynski, and T. Jaroszewicz, "AIM: adaptive integral method for solving large-scale electromagnetic scattering and radiation problems," *Radio Sci.*, vol. 31, pp. 1225-1251, 1996.
- [12] K. Zhao, M. N. Vouvakis, and J. F. Lee, "The adaptive cross approximation algorithm for accelerated method of moments computations of EMC problems," *IEEE Transactions on Electromagnetic Compatibility*, vol. 47, no. 4, pp. 763-773, 2005.
- [13] J. M. Tamayo, A. Heldring, and J. M. Rius, "Multilevel adaptive cross approximation (MLACA)," *IEEE Trans. Antennas Propag.*, vol. 59, no. 12, pp. 4600-4608, Feb. 2004.
- [14] Z. N. Jiang, R. S. Chen, Z. H. Fan, Y. Y. An, M. M. Zhu, and K. W. Leung, "Modified adaptive cross approximation algorithm for analysis of electromagnetic problems," *Applied Computational Electromagnetics Society (ACES) Journal*, vol. 26, no. 2, pp. 160-169, 2011.
- [15] K. Tap, *Complex Source Point Beam Expansions for Some Electromagnetic Radiation and Scattering Problems*, Ph.D. dissertation, Ohio State Univ., Columbus, OH, USA, 2007.
- [16] K. Tap, P. H. Pathak, and R. J. Burkholder, "Complex source beam-moment method procedure for accelerating numerical integral equation solutions of radiation and scattering problems," *IEEE Trans. Antennas Propag.*, vol. 62, pp.

2052-2062, 2014.

- [17] D. Z. Ding, Z. H. Fan, S. F. Tao, and R. S. Chen, "Complex source beam method for EM scattering from PEC objects," *Antennas and Wireless Propagation Letters*, vol. 14, pp. 346-349, 2015.
- [18] Z. H. Fan, X. Hu, and R. S. Chen, "Multilevel complex source beam method for electromagnetic scattering problems," *Antennas and Wireless Propagation Letters*, vol. 14, pp. 843-846, 2015.
- [19] D. H. Schaubert, D. R. Wilton, and A. W. Glisson, "A tetrahedral modeling method for electromagnetic scattering by arbitrarily shaped inhomogeneous dielectric bodies," *IEEE Trans. Antennas Propag.*, vol. 32, pp. 77-85, 1984.
- [20] S. M. Rao, D. R. Wilton, and A. W. Glisson, "Electromagnetic scattering by surfaces of arbitrary shape," *IEEE Trans. Antennas Propag.*, vol. 30, no. 3, pp. 409-418, 1982.



Zhenhong Fan was born in Jiangsu, China, in 1978. He received the M.Sc. and Ph.D. degrees in Electromagnetic Field and Microwave Technique from Nanjing University of Science and Technology (NJUST), Nanjing, China, in 2003 and 2007, respectively.

During 2006, he was with the Center of Wireless Communication in the City University of Hong Kong, Kowloon, as a Research Assistant. He is currently an Associate Professor with the Electronic Engineering of NJUST. He is the author or co-author of over 20 technical papers. His current research interests include computational electromagnetics, electromagnetic scattering and radiation.



Yanlong Hu received the B.Sc. degree in Information and Computing Sciences from Nanjing University of Information Science & Technology, Nanjing, China, in 2011. He is currently working towards the Ph.D. degree in Electro-

magnetic Fields and Microwave Technology at the School of Electrical Engineering and Optical Technique, Nanjing University of Science and Technology.

His current research interests include computational electromagnetics, antennas, electromagnetic scattering and propagation.



Dazhi Ding was born in Jiangsu, China, in 1979. He received the B.S. and Ph.D. degrees in Electromagnetic Field and Microwave Technique from Nanjing University of Science and Technology (NJUST), Nanjing, China, in 2002 and 2007, respectively.

During 2005, he was with the Center of Wireless Communication in the City University of Hong Kong, Kowloon, as a Research Assistant. He is currently an Associate Professor with the Electronic Engineering of NJUST. He is the author or co-author of over 30 technical papers. His current research interests include computational electromagnetics, electromagnetic scattering, and radiation.



Rushan Chen (M'01) was born in Jiangsu, China. He received the B.Sc. and M.Sc. degrees from the Department of Radio Engineering, Southeast University, China, in 1987 and 1990, respectively, and the Ph.D. degree from the Department of Electronic Engineering, City

University of Hong Kong, in 2001.

He joined the Department of Electrical Engineering, Nanjing University of Science and Technology (NJUST), China, where he became a Teaching Assistant in 1990 and a Lecturer in 1992. Since September 1996, he has been a Visiting Scholar with the Department of Electronic Engineering, City University of Hong Kong, first as Research Associate, then as a Senior Research Associate in July 1997, a Research Fellow in April 1998, and a Senior Research Fellow in 1999. From June to September 1999, he was also a Visiting Scholar at Montreal University, Canada. In September 1999, he was promoted to Full Professor and Associate Director of the Microwave and Communication Research Center in NJUST, and in 2007, he was appointed Head of the Department of Communication Engineering, NJUST. He was appointed as the Dean in the School of Communication and Information Engineering, Nanjing Post and Communications University in 2009. And in 2011, he was appointed as Vice Dean of the School of Electrical Engineering and Optical Technique, Nanjing University of Science and Technology. His research interests mainly include microwave millimeter-wave systems, measurements, antenna, RF-integrated circuits, and computational electromagnetics. He has authored or co-authored more than 200 papers, including over 140 papers in international journals.

Chen received the Science and Technology Advance Prize several times given by the National Military

Industry Department of China, the National Education Committee of China, and Jiangsu Province. He is the recipient of the Foundation for China Distinguished Young Investigators presented by the National Science Foundation (NSF) of China in 2003. In 2008, he became a Chang-Jiang Professor under the Cheung Kong Scholar Program awarded by the Ministry of Education, China. Besides, he was selected as a Member of Electronic Science and Technology Group by

Academic Degree Commission of the State Council in 2009. Chen is a Fellow of the Chinese Institute of Electronics (CIE), Vice-Presidents of Microwave Society of CIE and IEEE MTT/APS/EMC Nanjing Chapter. He serves as the Reviewer for many technical journals such as IEEE Trans. on AP and MTT, Chinese Physics etc., and now serves as an Associate Editor for the International Journal of Electronics.

Fast EM Scattering Analysis for the Hard Targets in a Layered Medium by Using the Hierarchical Vector Basis Functions

Liping Zha, Rushan Chen, and Ting Su

Department of Communication Engineering
Nanjing University of Science and Technology, Nanjing, 210094, China
daisy918@163.com, eerschen@njust.edu.cn, 290453607@qq.com

Abstract — This paper presents an efficient algorithm combining a higher order method of moments (MoM) with the adaptive cross approximation-singular value decomposition (ACA-SVD) algorithm for the three-dimensional perfect electric conductor (PEC) targets located in a planar layered medium. An efficient set of hierarchical divergence-conforming vector basis functions based on curved triangular mesh is used to expand the induced surface electric current density on the metal surface of the target in layer medium. A three level discrete complex images methods (DCIM) is applied to efficiently obtain the closed form spatial Green's functions. To be able to solve the electrically large problems, the ACA-SVD algorithm is proposed to accelerate the matrix-vector multiplication and reduce the memory requirements when the corresponding matrix equation is solved by a Krylov-subspace iterative method. The electromagnetic scattering from the practical model of hard targets buried in a lossy medium is analyzed in this paper, and numerical examples demonstrate the accuracy and efficiency of the proposed technique for the electrically large scattering problems in layered medium.

Index Terms — Complex electromagnetic scattering, hierarchical vector basis functions, modified adaptive cross approximation (ACA) algorithm.

I. INTRODUCTION

The development of an efficient method for computing electromagnetic scattering from targets located in layered medium has received intense attention during the past decades because of its important applications in many areas, such as, remote sensing, target identification, geophysical exploration, microwave imaging, and etc. [1]-[3]. Even so, the fast and accurate detection of arbitrary shaped electrically large hard targets in a multilayered media is still a challenging problem, and only very few of papers which truly deal with the electrically large electromagnetic scattering problems in a multilayered media were published in the past years [1]-[2]. The method of moments (MoM) [4] is one of the

most widely used techniques for solving electromagnetic scattering problems since they require fewer unknowns than differential equations solvers. Traditional MoM solution of the surface integral equation (SIE) utilizes the Rao-Wilton-Glisson (RWG) [4] or rooftop basis functions [5] that based on flat triangular or quadrilateral patches to expand the surface current density, which belongs to the low-order method. When the electrical size of the problem is very large, plane triangles used to discretize the surface will produce a large number of unknowns, but cannot provide enough flexibility and efficiency in modeling curved structures. Further more, the accuracy of solution while using the low-order bases is improved slowly with increases in the number of unknowns. By using higher order basis functions which are defined on curved elements to expand the unknowns, the higher order method [6] essentially reduces the computational unknowns, and enhances the accuracy of the solution at the same time. Higher order MoM solutions of the SIE have been successfully used to solve electrically large electromagnetic problems in free space [7]-[9]. Jorgensen [3] also uses the higher order technique to analyze the electromagnetic scattering problems for metallic objects in layered media, but hasn't combined any fast algorithm.

With N being the number of unknowns of the MoM solution, the computational complexity is $O(N^2)$ when an iterative method is applied. To reduce the memory requirement and speed up the matrix-vector multiplication, fast algorithms should be involved. One of the most popular techniques is fast multipole method (FMM) [10] or multilevel fast multipole algorithm (MLFMA) [11]-[14]. The MLFMA is based on the vector addition theorem and the plane wave expansion theory, which means the formulation, implementation, and occasionally performance of the MLFMA depends on a priori knowledge of Green's functions. Therefore, when the EM scattering problem is discussed in layered media, the MLFMA cannot be directly applicable due to the more complicated Green's functions. Fast fourier transform (FFT) based algorithms also have been used to accelerate the analysis of scattering from objects in

layered media [1]-[2], and the parallel implementation of the AIM was used to deal with the electrically large scattering problems in [1]. In contrast with the MLFMA and FFT based algorithms, the low-rank approximation based adaptive cross approximation (ACA) algorithm [15] is purely algebraic and, does not depend on the formulation of Green's functions. In general, the ACA requires considerable computation time and memory. To improve the efficiency, the ACA-SVD was studied by Bebendorf [16], which efficiently recompresses the matrices of ACA using the SVD technique. In this paper, the ACA-SVD technique is presented for solving electromagnetic problems in layered medium.

This paper is organized as follows. In Section II, we present the higher order hierarchical vector basis functions and the modified ACA formulations for electrically large scattering problems in layered medium. A three level discrete complex images methods (DCIM) is applied to efficiently obtain the closed form spatial Green's functions without any quasi-static and surface-wave extraction, that part has been reported in the conference paper [17]. A set of hierarchical divergence-conforming vector basis functions based on curvilinear triangle elements are used to expand the induced current density on the surface of targets in layered medium. The ACA-SVD technique is employed to reduce the memory requirements and computational complexity. In Section III, we present several results to verify the proposed method's accuracy and efficiency. In this section, the computational complexity and memory requirements of the presented method are discussed and compared with existing fast algorithms, the adaptive integral method (AIM), for electrically large scattering problems in layered medium. Finally, conclusions are summarized in Section IV.

II. THEORY AND FORMULATION

A. Integral equation in layered medium and higher order MoM formulation

Consider an arbitrarily shaped 3-D perfect electric conductor (PEC) targets located in the p th layer of a layered medium, as shown in Fig. 1. The background medium has N parallel layers with independent permittivity and permeability $(\epsilon_p, \mu_p, p = 1, \dots, N)$. Consider a general purpose scattering problem of a time-harmonic electromagnetic field \mathbf{E}^{inc} , incident on the PEC structure. Using the continual boundary condition for the tangential component of the total electric field on the PEC surface, we formulate the mixed potential electric field integral equation (MPIE) [18], as shown:

$$\hat{\mathbf{n}} \times [j\omega \mathbf{A}(\mathbf{r}) + \nabla \phi(\mathbf{r})] = \hat{\mathbf{n}} \times \mathbf{E}^{inc}(\mathbf{r}). \quad (1)$$

The vector magnetic potential $\mathbf{A}(\mathbf{r})$ and the scalar electric potential $\phi(\mathbf{r})$ due to the surface current density $\mathbf{J}(\mathbf{r}')$ can be expressed as:

$$\mathbf{A}(\mathbf{r}) = \int_{S'} \bar{\mathbf{G}}^A(\mathbf{r}, \mathbf{r}') \cdot \mathbf{J}(\mathbf{r}') dS', \quad (2)$$

$$\phi(\mathbf{r}) = \int_{S'} K^\phi(\mathbf{r}, \mathbf{r}') \nabla' \cdot \mathbf{J}(\mathbf{r}') dS', \quad (3)$$

where $\mathbf{r} = \rho \hat{\boldsymbol{\rho}} + z \hat{\mathbf{z}}$ and $\mathbf{r}' = \rho' \hat{\boldsymbol{\rho}} + z' \hat{\mathbf{z}}$ denote observer and source points, respectively. $\bar{\mathbf{G}}^A(\mathbf{r}, \mathbf{r}')$ is the dyadic green function and $K^\phi(\mathbf{r}, \mathbf{r}')$ is the scalar Green's functions in layered medium. These functions are derived using formulation C by Michalski and Zheng [15], and the traditional form of $\bar{\mathbf{G}}^A(\mathbf{r}, \mathbf{r}')$ and $K^\phi(\mathbf{r}, \mathbf{r}')$ are given by:

$$\bar{\mathbf{G}}^A(\mathbf{r}, \mathbf{r}') = (\hat{\mathbf{x}}\hat{\mathbf{x}} + \hat{\mathbf{y}}\hat{\mathbf{y}}) G_{xx}^A + \hat{\mathbf{z}}\hat{\mathbf{x}} G_{zx}^A + \hat{\mathbf{z}}\hat{\mathbf{y}} G_{zy}^A + \hat{\mathbf{z}}\hat{\mathbf{z}} G_{zz}^A, \quad (4)$$

$$K^\phi(\mathbf{r}, \mathbf{r}') = K^\phi(\rho; z|z'), \quad (5)$$

where

$$\begin{aligned} G_{xx}^A(\rho; z|z') &= S_0 \left\{ \tilde{G}_{vv}^A(k_\rho; z|z') \right\}, \\ G_{zz}^A(\rho; z|z') &= S_0 \left\{ \tilde{G}_{zz}^A(k_\rho; z|z') \right\}, \\ G_{zx}^A(\rho; z|z') &= -j \cos \varphi S_1 \left\{ \tilde{G}_{zu}^A(k_\rho; z|z') \right\}, \\ G_{zy}^A(\rho; z|z') &= -j \sin \varphi S_1 \left\{ \tilde{G}_{zu}^A(k_\rho; z|z') \right\}, \\ K^\phi(\rho; z|z') &= S_0 \left\{ \tilde{K}^\phi(k_\rho; z|z') \right\}. \end{aligned} \quad (6)$$

S_n denotes Sommerfeld integral (SI) of order n and is defined as:

$$S_n \left\{ \tilde{f}(k_\rho) \right\} = \frac{1}{2\pi} \int_0^\infty \tilde{f}(k_\rho) J_n(k_\rho \rho) k_\rho dk_\rho, \quad (7)$$

J_n is the Bessel function of order n . The three level discrete complex images methods (DCIM) proposed in [17] are used to calculate the SIs and obtain the closed form spatial Green's functions. The three levels DCIM can approximate the contribution of both the lateral waves and surface waves, and it is more stable and accurate than traditional method for the lossy stratified media [17].

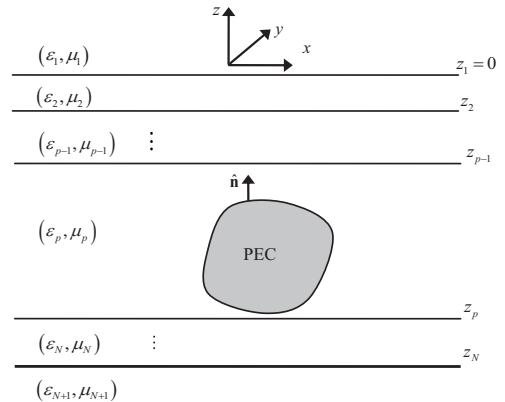


Fig. 1. Arbitrarily shaped 3-D PEC target in a layered medium.

To solve the Equation (1), the surface of scatterer should be discretized, and the induced current density should be expanded by basis functions. The PEC body in layered media is meshed using curved triangular patches of second order with associated parametric curvilinear coordinate systems defined by $0 \leq \xi_1, \xi_2, \xi_3 \leq 1$. The efficient higher order (HO) hierarchical divergence-conforming vector basis functions defined on curvilinear triangular patches used here were proposed in [9], and that have been proved could provide well-conditional linear system for iterative solution. For sake of simplicity, we only give the expression of hierarchical basis functions of order 1.5. The rest higher order's expressions of these basis functions can be found in [9]. The hierarchical basis functions of order 1.5 for one curved triangular element are defined as:

$$\begin{aligned} \mathbf{f}_{1,0}^e(\mathbf{r}') &= \frac{1}{J} \left[(\xi_1 - 1) \frac{\partial \mathbf{r}'}{\partial \xi_1} + \xi_2 \frac{\partial \mathbf{r}'}{\partial \xi_2} \right], \quad \mathbf{f}_{1,1}^e(\mathbf{r}') = \sqrt{3} (\xi_2 - \xi_3) \mathbf{f}_{1,0}^e(\mathbf{r}'), \\ \mathbf{f}_{2,0}^e(\mathbf{r}') &= \frac{1}{J} \left[\xi_1 \frac{\partial \mathbf{r}'}{\partial \xi_1} + (\xi_2 - 1) \frac{\partial \mathbf{r}'}{\partial \xi_2} \right], \quad \mathbf{f}_{2,1}^e(\mathbf{r}') = \sqrt{3} (\xi_3 - \xi_1) \mathbf{f}_{2,0}^e(\mathbf{r}'), \\ \mathbf{f}_{3,0}^e(\mathbf{r}') &= \frac{1}{J} \left[\xi_1 \frac{\partial \mathbf{r}'}{\partial \xi_1} + \xi_2 \frac{\partial \mathbf{r}'}{\partial \xi_2} \right], \quad \mathbf{f}_{3,1}^e(\mathbf{r}') = \sqrt{3} (\xi_1 - \xi_2) \mathbf{f}_{3,0}^e(\mathbf{r}'), \\ \mathbf{f}_{1,0}^f(\mathbf{r}') &= 2\sqrt{3}\xi_1 \mathbf{f}_{1,0}^e(\mathbf{r}'), \quad \mathbf{f}_{2,0}^f(\mathbf{r}') = 2\sqrt{3}\xi_2 \mathbf{f}_{2,0}^e(\mathbf{r}'), \end{aligned} \quad (8)$$

where the superscript denotes the edge or face-based functions, the first subscript denotes the local edge number for a fixed triangular element, the second subscript of the edge-based functions and the sum of the two number of the face-based functions' second subscript are both denote order of hierarchical polynomials, the \mathbf{r}' is the position vector of the source point determined by normalized face coordinated on curved parametric triangular patch, J is the element Jacobian. Obviously, the lowest order expansion (called order 0.5) is included in expression (8) (see the first three functions) and they are the well-known curvilinear Rao-Wilton-Glisson (RWG) functions [19]. The unknown current density $\mathbf{J}(\mathbf{r}')$ is expanded using N HO bases:

$$\mathbf{J}(\mathbf{r}') = \sum_{n=1}^N I_n \mathbf{f}_n(\mathbf{r}'), \quad (9)$$

where I_n are the unknown expansion coefficients, and N equations are obtained by applying Galerkin testing method:

$$\mathbf{Z}\mathbf{I} = \mathbf{V}. \quad (10)$$

B. ACA-SVD accelerated the higher order MoM solution

In contrast with the MLFMA and FFT based algorithms, the low-rank approximation based fast algorithms [15]-[16], [20]-[21] are purely algebraic, and do not depend on the formulation of Green's functions. An ACA based fast algorithm with recompress technique

is introduced here to reduce the memory requirements and computational complexity for electrically large scattering problems in layered medium.

The ACA employs the same octree data structure as in the MLFMA. The octal-tree algorithm is used to subdivide a box that encloses an object into smaller boxes. Figure 2 shows the box enclosing the object is subdivided into smaller boxes at multiple levels, in the form of an octal-tree. The largest boxes not touching each other are at level 2, while the smallest boxes are level L . The subdivision process runs recursively until the finest level L . With reference to Fig. 3, far interactions exist at levels 2 and higher. By using the fast algorithm, the impedance matrix \mathbf{Z} can be rewritten as:

$$\mathbf{Z} = \mathbf{Z}_{Near} + \mathbf{Z}_{Far}, \quad (11)$$

where the near field interactions are computed with the higher order MoM directly. Based octree grouping the far field interactions can be expressed as:

$$\mathbf{Z}_{Far} = \sum_{l=2}^L \sum_{i=1}^{M(l)} \sum_{j=1}^{Far(l(i))} [\mathbf{Z}_{lij}]_{m \times n}, \quad (12)$$

where $M(l)$ is the number of nonempty groups at level l and, $Far(l(i))$ denotes the number of far interaction groups of the i -th nonempty group for each observation group $l(i)$ at level l . The $[\mathbf{Z}_{lij}]_{m \times n}$ is the sub-matrix of far interaction between the observation group i and source group j , and the subscripts m, n denote the number of the basis functions in the observation and source groups, respectively. Since the sub-matrix $[\mathbf{Z}_{lij}]_{m \times n}$ is a low τ -rank matrix, in the ACA implementation, it can be approximate to the product of two small matrices:

$$[\mathbf{Z}_{lij}]_{m \times n} = [\mathbf{U}_{lij}]_{m \times r} [\mathbf{V}_{lij}]_{r \times n}, \quad (13)$$

where r is the τ -rank of the matrix $[\mathbf{Z}_{lij}]_{m \times n}$ and is much smaller than m and n . The error in this approximation is controlled by a threshold τ , which determines when to stop looking for more columns and rows of \mathbf{U}_{lij} and \mathbf{V}_{lij} , respectively. The ACA-SVD was presented by [11].

Since the matrices $[\mathbf{U}_{lij}]$ and $[\mathbf{V}_{lij}]$ generated by the ACA are usually not orthogonal, they may contain redundancies that can be removed by an algebraic compression technique. A SVD recompression of the obtained ACA decomposition can be performed utilizing two QR factorizations, so that either the $[\mathbf{U}_{lij}]$ or $[\mathbf{V}_{lij}]$ matrices in (13) can be done orthonormal, with an extra saving in memory, and the far field interactions in (12) can be rewritten as:

$$\mathbf{Z}_{Far} = \sum_{l=2}^L \sum_{i=1}^{M(l)} \sum_{j=1}^{Far(l(i))} [\hat{\mathbf{U}}_{lij}]_{m \times k} [\hat{\mathbf{V}}_{lij}]_{k \times n}, \quad (14)$$

where $k < r$. When higher order hierarchical vector basis functions are directly combined with the ACA-SVD algorithm, the higher order MoM's advantages of great reduction of the number of unknowns and acceleration of the convergence for iteration are keeping.

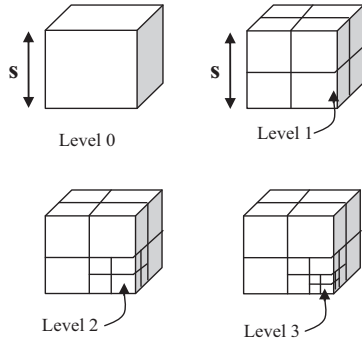


Fig. 2. Sketch of the octree structure.

III. NUMERICAL RESULTS

In this section, numerical results demonstrate efficiency of the higher order MoM solutions combined with the ACA-SVD technique for the 3D electromagnetic scattering problems in layered medium. For all computations, the threshold $\tau = 10^{-3}$. The flexible generalized minimal residual with deflated restarted (FGMRES-DR) [22] was used for the iterative solution of the system matrix. In the FGMRES-DR, all computations were carried out on a computer with 2.83 GHz CPU and 8.0 GB RAM.

The first example considers the bistatic radar cross section (Bi-RCS) of a PEC cylinder over a three-layer medium to test the accuracy of the proposed method. The three-layer medium is characterized by $\epsilon_1 = \epsilon_0$, $\epsilon_2 = 2.56\epsilon_0$, $\epsilon_3 = (6.5 - j0.6)\epsilon_0$, $\mu_1 = \mu_2 = \mu_3 = \mu_0$. The cylinder is 3 m long and has a radius of 0.5 m, and its bottom is located 0.2 m above the top interface of the three-layer dielectric medium as shown as in Fig. 3. The incident angles of plane wave are $\theta^{inc} = 60^\circ$, $\phi^{inc} = 0^\circ$ at 600 MHz. This scatterer is discretized with 572 curvilinear triangular patches for order 1.5 hierarchical basis functions, and giving raises to 2860 HO unknowns. The Bi-RCS at the scattered angle $\theta^{sca} = 60^\circ$ for both VV and HH polarization was shown in Fig. 5. The HO ACA-SVD results are compared with the 3-D adaptive integral method (AIM) [1], it can be found that there is an excellent agreement among them. The memory requirement for the HO ACA-SVD and the low order (LO) ACA-SVD (which use the CRWG basis functions and curvilinear triangular discretization to make a fair comparison) are compared in the Table 1. It can be found that, the use of higher order techniques greatly reduces the memory requirement for a given problem.

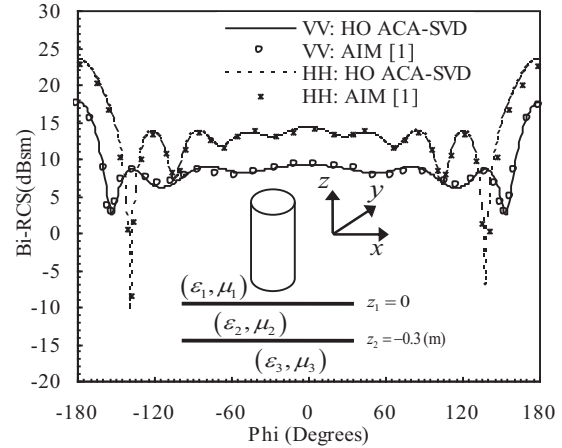


Fig. 3. Bistatic RCS of a PEC cylinder over a three-layer medium in the $\theta^{sca} = 60^\circ$ at 600 MHz.

Table 1: The memory requirement of HO ACA-SVD and LO ACA-SVD for the cylinder in layered medium

| | HO ACA-SVD | LO ACA-SVD |
|-------------------------------------|------------|------------|
| Total number unknowns | 2860 | 13383 |
| DCIM time (sec.) | 9.2 | 9.4 |
| Near field memory (MB) | 12.6 | 16.2 |
| Far field memory (MB) | 23.1 | 146.2 |
| Matrix-vector operation time (sec.) | 0.015 | 0.068 |
| Total iteration steps | 118 | 190 |

The second example considers the Bi-RCS of a PEC cuboid in a two-layer medium to test the efficiency of the proposed method. The two-layer medium is characterized by $\epsilon_1 = \epsilon_0$, $\epsilon_2 = (3.3 - j0.3)\epsilon_0$, $\mu_1 = \mu_2 = \mu_0$. The cuboid is 5.0 m long, 5.0 m wide and 2.0 m high, and its top is located 2.5 m below the interface of the two-layer dielectric medium as shown as in Fig. 4. The incident angles of plane wave are $\theta^{inc} = 60^\circ$, $\phi^{inc} = -90^\circ$ at 900 MHz. The Bi-RCS at the scattered angle $\theta^{sca} = 60^\circ$ for VV polarization was shown in Fig. 4. The HO-ACA results are compared with a reference fast inhomogeneous plane wave algorithm (FIPWA) accelerated MoM [23] and the 3-D AIM [1], it can be found that there is an excellent agreement among them. This scatterer is discretized with 9144 curvilinear triangular patches for order 1.5 hierarchical basis functions, and giving rise to 45720 HO unknowns. This simulation required 3.121 GB total memory and 4941s CPU time. The CPU time of the calculation of the spatial-domain layered medium

Green's functions by DCIM is only 24s. The far-field calculation accelerated by the modified ACA-SVD required 2.973 GB memory and 4784s for filling the far-field matrices. Figure 5 shows the required memory and the CPU time as a function of the number of HO unknowns increases, respectively. The MVP refers to a matrix-vector operation in Fig. 5 (b). Increasing the frequencies of the incident wave from 300 MHz to 1.2 GHz, and fixing the electrical mesh size equal to 0.45λ , that will result in the increasing number of total unknowns. As can be observed from the Fig. 5, the total memory and the CUP time of the higher order ACA-SVD is much less than of the higher order ACA with a fixed proportion. It also can be concluded that the complexity of the higher order ACA-based algorithms are scaled as $N^{4/3} \log N$ for memory and CPU time, respectively, where N denotes the number of HO unknowns.

The third example considers the scattering of a tank model located in a four-layer medium which imitates a complex environment. The four-layer medium is characterized by $\epsilon_1 = \epsilon_0$, $\epsilon_2 = (5.02 - j0.2)\epsilon_0$, $\epsilon_3 = \epsilon_0$, $\epsilon_4 = (10.8 - j0.2)\epsilon_0$, $\mu_1 = \mu_2 = \mu_3 = \mu_4 = \mu_0$. The tank model has a size $12.63 \text{ m} \times 4.33 \text{ m} \times 2.8 \text{ m}$ as shown as in Fig. 6. The bistatic RCS was plotted at a frequency of 500 MHz and an angle $\theta^{inc} = 30^\circ$, $\phi^{inc} = 0^\circ$ for both VV polarization as shown in Fig. 7, the results are compared with the scattering for the one in free space. This scatterer is discretized with 7094 curvilinear triangular patches for order 1.5 hierarchical basis functions, and giving rise to 35470 HO unknowns. This simulation required 2.262 GB memory and 6517s CPU time. The CPU time of the calculation of the multilayered Green's functions by DCIM is only 260s. The far-field calculation accelerated by the ACA-SVD required 1.932 GB memory and 2432s for filling the far-field matrices.

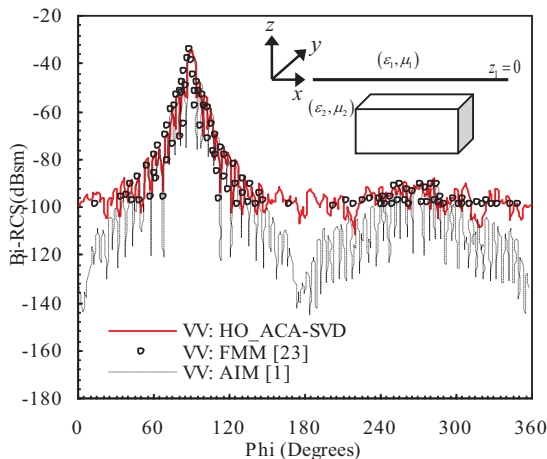


Fig. 4. Bistatic RCS of a PEC cuboid in a two-layer medium for the $\theta^{sca} = 60^\circ$ at 900 MHz.

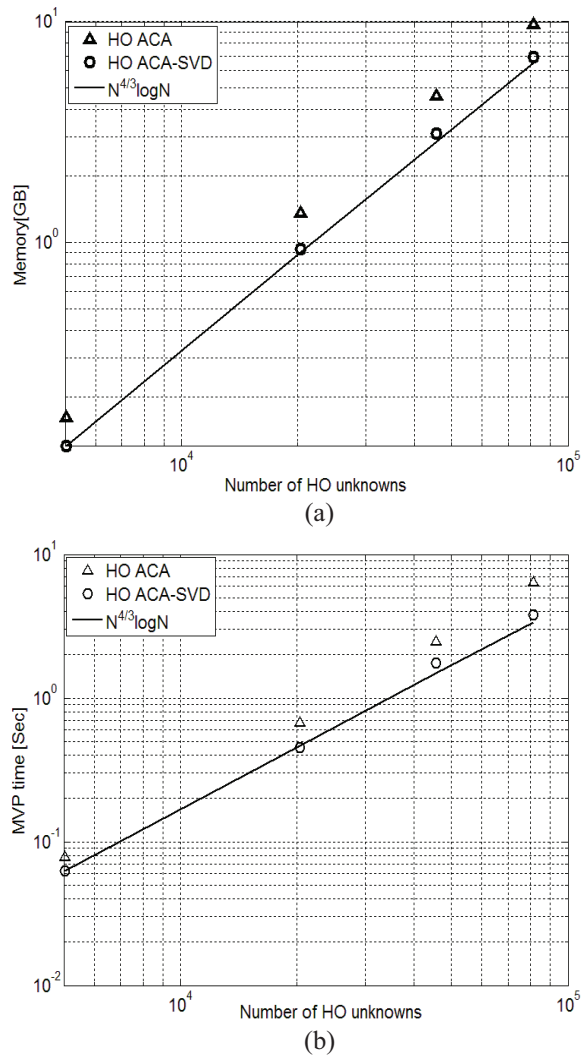


Fig. 5. (a) Memory requirement, and (b) CPU time for a matrix-vector operation, as a function of the number of HO unknowns for the cuboid in layered medium.

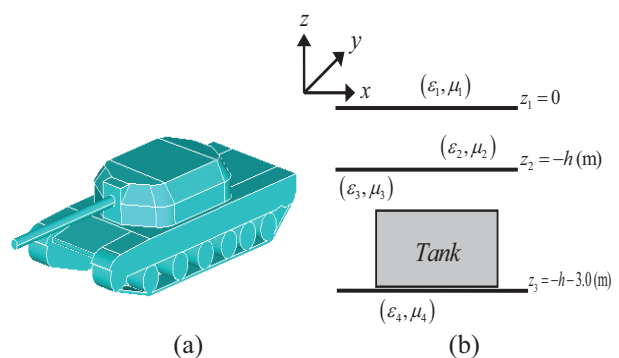


Fig. 6. A complex electrically large hard target located in a four-layer medium: (a) the simulation model of tank, and (b) illustration of the tank located in the four-layer medium.

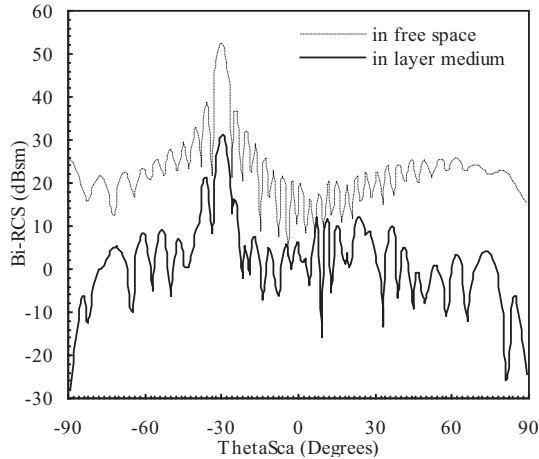


Fig. 7. Bistatic RCS of tank model in layered medium for the $\varphi^{sca} = 0^\circ$ at 500 MHz, and the result compared with that in free space.

IV. CONCLUSION

This paper provided an efficient technique for the electromagnetic scattering from the electrically large hard targets located in layered medium, which use the higher order method to discretize the unknown surface current density and the integral equations, and then use the ACA-SVD algorithm to accelerate the higher order MoM solutions. The numerical results demonstrated that the higher order ACA-SVD required much less memory and the CPU time than the low order ACA based algorithm or the higher order MoM solutions.

ACKNOWLEDGMENT

The authors would like to thank the support of Major State Basic Research Development Program of China (973 Program: 2009CB320201), Natural Science Foundation of 61171041, and Jiangsu Natural Science Foundation of BK2012034 and BK2009387.

REFERENCES

- [1] K. Yang and A. E. Yilmaz, "A three-dimensional adaptive integral method for scattering from structures embedded in layered media," *IEEE Trans. Geosci. Remote Sens.*, vol. 50, no. 4, pp. 1130-1139, Apr. 2012.
- [2] L. Zhuang, S. Y. He, X. B. Ye, W. D. Hu, and G. Q. Zhu, "The BCGS-FFT method combined with an improved discrete complex image method for EM scattering from electrically large objects in multilayered media," *IEEE Trans. Geosci. Remote Sens.*, vol. 48, no. 3, pp. 1180-1185, Mar. 2010.
- [3] E. Jorgensen, J. L. Volakis, P. Meincke, and O. Breinbjerg, "Higher order hierarchical discretization scheme for surface integral equations for layered media," *IEEE Trans. Geosci. Remote Sens.*, vol. 42, no. 4, pp. 764-772, Apr. 2004.
- [4] S. M. Rao, D. R. Wilton, and A. W. Glisson, "Electromagnetic scattering by surfaces of arbitrary shape," *IEEE Trans. Antennas Propag.*, vol. 30, no. 5, pp. 409-418, May 1982.
- [5] A. W. Glisson and D. R. Wilton, "Simple and efficient numerical methods for problems of electromagnetic radiation and scattering from surfaces," *IEEE Trans. Antennas Propag.*, vol. 28, pp. 593-602, Sep. 1980.
- [6] B. M. Notaros, "Higher order frequency-domain computational electromagnetics," *IEEE Trans. Antennas Propag.*, vol. 56, no. 8, pp. 2251-2276, Aug. 2008.
- [7] R. D. Graglia, D. R. Wilton, and A. F. Peterson, "Higher order interpolatory vector bases for computational electromagnetics," *IEEE Trans. Antennas Propag.*, vol. 45, no. 3, pp. 329-342, Mar. 1997.
- [8] E. Jorgensen, J. L. Volakis, P. Meincke, and O. Breinbjerg, "Higher order hierarchical Legendre basis functions for electromagnetic modeling," *IEEE Trans. Antennas Propag.*, vol. 52, no. 11, pp. 2985-2995, Nov. 2004.
- [9] L. P. Zha, Y. Q. Hu, and T. Su, "Efficient surface integral equation using hierarchical vector bases for complex EM scattering problems," *IEEE Trans. Antennas Propag.*, vol. 60, no. 2, pp. 952-957, Feb. 2012.
- [10] R. Coifman, V. Rokhlin, and S. Wandzura, "The fast multipole method for the wave equation: a pedestrian prescription," *IEEE Trans. Antennas Propag. Mag.*, vol. 35, no. 3, pp. 7-12, Jun. 1993.
- [11] J. M. Song and W. C. Chew, "Multilevel fast multipole algorithm for solving combined field integral equation of electromagnetic scattering," *Microw. Opt. Tech. Lett.*, vol. 10, no. 1, pp. 14-19, Sep. 1995.
- [12] S. Velamparambil, W. C. Chew, and J. Song, "10 million unknowns: is it that big?," *IEEE Trans. Antennas Propag.*, vol. 45, no. 2, pp. 43-58, Apr. 2003.
- [13] H. P. Zhao, J. Hu, and Z. P. Nie, "Parallelization of MLFMA with composite load partition criteria and asynchronous communication," *Applied Computational Electromagnetics Society (ACES) Journal*, vol. 25, no. 2, pp. 167-173, Feb. 2010.
- [14] O. Ergul and L. Gurel, "Accurate solutions of extremely large integral equation problems in computational electromagnetics," *IEEE Proceedings.*, vol. 101, no. 2, pp. 342-349, Feb. 2013.
- [15] K. Zhao, M. N. Vouvakis, and J. F. Lee, "The adaptive cross approximation algorithm for accelerated method of moments computations of EMC problems," *IEEE Trans. Electromang. Compat.*, vol. 47, no. 4, pp. 763-773, Nov. 2005.

- [16] M. Bebendorf and S. Kunis, "Recompression techniques for adaptive cross approximation," *J. Integ. Equat. Appl.*, vol. 21, no. 3, pp. 331-357, 2009.
- [17] T. Su, Z. W. Yang, M. M. Li, and R. S. Chen, "Electrically large 3-D PEC objects buried in a lossy stratified medium," in *Microwave and Millimeter Wave Technology, ICMMT.*, pp. 1-4, 2012.
- [18] K. A. Michalski and D. Zheng, "Electromagnetic scattering and radiation by surfaces of arbitrary shape in layered media: I. theory," *IEEE Trans. Antennas Propag.*, vol. 38, no. 3, pp. 335-344, Mar. 1990.
- [19] H. Y. Chao, J. S. Zhao, and W. C. Chew, "Application of curvilinear basis functions and MLFMA for radiation and scattering problems involving curved PEC structures," *IEEE Trans. Antennas Propag.*, vol. 51, no. 2, pp. 331-336, 2003.
- [20] Z. N. Jiang, R. S. Chen, Z. H. Fan, and M. M. Zhu, "Novel postcompression technique in the matrix decomposition algorithm for the analysis of electromagnetic problems," *Radio Sci.*, 47, RS 2003, doi:10.1029/2011RS004921, 2012.
- [21] Z. N. Jiang, Z. Fan, D. Ding, R. Chen, and K. W. Leung, "Preconditioned MDA-SVD-MLFMA for analysis of multi-scale problems," *Applied Computational Electromagnetics Society (ACES) Journal*, vol. 25, no. 11, pp. 914-925, 2010.
- [22] X. Q. Hu, M. Chen, D. Z. Ding, and R. S. Chen, "A novel flexible GMRES with deflated restarted for efficient solution of electromagnetic scattering," *Microwave and Optical Technology Letters*, vol. 53, no. 6, pp. 1360-1364, June 2011.
- [23] B. Hu, *Fast Inhomogeneous Plane Wave Algorithm for Electromagnetic Scattering Problems*, Ph.D. dissertation, Dept. Elect. Comput. Eng., Univ. Illinois at Urbana-Champaign, Champaign, IL, 2001.



Liping Zha was born in Anhui Province, China, in 1987. She received the B.S. degree in Electronic Information Engineering from Anhui University of Architecture, China, in 2008, and is currently working toward the Ph.D. degree at Nanjing University of Science and Technology (NJUST), Nanjing, China.

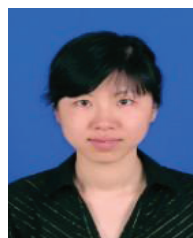
Her current research interests include computational electromagnetics, electromagnetic modeling of scattering problems, wave scattering and propagation from random

media, and numerical techniques for electrically large objects.



Rushan Chen was born in Jiangsu, P. R. China. He received his B.Sc. and M.Sc. degrees from the Dept. of Radio Engineering, Southeast University, in 1987 and in 1990, respectively, and his Ph.D. from the Dept. of Electronic Engineering, City University of Hong Kong in 2001.

He joined the Dept. of Electrical Engineering, Nanjing University of Science & Technology (NJUST), where he became a Teaching Assistant in 1990 and a Lecturer in 1992. He has authored or co-authored more than 200 papers, including over 140 papers in international journals. He is the recipient of the Foundation for China Distinguished Young Investigators presented by the National Science Foundation (NSF) of China in 2003. In 2008, he became a Chang-Jiang Professor under the Cheung Kong Scholar Program awarded by the Ministry of Education, China. His research interests mainly include microwave/millimeter-wave systems, measurements, antenna, RF-integrated circuits, and computational electromagnetics.



Ting Su was born in Anhui Province, China, in 1985. She received the B.S. degree in Communication Engineering from Nanjing University of Science and Technology (NJUST), China, in 2006, and is currently working toward the Ph.D. degree at Nanjing University of Science and Technology (NJUST), Nanjing, China.

Her current research interests include computational electromagnetics, antennas and electromagnetic scattering and propagation, electromagnetic modeling of microwave integrated circuits.

Waveguide Microwave Imaging: Solids Volume Fraction of Particulate Materials

Alexander V. Brovko¹, Ethan K. Murphy^{2,3}, and Vadim V. Yakovlev²

¹Department of Applied Information Technologies
Yury Gagarin State Technical University of Saratov (SSTU), Saratov 410054, Russia
brovkoav@gmail.com

²Department of Mathematical Sciences
Worcester Polytechnic Institute, Worcester, MA 01609, USA
vadim@wpi.edu

³Thayer School of Engineering
Dartmouth College, Hanover, NH 03755, USA
ethan.k.murphy@dartmouth.edu

Abstract — An original modeling-based microwave imaging technique for determining the volume fraction of solid material in dielectric powders is described. The desired characteristic is determined by analyzing S -parameter measurements in a waveguide containing the sample with the help of an artificial neural network trained by data from 3D FDTD simulation. The powder sample is represented by a mixture of air and millimeter-scale particles reproduced in the FDTD model. Computational tests with 20 to 40 mm cubic samples of SiC and ZrO₂ powders in WR340 show that the solids volume fraction is determined with less than 5% error.

Index Terms — Artificial neural network, FDTD modeling, microwave imaging, particulate materials, solids volume fraction.

I. INTRODUCTION

High-temperature microwave processing methods, including sintering, are known to be promising technologies that, when carried out in properly designed systems, could facilitate energy savings and high quality processing of powders and particulate materials [1-4]. There is a growing effort to develop corresponding multiphysics models and computational tools capable of assisting engineers in designing systems for efficient high-temperature microwave processing (see, e.g., [5-9]). Characterization of material properties is an integral part of the modeling process, but reliable experimental data on electromagnetic and thermal parameters of the processed material are not always available.

Thermal conductivity is a critically important input parameter in the computation of microwave-induced temperature fields. For many powders, it can be relatively

accurately estimated using advanced physical models for thermal conductivity of porous materials [10,11]. However, this approach requires the solids volume fraction ϕ (or porosity $\psi = 1 - \phi$) of the powder to be known. For many materials the data provided by the manufacturers or in handbooks is available in only a certain range, so the resulting value of thermal conductivity becomes necessarily uncertain [12]. This, in turn, may impact the results of computer simulation.

Effective complex permittivity ϵ_{eff} is another critical input parameter of the related multiphysics models. All (classical and contemporary) mixing formulas which can be used for determining ϵ_{eff} of the powder material (interpreted as a mixture of air and a solid component) require ϕ to be a known parameter [13].

Data on ϕ is also important to the accurate design and valid modeling of behavior of particulate materials in fluidized beds, solid fuel combustion, and other industrial processes. While a variety of measurement techniques (including non-invasive microwave and optical sensing methods) have been reported [14-18], experimental determination of the concentration of solid in these applications may be technically difficult, expensive and not always practically possible.

In this paper, we describe an original modeling-based microwave imaging technique for determining the solids volume fraction of dielectric particulate materials. The proposed approach further develops the authors' earlier artificial neural network (ANN) inversion technique for finding the position and size of an object inside a dielectric sample in a waveguide system [19,20]. The ANN is trained with multiple S -parameter data from full-wave numerical simulations; the network determines ϕ when it is given the data on a corresponding single

measurement. In the model, a sample of micro- or nano-powder is represented by a collection of inclusions (comparable in their dimensions with the size of the unit of spatial discretization) enclosed in the sample's volume. Legitimacy of such a representation is supported by computational tests showing an insensitivity of frequency characteristics of the S -parameters to the particle size in different scenarios with the same ϕ . We find that both solid-in-air and air-in-solid material models are operational with the inclusions of both rectangular and cylindrical shapes, but the model with air parallelepipeds in solid appears to be computationally most efficient. Functionality of the proposed technique is demonstrated with silicon carbide (SiC) and zirconium dioxide (ZrO₂) (zirconia) powders in a rectangular waveguide; the solids volume fraction of the powders with $\phi = 60\text{-}80\%$ is reconstructed with less than 5% error.

II. TECHNIQUE AND MATERIALS

Our approach to determining the solids volume fraction of powders and particulate materials is based on simple measurement of S -parameters of a waveguide containing a tested sample and an ANN inversion procedure, backed by data on the reflection coefficient S_{11} and the transmission coefficient S_{21} in a finite-difference time-domain (FDTD) simulation of this system. We consider complex reflection and transmission coefficients in a two-port waveguide structure shown in Fig. 1; for the sake of computational convenience, the tested powder material is considered in this paper to be of rectangular shape of A , B , and C mm in the directions of the x -, y -, and z -axes, respectively. In principle, the technique remains the same for the samples of any shape, and the measurement system remains the same for the samples of different shapes and sizes.

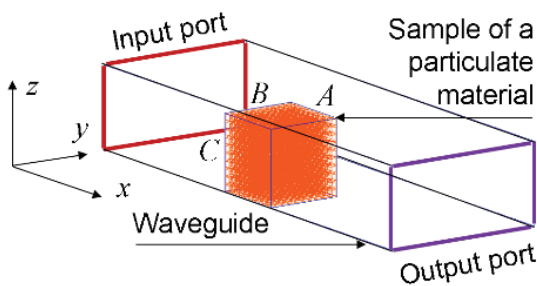


Fig. 1. Microwave system with the tested sample; output port is supposed to be a perfect load.

We introduce the characteristic of the solids volume fraction ϕ assuming that the sample consists of two media, air and solid, and they are arranged as in one of the lattices in Fig. 2: multiple solid inclusions (of rectangular or cylindrical shape) in air, or multiple air inclusions (of rectangular or cylindrical shape) in solid. While typical powders to be sintered consist of micro- or

nanometer particles, the sizes of the inclusions in our technique are comparable with cells in an applicable practical FDTD mesh; thus, for the microwave frequency range, they are of millimeter-scale size. Two examples of a volumetric structure of the tested sample (taken for convare) shown in Fig. 3.

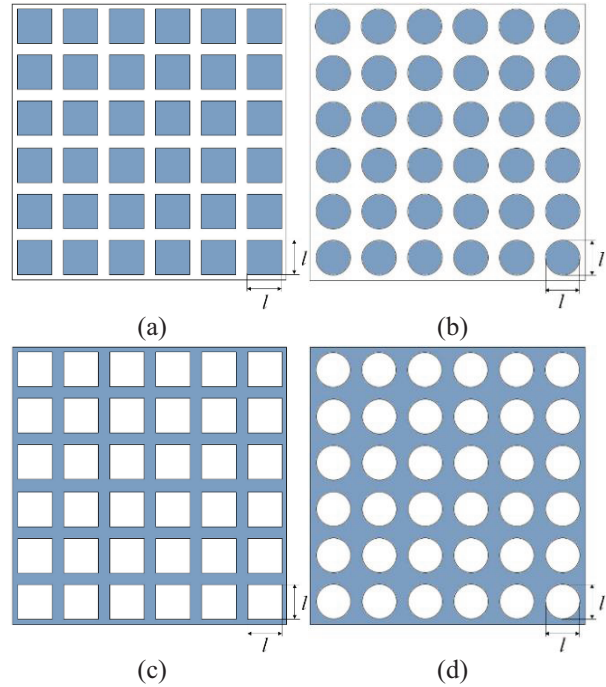


Fig. 2. Solid-in-air (a), (b) and air-in-solid (c), (d) models of a particular material – cubic/rectangular (a), (c) and cylindrical (b), (d) inclusions.

The adequacy of such a representation is suggested by the key principle of microwave imaging: the observed electric field responses to the effective complex permittivity of a dielectric mixture that depends on the volume fraction of the inclusions rather than on their individual dimensions. Furthermore, following the classical mixing approach [13], in this paper, we work with the samples in which the inclusions are assumed to be of sizes randomly distributed within certain ranges and randomly positioned within their immediate neighborhoods. The solids volume fraction ϕ is calculated as the ratio:

$$\phi = V_i/V_s,$$

where V_s is the volume of the sample (in our case, $V_s = ABC$) and V_i is the total volume occupied by the inclusions and calculated as:

$$V_i = \begin{cases} \sum_{j=1}^N a_j b_j c_j, & \text{for rectangular inclusions,} \\ \sum_{j=1}^N \pi \left(\frac{d_j}{2}\right)^2 h_j, & \text{for cylindrical inclusions,} \end{cases}$$

where a_j , b_j , c_j , d_j , and h_j are the dimensions of N rectangular or cylindrical inclusions, as shown in Fig. 3.

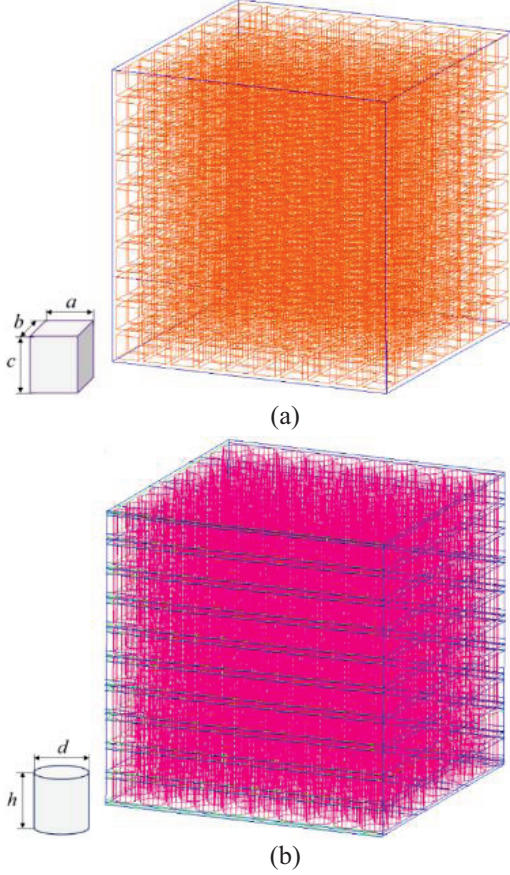


Fig. 3. 3D views of the tested samples with rectangular boxes (a) and cylinders (b) homogeneously embedded as inclusions in an isotropic environment of cubic shape.

We use an ANN with global cubic radial basis functions (RBF) for single hidden layer neurons [21,22] as an inversion mechanism for determining ϕ of the powder in the sample. The network architecture is shown in Fig. 4. The ANN inputs, \mathbf{X} , are the real and imaginary parts of the S -parameters at P points in the considered frequency range ($4P$ input nodes); the output of the ANN is the predicted value of solids volume fraction ϕ^* . The hidden layer of neurons consist of N_C nodes, which have form:

$$g_i(\mathbf{X}) = \|\mathbf{X} - \mathbf{C}_i\|^3,$$

where \mathbf{C}_i are the centers of the RBFs and $i = 1, \dots, N_C$. The S -parameters of the waveguide system partially filled with the sample (Fig. 1) are computed with the FDTD model and used for ANN training. For each simulation, a distribution of inclusions in the sample is generated assuming the particles to be of sizes randomly distributed from l_1 to l_2 mm. It is also assumed that $a \ll A$, $b \ll B$, $c \ll C$, and that a, b, c are much less than the wavelength in the waveguide.

The output of the ANN is a linear combination of outputs from each RBF. The trained network finds the

weights, i.e., coefficients of each RBF, such that the linear system is best fit in a least squares sense. That is, given N_T training samples, we have N_T input-output pairs (\mathbf{X}_j, ϕ_j) , so, to train the network, we find a solution to the linear system:

$$\mathbf{G}(\mathbf{X})\mathbf{w} = \begin{bmatrix} g_1(\mathbf{X}_1) & g_2(\mathbf{X}_1) & \dots & g_{N_C}(\mathbf{X}_1) \\ g_1(\mathbf{X}_2) & g_2(\mathbf{X}_2) & \dots & g_{N_C}(\mathbf{X}_2) \\ \vdots & \vdots & \ddots & \vdots \\ g_1(\mathbf{X}_{N_T}) & g_2(\mathbf{X}_{N_T}) & \dots & g_{N_C}(\mathbf{X}_{N_T}) \end{bmatrix} \begin{bmatrix} w_1 \\ w_2 \\ \vdots \\ w_{N_C} \end{bmatrix} = \begin{bmatrix} \phi_1 \\ \phi_2 \\ \vdots \\ \phi_{N_T} \end{bmatrix} = \boldsymbol{\phi},$$

with the weight vector \mathbf{w} . We employ a zero training error regime for selection of centers, i.e., the training set is the set of centers chosen [23]. This means that $N_C = N_T$ and $\mathbf{G}(\mathbf{X})$ is a $N_T \times N_T$ matrix. The trained network in Fig. 4 can therefore be described by the formula:

$$\mathbf{G}(\mathbf{X})\mathbf{w}^* = \boldsymbol{\phi}^*,$$

where \mathbf{w}^* is the best fitting weights and $\boldsymbol{\phi}^*$ is the ANN's approximation to $\boldsymbol{\phi}$. The linear system is solved using singular value decomposition.

After sufficient training, the ANN is able to reconstruct the solids volume fraction of the tested material from S -parameters obtained by a physical measurement. While in general this technique of numerical inversion is similar to our earlier ANN methodology [19,20], here it results not in reconstruction of parameters of each individual inclusion, but in the characteristic of their group with possible random deviations in their positions and sizes.

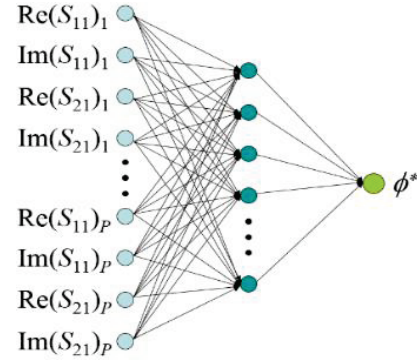


Fig. 4. The ANN structure with one hidden layer.

III. RESULTS

The proposed technique was tested with three cubic samples ($A = B = C = 40, 30$, and 20 mm) of SiC and ZrO_2 powder in a section of WR340 waveguide of 250 mm length. For the considered range around the frequency of microwave sintering (2.45 GHz), we chose, in order to keep the required CPU time reasonable, the minimum cell size of the FDTD model to be 0.5 mm; therefore, the size distribution of the inclusions was chosen between $l_1 = 2$ mm and $l_2 = 8$ mm. The dielectric constant ϵ' and electric conductivity σ of the bulk materials were taken

to be $\epsilon' = 10.4$ and $\sigma = 0.1225$ S/m for SiC [1] and $\epsilon' = 6.69$ and $\sigma = 0.0258$ S/m for ZrO₂ [24].

The underlying computation of S -parameters was performed with the 3D conformal FDTD simulator QuickWave 2014 [25]. In the process of ANN training, we applied a coarse mesh with cell size 1 mm inside the sample and 5 mm outside the sample; the number of cells was 138,000, and steady state was reached after about 10,000 iterations. One single simulation took about 1.5 minutes on a PC with an AMD Athlon 6000+ 3 GHz processor. When computing S -parameters for different sizes of inclusions, we applied a finer mesh with cell size 0.5 mm inside the sample and 5 mm outside the sample; in this case, the number of cells in the model was near 1 million, and steady state was reached after about 25,000 iterations. A single run on the aforementioned PC took about 30 minutes.

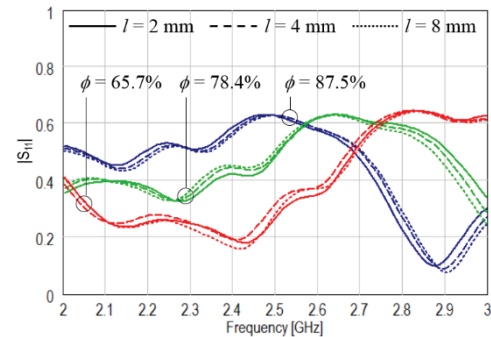
All material models presented in Fig. 2 were tested, and while all four were found operational, the FDTD model with rectangular air-in-solid inclusions turned out to be most efficient (as required minimum computational resources) as well as stable and controllable: the lattice in Fig. 2 (c) can be kept in quite wide ranges of l and ϕ .

A series of frequency-dependent characteristics of $|S_{11}|$ typical for the air-in-solid rectangular inclusions in the cubic sample are shown in Fig. 5. It can be seen that the curves corresponding to different particle sizes, but the same solids volume fraction, are very close to each other, whereas the curves corresponding to different ϕ are fairly distinct. ($|S_{21}|$ curves are not presented here, but their behavior is very similar.) The computations suggest that we can expand the results obtained for the samples with large (millimeter-scale) inclusions to samples of powders containing micro- and/or nanometer-scale particles without reproducing their actual sizes with the nano-scale cells of the FDTD model.

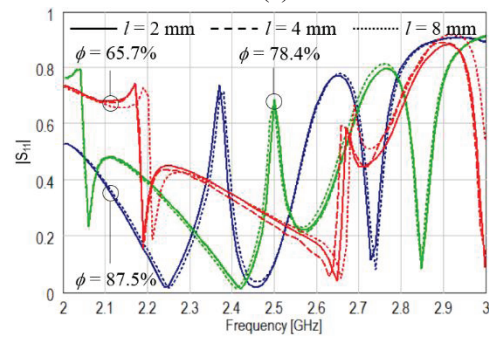
The diagrams in Figs. 6-7 characterize the quality of learning of the ANN with $P = 21$ (i.e., with 20 equal intervals in the 2 to 3 GHz frequency range) for random-size particle distributions and different shapes of the inclusions. For both powders and both air-in-solid and solid-in-air material models, the ANN is trained with 800 distributions of particles of the material in air. It is seen that for cubic samples larger than 20 mm in size, reconstructed values of ϕ appear to be very close to the testing values.

Table 1 shows the reconstructed solids volume fractions of six samples in comparison with their actual values. For powders of lower density ($\phi < 0.75$), the reconstruction error does not exceed 1.5%. When the sample appears to be closer to a solid ($\phi \sim 0.8$), the reconstruction is less accurate, but the errors are still less than 5%. The accuracy is worse in the case of small samples with low-density powders. Since in these examples, the experimental data for S -parameters are

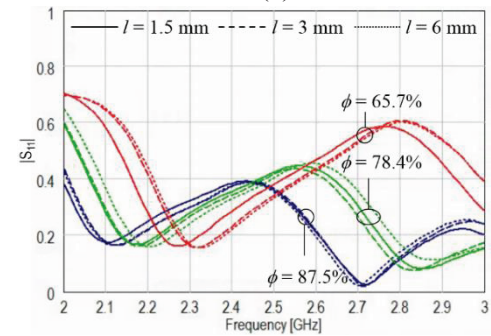
simulated using a computer model, we expect that a practical implementation of this technique might suffer somewhat lower accuracy. However, the reconstructed solids volume fraction is still anticipated to be sufficiently accurate for subsequent use in physical models for thermal conductivity, especially in the absence of experimental data, and in other applications.



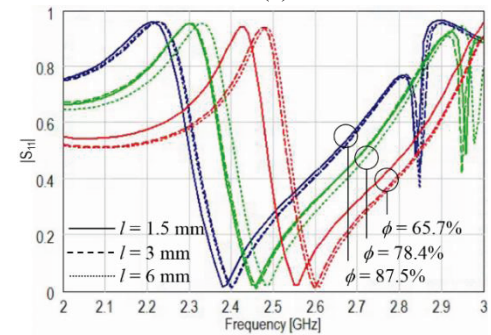
(a)



(b)



(c)



(d)

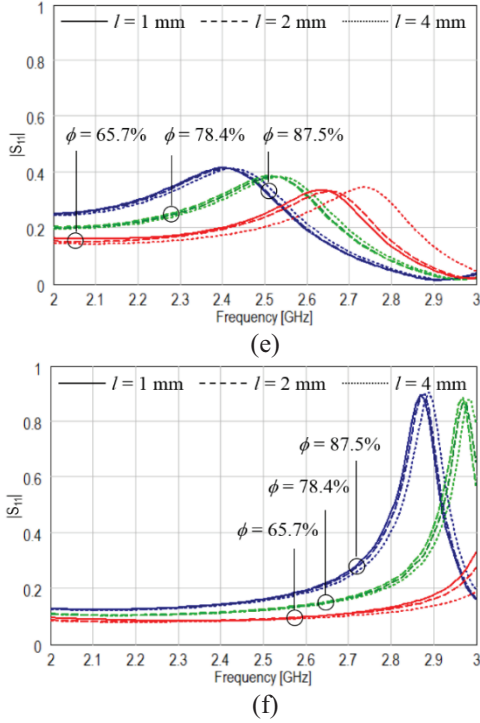


Fig. 5. Frequency characteristics of $|S_{11}|$ for different particle size l and solids volume fraction ϕ in the lattice Fig. 2 (c) for cubic samples $A = B = C = 20$ mm (a, b), 30 mm (c, d), and 40 mm (e, f) of SiC (a), (c) (e) and ZrO₂ (b), (d), (f).

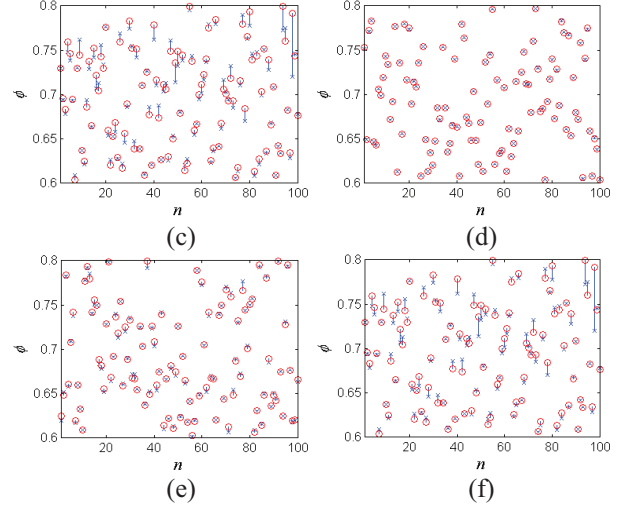
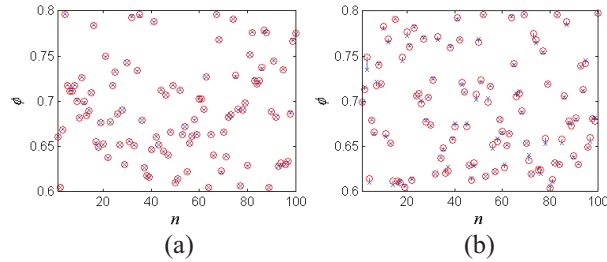


Fig. 6. ANN performance for the system with a solid-in-air (Fig. 2 (a)) cubic sample $A = B = C = 20$ mm (a), (d), 30 mm (b), (e), and 40 mm (c), (f) of SiC power (a)-(c) and ZrO₂ powder (d)-(f) represented by rectangular inclusions for $n = 100$ testing points; \times : testing points; o : network responses.

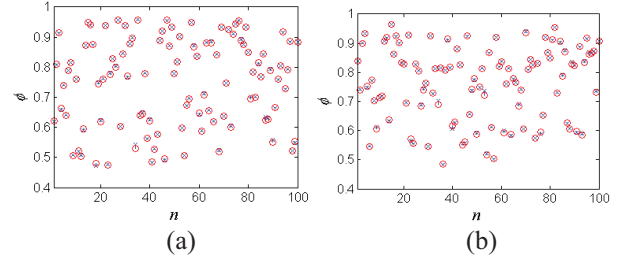


Fig. 7. ANN performance for the system with an air-in-solid (Fig. 2 (c)) cubic sample $A = B = C = 30$ mm of SiC power (a) and ZrO₂ powder (b) represented by cylindrical inclusions for $n = 100$ testing points; \times : testing points; o : network responses.

Table 1: Solids fractions of the powders reconstructed by the trained ANN

| Powder | Sample: 40×40×40 mm | | | 30×30×30 mm | | 20×20×20 mm | |
|------------------|---------------------|----------------------|--------------------|----------------------|--------------------|----------------------|--------------------|
| | Actual ϕ | Reconstructed ϕ | Relative Error (%) | Reconstructed ϕ | Relative Error (%) | Reconstructed ϕ | Relative Error (%) |
| SiC | 0.60 | 0.601 | 0.1 | 0.603 | 0.5 | 0.644 | 7.3 |
| | 0.65 | 0.643 | 1.1 | 0.644 | 0.9 | 0.649 | 0.2 |
| | 0.70 | 0.690 | 1.4 | 0.704 | 0.6 | 0.701 | 0.1 |
| | 0.75 | 0.746 | 0.5 | 0.747 | 0.4 | 0.748 | 0.3 |
| | 0.80 | 0.766 | 4.3 | 0.792 | 1.0 | 0.801 | 0.1 |
| ZrO ₂ | 0.60 | 0.597 | 0.5 | 0.601 | 0.2 | 0.463 | 22.8 |
| | 0.65 | 0.643 | 1.1 | 0.641 | 1.4 | 0.649 | 0.2 |
| | 0.70 | 0.690 | 1.4 | 0.707 | 1.0 | 0.701 | 0.1 |
| | 0.75 | 0.751 | 0.1 | 0.748 | 0.3 | 0.749 | 0.1 |
| | 0.80 | 0.777 | 2.9 | 0.790 | 1.3 | 0.801 | 0.1 |

IV. CONCLUSION

A new modeling-based technique for determining the solids volume fraction of particulate materials by the means of waveguide microwave imaging has been outlined. The required characteristic is extracted from S -parameters of a waveguide system containing the tested sample and is independent on the size of millimeter-scale inclusions representing micro- and nano-particles of the powder. It has been shown that, when backed by FDTD data in the 2 to 3 GHz frequency range, the ANN with global cubic RBF determines ϕ with a sufficiently high resolution. Functionality of the technique has been illustrated in computational experiments with silicon carbide and zirconia powders. It was shown that with both materials excellent accuracy (less than 5% error) was achieved. It should be noted that this level of quality of reconstruction is reached with the use of minimal computational resources.

In further developments, with an appropriate alteration of the ANN structure, the proposed technique can be transformed for determining the effective complex permittivity of particulate materials.

REFERENCES

- [1] D. E. Clark and W. H. Sutton, "Microwave processing of materials," *Annual Review of Material Science*, vol. 26, pp. 299-331, 1996.
- [2] Y. V. Bykov, K. I. Rybakov, and V. E. Semenov, "High-temperature microwave processing of materials," *J. Phys. D: Appl. Phys.*, vol. 34, pp. R55-75, 2001.
- [3] M. Oghbaei and O. Mirzaee, "Microwave versus conventional sintering: a review of fundamentals, advantages and applications," *J. Alloys and Compounds*, vol. 494, pp. 175-189, 2010.
- [4] D. Agrawal, "Microwave sintering of ceramics, composites and metallic materials, and melting of glasses," *Trans. Indian Ceramic Soc.*, vol. 65, pp. 129-144, 2006.
- [5] Y. Duan, D. C. Sorescu, and J. K. Johnson, "Finite element approach to microwave sintering of oxide materials," *Proc. COMSOL Users Conference*, Boston, 2006.
- [6] D. Bouvard, S. Charmond, and C. P. Carry, "Multiphysics simulation of microwave sintering in monomode cavity," *Ceram. Trans.*, vol. 209, pp. 173-180, 2010.
- [7] S. A. Bogachev, D. Bouvard, E. M. Kiley, and V. V. Yakovlev, "A macroscopic iterative routine for modeling electromagnetic, thermal, and mechanical phenomena in microwave sintering," in *Microwave and RF Power Applications*, J. Tao, Ed., Cépaduès Éditions, pp. 372-375, 2011.
- [8] K. I. Rybakov, E. A. Olevsky, and E. V. Krikun, "Microwave sintering: fundamentals and modeling," *J. Am. Ceram. Soc.*, vol. 96, pp. 1003-1020, 2013.
- [9] E. M. Moon, C. Yang, and V. V. Yakovlev, "Microwave-induced temperature fields in cylindrical samples of graphite powder - experimental and modeling studies," *Intern. J. Heat & Mass Transfer*, vol. 87, pp. 359-368, 2015.
- [10] P. Cheng and C-T. Hsu, "The effective stagnant thermal conductivity of porous media with periodic structures," *J. Porous Media*, vol. 2, pp. 19-38, 1999.
- [11] M. Kandula, "On the effective thermal conductivity of porous packed beds with uniform spherical particles," *J. Porous Media*, vol. 14, pp. 919-926, 2011.
- [12] E. M. Moon, C. Yang, M. Patel, H. He, and V. V. Yakovlev, "Microwave-induced temperature fields in graphite powder heated in a waveguide reactor," *IEEE MTT-S Intern. Microwave Symp. Dig.*, Tampa, FL, 978-1-4799-3869-8/14, June 2014.
- [13] A. Sihvola, *Electromagnetic Mixing Formulas and Applications*, IEE, London, 1999.
- [14] H. Johnsson and F. Johnsson, "Measurements of local solids volume-fraction in fluidized bed boilers," *Powder Technology*, vol. 115, pp. 13-26, 2001.
- [15] J. M. Link, W. Godlieb, P. Tripp, N. G. Deen, S. Heinrich, J. A. M. Kuipers, M. Schönherr, and M. Peglow, "Comparison of fibre optical measurements and discrete element simulations for the study of granulation in a spout fluidized bed," *Powder Technol.*, vol. 189, pp. 202-217, 2009.
- [16] Y. Liu, Z. Huang, H. Ji, and H. Li, "Solid volume fraction measurement of gas-solid two-phase flow based on terahertz time-domain spectroscopy technique: a preliminary study and static experimental results," *IEEE Trans. Instrum. Meas.*, vol. 58, pp. 1585-1592, 2009.
- [17] J-P. Laviolette, G. S. Patience, and J. Chaouki, "Fibre-optic probe for the simultaneous measurement of gaseous species composition and solids volume fraction," *Proc. 13th Intern. Conf. on Fluidization - New Paradigm in Fluidization Engineering*, Montreal, 2010.
- [18] G. Xu, C. Liang, X. Chen, D. Liu, P. Xu, L. Shen, and C. Zhao, "Investigation on dynamic calibration for an optical-fiber solids concentration probe in gas-solid two-phase flows," *Sensors*, vol. 13, pp. 9201-9222, 2013.
- [19] A. V. Brovko, E. K. Murphy, M. Rother, H. P. Schuchmann, and V. V. Yakovlev, "Waveguide microwave imaging: spherical inclusion in a dielectric sample," *IEEE Microwave and Wireless Comp. Lett.*, vol. 18, pp. 647-649, 2008.
- [20] A. V. Brovko, E. K. Murphy, and V. V. Yakovlev, "A modeling-based technique for nondestructive evaluation of metal powders undergoing microwave sintering," *IEEE MTT-S Intern. Microwave Symp. Dig.*, Anaheim, CA, pp. 1428-1431, May 2010.

- [21] E. K. Murphy and V. V. Yakovlev, "RBF network optimization of complex microwave systems represented by small FDTD modeling data sets," *IEEE Trans. Microwave Theory Tech.*, vol. 54, pp. 3069-3083, 2006.
- [22] A. V. Brovko, E. K. Murphy, and V. V. Yakovlev, "Waveguide microwave imaging: neural network reconstruction of functional 2-D permittivity profiles," *IEEE Trans. Microwave Theory Tech.*, vol. 57, pp. 406-414, 2009.
- [23] M. Kirby, *Geometric Data Analysis*, Wiley, New York, 2001.
- [24] V. V. Yakovlev, S. M. Allan, M. L. Fall, and H. S. Shulman, "Computational study of thermal runaway in microwave processing of zirconia," in *Microwave and RF Power Applications*, J. Tao, Ed., Cépaduès Éditions, pp. 303-306, 2011.
- [25] QuickWave 2014™, QWED Sp. z o. o., <http://www.qwed.com.pl/>.



Alexander V. Brovko received the M.Sc. and Ph.D. degrees in Radio Physics and Electronics from Saratov State University, Saratov, Russia, in 1996 and 1999, respectively. From 1999 to 2005, he was an Assistant Professor and Associate Professor with Saratov State University. Since 2005, he has been with the Department of Applied Information Technologies, Saratov State Technical University (SSTU), where he is currently Associate Professor. From 2010 to 2012, he served as the Vice-Dean of Research at the Faculty of Applied Information Technologies.

Starting 2000, Brovko held a number of short-term Visiting Research positions in Chalmers University of Technology, Swiss Federal Laboratories for Materials Science and Technology, Democritus University of Thrace, and Karlsruhe Institute of Technology. He has authored over 50 papers in referred journals and conference proceedings. His research interests include computational electromagnetics, finite element and FDTD methods, optimization techniques, inverse electromagnetic problems, and optical devices.



Ethan K. Murphy received the M.S. degree in Industrial Mathematics from Worcester Polytechnic Institute (WPI), Worcester, MA in 2003 and the Ph.D. degree in Mathematics from Colorado State University, Fort Collins, CO in 2007. He then held research and teaching positions at WPI, Rensselaer

Polytechnic Institute, and Applied Mathematics, Inc. Currently he is a Research Associate at Dartmouth's Thayer School of Engineering studying Medical Imaging and in particular Electrical Impedance Tomography. His research interests include inverse problems, microwave optimization, microwave imaging, and computational mathematics. He has authored more than 40 papers in referred journals and conference proceedings. Murphy is a Member of SIAM and Pi Mu Epsilon.



Vadim V. Yakovlev received his Ph.D. degree in Radio Physics from Institute of Radio Engineering and Electronics (IRE) of the Russian Academy of Sciences (RAS), Moscow, Russia in 1991. From 1984 to 1996, he held junior to senior research positions with the IRE RAS and in 1993 worked as Visiting Researcher at Electricité de France (Centre "Les Renardières").

In 1996, he joined the Department of Mathematical Sciences, Worcester Polytechnic Institute, Worcester, MA and currently holds there a position of Research Associate Professor. Yakovlev is a Head of the Industrial Microwave Modeling Group which he established in 1999 as a division of the WPI's Center for Industrial Mathematics and Statistics. Yakovlev's research interests in computational electromagnetics include neural-network-based optimization, microwave imaging, multiphysics modeling, microwave power engineering, and broadband/multiband antennas. He is an author of more than 150 papers in referred journals and conference proceedings. Yakovlev is a Senior Member of the IEEE and a Member of the IEEE MTT-S IMS TPRC. He is a Member of the Board of Governors of International Microwave Power Institute (IMPI), a Member of Association for Microwave Power in Europe for Research and Education (AMPERE) and a Member of the Massachusetts Institute of Technology (MIT) Electromagnetics Academy. He serves as a Reviewer for several journals and as a Member of program committees of several conferences.

Size Reduced Array Antenna with Enhanced Directivity

Sheikh S. I. Mitu and Farooq Sultan

Department of Electrical Engineering
King Fahd University of Petroleum and Minerals (KFUPM), Dhahran 31261, Saudi Arabia
sheikhsi@kfupm.edu.sa, farooqstn@hotmail.com

Abstract— Small array antennas with directive coverage are an attractive solution for size limitation in wireless devices. In this paper, the design of a directive 10 GHz antenna with reduced size microstrip array and frequency selective superstrate (FSS) is presented. Inductive loading and reduced patch separation is used to incorporate 7-elements within a $100 \times 30 \text{ mm}^2$ array aperture. The superstrate (FSS) layer is optimized to properly excite the Fabry-Perot cavity and further increase the antenna directivity. Using HFSS software, the reflection response and the radiation pattern of the antenna array is optimized. The simulated responses agreed well with the measured results.

Index Terms — Antenna array, enhanced directivity, frequency selective surface, inductive loading, shorting posts.

I. INTRODUCTION

Recent communication devices require miniature microstrip array antennas with high directivity and reconfigurable coverage. Over the past decade, many techniques have been adopted to reduce the size of a microstrip antenna without sacrificing its directivity. One method to reduce antenna size is to use high dielectric constant (ϵ_r) substrate, but this comes at the cost of increased surface wave losses [1]. Another popular technique is to introduce electrical short between the patch and the ground plane to reduce the antenna size [2]. Shorting posts are modeled as a short piece of transmission line, which introduces a series inductance and a shunt capacitance due to self-inductance and close proximity of the shorting posts, respectively [3]. By optimizing the diameter, number and separation of the shorting posts, the desired resonant response of the antenna can be achieved [4].

The directivity and beam forming characteristics of a uniform microstrip array antenna are controlled through the magnitude and phase of the patch excitation signals [5]. Controlling the input excitation, however, requires the design of complicated array feeder networks to ensure correct magnitude and phase values are fed to the radiating elements [6]. An alternative is to use a Fabry-Perot cavity (FPC) resonator, formed between the array of microwave radiators and a partially reflecting frequency selective

superstrate (FSS) [7]. A side view of an FPC excited by a 7-element array is shown in Fig. 1. Multiple reflections inside the cavity result in constructive addition of the signal resulting in stronger radiated signal. To achieve maximum directivity, design parameters like height, size, position and composition of the cavity and the superstrate need to be optimized. This allows the cavity resonator to build up required field distribution without introducing significant resonator losses [8]. Through proper excitation, the side-lobe level (SLL) of the FPC antenna can also be controlled.

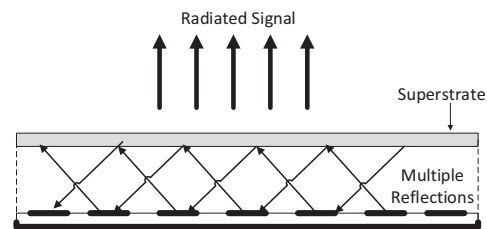


Fig. 1. Side view schematic of an FPC excited by a 7-patch linear antenna array.

In this paper, the positions and dimension of the shorting posts are carefully selected to reduce the width of the 10 GHz shorted patch array antenna by 50%. To further increase the antenna directivity, this 7-element linear array is used to optimally excite the FPC formed between the array ground and an optimally designed FSS.

II. SHORTED ANTENNA ARRAY DESIGN

Initially a $(3.3 \times 1)\lambda_0$ or a $100 \times 30 \text{ mm}^2$ antenna aperture was selected for the 10 GHz antenna array. For a patch separation of $0.5\lambda_0$, a maximum of 3-radiating patches were accommodated within the array aperture, as shown in Fig. 2 (a). The aim was to improve the directivity by increasing radiating patches within the same array aperture. This required shortening the patch width (W_p) with minimum effects on array efficiency, matching and radiation pattern. Based on the impedance distribution of a radiating patch, shorting posts were introduced to neutralize the changes in the input impedance due to shortening the patch width. The number, location and radius of the shorting

posts were optimized to accommodate 7-radiating shorted patches; instead of 3-radiating normal patches within the array aperture of 100 mm.

The 10 GHz array antenna with 7 shorted-patches is shown in Fig. 2 (b). Note that both antenna arrays of Fig. 2 are based on a 100 mm ($W_T = 3.3\lambda_0$) wide Duroid substrate with $\epsilon_r = 2.2$ and thickness, $h = 1.6$ mm. The antenna dimensions of the 3-patch 10 GHz array of Fig. 2 (a) were $L_p = 0.32\lambda_0$ (9.5 mm), $W_p = 0.45\lambda_0$ (13.6 mm) and $d_2 = 0.5\lambda_0$. The design parameters for 7-patch array shown in Fig. 2 (b) were $L_p = 0.32\lambda_0$ (9.5 mm), $W_p = 0.13\lambda_0$ (4 mm) and $d_2 = 0.37\lambda_0$. Three shorting posts, each with a radius of 0.25 mm and inter-post separation of 0.5 mm were placed inside each of the 7 rectangular patches. This reduced the width of each 10 GHz patch by more than 50% and allowed the replacement of the 3x1 patch array with 7x1 shorted-patch array on the same array aperture of $3.3\lambda_0$ (100 mm).

The simulated reflection responses of the 3-element and the 7-element array are superimposed in Fig. 3. Note that the shorted patches with reduced inter-element distance (d) have little effect on the impedance bandwidth of the antenna. The radiation patterns of these two antennas are plotted in Fig. 4, without including the feeder losses. As expected, the 7-element array exhibited a 25% increase in the antenna directivity.

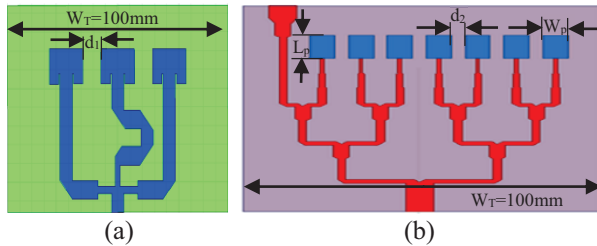


Fig. 2. 10 GHz array antenna with: (a) 3-element array of standard patches with inter-element spacing, $d_1 = 0.5\lambda_0$ and, (b) 7-element array of shorted patches with inter-element spacing, $d_2 = 0.37\lambda_0$.

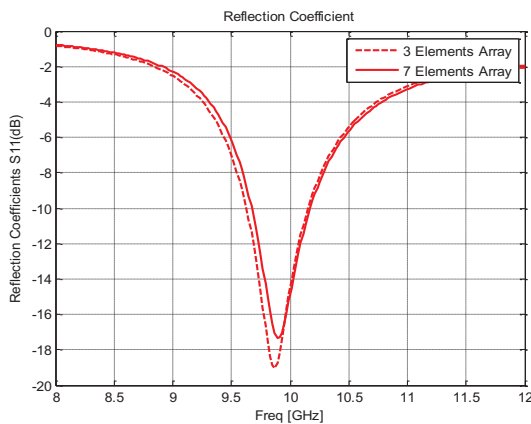


Fig. 3. Simulated reflection response (S_{11}) of the 3-element and the 7-element shorted patch antenna array.

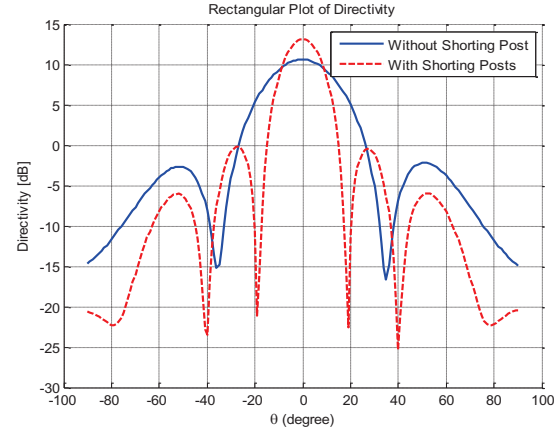


Fig. 4. Simulated E-plane radiation patterns of the 3-element and the 7-element shorted-patch array.

III. SHORTED ARRAY WITH FREQUENCY SELECTIVE SUPERSTRATE

To further increase the antenna directivity, the 7-element shorted patch array is used to excite an FPC resonator, formed between the array ground plane and the partially reflecting superstrate. Figure 5 shows the HFSS simulated model of the FPC antenna with FSS with the inset showing the dimensions of the dipole unit-cell. The shape and design of the FSS unit-cell plays a vital role in determining the response of the superstrate layer. Amongst the numerous unit-cell configurations used in literature [9], the simple design and ease in fabrication associated with the dipole unit-cell has made it the choice for the proposed FPC antenna array. The dimensions of the dipole unit-cell have been extracted using the empirical relations presented by Lee et al. in [10], and optimization has been achieved by using plane wave simulations in HFSS [11].

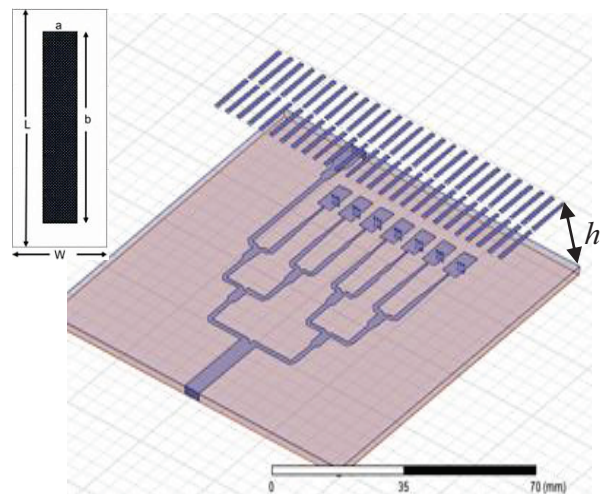


Fig. 5. HFSS simulation model of the 7-patch shorted antenna array with FSS layer forming the FPC.

To cover the entire aperture ($100 \times 30 \text{ mm}^2$) of the antenna array, the FSS required two layers of dipole unit-cells with 27 unit cells per layer as shown in Fig. 5. The simulated results demonstrate maximum radiation at 10 GHz for optimized cavity height (h) of $0.5\lambda_0$ (16 mm) and dipole unit-cell parameters of $L = 0.49\lambda_0$ (14.76 mm), $W = 0.12\lambda_0$ (3.69 mm), $a = 0.04\lambda_0$ (1.23 mm) and $b = 0.45\lambda_0$ (13.58 mm). This FSS layer can be implemented by using the packaging of the antenna. The formulation of the FPC using the FSS layer results in a 3.21 dB increase in the simulated directivity of the shorted 7-patch antenna array. Figure 6 shows the simulated E-plane radiation patterns with and without the FSS layer. As a result of an increased number of radiating elements, the shorted 7-patch antenna array has a simulated radiation efficiency of 73.15% which is 3.23% less than the 3-patch normal array. Placement of the FSS results in a further decrease in the simulated efficiency of the 7-element shorted antenna from 73.15% to 69.88%. In addition to the increase in peak directivity, an increase in the SLL is also observed, which can be countered by embedding the FSS on a stepped dielectric superstrate; a dielectric superstrate with varying ϵ_r . The reason for reduced SLL is the uneven partial reflections from the stepped dielectric superstrate, with central low- ϵ_r material sandwiched between the high- ϵ_r materials.

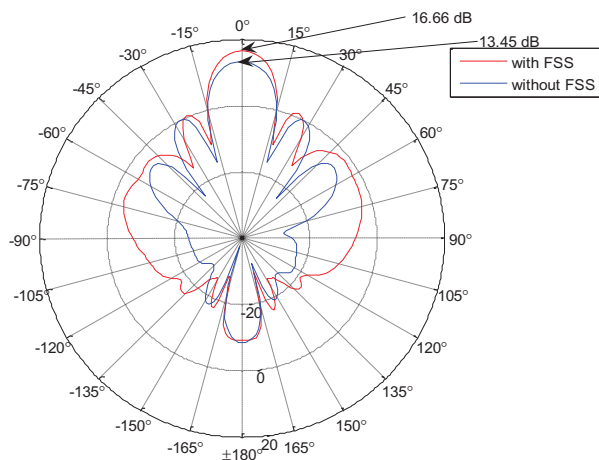


Fig. 6. Simulated E-plane directivity pattern comparison for the shorted 7-patch antenna array with and without the FSS.

IV. MEASUREMENT RESULTS

The 7-patch shorted antenna array along with the FSS has been fabricated according to the design parameters mentioned in Sections II and III. A snapshot of the fabricated FPC antenna array is shown in Fig. 7. Upon measuring the reflection characteristics of the

fabricated antenna array, it is evident from Fig. 8 that addition of the FPC results in a slight decrease (100 MHz) in the resonant frequency (9.8 GHz) as compared to the no FSS case (9.9 GHz). Additionally the impedance bandwidth of the FPC antenna also increases to 530 MHz as compared to 253 MHz for the without FSS case. A view of the measured E-plane directivity of the designed antenna, shown in Fig. 9, reveals that the addition of the FSS, and hence the formation of the FPC, results in a further increase of 3.41 dB in the measured directivity of the antenna. Note that, although for the directivity measurements the antenna array was used as a receiver, owing to reciprocity, the same performance is expected if used as a transmitter.

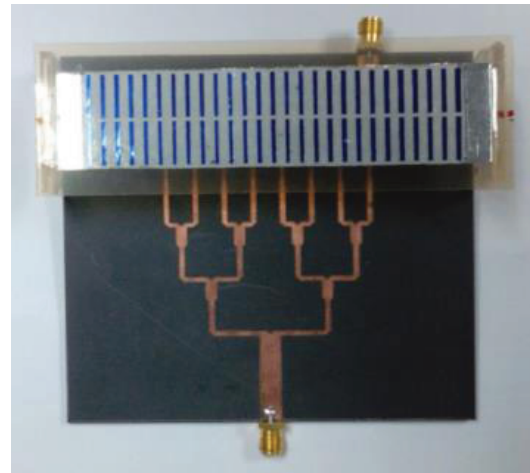


Fig. 7. Fabricated shorted 7-patch FPC antenna array with dipole unit-cell based FSS superstrate.

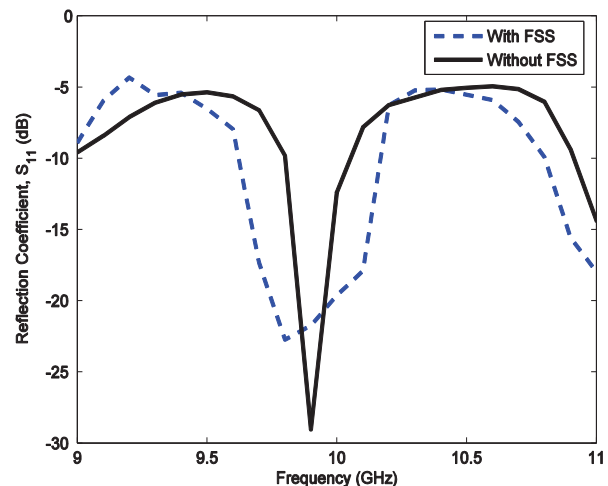


Fig. 8. Reflection characteristics (S_{11}) for the shorted 7-patch antenna array with and without the FSS superstrate.

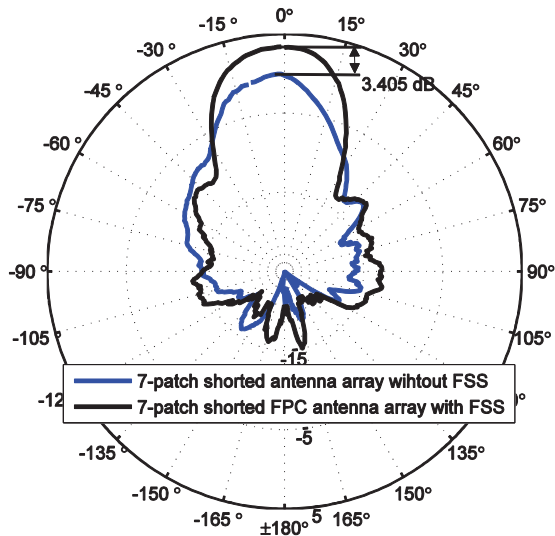


Fig. 9. Measured E-plane directivity patterns for the shorted 7-patch antenna array with and without the FSS superstrate.

V. CONCLUSION

The design of a $100 \times 30 \text{ mm}^2$ linear array antenna with 7-shortened patches and a frequency selective superstrate is presented. The antenna demonstrated an increased directivity of 6.2 dB due to increased number of radiating elements and optimized resonance by FPC using a dipole unit-cell based FSS. Inductive loading of the radiating patches enables placement of 7 radiating elements instead of 3 within the fixed antenna aperture of $3.3\lambda_0$ (100 mm). The thickness of the cavity is optimized to keep the antenna dimensions small. Since all the design parameters are a function of the operational wavelength (λ_0), the presented antenna design can be scaled to any frequency of operation. The measured results agree well with the simulated (HFSS) responses of the antenna presented design.

ACKNOWLEDGMENT

The authors would like to thank the King Abdulaziz City of Science and Technology (KACST) for funding the research project under grant no. AT-29-104 and the Deanship of Scientific Research (DSR) at KFUPM for supporting this research.

REFERENCES

- [1] K-L. Wong, *Compact and Broadband Microstrip Antennas*, John Wiley Sons Inc., 2002.
- [2] P. Kumar and G. Singh, "Microstrip antennas loaded with shorting posts," *Scientific Research*, 2009.
- [3] M. Sanad, "Effect of the shorting posts on short circuit microstrip antennas," *IEEE Antenna Propagation Symposium*, vol. 2, pp. 794-797, June

1994.

- [4] A. Pandey and A. K. Singh, "Compact H-shaped microstrip antenna with shorting posts using IE3D," *IEEE International Conference on Recent Advances in Microwave Theory and Applications*, 2008.
- [5] C. A. Balanis, *Antenna Theory: Analysis and Design*, Wiley Interscience, 2005.
- [6] S. S. I. Mitu, S. M. Al-Shahrani, and U. Johar, "24 GHz active phased array antenna for microwave sensors," *7th International Conference on Electronics, Hardware, Wireless and Optical Communication (EHAC'09)*, Cambridge UK, Feb. 21-23, 2009.
- [7] N. Guérin, S. Enoch, G. Tayeb, P. Sabouroux, P. Vincent, and H. Legay, "A metallic Fabry-Perot directive antenna," *IEEE Trans. Ant. Prop.*, vol. 54, no. 1, pp. 220-224, 2006.
- [8] R. Sauleau, "Fabry Perot resonators," *Encyclopedia of RF and Microwave Engineering*, vol. 2, pp. 1381-1401, 2005.
- [9] J. Shaker, R. Chaharmir, and H. Legay, "Investigation of FSS backed reflectarray using different classes of cell elements," *IEEE Transactions of Antennas and Propagation*, 2008.
- [10] Y. J. Lee, J. Yeo, R. Mittra, and W. S. Park, "Design of a high-directivity electromagnetic band-gap (EBG) resonator using a frequency selective surface (FSS) superstrate," *Microwave and Optical Technology Letters*, 2004.
- [11] F. Sultan, R. Hussain, and S. S. I. Mitu, "Design of reduced-size 7-patch antenna array with FSS based directivity enhancement," *2013 IEEE International Symposium on Phased Array Systems and Technology (ARRAY'13)*, Oct. 2013.



Sheikh Sharif Iqbal Mitu is an Associate Professor in EE Department of KFUPM, Dhahran, KSA. He has completed his M.Sc. and Ph.D. degrees from the EEE Department of University of Manchester, UK. He has authored 55+ referred journal/conference papers, 30+ technical reports and worked/working with 25+ projects funded by university, government (SABIC, KACST) and industry (Schlumberger).

He is a Fellow of IET, Senior Member of IEEE and Honorary Treasurer of IET Saudi section. His achievements includes several awards related to teaching, research and supporting student activities.



Farooq Sultan completed his M.Sc. and Ph.D. degrees from KFUPM, Dhahran, Saudi Arabia. His research interests comprise mainly of antenna array designs; however, he also has experience in wireless sensor network designs for practical applications. He has extensive research experience with antenna array designs and has authored/co-authored

a number of journal as well as conference publications along with a few US patents.

Currently, he chairs the Student Branch of the IEEE KFUPM section and is an IEEE Student Member as well.

Wide Bandwidth Endfire Antenna with Log-Period Directors

Yuanhua Sun¹, Guangjun Wen¹, Haiyan Jin¹, Ping Wang^{1,2}, Yongjun Huang¹,
and Jian Li¹

¹Centre for RFIC and System Technology, School of Communication and Information Engineering
University of Electronic Science and Technology of China, Chengdu 611731, China
sunyuanhua17@gmail.com

²Department of Electronic Engineering, College of Electronic and Information Engineering
Chongqing Three Gorges University, Chongqing 404000, China
cqrainycity@yahoo.com.cn

Abstract — This paper presents the design and implementation of a novel wide bandwidth endfire antenna with log-periodic directors. The feeding structure of the proposed antenna includes a balun which is formed using a pair of microstrip-to-slotline transitions. The proposed antenna has three resonant frequencies in the operating frequency band. Both simulation and measurement results show that the operating frequency band of the antenna for $S_{11} < -10$ dB covers the wide bandwidth (5 GHz – 10 GHz), and the relative bandwidth is 67%. Far field measurements in azimuth plane and elevation plane show that the radiation patterns are stable and end fire within the operating band at frequencies of 5 GHz, 7 GHz, 8 GHz, 10 GHz. The proposed antenna radiates a well-defined endfire beam, with a front-to-back ratio > 18 dB and cross polarization level below -28 dB. The dimension of the proposed antenna is 26 mm \times 27 mm. Good return loss and radiation pattern characteristics are obtained and measured results are presented to validate the usefulness of the proposed antenna structure for wide bandwidth endfire applications.

Index Terms — Endfire antenna, front-to-back ratio, log-period directors, wide bandwidth antenna.

I. INTRODUCTION

The advantages of a printed endfire antenna include not only the characteristics of a radiational Yagi antenna with endfire radiation pattern [1], [2], but also the characteristic of a microstrip antenna with low profile, miniature size, easy fabrication and low cost [3-6]. The feeding structure of quasi-Yagi antenna plays the crucial role in the performance. The odd-mode excitation needed for the driver, which is in the form of a centre-fed dipole, has to be maintained over the whole bandwidth by using a suitable balun. Baluns that are based on different types of transitions [7-9]. In [10] and [11], a hook-shaped balun is proposed for the feed of

the antenna. A broadband dipole antenna fed by an end-open “J” balun with integrated via-hole is presented in [12]. Due to the need to cover wide bandwidth, designs of endfire antennas focus on implementing new techniques aimed at increasing the bandwidth. The key factors to achieve wide bandwidth include using wide bandwidth baluns in the feeding structure of the antenna and modifying the shape of the radiator [13-15]. The maximum achieved bandwidth in those techniques is around 60% but the dimensions are large.

In this paper, the proposed antenna consists of the balun, driver, log-periodic directors and reflector in the form of truncated ground plane. The proposed antenna is compacted, the dimension of the proposed antenna is 26 mm \times 27 mm. An ultra-wideband microstrip-to-coplanar stripline balun is presented. The proposed antenna is fed by the ultra-wideband balun. The proposed antenna includes tapered drivers, log-periodic directors and a truncated ground plane acting as a reflector. The antenna should find wide application in a great variety of wireless systems such as microwave imaging system.

As shown in Fig. 1, the configuration of the balun is a part of the complete antenna structure. The input port is converted from a microstrip line to a slotline using a wideband microstrip-to-slotline transition. The circular slots at the bottom layer and circular microstrip patch at the top layer are used to achieve the required impedance matching between the input microstrip line and the output slotline across an ultra-wideband. The slotline at the bottom layer is coupled to a coplanar stripline (CPS) at the top layer using another slotline to microstrip transition. The balun creates equal in magnitude and out-of-phase signals across a wide frequency band in the CPS output. The input microstrip line of the balun is designed to have 50 Ω impedance for a perfect matching with the input feeder. To simulate the characteristics of the designed antenna, we used the simulation software high frequencies in the operating

frequency bandwidth. The effects on each resonant frequency caused by the key antenna parameters such as the length of driven element, the length of director, the distance between the driven element and the director, the length of ground gap and diameter of the metal circle patch. Through optimizing three resonant frequencies, a wideband endfire antenna is designed and fabricated. Then, a series of measurements are conducted with a Vector Network Analyzer in an anechoic chamber. The measured results show that the relative bandwidth for $S_{11} < -10$ dB is about 67%. The radiation patterns at 5 GHz, 7 GHz, 8 GHz and 10 GHz also show that the antenna works well in an end-fire state and has a stable characteristic.

The taper driver and log-periodic directors are used to increase the operational bandwidth. In the presented design, a pair of microstrip-to-slotline transitions is used to feed the antenna and the size of the antenna is not increasing significantly. The performance of the designed antenna is simulated using the simulation tool HFSS v13. The antenna radiates a well-defined end-fire beam, with a front-to-back ratio (> 20 dB) and cross-polarization level below -18 dB.

II. ANTENNA DESIGN AND PARAMETERS STUDY

The configuration of the proposed end-fire antenna is shown in Fig. 1. The antenna is printed on Rogers RT6010LM substrate which has a thickness of 0.635 mm. The relative permittivity of the substrate is 10.2 and the dielectric loss tangent is 0.0023. The feeding structure consists of a 50Ω microstrip connected to 50Ω SMA connector, and a balun which is composed of two microstrip-to-slotline transitions and T-junction of microstrip slotline. The utilized transitions to form the balun are designed following the guidelines in [16].

The gap between the two arms of the driver is chosen for the best possible matching with coplanar stripline feeder of the driver. The driver of the proposed antenna is in the form of center-fed dipole with tapered width in the form of a bow-tie. The reflector is in the form of truncated ground. The feeding structure of the antenna includes a balun that is formed from two microstrip-to-slotline transitions and T-junction of microstrip slotline. The driver is made up by taper arms with total length equal to half of the effective wavelength at the center of band. Directors in form of log-periodic rectangular arms are placed in front of the driver and at a distance between the ground plane and the driver. The overall dimensions of the proposed antenna and the feeding structure are optimized using the simulation tool HFSS v13. The overall dimensions of the antenna are $26 \text{ mm} \times 27 \text{ mm}$ indicating a compact size.

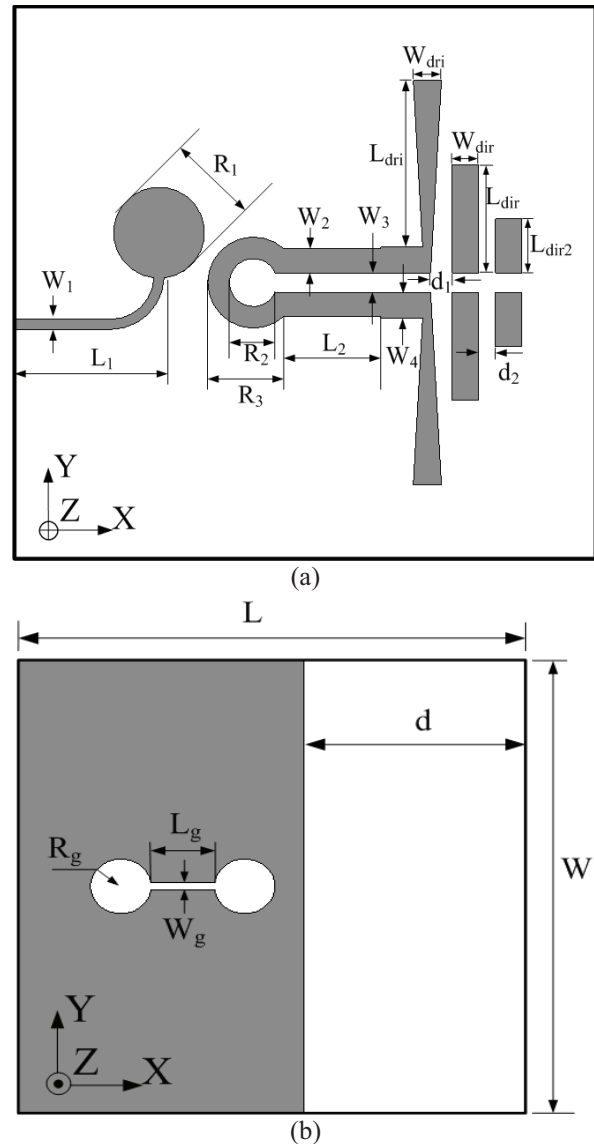


Fig. 1. Configuration of the proposed antenna: (a) front view, and (b) back view.

A. Effects of the driven element

L_{dri} becomes shorter than a quarter of wavelength at the first resonant frequency [17]. Figure 2 (b) shows the width of gap between two driver elements. From Fig. 2 (b), it is found that W_3 does significantly improve the bandwidth of the proposed antenna. The bandwidth defined by $S_{11} < -10$ dB increases when W_3 is decreased from 1.5 mm to 0.6 mm. However, when $W_3 < 0.6$ mm, the bandwidth changed badly. The simulation results show that all of the resonances from high frequencies to low frequencies shifted slightly while W_3 decreased. These results illustrate that the lowest operating frequency of the antenna depends primarily on the length L_{dri} and W_3 .

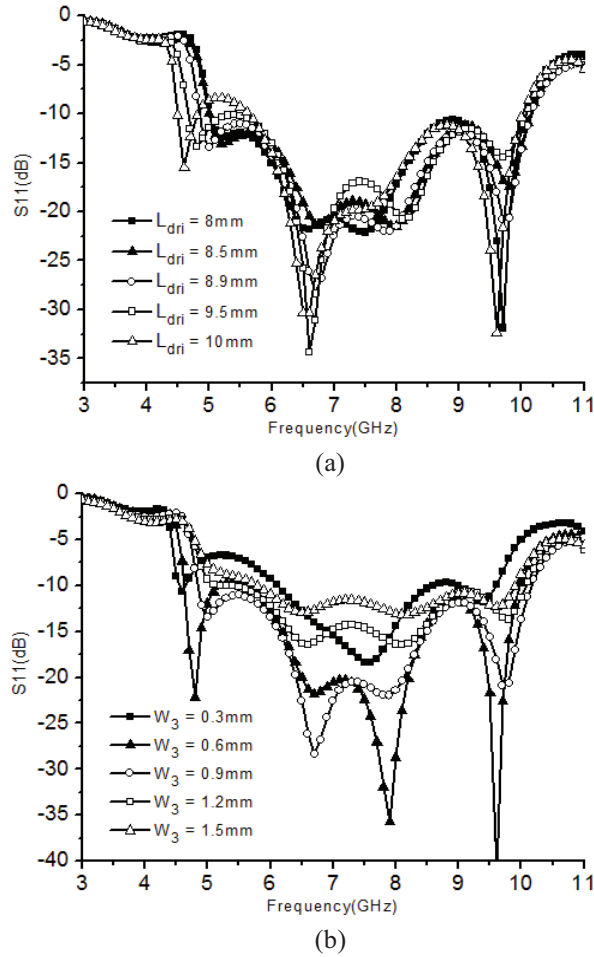


Fig. 2. Effects of the driven element: (a) simulated S_{11} with different L_{dir1} , other parameters are the same as Fig. 1. (b) Simulated S_{11} with different W_3 , other parameters is the same as Fig. 1.

B. Effects of the directors

The director of the traditional Yagi antenna obtains its energy by electromagnetic coupling from the driven element. The length of the director and the spacing relative to the driven element affect the gain and bandwidth of the Yagi antenna. According to [18], the typical length of the director is shortened by 10-20% from the length of the driver. The log-periodic directors are used to improve the bandwidth of the proposed antenna. The effects of the director are shown in Fig. 3.

Figure 3 (a) shows the S_{11} of the proposed antenna corresponding to different lengths of the first director element, L_{dir1} . From the Figure 3 (a), it can be observed that the third resonant frequency is significantly decreased such that the bandwidth of the proposed antenna becomes narrow when L_{dir1} is increased from 5 mm to 8 mm. From the Fig. 3 (b), it can be observed that the third resonant frequency decreased and the fourth resonant frequency changed badly when W_{dir} is increased

from 0.5 mm to 2 mm. Therefore, the highest operating frequency of the antenna depends primarily on the length of the first director.

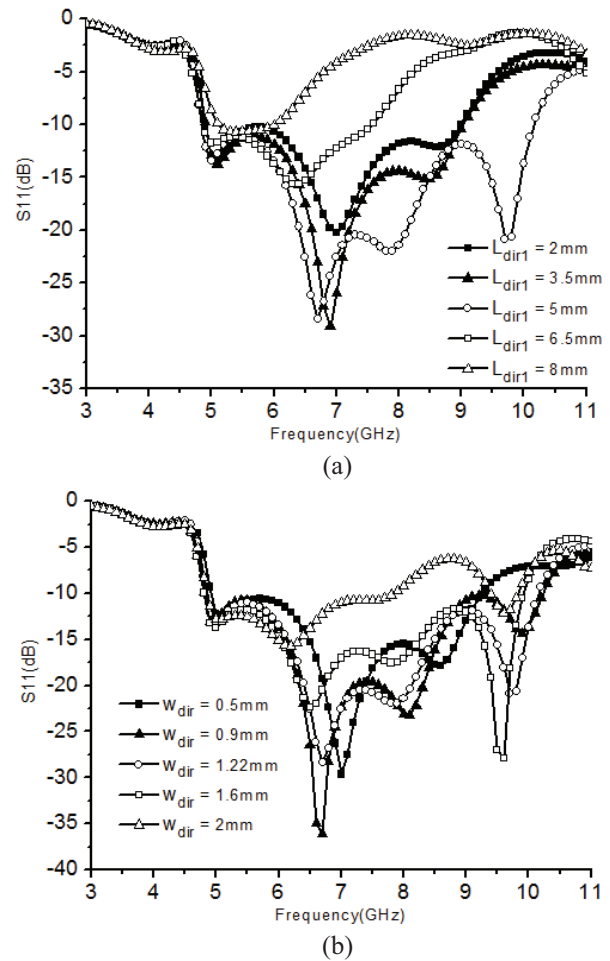


Fig. 3. Effects of the director: (a) simulated S_{11} with different L_{dir1} , other parameters are the same as Fig. 1. (b) Simulated S_{11} with different W_{dir} , other parameters is the same as Fig. 1.

C. Effects of the feeding system

Figure 4 shows the effects of the feed system of the antenna. The S_{11} of the proposed antenna corresponds to different lengths of the slotline transition, L_g in the ground plane, shown in Fig. 4 (a). Increasing L_g from 2.5 mm to 4 mm causes a decrease of the second resonant frequency. As a result, the impedance match becomes better within the low-frequency band, but it becomes worse within high-frequency band. Figure. 4 (b) shows the S_{11} with respect to the different diameters of the circle patch in the top layer, R_1 .

Similar to the trend of L_g , increasing R_1 results in a decrease of the second resonant frequency and a better impedance match in the low-frequency band and a worse impedance match in the high-frequency band.

Figure 4 (c) shows the S_{11} with respect to the different diameters of the tap circle in the ground plane, R_s .

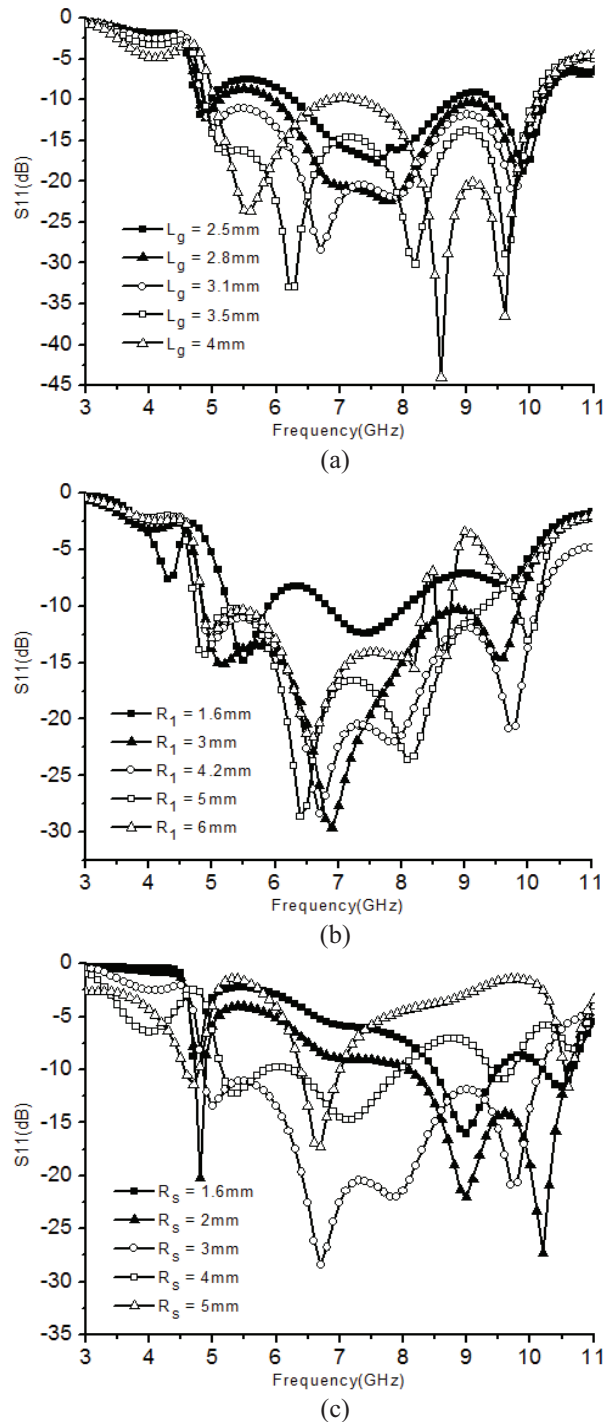


Fig. 4. Effects of the feed system: (a) Simulated S_{11} with different L_g , other parameters are the same as Fig. 1. (b) Simulated S_{11} with different R_1 , other parameters are the same as Fig. 1. (c) Simulated S_{11} with different R_s , other parameters are the same as Fig. 1.

From the Fig. 4 (c), it can be observed that the third resonance is increased badly and the bandwidth of the proposed antenna becomes narrow when R_s is increased from 1.6 mm to 5 mm. Essentially, the second resonance and third resonance around the center of the operating frequency are determined by the feed structure.

III. SIMULATION AND MEASUREMENT RESULTS

According to the results discussed in the previous section, the optimal parameters of the proposed antenna are listed as follows: $L=27$ mm, $W=26$ mm, $L_g=3.1$ mm, $L_{dir1}=8.9$ mm, $L_{dir2}=6.5$ mm, $L_{dir3}=2.5$ mm, $W_{dir1}=1.3$ mm, $W_{dir2}=1.22$ mm, $W_3=0.9$ mm, $R_1=4.2$ mm, $R_s=3$ mm, $R_2=2.1$ mm, $R_3=3.5$ mm, $W_1=0.46$ mm, $W_2=1.1$ mm, $W_3=0.9$ mm, $W_4=1.2$ mm, $L_1=7$ mm, $L_2=4.48$ mm, $d_1=1.0$ mm, $d_2=0.78$ mm. To verify the proposed antenna design, a prototype is fabricated as shown in Fig. 5 and the results are presented here.

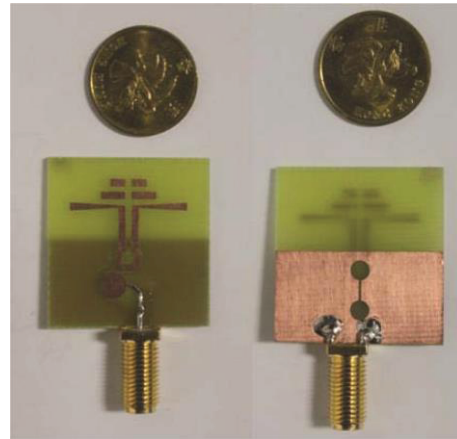


Fig. 5. Fabricated prototype of the proposed antenna.

All the measured results are carried out in anechoic chamber using a vector network analyzer (VNA) and other microwave test instruments. The variations of the reflection coefficient and gain with frequency are shown in Fig. 6. As shown in Fig. 6, the S_{11} from the measurement is compared with the simulation results, which shows accordance between measured and simulated values. The operating frequency defined by $S_{11} < -10$ dB ranges from 5 GHz to 10 GHz, and the relative bandwidth of the proposed antenna is 67%.

Within the operating frequencies, the measurement gain of the antenna is between 3 dB and 7.5 dB, as shown in Fig. 6. It is possible to increase the gain, if required, by adding director, but this would be at the cost of increasing the size of the antenna slightly. Co- and cross-polarization of far field radiation patterns in the E- and H-plane at 5 GHz, 6 GHz, 7 GHz, and 8 GHz were measured and plotted in Fig. 7. As shown in Fig. 7,

a well-defined end-fire pattern is observed with a front-to-back ratio of 18 dB and a maximum cross-polarization level of -28 dB. It is clear that the antenna has a reasonable directivity where the front-to-back ratio varies from around 7 dB to 10 dB across the 67% bandwidth. It can be observed from the figure that the radiation patterns are stable at these four operating frequencies in the xoy and xoz planes. The antenna works in an endfire state and the maximum radiation in the direction of the +x axis.

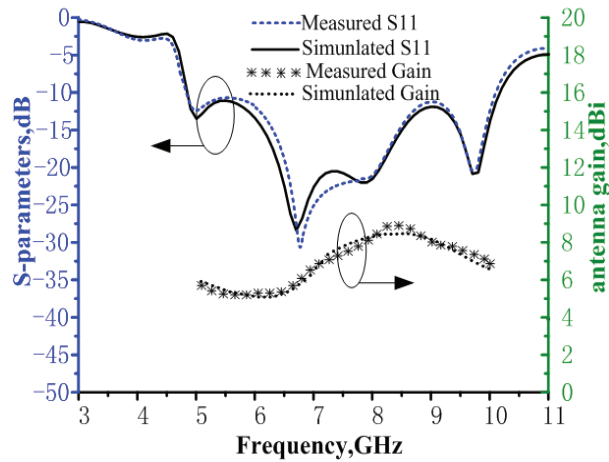


Fig. 6. The simulation and measurement reflection coefficient and measured gain.

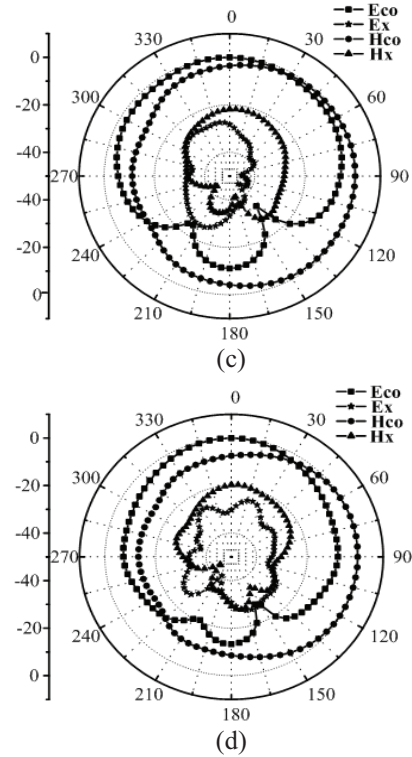
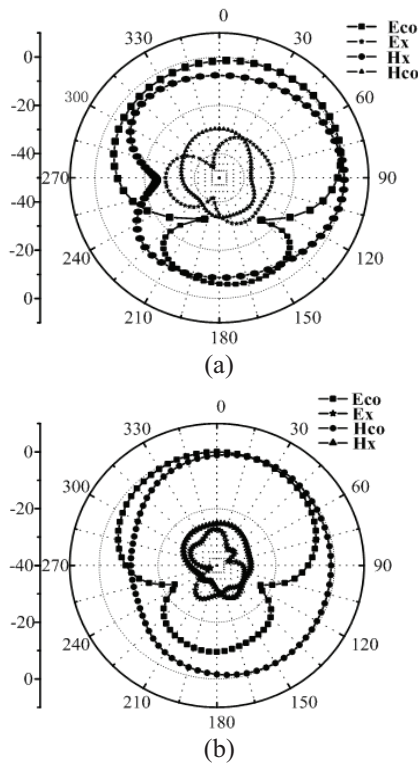


Fig. 7. The measured radiation pattern: (a) 5 GHz, (b) 7 GHz, (c) 8 GHz, and (d) 10 GHz.



IV. CONCLUSION

In this paper, a novel endfire wide bandwidth antenna with log-periodic directors has been presented. The antenna is compact and easy to fabricate, and achieves extremely wide bandwidth and good radiation characteristics in items of beam pattern, front-to-back ratio and cross-polarization. Both simulation and measurement results show that the antenna achieves a relative frequency bandwidth of 67%. The stable radiation patterns at 5, 7, 8, 10 GHz show that the antenna works in an endfire state and that the maximum radiation is in the direction of the +x axis. The front-to-back ratio of the proposed antenna is more than 28 dB. The cross polar performance is good and better than -18 dB. Further improvement to the radiation pattern and gain would require an additional director element. The antenna should find wide application in a great variety of wireless systems such as microwave imaging system.

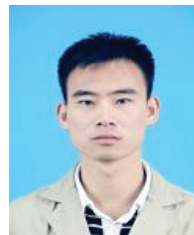
ACKNOWLEDGMENT

This work is supported by Research Fund for the Doctoral Program of Higher Education of China (No. 20110185110014), Science and Technology on Electronic Information Control Laboratory of China and National Nature Science Foundation of China

(No. 60901019/F0106).

REFERENCES

- [1] P.-Y. Qin, A. R. Weily, Y. J. Guo, T. S. Bird, and C.-H. Liang, "Frequency reconfigurable quasi-Yagi folded dipole antenna," *IEEE Transactions on Antennas and Propagation*, vol. 58, pp. 2742-2747, 2010.
- [2] N. Nikolic and A. R. Weily, "Compact E-band planar quasi-Yagi antenna with folded dipole driver," *IET Microwaves, Antennas & Propagation*, vol. 4, pp. 1728-1734, 2010.
- [3] B. Honarbakhsh and A. Tavakoli, "Analysis of thin microstrip antennas by meshless methods," *The Applied Computational Electromagnetic Society*, vol. 27, pp. 983-990, 2012.
- [4] Y. Li, P. Yang, F. Yang, and S. He, "A method to reduce the back radiation of the fold PIFA antenna with finite ground," *The Applied Computational Electromagnetic Society*, vol. 28, pp. 110-115, 2013.
- [5] M. Ojaroudi, N. Ojaroudi, and N. Ghadimi, "Enhanced bandwidth small square slot antenna with circular polarization characteristics for WLAN/WIMAX and C-band applications," *The Applied Computational Electromagnetic Society*, vol. 28, pp. 156-161, 2013.
- [6] Y. Li, W. Li, and W. Yu, "A multi-band/UWB MIMO/diversity antenna with an enhanced isolation using radial stub loaded resonator," *The Applied Computational Electromagnetic Society*, vol. 28, pp. 8-20, 2013.
- [7] Z. P. Wang, "Yagi antenna with improved out-of-band gain suppression," *IET Electronics Letters*, vol. 48, pp. 546-548, 2012.
- [8] T.-G. Ma, C.-W. Wang, R.-C. Hua, and J.-W. Tsai, "A modified quasi-Yagi antenna with a new compact microstrip-to-coplanar strip transition using artificial transmission lines," *IEEE Trans. Antenna Propag.*, vol. 57, pp. 2469-2474, 2009.
- [9] H. K. Kan, A. M. Abbosh, R. B. Waterhouse, and M. E. Bialkowski, "Compact broadband coplanar waveguide-fed curved quasi-Yagi antenna," *IET Microw. Antennas Propag.*, vol. 3, pp. 572-574, 2007.
- [10] S. J. Wu, C. H. Kang, K. H. Chen, and J. H. Tarn, "A multiband quasi-Yagi type antenna," *IEEE Transactions on Antennas and Propagation*, vol. 58, pp. 593-596, 2010.
- [11] D. C. Chang, C. B. Chang, and J. C. Liu, "Modified planar quasi-Yagi antenna for WLAN dual-band operation," *Microwave and Optical Technology Letters*, vol. 46, pp. 443-446, 2005.
- [12] E. A. Navarro, B. Schoenlinner, and G. M. Rebeiz, "Broadband printed dipole with integrated via-hole balun for WiMAX applications," *Microwave and Optical Technology Letters*, vol. 53, pp. 52-55, 2011.
- [13] Z. Y. Zhang, G. Fu, S. L. Zuo, and X. Gong, "Wideband unidirectional patch antenna with Γ -shaped strip feed," *Electronics Letters*, vol. 46, pp. 24-26, 2010.
- [14] N. K. Nahar, B. Raines, R. G. Rojas, and B. Strojny, "Wideband antenna array beam steering with free-space optical true-time delay engine," *IET Microwaves, Antennas & Propagation*, vol. 5, pp. 740-746, 2011.
- [15] H. Kan, R. Waterhouse, A. Abbosh, and M. Bialkowski, "Simple broadband planar CPW-fed quasi-Yagi antenna," *IEEE Antennas Wireless Propag. Letters*, vol. 6, pp. 18-20, 2007.
- [16] M. E. Bialkowski and A. M. Abbosh, "Design of a compact UWB out-of-phase power divider," *Progress In Electromagnetics Research*, vol. 116, pp. 18-20, 2007.
- [17] O. Tze-Meng, K. G. Tan, and A. W. Reza, "A dual-band omni-directional microstrip antenna," *Progress In Electromagnetics Research*, vol. 106, pp. 363-376, 2010.
- [18] W. L. Stutzman and G. A. Thiele, *Antenna Theory and Design*, New York, Wiley, 1998.



Yuanhua Sun received the B.S. degree in Communication Engineering from the Liaocheng University in 2007, and M.S. degree in Signal and Information Processing from Chengdu University of Information Technology in 2010. He is working toward the Ph.D. degree in UESTC. His research interests include analytical and numerical modeling of metamaterials and antenna theory and design and signal processing.



Guangjun Wen was born in Sichuan, China, in 1964. He received his M.S. and Ph.D. degrees in Chongqing University of China in 1995 and UESTC in 1998, respectively. He is currently a Professor and Doctor Supervisor in UESTC.

His research and industrial experience covers a broad spectrum of electromagnetics, including RF, Microwave, Millimeter wave Integrated Circuits and Systems design for Wireless Communication, Navigation, Identification, Mobile TV applications, RFIC/MMIC/MMMIC device modeling, System on Chip (SoC) and System in Package (SiC) Design,

RF/Microwave/Millimeter wave Power source Desdgn, "The Internet of things" devices and system, RFID system and networks, antennas, as well as model of electromagnetic metamaterial and its application in microwave engineering area.



Haiyan Jin received the M.S. and Ph.D. degrees in Electrical Engineering and Communication and Information Engineering from University of Electronic Science and Technology of China in 2006 and 2010, respectively. He now is Associate Professor with School of Communication and Information Engineering, University of Electronic Science and Technology of China.



Ping Wang received the B.S. degree in Physics from Western Chongqing University of China in 2005 and the M.S. degree in Theoretical Physics from Chongqing University, Chongqing, in 2008. Currently, he is working toward the Ph.D. degree in UESTC. His current research interests include patch antennas, wideband antennas, and arrays.



Yongjun Huang received the B.S. degree in Mathematics from Neijiang Normal University of China in 2007, M.S. degree in Communication Engineering from University of Electronic Science and Technology of China (UESTC) in 2010, and is currently working toward a Ph.D. degree in UESTC. His research activities are electromagnetic metamaterial and its application in microwave engineering area, FDTD and CAD analysis for the metamaterial model and characteristics.



Jian Li received the B.S. and M.S. degrees in Communication Engineering from UESTC in 2007 and 2010, respectively, and is currently working toward a Ph.D. degree in UESTC. His research interests include RF, Microwave, and Millimeter wave Integrated Circuits and system. His is also interested in electromagnetic metamaterial and its applications in substrate integrated waveguide.

A Simple Electromagnetically Fed Circularly-Polarized Circular Microstrip Antenna

Mursyidul I. Sabran¹, Sharul Kamal A. Rahim¹, Ping Jack Soh², Chee Y. Leow¹,
and Guy A. E. Vandenbosch³

¹ Wireless Communication Centre (WCC), Faculty of Electrical Engineering
Universiti Teknologi Malaysia, UTM Skudai, 81310, Johor, Malaysia
mursyid@fkegraduate.utm.my, sharulkamal@fke.utm.my, bruceleow@fke.utm.my

² The Advanced Communication (ACE) Centre of Excellence, School of Computer and Communication Eng.
Universiti Malaysia Perlis (UniMAP), 02600 Arau, Perlis, Malaysia
pjsoh@unimap.edu.my

³ ESAT-TELEMIC Research Div.
KU Leuven, Kasteelpark Arenberg 10, 3001 Leuven, Belgium
guy.vandenbosch@esat.kuleuven.be

Abstract — Existing literature on circularly polarized antennas fed with a microstrip transmission line does not include a systematic methodology to control and tune the reflection coefficient (S_{11}) and axial ratio (AR). To enable systematic tuning of those performance metrics, this study proposes a new, circularly polarized, circular microstrip patch antenna with truncated square slot. A combination of an edge-truncated square-slot and non-contacted electromagnetic coupling methods implemented in combination with circular patch results in a directional, left-handed circularly polarized (LHCP) pattern. This article discusses the analysis of several slot shapes that contribute to a good circularly polarized antenna. It also shows that the square slot with truncated edges is more effective in producing circular polarization than the conventional circular and usual square slot. Simulated and experimental results are in good agreement and indicate a -10 -dB S_{11} and a 3-dB AR bandwidth of about 90 MHz and 25 MHz, respectively.

Index Terms—Antenna, circular patch, circular polarization, electromagnetically coupled feeding.

I. INTRODUCTION

In recent years, research on circularly polarized (CP) antennas has intensified due to their many advantages compared to linearly polarized antennas. This is due mainly to CP antennas' ability to operate with similar radiation performance despite being installed in various random orientations [1]. However, a CP antenna design is more complicated, since S_{11} , AR, and efficiency must be tuned simultaneously for satisfactory performance. Theoretically, a CP antenna can be produced when two

orthogonal modes are excited with the same amplitude and 90° phase difference. Therefore, a rectangular-shaped patch usually is chosen, since it is easier to excite two orthogonal modes. In addition, the antenna shape can be structured to realize a circularly polarized antenna, as is the case in the Archimedean Spiral antenna [2]. Various methods have been presented to produce CP characteristics in rectangular-patch antennas. One example is reported in [3] where two methods are combined to enable CP. One of the most popular methods of implementing CP antennas is by truncating square patches fed by microstrip transmission lines (MTL), as in [4]. However, optimization needs to be performed carefully due to the multiple antenna parameters involved.

Note that using a $50\text{-}\Omega$ probe feed is more flexible than an MTL implemented on the same surface. This is because a probe feed implemented using a coaxial connector can be positioned anywhere on the patch without affecting the main modal current distribution. Conventionally, an MTL easily can produce CP characteristics using the contacted feeding method, in which the MTL is connected directly to the patch. For circular polarization excitation, the MTL is located with an optimum offset from the center of the patch edges. Meanwhile, an MTL also can create CP characteristics by using a non-contacted method, in which the MTL is placed near the edges of the patch structure with the ideal gap between them.

One of the main challenges in enabling circular polarization for a circular-patch antenna is the unavailability of corners for orthogonal phase excitation. Several recent studies have investigated circular-shaped CP antennas [5-7]. In [5], several peripheral cuts are introduced at the

edge of the circular patch with optimum probe-feed to produce a CP antenna. In [6], good AR performance is obtained by introducing unbalanced circular slots on the radiating element. In addition, an unequal cross-shape on the ground plane with proper feeding point can function as a CP antenna, as reported in [7]. Unfortunately, these techniques are more complex due to the need for optimal slots or feed points.

In [8,9], a single MTL located closely beside the radiating element is used to produce an electromagnetically coupled feed. An optimal air gap produces a good CP antenna. This method is conventionally implemented for square-, meander- [8] and fractal-shaped ring [9] radiating elements. Corners available from these shapes facilitate excitation of the two orthogonal modes. However, existing literature does not discuss explicitly how to control and tune the S_{11} and AR [8,9] simultaneously. Modifying the antenna design affects both performance metrics, that is, impedance and AR bandwidth. Therefore, it is critical to know how the parameters of the antenna affect the S_{11} and AR.

In this investigation, a single, curved MTL is used to feed a circularly shaped patch antenna. To our best knowledge, this simple but novel technique has yet to be reported in open literature. The physical characteristics of the proposed antenna allow its AR and S_{11} to be tuned separately for operation in the 2.45 GHz industrial, medical and scientific (ISM) band. Before arriving at the final structure, several variations of the circular patch were investigated. The final antenna structure integrates a truncated square slot because of its capability to perform optimally as a CP antenna and its simplicity in tuning. Both simulation and measurement results show that the proposed antenna attains a satisfactory performance with a -10 -dB impedance bandwidth of 90 MHz (2.41–2.50 GHz) and a 3-dB AR bandwidth of 25 MHz (2.433–2.458 GHz).

II. DESIGN APPROACH

Figure 1 depicts the basic circular microstrip-patch topology that was considered. The initial radius of the circular patch was obtained by using the procedure outlined in [10]. The antenna was fed by a 3-mm-wide transmission line, which matched to a 50- Ω SMA connector. Both antenna elements were implemented on an inexpensive 1.6-mm-thick FR4 substrate sized at $W_{\text{Sub}} \times L_{\text{Sub}}$, with a relative permittivity (ϵ_r) of 4.5 and a loss tangent ($\tan\delta$) of 0.019. Simulations were performed using CST Microwave Studio, which is based on the finite integration technique (FIT). The time domain solver was used for numerical calculations, and the overall structure was divided into a maximum of 222,156 mesh cell. The 50- Ω port was excited by using a waveguide port.

Since it is well known that a properly excited circular patch generates circular polarization easily, it was chosen as the basis of this antenna. The curved 50- Ω MTL was used to feed power to the patch via electromagnetic

coupling. The start and end of the curved section were designed to enable excitation of two transverse modes with equal amplitudes and orthogonal phases, similar to a conventional patch, fed using a dual-feed, hybrid coupler.

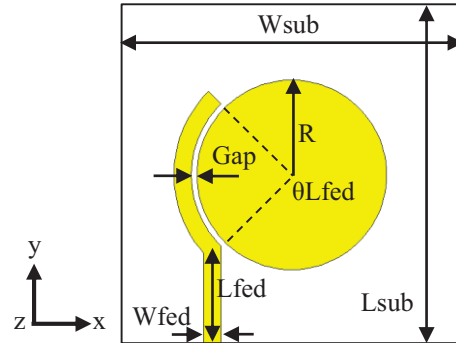


Fig. 1. Initial design of the proposed circular-patch antenna.

Figure 2 (a) shows the current distribution of the initial structure with the circular patch. It is observed that the current flows from the bottom corner of the circular patch around its perimeter. This structure was investigated further by adding a simple circular slot to form a ring. Figure 2 (b) shows this ring and the current distribution.

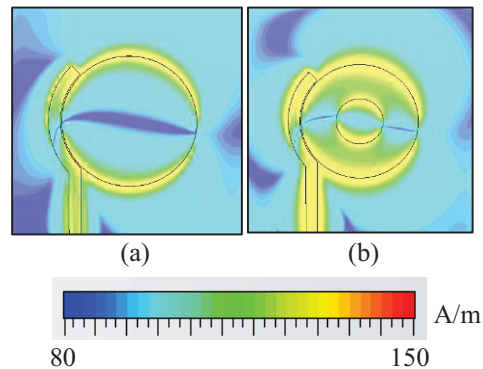


Fig. 2. Simulated current distribution at 2.45 GHz: (a) circular patch, and (b) circular ring.

It is evident that introducing a slot centered inside the radiator modifies the current distribution along the ring. This motivated further investigation of the circular-polarization characteristic. Parameterization of patch and slot sizes, which influence the S_{11} and AR simultaneously, increases the complexity in optimizing the circular-polarization characteristic when a circular ring slot is used. Therefore, the next section analyzes the slot shapes considered.

III. ANALYSIS OF PATCH SLOTS

This section describes the detailed analysis conducted on several slot shapes embedded within the circular patch. The analysis was performed with the objective of

identifying optimum slot shapes for satisfactory S_{11} and AR. Circular, square, and edge-truncated square slots were investigated.

First, analogous to [8], in which a square slot is embedded within a square patch, a circular slot embedded within a circular patch was investigated. Figure 3 (a) shows in a dashed box the circular slot centered within the circular patch antenna and its parameters. The radius of the circular patch is labeled R , and the radius of the circular slot is labeled R_s . Three different values of parameter R_s were examined, while R was fixed. Figures 3 (a) and 3 (b) show the S_{11} and AR when the circular slot was introduced to the patch antenna. Results show that the resonant frequency was slightly shifted with respect to the target resonance of 2.45 GHz when R_s was decreased (see Fig. 3 (a)), while its AR was above 10-dB (see Fig. 3 (b)). In contrast to the results in [8,9], in which ring shapes successfully enable circular polarization, it was concluded that the circular ring is not a good option to produce circular polarization for the proposed antenna.

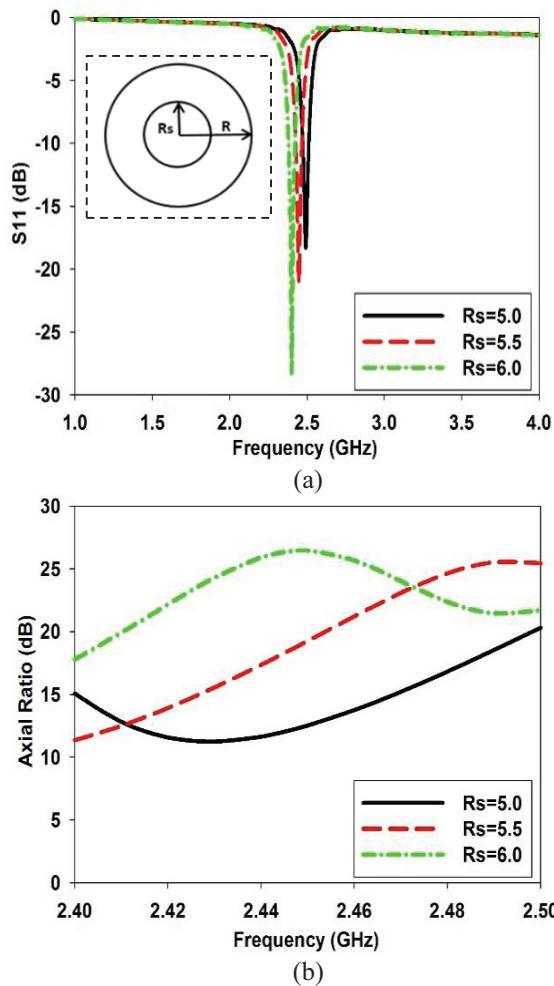


Fig. 3. Parametric study on the circular slot: (a) reflection coefficient, and (b) axial ratio.

The next investigation concerned a square slot on the circular-patch antenna. The parameter S is the length of the square slot centered on the circular patch. Figure 4 shows the S_{11} and AR for this proposed structure. It can be seen that the resonance also is slightly shifted upward when the length of the square slot is decreased, as shown in Fig. 4 (a).

This characteristic also was observed in the previous structure. Thus, it can be concluded that the various slot shapes do not affect the S_{11} of this antenna significantly. However, the AR is highly affected by changes in the square-slot length. Figure 4 (b) indicates that an AR of less than 10-dB can be achieved. Its lowest point shifts upward when the value of S is decreased, similar to the behavior of S_{11} . Hence, this square-slot structure is more suitable to excite a circularly polarized characteristic on a regular circular-patch antenna. The same was observed in [8].

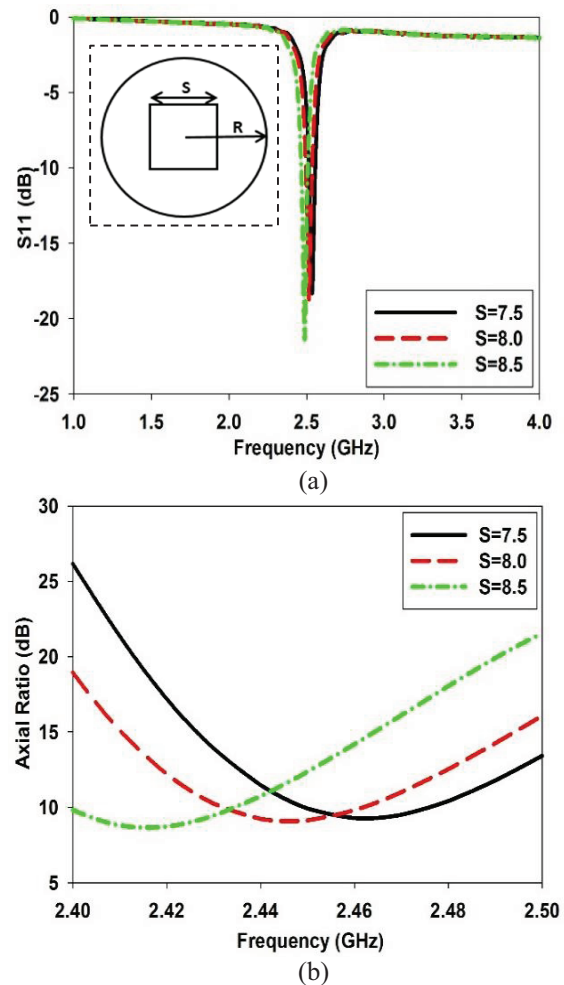


Fig. 4. Parametric study on the square slot: (a) reflection coefficient, and (b) axial ratio.

By modifying the topology of the antenna in the

previous section, a truncated square slot with various truncation sizes was proposed and analyzed. In Fig. 5, the small dashed box shows the truncated square slot, with C representing its truncation length. A significant improvement of the AR was observed, while the S_{11} remained unchanged at 2.45 GHz, as shown in Fig. 5 (a). Therefore, it can be concluded that the truncation length, C , affects only the AR and not the resonant frequency, as evident in Fig. 5 (b). Consequently, the CP characteristic of the antenna is controllable via the truncation length and slot shape.

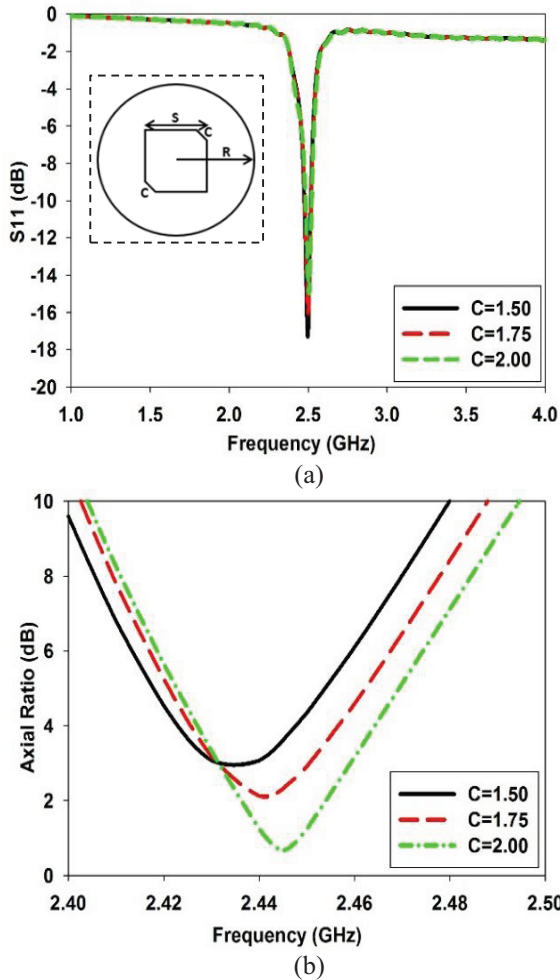


Fig. 5. Parametric study on the edge-truncated square slot: (a) reflection coefficient, and (b) axial ratio.

Because of its good AR, the truncated square slot was selected as the slot type to be integrated into the circular patch. The truncation length, C , can be adapted easily to tune the target AR; while the square-slot size, S , and radius of the patch, R , modify its S_{11} . Proper optimization of C excites two orthogonal modes similar in amplitude and 90° out of phase at 2.45 GHz. Then, this phase difference produces a good circularly polarized

antenna. Having identified the critical parameters, the final investigation was performed on the gap between the transmission line and patch, as it also influences antenna performance.

Figure 6 shows the parametric studies for several values of the gap between the transmission line and patch. Figure 6 (a) demonstrates the effect of several gap values on the S_{11} . Results show the S_{11} degrades to approximately -10 -dB as the gap value is increased. This occurs because the intensity of the electromagnetic (EM) field coupled to the radiating element is decreased, along with a simultaneous decrease in power received by the patch element, causing degradation in the S_{11} . In addition, as Fig. 6 (b) shows, the AR is shifted to the higher frequencies, and its magnitude degrades as the gap increases. However, this degradation is not severe, and the values are maintained below 3-dB.

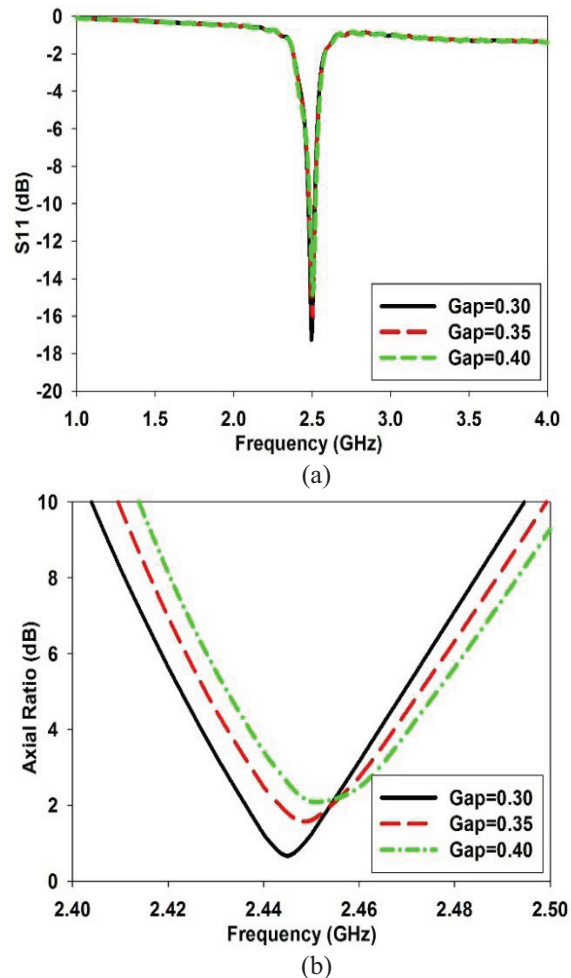


Fig. 6. Parametric study on the gap between transmission line and patch element: (a) reflection coefficient, and (b) axial ratio.

Figure 7 shows the simulated E-field distribution of

the edge-truncated structure. It is observed that the current flows circularly with left-handed CP, thus contributing to the left-hand circular-polarization radiation characteristic. The final step in the design process was to tune all parameters via simulations to optimize the antenna operation at 2.45 GHz in terms of S_{11} , AR, and gain. Table 1 summarizes the final dimensions of the proposed antenna. The overall dimension is $60 \times 60 \times 1.67 \text{ mm}^3$.

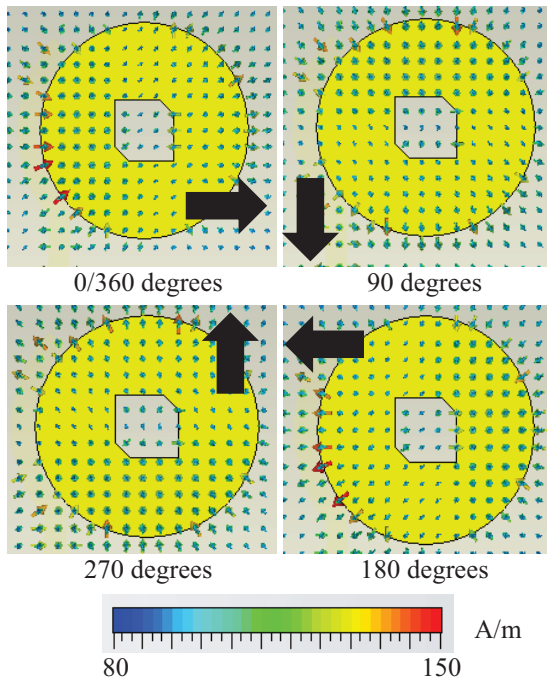


Fig. 7. Simulated current distribution of the edge-truncated square slot with different angles.

Table 1: Optimal dimensions of the proposed antenna (in mm)

| Parameter | Value | Description |
|-----------|-------|-------------------|
| Wfed | 2.98 | Width of the MTL |
| Lfed | 17.45 | Length of the MTL |
| R | 15.05 | Affects S_{11} |
| S | 8.52 | Affects S_{11} |
| C | 2.15 | Affects to AR |
| Gap | 0.35 | Affects to AR |

IV. RESULTS AND DISCUSSION

Figure 8 shows the proposed antenna with the optimum value as fabricated after the simulation process. Its S_{11} performance is measured using a Rohde & Schwarz ZVL network analyzer.

Figure 9 shows the comparison between simulation and measurement. Results show good agreement between the measured and simulated S_{11} . The proposed antenna is excited at 2.45 GHz with -10 -dB impedance bandwidth of 90 MHz (2.41–2.50 GHz). Maximum simulated S_{11} of

-17.32 and -13.73 -dB were obtained for simulated and measured results, respectively.

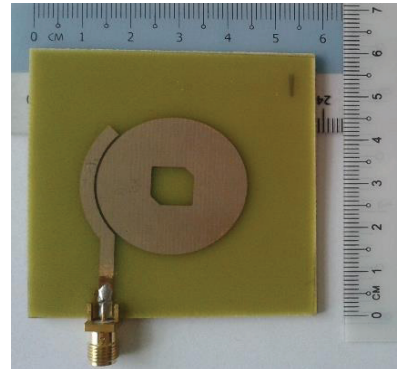


Fig. 8. Photograph of the prototyped antenna.

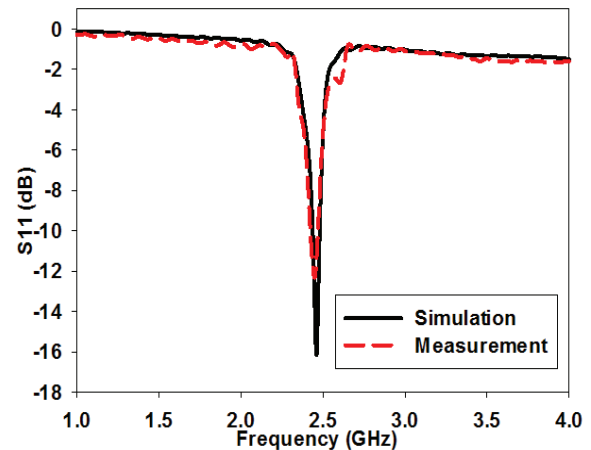


Fig. 9. Simulated and measured reflection coefficients.

Figure 10 shows the comparison between simulated and measured AR of the proposed antenna. The results show comparable agreement between measured and simulated values.

The minimum AR value from simulation is 0.33-dB, achieved at 2.45 GHz, and from measurement, 1.07-dB, achieved at 2.44 GHz. The simulated and measured 3-dB AR bandwidths are 34 MHz, or 1.39% (from 2.431–2.465 GHz), and 25 MHz, or 1.02% (from 2.433–2.458 GHz), respectively. Table 2 compares the proposed design to other single-band, single-layered, circular-patch antennas operating at 2.45 GHz using FR-4 substrate. It indicates that all antennas produced a narrow AR bandwidth, between approximately 1 and 1.5%.

From this investigation, it is clear that the proposed antenna topology enables simple AR tuning without altering S_{11} performance. In addition, it can be observed that the narrow impedance and AR bandwidths are due mainly to the fact that a single-layered topology was used. This narrow bandwidth characteristic is advantageous

for very specialized applications, such as wireless power transfer. A narrow impedance bandwidth and circular polarization enable efficient power transfer via reception of randomly polarized incident fields. For applications that require additional bandwidth, this structure can be improved further by adding additional substrate layers, at the cost of increased design complexity.

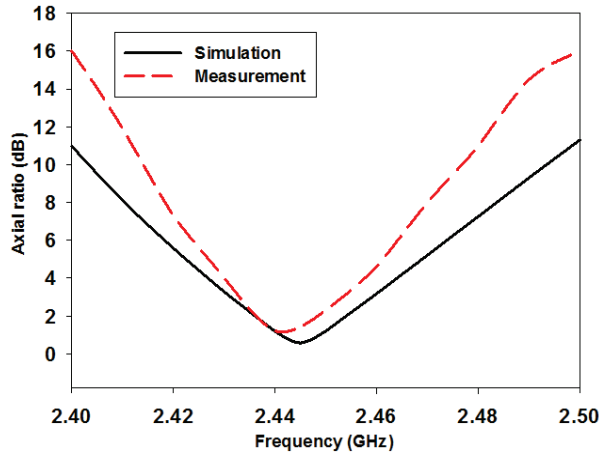


Fig. 10. Simulated and measured antenna axial ratio.

Table 2: Comparison of the 3-dB axial ratio bandwidth for a 2.45 GHz circular-patch antenna realized using FR-4 substrate

| Ref. | AR BW | | Ant Size | Feeding Technique |
|-----------|-------|-----|---------------|---------------------------|
| | MHz | % | | |
| [5] | 29 | 1.2 | 0.49λ | Contacted: coaxial |
| [6] | 30 | 1.2 | 0.49λ | Contacted: coaxial |
| [7] | 30 | 1.2 | 0.49λ | Contacted: coaxial |
| This work | 25 | 1.0 | 0.49λ | Non-contacted: EM coupled |

Figure 11 shows a comparison of the proposed antenna’s simulated and measured right-hand circular polarization (RHCP) and left-hand circular polarization (LHCP) radiation patterns in the xz -plane and yz -plane. Simulations and measurements show good agreement. It can be seen that the proposed antenna radiates with a left-hand circular polarization in the upper half-space toward the $+z$ -direction. Comparison between $\phi = 0^\circ$ and 90° clearly shows that the RHCP magnitude is at least 15-dB below the LHCP in both xz - and yz -planes in the forward direction. The proposed antenna produces an almost symmetrical radiation pattern for 2.45 GHz and a maximum directivity of 6.528 dBi in the positive z -direction. At 2.45 GHz, the half-power beam width (HPBW) of the proposed antenna is about 94.2° . Figure 12 illustrates simulated and measured antenna radiation efficiency. The measured efficiency between 40% and 55% within the 2.4–2.5 GHz band is shifted slightly to higher frequencies compared to the simulated efficiency.

Nonetheless, it still is considered relatively high, making it suitable for either WLAN or rectenna applications.

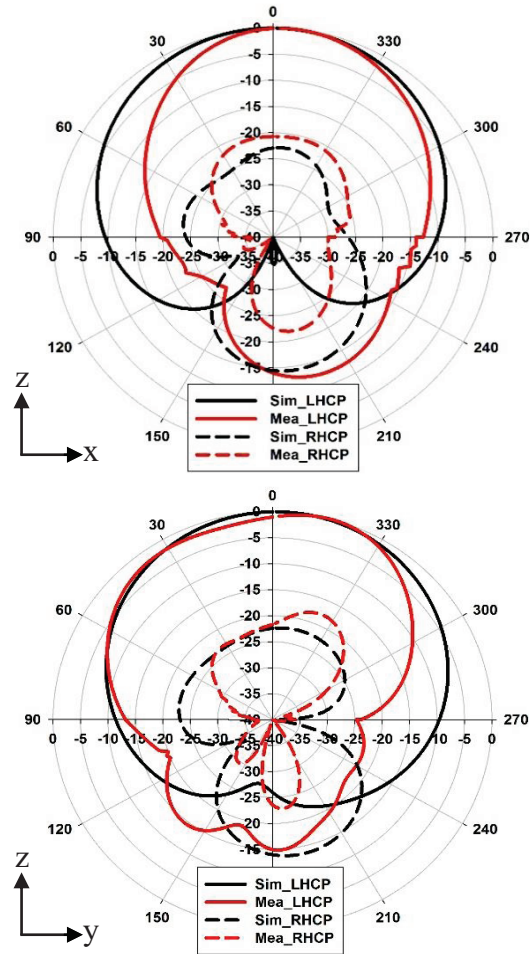


Fig. 11. Simulated and measured radiation pattern in the xz -plane and yz -plane at 2.45 GHz.

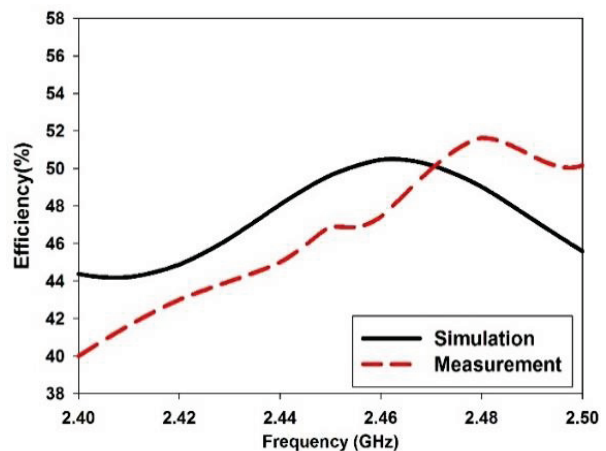


Fig. 12. Simulated and measured antenna radiation efficiency.

V. CONCLUSION

This work presents a novel, simple, low-cost circular-patch antenna with circular-polarization capability that enables controllable tuning of AR and S_{11} . The proposed antenna consists of a patch integrated with a truncated square slot and is electromagnetically coupled to a single microstrip transmission line for operation in the 2.45 GHz ISM band. Circular-polarization behavior is enabled via a truncated rectangular slot and is easily tunable without affecting the overall structure's impedance matching. The antenna attains satisfactory performance, with a -10 -dB impedance bandwidth of 90 MHz (2.41–2.50 GHz) and a 25-MHz (2.433–2.458 GHz) 3-dB AR bandwidth.

ACKNOWLEDGMENTS

The authors would like to acknowledge the Ministry of Higher Education (MOHE), Universiti Teknologi Malaysia (UTM), and the Wireless Communication Centre (WCC) for financing this project.

REFERENCES

- [1] Q. Liu, Y. Liu, Y. Wu, M. Su, and J. Shen, "Compact wideband circularly polarized patch antenna for CNSS applications," *IEEE, Antennas and Wireless Propagation Letters*, vol. 12, pp. 1280-1283, 2013.
- [2] O. A. Mashaal, S. K. A. Rahim, A. Y. Abdulrahman, M. I. Sabran, M. S. A. Rani, and P. S. Hall, "A coplanar waveguide fed two arm archimedean spiral slot antenna with improved bandwidth," *IEEE Transactions on Antennas and Propagation*, vol. 61, no. 2, pp. 939-943, Feb. 2013.
- [3] M. I. Sabran, S. K. A. Rahim, M. S. A. Rani, and M. Z. M. Nor, "A single band dual-fed circular polarization microstrip antenna for RFID application," *2011 IEEE International RF and Microwave Conference (RFM)*, Seremban, Negeri Sembilan Malaysia, pp. 137-140, Dec. 12-14, 2011.
- [4] S. M. Noghabaei, S. K. A. Rahim, P. J. Soh, M. Abedian, and G. A. E. Vandenbosch, "A dual-band circularly-polarized patch antenna with a novel asymmetric slot for WiMAX application," *Radioengineering*, vol. 22, no. 1, 2013.
- [5] F. J. Huang, T. C. Yo, C. M. Lee, and C. H. Luo, "Design of circular polarization antenna with harmonic suppression for rectenna application," *IEEE Antennas and Wireless Propagation Letters*, vol. 11, pp. 592-595, 2012.
- [6] T. C. Yo, C. M. Lee, C. M. Hsu, and C. H. Luo, "Compact circularly polarized rectenna with unbalanced circular slots," *IEEE Transactions on Antennas and Propagation*, vol. 56, no. 3, pp. 882-886, Mar. 2008.
- [7] W. S. Yoon, D. H. Lee, K. J. Lee, S. H. Kim, S. M. Han, and Y. S. Kim, "A circular patch antenna for a switchable circular polarization sense with a slotted ground structure," *Antennas & Propagation Conference, 2009. LAPC 2009*, Loughborough, pp. 309-312, Nov. 16-17, 2009.
- [8] J. Choi, S. Pyo, S. M. Han, and Y. S. Kim, "Circularly polarized microstrip antennas using single-fed EM coupled ring resonators," *International Symposium on Antenna and Propagation (ISAP)*, Bangkok, Thailand, Oct. 20-23, 2009.
- [9] M. A. M. Yusop, M. K. A. Rahim, M. F. Ismail, and A. Wahid, "Circular polarization fractal koch microstrip patch antenna using single-fed EM coupled ring resonators," *2010 IEEE Asia-Pacific Conference on Applied Electromagnetics (APACE)*, Port Dickson, Malaysia, pp. 1-4, Nov. 9-11, 2010.
- [10] C. A. Balanis, *Antenna Theory: Analysis and Design*, 2nd ed., Hoboken, NJ, John Wiley & Son, 1997.



Mursyidul Idzam Sabran was born in Selangor, Malaysia. He obtained his degree in Electrical Engineering (Telecommunication) in 2009 and M.Sc. in Master of Engineering (Electrical) in 2012 from UTM Skudai, Johor Malaysia. He is currently a full-time Ph.D. Research Student at the Wireless Communication Centre (WCC), Faculty of Electrical Engineering, Universiti Teknologi Malaysia (UTM), Johor, Malaysia.



Sharul Kamal Abdul Rahim received his first degree from University of Tennessee, USA majoring in Electrical Engineering, graduating in 1996, M.Sc. in Engineering (Communication Engineering) from Universiti Teknologi Malaysia (UTM) in 2001, and Ph.D. in Wireless Communication System from University of Birmingham, UK in 2007. Currently, he is an Associate Professor at Wireless Communication Centre, Faculty of Electrical Engineering, UTM. His research interest is Smart Antenna on Communication System.



Ping Jack Soh was born in Sabah, Malaysia. He received the Bachelor and Master degrees in Electrical Engineering (Telecommunication) from Universiti Teknologi Malaysia (UTM) in 2002 and 2005, respectively, and the Ph.D. degree in Electrical Engineering from KU Leuven, Belgium in 2013. He is currently a Senior Lecturer at the

School of Computer and Communication Engineering, Universiti Malaysia Perlis (UniMAP) and the Deputy Dean of the University's Research Management and Innovation Center (RMIC). Soh was the recipient of the IEEE Antennas and Propagation Society (AP-S) Doctoral Research Award in 2012, the IEEE Microwave Theory and Techniques Society (MTT-S) Graduate Fellowship for Medical Applications in 2013 and the International Union of Radio Science (URSI) Young Scientist Award in 2015. He was also the second place winner of the IEEE Presidents' Change the World Competition and IEEE MTT-S Video Competition, both in 2013, besides being awarded the Computer Simulation Technology (CST) University Publication Award in 2011 and 2012.



Chee Yen Leow obtained his B.Eng. degree in Computer Engineering from Universiti Teknologi Malaysia (UTM) in 2007. Since July 2007, he has been an Academic Staff in the Faculty of Electrical Engineering, UTM. In 2011, he obtained a Ph.D. degree from Imperial College London. He is currently a Senior Lecturer in the faculty and a Member of the Wireless Communication Centre (WCC), UTM.



Guy A. E. Vandebosch received the M.S. and Ph.D. degrees in Electrical Engineering from the Katholieke Universiteit Leuven, Leuven, Belgium, in 1985 and 1991, respectively. From 1991 to 1993, he held a Postdoctoral Research Position at the Katholieke Universiteit Leuven. Since 1993, he has been a Lecturer, and since 2005, a Full Professor at the same university.

His research interests are in the area of electromagnetic theory, computational electromagnetics, planar antennas and circuits, nano-electromagnetics, EM radiation, EMC, and bio-electromagnetics. His work has been published in ca. 220 papers in international journals and has been presented in ca. 300 papers at international conferences. Vandebosch has convened and chaired numerous sessions at many conferences. He was co-chair and vice-chair of the European Microwave Week in Amsterdam in 2004 and 2012, respectively. In 2004, he chaired the TPC of the European Microwave Conference within this Week. He was a Member of the TPC of the European Microwave Conference in 2005, 2006, 2007, and 2008. He was one of the vice chairs within the team organizing the EuCAP conference 2014 in The Hague, The Netherlands.

The Effect on a Human Heart Model from Dipole Antenna, with and without Shield on SAR and Temperature Increase

S. I. Zonoori¹, S. V. Makki², and A. Torabi¹

¹ Communication Department, Engineering Faculty
Ghiaseddin Jamshid Kashani University, Abyek, Iran
imanzonoori@gmail.com, torabi@ee.sharif.edu

² Electrical Department, Engineering Faculty
Razi University, Kermanshah, Iran
v.makki@razi.ac.ir

Abstract — In this paper, investigate effect of dipole antenna over human heart and a comparative study of temperature increased at heart and specific absorption rate (SAR) without and with different material shields. These structures are modeled and numerically tested by using finite element method (FEM) by using Comsol Multiphysics. The created virtual models using 3D simulation and computation software proved that used shield around human heart reduce the effects of EM fields. The simulation outputs used as measures for this comparative study include the increased temperature and specific absorption rate (SAR), which SAR determines the amount of radiation that human tissue absorb. In addition, study effects of variation of distance of shield from antenna and simulated temperature and SAR.

Index Terms — Comsol Multiphysics, dipole antenna, FEM method, SAR.

I. INTRODUCTION

The increasing use of wireless devices has also increased the amount of radiation energy to which human bodies are exposed, so it is important to achieve conditions under which human heart absorbs minimum radiation. For the analysis and assessment of microwaves penetration in human heart, in particular conditions specific to the use of mobile communication devices.

Several anatomical body and tissue models are presented by the scientific literature, like Gabriel and et al. (1996) obtained biologically electric properties (conductivity and permittivity) for 40 types of tissues at different frequencies [1-3].

The most typical example is the use of a mobile phone near human head, and like this, as an example of Baumann's and et al. work in USA (1997) can be mentioned. Baumann worked on electrical conductivity of human cerebrospinal fluid at body temperature. He

measured average conductivity and standard deviation of seven cerebrospinal fluid samples at room temperature (25°C) and at body temperature (37°C), across the frequency range of 10 Hz–10 kHz [4]. Schmid and et al. (2000) research examined dielectric properties of the human brain measured less than 10 hours post mortem in the frequency range from 800 to 2450 MHz and for each brain a mean value was calculated from 8 single measurement positions on 20 human brains less than 10 hours after death. The tissue temperature was different for each brain and ranged between 18°C and 25°C [5].

Yioultsis and et al. (2002) performed a comparative study of the biological effects on various mobile phone and wireless LAN antennas simulated by finite difference time domain (FDTD) method. This was one of the first studies that deal with a wide-range comparative investigation of modern cell phones on modern cell phones using monopole, helical, side-mounted planar inverted-F antenna (PIFA), patch antennas and WLAN antenna [6]. Also Ismail and Jenu (2007) modeled of electromagnetic wave penetration in a human head due to emissions from cellular phone by FDTD method by 2D human head model. The results indicated distribution of SAR at different position and at different angle of the phone [7].

Using FDTD method, Faruque and et al. (2010) compared study of a monopole, a helical, a patch and a PIFA antenna at 1.8-2.2 GHz frequency and SAR analyzed in human head tissues [8]. Ragha and Bhatia (2010) evaluated of SAR reduction for mobile phones using RF shields. For reduced SAR in the human head they used RF shield made of a ferrimagnetic material to the front side of the mobile phone. They studied numerically by using field simulation software, CST MWS and FDTD method [9].

Tomovski and et al. (2011) utilized 2D finite difference time domain (FDTD) to obtain the effects of

electromagnetic field over a human body, SAR simulation with and without nanotextile in the frequency range 0.9-1.8 GHz. The results of this study have been shown that reduction of the SAR levels in the brain tissue is best noticed in the case of usage of both materials (nanoferrite textile and carbon fiber textile shielding). The combined use of textiles with the right properties provided great possibilities for reduction of the RF effects over the human body [10].

Lak and Oraizi (2012) carried out on a numerical simulation the effects the distance of human head model to EM sources has on SAR. Their results have been shown that the distance from exposure source was important. The longer the distance to exposure source is, the lower the amount of SAR will be; therefore, it may be advisable to wear hands free device while using mobile phones, because it keeps phone further away from the head [11]. Islam and et al. (2012) have been studied variability of SAR value of a human head due to different materials in the vicinity of the handset exposed radio frequency electromagnetic fields. They investigated the effects of the human hand, handset chassis and additional conductive material, particularly hand-ring jewelry. FDTD method was used to analyze different positions of the conductive ring materials within the hand model. The results showed holding the mobile phone in a hand reduced the average peak SAR in the head and thus reduced the power absorbed by the head. A ring worn on the human hand caused the SAR distribution to increase because position of the ring behind mobile antenna [12].

But in this case, we find the need to characterize and quantify energy levels absorbed by human heart near dipole antenna with and without shield at 900 MHz and 1800 MHz frequencies (commonly created in real life by mobile GSM system) and using FEM method to carry out numerical calculations.

The parameter used is the specific absorption rate (SAR) representing the levels at which it is absorbed by a mass unit of tissue. Units for expressing SAR are Watt by kilogram of tissue exposed [W/kg]. SAR is usually averaged either over the whole body, or over a small sample volume (typically 1 g or 10 g of tissue). In the case of our research, only partial SAR levels are calculated. SAR can be calculated as:

$$SAR = \frac{\sigma |E|^2}{\rho}, \quad (1)$$

where:

- σ = conductivity of the tissue (S/m);
- ρ = mass density of the tissue (kg/m³);
- E = RMS electric field strength (V/m).

While a-thermal biologic effects are suspected to occur too inside bodies exposed to microwave radiation, the electric field strength and the absorbed power are quantitatively related with the temperature rise and

remain the relevant dosimetric indexes currently applied in biophysical research [13].

In this study, a realistic human heart model was used to simulate the SAR distribution and temperature distribution over the realistic human heart at different frequencies and dipole antenna with and without different material shields. Also, location of shield was changed to identify effects of distance between the source and shield.

Electromagnetic waves propagating into human heart were calculated using Maxwell's equations. Heat transfer in human heart exposed to electromagnetic waves was calculated using the bioheat equation [14,15]. The effects of operating frequencies (900 MHz and 1800 MHz) and once without shield and once with shield between the mobile phone and the human heart distributions on SAR and temperature distributions within the human heart were investigated systematically.

II. METHODOLOGY AND MATERIALS

Dipole antenna and its interaction with the heart tissues with and without shield at frequencies 900 and 1800 MHz and change distance of shield are solved by Comsol Multiphysics software and the finite elements method (FEM) is used to carry out most of numerical calculations.

A. Physical model

In this study, it was assumed that antenna of the mobile phone located at the front of human heart, where shield placed between antenna and heart and used different material for shield, and compared between their materials. Information about dielectric properties of tissues is taken from Gabriel [1]. It consisted of electrical properties of some tissues inside a human heart at 900 MHz and 1800 MHz. The dielectric properties of tissues are shown in Table 1.

Table 1: The properties of the tissues

| Material | 900 MHz | | | 1800 MHz | | | ρ (kg/m ³) |
|----------|--------------|---------|-------------------|--------------|---------|-------------------|--------------------------------|
| | ϵ_r | μ_r | σ (s/m) | ϵ_r | μ_r | σ (s/m) | |
| Heart | 59.8 | 1 | 1.229 | 56.32 | 1 | 1.771 | 1060 |
| Bone | 5.50 | 1 | 0.040 | 5.37 | 1 | 0.068 | 1850 |
| Blood | 61.3 | 1 | 1.537 | 59.37 | 1 | 2.043 | 1035 |
| Skin | 41.4 | 1 | 0.866 | 38.87 | 1 | 1.184 | 1050 |
| Air | 1 | 1 | 3e-15 | 1 | 1 | 3e-15 | 1.16 |

About this model, we consider shield with height = 8.25 cm, width = 0.45 cm, thickness = 0.3 cm and placed between heart and antenna to evaluate SAR reduction and dimension of antenna is = 8.25 cm (each length = 4 cm and gap = 0.25 cm), width = 0.15 cm, thickness = 0.15 cm. Data were calculated where shield varied from antenna distance of 2, 4, 6, 8 and 10 mm. For shield we selected aluminum from conductor material

and mica and teflon from insulator material, with parameters in Table 2 to investigate effect of material which used in shield.

Table 2: Dielectric parameters of shield material

| Shield Material | 900 MHz | | | ρ (kg/m ³) |
|-----------------|--------------|----------|----------------|--------------------------------|
| | ϵ_r | μ_r | σ (s/m) | |
| Aluminum | 1 | 1.000021 | 3.96e7 | 2700 |
| Mica | 1 | 6 | 1e-15 | 2883 |
| Teflon | 1 | 2.1 | 1e-20 | 2200 |

B. FEM implementation and boundary condition

FEM methodology was derived from Maxwell equations which mathematically describe the interdependence of the electromagnetic waves. Maxwell's equations were simplified to demonstrate the electromagnetic field penetrated in human heart as follows:

$$\nabla \times \frac{\nabla \times E}{\mu_r} - k_0^2 \epsilon_r E = 0, \quad (2)$$

where E is the electric field intensities (V/m), μ_r is relative magnetic permeability, ϵ_r is relative dielectric constant and k_0 is the free space wave number (m⁻¹).

Electromagnetic energy is emitted by the dipole antenna and strikes the human heart with a particular radiated power. The lumped port was used to determine a voltage drop for center feed legs of antenna. And on the antenna, an electromagnetic simulator employs lumped port boundary conditions with specified radiated power:

$$Z_{in} = \frac{V}{I} = \frac{EL}{I}, \quad (3)$$

where Z_{in} is the input impedance (Ω), V is the voltage along the edges (V), I is the electric current magnitude (A), E is the electric field along the source edge (V/m) and L is the edge length (m). The dipole must be made in odd number of half wavelengths long, with the basic dipole being only 1/2 wave of a wavelength long.

For all cases, the dipole antenna shown in Fig. 1 was modeled as a perfect electric conductor (PEC) box having length (L) = 4 cm, considering feeding with input power of 1 Watt, impedance is $Z = 50 \Omega$, and distance from heart is 1 cm. The patch of the antenna acts approximately as a cavity which assuming the perfect electric conductor on inner and outer surfaces is assumed. Hence, the perfect-electric-conductor boundary condition along the patches on the antenna is considered:

$$n \times E = 0. \quad (4)$$

Boundary conditions along the interfaces between different mediums, for example, between air and tissue or tissue and tissue or tissue and shield, were considered as continuity boundary condition:

$$n \times (E_1 - E_2) = 0. \quad (5)$$

Outer sides of the calculated domain, i.e., free space, were considered:

$$n \times (\nabla \times E) - jkn \times (E \times n) = -n \times (E_0 \times jk(n-k) \exp(-jk.r)). \quad (6)$$

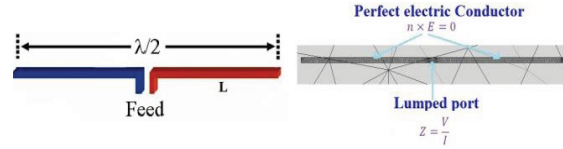


Fig. 1. Dipole antenna.

Therefore, boundary conditions for solving electromagnetic wave propagation, as shown in Fig.2, are described as follows.

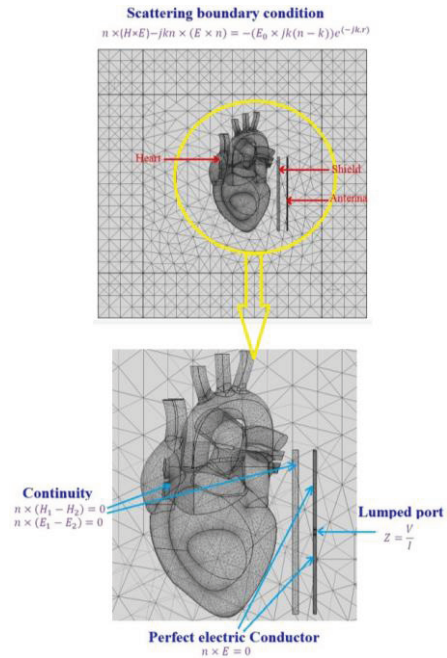


Fig. 2. Boundary conditions and mesh.

III. RESULTS AND DISCUSSION

Effects on a human heart model from dipole antenna at 900 MHz and 1800 MHz frequencies, with and without shield on SAR were studied, computed and simulated. Figure 3 (a) shows local temperature increases (from 37°C) without shield at frequency 900 MHz and Fig. 3 (b) shows it at frequency 1800 MHz.

Figure 3 shows that increase in heart temperature is more at frequency 1800 MHz than at 900 MHz one, also at 1800 MHz the former covers more with of heart. Maximum temperature increases, as seen from figure, are about 0.36°C and 0.22°C at 1800 MHz and 900 MHz frequencies, respectively, at the closest point of heart to antennas where the distance is 1 cm.

The differences in electrical properties become visible by plotting the local SAR value on a log-scale; so Fig. 4 (a) shows the results for log-scale slice plot at

frequency 900 MHz obtained due to radiation sources without shield and distance between antenna and heart is 1 cm, and Fig. 4 (b) shows at frequency 1800 MHz.

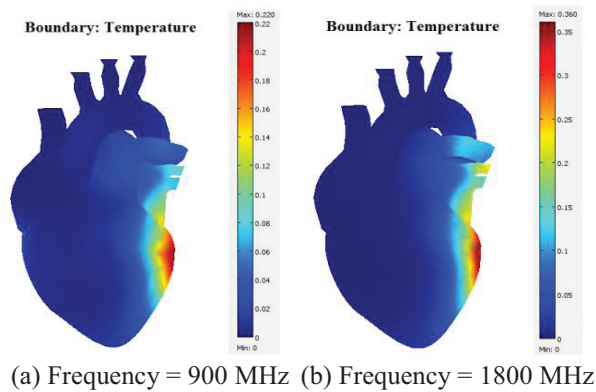


Fig. 3. Increase in temperature heart at: (a) 900 MHz and (b) 1800 MHz without shield.

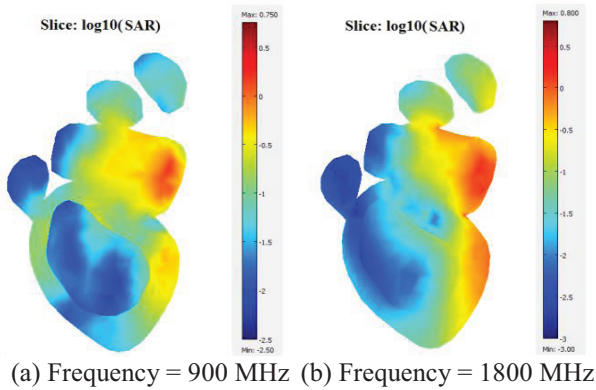


Fig. 4. Log-scale slice plot of the SAR value heart at: (a) 900 MHz and (b) 1800 MHz without shield.

Results show that the increase in frequency cause increase in SAR value and temperature. But near antenna more increased temperature difference than far from antenna and difference between SAR values like temperatures. So far from antenna difference temperature and SAR value at both frequencies are same but near antenna have different values.

As Fig. 5 shows, the heart line close to the center of antennas was selected to analyze temperature and SAR values in all models. Figure 6 illustrated comparison temperatures and Fig. 7 illustrated SAR values. As expected, heart temperature and SAR value exhibited some increases at points close to antennas, as shown in Figs. 6 and 7.

It is interesting to note that, for dipole antenna, depths of temperature penetration into human heart were similar for both 900 MHz and 1800 MHz frequencies as shown in Fig. 6, but the maximum temperature increase in skin and heart at 1800 MHz frequency is higher than

that at 900 MHz frequency. The SAR value in skin of 1800 MHz frequency is higher than that of 900 MHz frequency but in heart of 1800 MHz is lower than that of 900 MHz frequency.

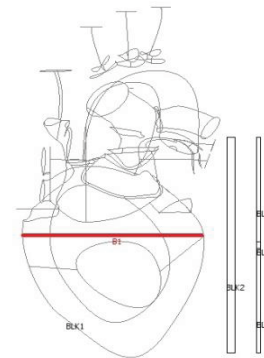


Fig. 5. Line of points selected for comparison purposes.

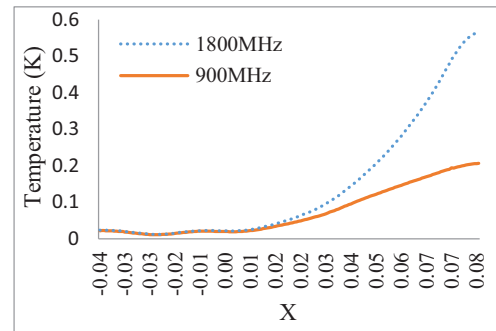


Fig. 6. Comparison of results for heart temperatures increases at 900 MHz and 1800 MHz without shield.

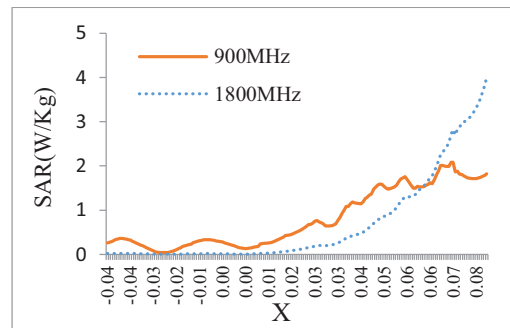


Fig. 7. Comparison of results for SAR values at 900 MHz and 1800 MHz without shield.

Figure 8 illustrated the temperature distribution in human heart exposed to mobile phone radiation with different material used for shield. For human heart exposed to the mobile phone radiation with a different material shield, the temperature within the human heart has different temperature increased, it is found comparison of them at Fig. 9.

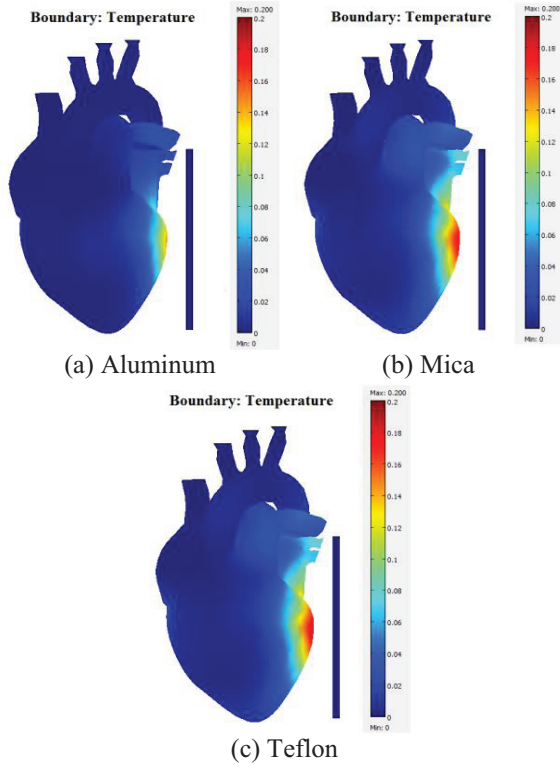


Fig. 8. Increase in temperature heart at 900 MHz with different material shields.

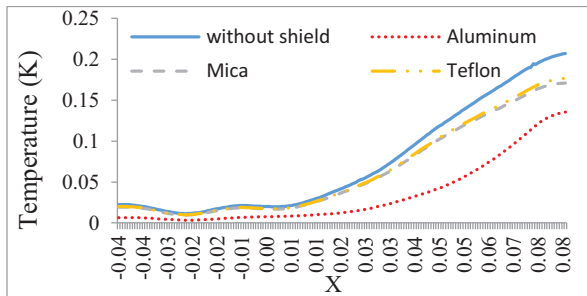


Fig. 9. Comparison of results for heart temperature increase at 900 MHz with different material shields.

More carefully study of above figures indicates that the aluminum is better material to reduce effect of electromagnetic field because the conductivity value of that is more than other and the region with high absorption values is small and close to the feed point of the antenna.

Figure 10 illustrates the penetration of the local SAR value on a log-scale in a 3D human heart due to different material shield. It is found comparison of them at Fig. 11. The results show that change material of shield, depth of temperature and SAR value are different as shown in Figs. 8 to 11 penetrates into a human heart with aluminum is lower than others, but in view of the fact that the temperature distribution always correlate with the SAR value. More carefully study of above figures

indicates that the aluminum is better material for reduce effect of electromagnetic field.

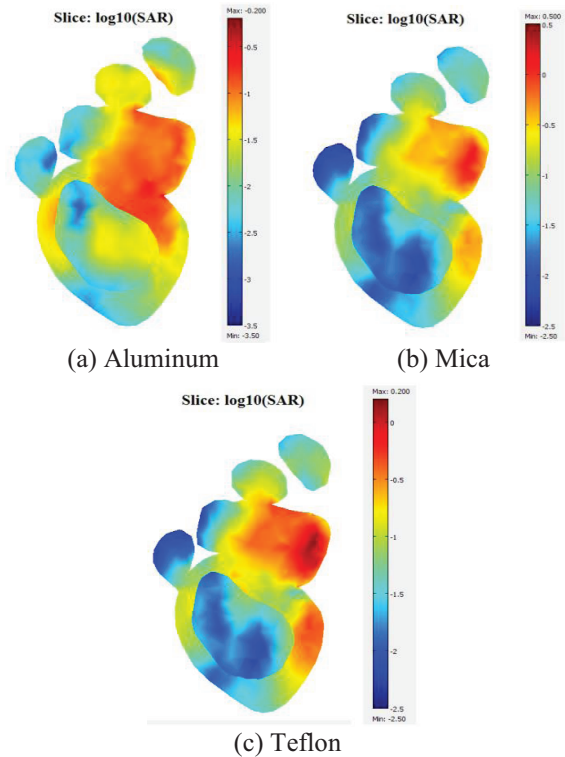


Fig. 10. Log-scale slice plot of the SAR values heart at 900 MHz with different material shields.

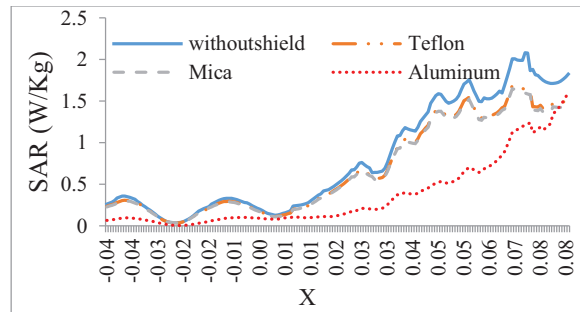


Fig. 11. Comparison of results for SAR values heart at 900 MHz with different material shield.

Obviously SAR and temperature are decreased by increasing the distance from exposure source [11]. So at Fig. 12 illustrates temperature increases (from 37 C) where distance between shield (select aluminum for material of shield) and antenna is varied 2, 4, 6, 8, and 10 mm, respectively. In constant distance between heart and antenna, by increasing the distance of shield from antenna temperature and SAR values increase and the results show that the distance from exposure source is important and if shield is near antenna the temperature of heart is decreased.

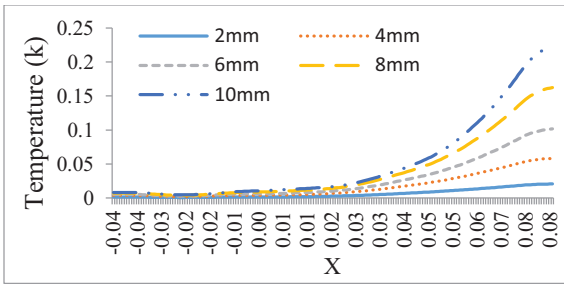


Fig. 12. Comparison of results for heart at 900 MHz where change position of shield.

REFERENCES

- [1] C. Gabriel, S. Gabriel, and E. Corthout, "The dielectric properties of biological tissues: I. literature survey," *Phys. Med. Biol.*, 41, 2231-49, 1996.
- [2] S. Gabriel, R. W. Lau, and C. Gabriel, "The dielectric properties of biological tissues: II. measurements in the frequency range 10 Hz to 20 GHz," *Phys. Med. Biol.*, 41, 2251-69, 1996.
- [3] S. Gabriel, R. W. Lau, and C. Gabriel, "The dielectric properties of biological tissues: III. parametric models for the dielectric spectrum of tissues," *Phys. Med. Biol.*, 41, 2271-93, 1996.
- [4] S. B. Baumann, D. R. Wozny, S. K. Kelly, and F. M. Meno, "The electrical conductivity of human cerebrospinal fluid at body temperature," *IEEE Transactions on Biomedical Engineering*, vol. 44, no. 3, 1997.
- [5] G. Schmid, G. Neubauer, and P. R. Mazal, "Dielectric properties of the human brain measured less than 10 hours post mortem," *Austria*, reference no. 285, 2000.
- [6] T. V. Yioultis, T. I. Kosmanis, E. P. Kosmidou, T. T. Zygiridis, N. V. Kantartzis, T. D. Xenos, and T. D. Tsiouboukis, "A comparative study of the biological effects of various mobile phone and wireless LAN antennas," *IEEE Transactions on Magnetic*, vol. 38, no. 2, Mar. 2002.
- [7] N. Ismail and M. Z. bin Mohd Jenu, "Modeled of electromagnetic wave penetration in a human head due to emissions from cellular phone," *APACE*, Malaysia, Dec. 2007.
- [8] M. R. I. Faruque, M. T. Islam, and N. Misram, "SAR analysis in human head tissues for different types of antennas," *World Applied Sciences Journal*, vol. 11, no. 9, 2010.
- [9] L. K. Ragha and M. S. Bhatia, "Evaluation of SAR reduction for mobile phones using RF shields," *International Journal of Computer Applications*, vol. 1, no. 13, 2010.
- [10] B. Tomovski and F. Grabner, "Effects of electromagnetic field over a human body, SAR simulation with and without nanotextile in the frequency range 0.9-1.8 Ghz," *Journal of Electrical Eng.*, vol. 62, no. 6, 2011.
- [11] A. Lak and H. Oraizi, "The effect of distance of human head model from EM sources on SAR," *Journal of Basic and Applied Scientific Research*, vol. 2, no. 9, 2012.
- [12] M. T. Islam and H. Z. Abidin, "Analysis of materials effects on radio frequency electromagnetic fields in human head," *Progress in Electromagnetics Research*, vol. 128, 2012.
- [13] R. J. Spiegel, "A review of numerical models for predicting the energy deposition and resultant thermal response of humans exposed to electromagnetic fields," *IEEE Trans. Microwave Theory Tech.*, vol. 32, no. 8, 1984.
- [14] D. Ratovoson and V. Huon, "Numerical combined model of human skin – heat transfer in the vein and tissue: experimental and numerical study," *Quantitative Infrared Thermography Journal*, vol. 8, no. 2, 2011.
- [15] H. H. Pennes, "Analysis of tissue and arterial blood temperatures in the resting human forearm," *J. Appl. Physiol.*, 85, 1998.



Seyed Iman Zonoori received his B.Sc. degree in Electrical Engineering from Razi University of Kermanshah, Iran in 2006 and the M.Sc. degree in Communication Engineering from Ghiaseddin Kashani University, Abyek, Iran in 2013. His areas of research include applied electromagnetic and multiphysics simulations.



Seyed Vahab AL-Din Makki received his Ph.D. in Electrical Engineering-Waves from Khaje Nasir Toosi University in 2008. His current research interests include modern digital radio propagation systems, microwave devices and radio transmitters. He is with the Electrical Engineering Department of Razi University in Kermanshah, since 2008.



Abdorreza Torabi received the B.Sc. and M.Sc. degrees from the Sharif University of Technology, Tehran, Iran, in 2007 and 2009, respectively, where he is currently working toward the Ph.D. degree in the Department of Electrical Engineering. His current research interests include analytical and computational electromagnetics, multilayered Green's functions, and scattering from rough surfaces.

Optimized Polygonal Slit Rectangular Patch Antenna with Defective Ground Structure for Wireless Applications

Sanjeeva Reddy B. Rama and Damera Vakula

Department of ECE

National Institute of Technology, Warangal, 506004, India

sanjeev.antenna@gmail.com, vakula@nitw.ac.in

Abstract — A novel triple-band polygonal shaped slit rectangular patch antenna with defective ground structure (DGS) is proposed for WLAN and WiMAX applications. The proposed probe-fed antenna consists of a rectangular patch, zig-zag shaped slit, dual T-shaped slits on both sides and circular dumbbell shaped defected ground. The designed antenna can generate three separate resonant frequencies to cover both the 2.45/5.28 GHz WLAN bands and the 3.5 GHz WiMAX bands while maintaining a small overall size of 40 mm x 28 mm x 3.175 mm. The location and dimension of loaded polygonal slit is obtained with the aid of interfacing a genetic algorithm (GA) model with an IE3D simulator. The results obtained from simulated antenna show 5.23% impedance matching bandwidth at 2.29 GHz, 1.14% at 3.5 GHz, 5.17% at 4.64 GHz. The antenna is experimentally tested, which gives good radiation patterns and sufficient antenna gains over the operating bands.

Index Terms — Defective ground structure, polygonal slit, radiation pattern.

I. INTRODUCTION

Multiband antennas play a vital role in integrating more than one communication applications on a single compact size structure. The desired characteristics of the multiband antenna are wide impedance bandwidth over the resonant frequency, better gain and good radiation properties [1]. Numerous antenna designs for tri-bands have been recently investigated employing various shapes of defective ground planes [2], [3]. Applying defective ground structures is found to be simple and effective method in size reduction as well as excite additional resonant modes [4].

Wang et al. proposed a monopole antenna with DGS which excites for triple resonant frequencies [5]. For obtaining triple resonant frequencies a DGS unit cell is etched out as a single defect on the ground plane of PCB. The single defect radiates over the desired frequency range by stopping wave propagation through the substrate. Cap et al. highlights about the compact design with slits

introduced into a conventional patch antenna for dual-band operation [6]. The attractive feature of genetic algorithm (GA) is its ability to achieve the desired performance by using a single, unique patch shape. Johnson et al. [7] designed a dual-band microstrip antenna on air substrate using GA approach. Proper selection of the microstrip patch antenna parameters such as length, thickness, shape, feed point position and method will excite the desired bands. Paitoon et al. [8] demonstrated slot cuts at radiating edges add a reactive load which alters the equivalent circuit of loaded patch, and hence adjust the dual frequency operation. Reactive loads added to the basic patch will change surface current distribution, which ultimately changes the excited resonance modes.

Guha et al. discussed about reducing interference effects with metallic backing to the patch. Metallic backing behind the defective ground structure is done to suppress leakage which reduces mutual coupling for microstrip antenna arrays [9]. A defect changes the current distribution in the ground plane of the patch antenna, giving rise to an equivalent inductance and capacitance. Hence, the DGS behaves like a LC resonator. When RF signal is transmitted to the patch antenna, strong coupling occurs between the top surface of the patch and DGS around the resonant frequency. LC parameters are determined by the shape and size of the defect geometry [10-14].

In this paper, a novel multiband planar antenna with defective ground structure is proposed. The antenna consists of a zig-zag shaped slit inserted on the radiating rectangular patch, dual T-shaped slits on either side of the patch and the ground plane modified by loading it with a circular shaped dumbbell as shown in Fig. 1. By properly selecting and varying the dimensions through implementation of GA for proposed structure, it can provide operating frequencies of interest, improve impedance bandwidths, and simultaneously work at multibands.

The effect of key structure parameters on the antenna performance are also analyzed and discussed in Sections II and III.

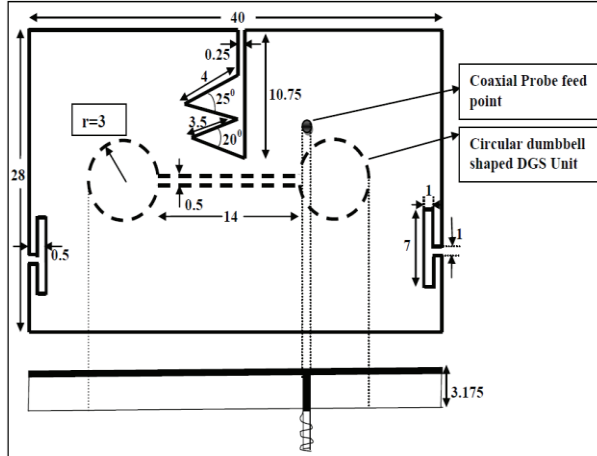


Fig. 1. Geometry of proposed antenna structure (dimensions are in mm).

II. DESIGN OF PROPOSED ANTENNA

A. Zig zag shaped polygonal slit and T-shaped slits

The conventional rectangular patch antenna is chosen with dimensions $L \times W$:

$$L = \frac{c}{2f_r \sqrt{\epsilon_e}} - 2\Delta L, \quad W = \frac{c}{2f_r} \sqrt{\frac{2}{\epsilon_r + 1}}, \quad (1)$$

$$\Delta L = \frac{0.412h(\epsilon_e + 0.3)(W/h + 0.264)}{(\epsilon_e - 0.258)(W/h + 0.8)}, \quad (2)$$

$$\epsilon_e = \frac{(\epsilon_r + 1)}{2} + \frac{(\epsilon_r - 1)}{2} \left[1 + \frac{12h}{W} \right]^{-1/2}, \quad (3)$$

where ϵ_r is the substrate permittivity, f_r is the resonant frequency and h is the substrate thickness.

In the first part of work, an extensive search of changing the shapes with different iterations is fixed for the conventional design in order to approach near desired frequencies. Several geometries of reactive loads were analyzed using IE3D tool solver. During the process, a linear T-shaped rectangular slits are placed on either side of the radiating patch, the antenna resonates at multibands. The lengths of the slits can be varied to get dual- or tri-band operation. In the present paper after optimizing the lengths, dual-band is obtained with reasonable bandwidth. The resonant bands can be increased by introducing additional slits. In the present antenna, a zig-zag polygonal slit is selected. The dimensions of the slit are varied to get a third resonant band. The placements of the slits are selected to get better radiation patterns and return loss characteristic. However, manually finding the accurate desired frequencies for the problem was difficult and selected the approach of optimization tool.

B. Optimization process using genetic algorithm

In the second part, GA tool is used as an optimization tool to find the desired frequency response. GA keeps the

fit solution to an optimization problem. This is done by converting optimized parameters to genes; these genes form chromosomes to the optimization problem. GA evaluates the fitness of the solution and keeps ones that most fit. GA main program is interpreted by MATLAB and Fig. 2 shows the flow chart of GA and IE3D interaction. During the GA approach, twenty chromosomes in each generation are evaluated, cost is computed for each individual as sum of return losses at desired frequencies and the fitness is to minimize the cost:

$$\text{Cost function} = \sum_{m=1}^3 S_{11}(f_m), \quad (4)$$

where S_{11} is the return loss, f_m is the m_{th} desired resonance frequency. Mutation rate is selected to be 5%, pairing chromosomes is done using cost weighting. The resultant antenna with the optimized parameters (in mm) as follows: $L=38.5$, $W=25.6$, probe feed position (5, 4.5), the length and width of DGS slot dimensions respectively (13.7, 0.47).

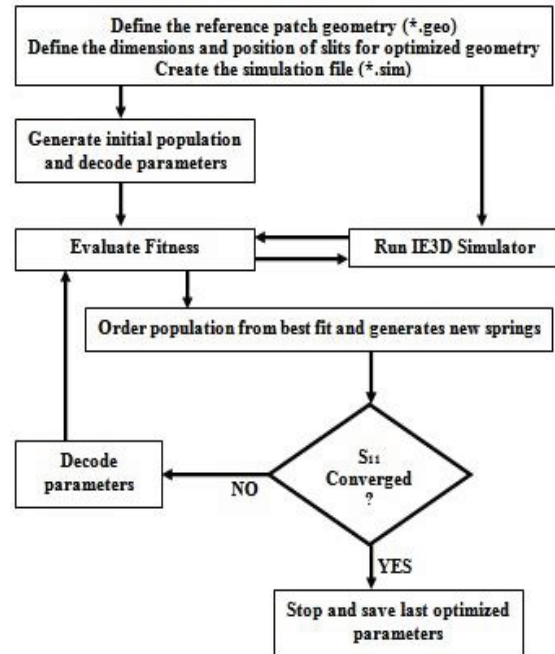


Fig. 2. Flow chart of genetic search with IE3D simulator.

The achieved impedance bandwidth can be increased by introducing a defect element on the ground plane. The selection of the shape and size of the DGS and analysis involved for defect element is briefly discussed in next section. A narrow length circular shaped dumbbell slot is cut on the ground plane to shift resonant frequencies with improved impedance bandwidth. The probe feed technique is chosen to have advantage of placing the feed at any desired location of the patch. This results in enhancing the gain, narrow bandwidth and impedance matching when compared with line feed [15]. The SMA

connector and coaxial cable were included in all the simulations in order to fully characterize their effects on the antenna performance.

III. ANALYSIS OF DEFECTIVE GROUND STRUCTURE

Different defective ground structures are shown in Fig. 3. These DGSs are used in the design of filters, suppress unwanted surface waves, control harmonics in microstrip antennas, reduce size of microwave circuits and microwave applications. DGS are introduced to improve performance by size reduction and ease of design [16]. Circular shaped dumbbell defect element allows us to vary the resonant frequency by changing the length without affecting the dimensions of the antenna.

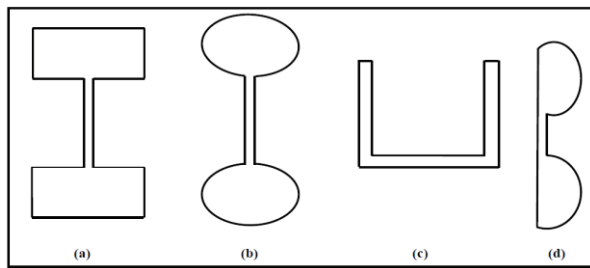


Fig. 3. Different DGS geometries: (a) rectangular dumbbell-shaped, (b) circular head dumbbell, (c) U-shaped, and (d) half-circle.

The circuit model for the DGS slot is represented in the form of a shunt capacitance C_μ and L_μ [12], and as shown in Fig. 4:

$$C_\mu = \frac{\sqrt{\epsilon_{eff}^{slot}}}{c_0 Z_0^{slot}} \frac{l}{N_s} \text{ and } L_\mu = (Z_0^{slot})^2 C_\mu, \quad (5)$$

where l is the length of the slot, N_s is number of slots, Z_0^{slot} is impedance of the slot and c_0 is the operating velocity. Figure 4 represents the equivalent circuit of DGS element and the values of L , C and R are determined by the slot dimension and location of the line. The change in dielectric constant changes the resonant frequency. The gain of the antenna is reduced for the antenna structure when DGS is applied to a conventional rectangular patch.

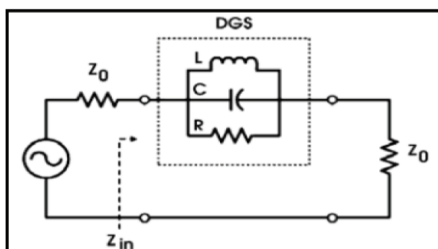


Fig. 4. Equivalent circuit of the DGS element.

IV. RESULTS AND DISCUSSION

A. Return loss and VSWR

The geometry of the proposed antenna is designed on a low-cost, RT Duriod 5880 substrate with dielectric constant $\epsilon_r=2.33$, dielectric loss tangent $\tan\delta=0.012$ and height=3.175 mm. The probe feed position is optimized and selected at (4, 4) for better return loss characteristics and impedance variations. The measured and simulated return loss curves for the proposed structure without the defect element is represented in Fig. 5. It is observed that return loss values are 11.04 dB, 20.25 dB, 10.23 dB at 3.121 GHz, 3.677 GHz and 4.687 GHz respectively, without DGS on the ground plane.

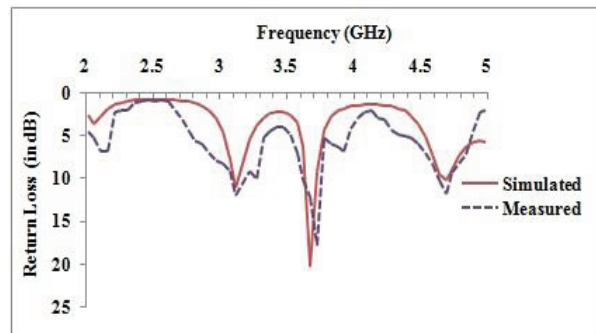


Fig. 5. Measured and simulated return loss curve for structure without DGS.

The VSWR values for the corresponding frequencies are extracted as 1.78, 1.215 and 1.89 respectively. The measured and simulated return loss curves for the proposed structure with the circular shaped single defective element is represented in Fig. 6, and noted that return loss values are 12.65 dB, 12.89 dB, 14.9 dB at 2.29 GHz, 3.5 GHz and 4.64 GHz respectively, with the DGS slot. The VSWR values for the corresponding frequencies are found to be 1.608, 1.682 and 1.5 respectively. The top layer and bottom layer of the fabricated antenna is as shown in Fig. 7.

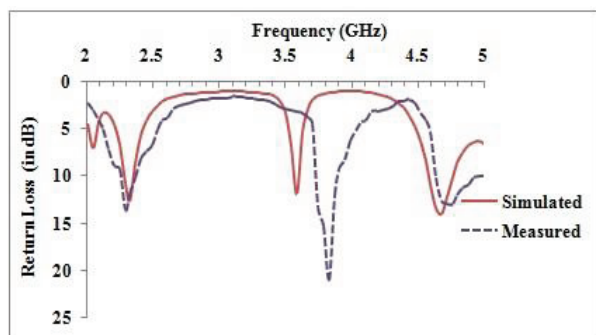


Fig. 6. Measured and simulated return loss curves for structure with DGS.

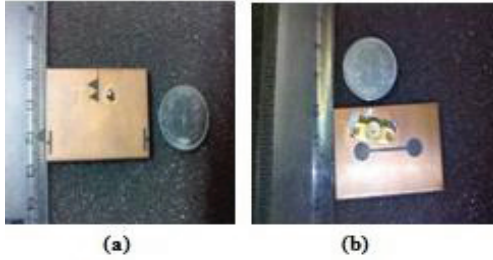


Fig. 7. Fabricated antenna: (a) top layer and (b) bottom layer.

B. Current distribution at tri-bands without DGS and with DGS

The surface current distributions of the antenna without DGS and with DGS are represented in Fig. 8 and Fig. 9 respectively, for the given frequency values.

It is clearly observed that the surface current density is much less at the radiating edges of the antenna without DGS. The current density of the patch at the radiating edge can be increased by introducing additional slots. Through a number of simulations the position and dimensions of the slits and slots are optimized for multibands. By introducing DGS, the current path is increased by which reduction in frequency occurs. Hence, the compact size is achieved that affects the distribution of surface current density.

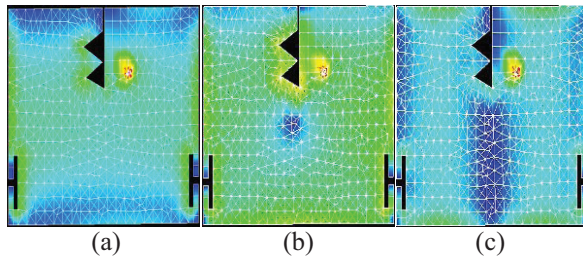


Fig. 8. Average and vector current distributions: (a) 3.121 GHz, (b) 3.677 GHz, and (c) 4.687 GHz.

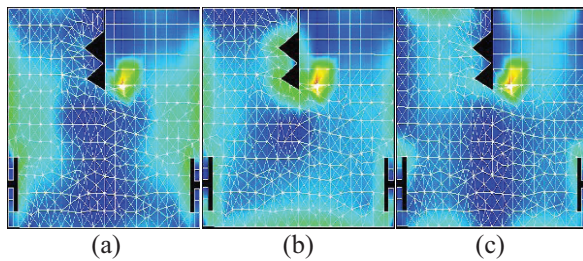


Fig. 9. Average and vector current distributions: (a) 2.29 GHz, (b) 3.5 GHz, and (c) 4.64 GHz.

C. Radiation patterns for the structure without DGS and with DGS

Figure 10 shows the radiation pattern characteristics

taken at $\phi=0^0$ and $\phi=90^0$ for the structures without DGS. Figure 11 shows the radiation pattern at $\phi=0^0$ and $\phi=90^0$ with DGS. The gain value is compromised when the DGS is placed on the ground plane and list of values are displayed in Table 1. Figure 12 shows the measured radiation patterns for multiband frequencies. The variations in the percentage impedance bandwidth value are also tabulated for the resonant frequencies. As observed, the lower frequency is shifted with an improved percentage bandwidth. This shows the impact on the size reduction capability with the applied DGS element on to the planar patch antenna. The size optimization can also be obtained placing multiple unit DGS cells on the ground plane. The gain versus frequency for the structure without DGS is as shown in the Fig. 13, and the response curve for the structure with DGS is represented by Fig. 14.

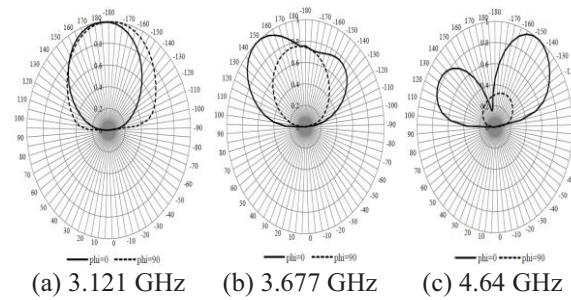


Fig. 10. Simulated E-plane radiation patterns without DGS: (a) 3.121 GHz, (b) 3.677 GHz, and (c) 4.687 GHz.

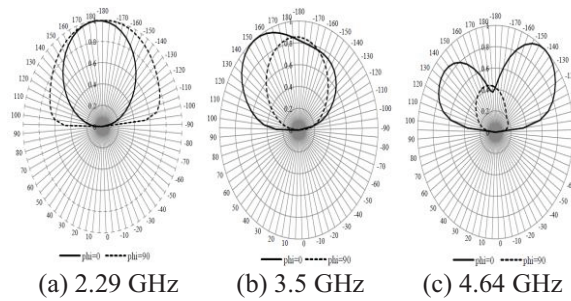


Fig. 11. Simulated E-plane radiation patterns with DGS: (a) 2.29 GHz, (b) 3.5 GHz, and (c) 4.64 GHz.

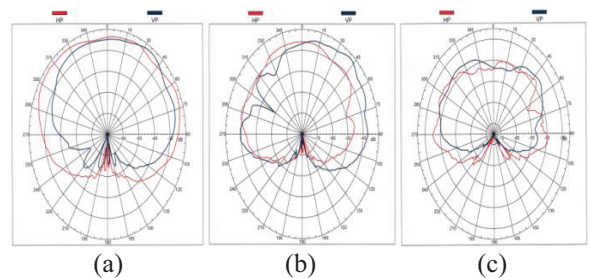


Fig. 12. Measured E-plane radiation patterns with DGS: (a) 2.29 GHz, (b) 3.5 GHz, and (c) 4.64 GHz.

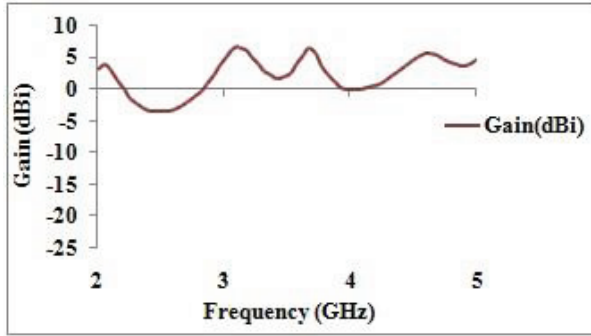


Fig. 13. Gain versus frequency for antenna without DGS.

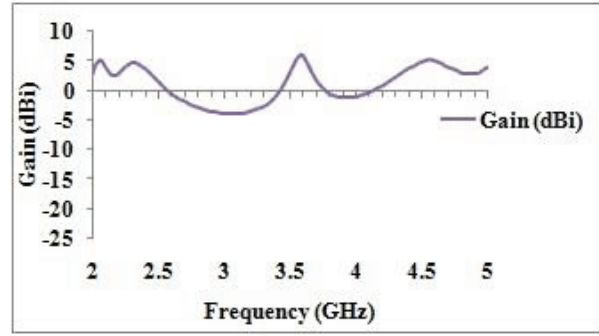


Fig. 14. Gain versus frequency for antenna with DGS.

Table 1: Value of gain and impedance bandwidth

| Structures | Frequencies (GHz) | Simulated Gain (dBi) | Measured Gain (dBi) | Simulated Impedance Bandwidth | Measured Impedance Bandwidth |
|-------------|-------------------|----------------------|---------------------|-------------------------------|------------------------------|
| Without DGS | 3.121 | 6.548 | 5.97 | 3.24% | 3.96% |
| | 3.677 | 6.47 | 6.81 | 2.36% | 2.63% |
| | 4.687 | 5.204 | 6.21 | 2.13% | 3% |
| With DGS | 2.29 | 4.63 | 5.27 | 5.23% | 5.94% |
| | 3.5 | 3.436 | 3.2 | 1.14% | 3.12% |
| | 4.64 | 4.67 | 5.78 | 5.17% | 5.03% |

D. Optimized metrics using genetic algorithm (GA)

The optimized parameters in the antenna design are position of the feed probe, length and position of the slits, length and width of the patch with minimum changes from its original dimensions of the patch. The shapes can be scaled in size to different operating frequencies of interest with minor modifications with substrate materials. The return loss values are 15.2 dB, 13 dB and 19.1 dB at respective operating resonant frequencies of 2.3, 3.4 and 4.7 GHz using GA technique. It is observed that a slight improvement is observed with the performance of the GA optimizer when compared to the simulated response curve.

The results of simulated, experimental and GA optimized responses are displayed for performance comparison. The return loss response of the GA optimizer with the best performance is represented in Fig. 15.

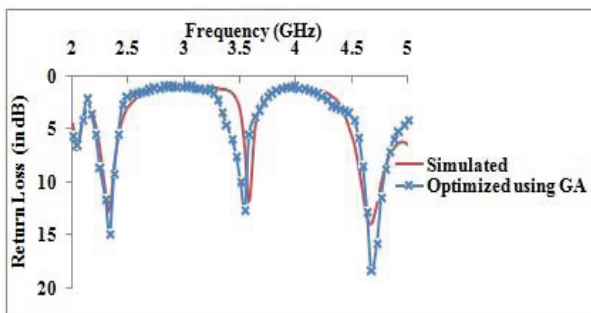


Fig. 15. Return loss response of simulated and GA optimization.

V. CONCLUSION

A novel shaped compact polygonal slit shaped planar antenna with defective ground plane is presented. The structure supports the operations for tri-band applications such as WiMax, WLAN and some bands of UWB. The major advantages of introducing DGS on metallic ground plane is to shift the resonant frequencies for different bands and also to increase the bandwidth for these bands. The optimized dimensions of the proposed patch antenna are also performed using genetic algorithm technique. The gain value decreases proportionally with the method applied for the patch antenna design. Impedance bandwidth and better radiation patterns are obtained for antennas with DGS when compared with the structure without DGS. A good agreement is obtained between simulated and measured return loss, radiation patterns and also for the gain values for this structure.

REFERENCES

- [1] J. Costantine, K. Y. Kabalan, A. El-Hajj, and M. Rammal, "New multiband microstrip antenna design for wireless communications," *IEEE Trans. Antennas Propag. Mag.*, vol. 49, no. 6, pp. 181-186, 2007.
- [2] J. Pei, A. G. Wang, S. Gao, and W. Leng, "Miniaturized triple band antenna with a defective ground plane for WLAN/WiMAX applications," *IEEE Antennas Wireless Propagation Letters*, vol. 10, pp. 298-301, 2011.
- [3] Q. Zhao, S. X. Gong, W. Jiang, B. Yang, and J. Xie, "Compact wide slot tri band antenna for WLAN/WiMAX applications," *Progress in Electromagnetic*

- Research (PIER) Letters*, vol. 18, pp. 9-18, 2010.
- [4] G. Breed, "An introduction to defective ground structures in microstrip circuits," *High Frequency Electronics, Summit Technical Media*, pp. 50-54, 2008.
- [5] T. Wang, Y. Z. Yin, J. Yang, Y. L. Zhang, and J. J. Xie, "Compact tri band antenna using defected ground structure for WLAN/WIMAX applications," *PIER Letters*, vol. 35, pp. 155-164, 2012.
- [6] A. Cap, H. Z. Raida, and R. Lamadrid, "Multi-band planar antennas: a comparative study," *Radio Engineering*, vol. 14, no. 4, pp. 11-20, 2005.
- [7] J. M. Johnson and Y. Rahmat-Samii, "Genetic algorithms and method of moments (GA/MOM) for the design of integrated antennas," *IEEE Trans. Antennas Propagat.*, vol. 47, pp. 1606-1614, Oct. 1999.
- [8] R. Paitoon, A. Noppin, J. Kanok, and W. Toshio, "Multiband microstrip fed right angle slot patch antenna design for wireless communication systems," *ETRI Journal*, vol. 31, no. 3, pp. 271-281, 2009.
- [9] D. Guha, S. Biswas, M. Biswas, J. Y. Siddiqui, and Y. M. M. Antar, "Concentric ring-shaped defected ground structures for microstrip applications," *IEEE Antennas Wireless Propagation Lett.*, vol. 5, pp. 402-405, 2006.
- [10] D. Ahn, J. S. Park, C. S. Kim, J. Kim, Y. Qian, and T. Itoh, "A design of low pass filter using the novel microstrip defective ground structure," *IEEE Trans. Microwave Theory Tech.*, vol. 49, no. 1, pp. 86-93, Jan. 2001.
- [11] C. Caloz, H. Okabe, T. Iwai, and T. Itoh, "A simple and accurate model for microstrip structures with slotted ground plane," *IEEE Microwaves Wireless Components. Lett.*, vol. 14, no. 4, pp. 133-135, Apr. 2004.
- [12] J. S. Hong and M. J. Lancaster, *Microstrip Filters for RF/Microwave Applications*, John Wiley & Sons, Inc., New York, 2007.
- [13] H. J. Chen, T. H. Huang, and C. S. Chang, "A novel cross shape DGS applied to design ultra wide stopband low pass filters," *IEEE Microwave Compon. Lett.*, vol. 16, pp. 252-254, 2006.
- [14] C. Insik and L. Bomson, "Design of defective ground structures for harmonic control of active microstrip antenna," *IEEE Antennas Propag. Soc. Int. Symp.*, vol. 2, pp. 852-855, 2002.
- [15] R. Garg, P. Bhartia, I. Bahl, and A. Ittipiboon, *Microstrip Antenna Design Handbook*, 2nd ed., Canton, MA: Artech House, 2001.
- [16] H. Liu, Z. Li, and X. Sun, "Compact defective ground structure in microstrip technology," *Electronic Letters*, vol. 41, no. 3, Feb. 2005.



India.

Sanjeeva Reddy B. R received his B.E. degree from Bangalore University and M.E. degree in Microwaves from Government College of Engineering, Pune, India. Currently working in the field of Multifunction Antennas towards progress in Ph.D. at National Institute of Technology, Warangal,



Damera Vakula obtained her Bachelor's degree in Electronics and Communication Engineering from Nagarjuna University, AP, India and Master's degree from Birla Institute of Technology, Mesra India, with Microwave Specialization in 1992 and 1994, respectively. She obtained Ph.D. on Fault Diagnostics of Antenna Arrays from National Institute of Technology, Warangal, India in 2010. She has been working as an Assistant Professor at National Institute of Technology, Warangal, India since 2006. She has published 20 papers in various International Conferences and Journals. Her areas of interest include phased array antennas, ultra wide band antennas, multiband antennas, fault diagnostics, and neural network.

Theoretical Approach for the Design of a New Wideband Ku-band Printed Antenna

A. Harrabi^{1,2}, T. Razban¹, Y. Mahe¹, L. Osman², and A. Gharsallah²

¹Institute of Electronic and Telecommunication of Rennes, IETR-UMR CNRS 6164
Polytechnic Engineering School of Nantes, University of Nantes, Nantes, 44603, France
amal.harrabi@univ-nantes.fr, tchanguiz.razban@univ-nantes.fr, yann.mahe@univ-nantes.fr

²Department of Physics, UR "CSEHF" 13ES37
Faculty of Sciences of Tunis, University of Tunis El Manar, 2092 Tunisia
lotfi.osman@supcom.rnu.tn, ali.gharsallah@gmail.com

Abstract — A design of a broadband Ku-band low-cost printed circuit board technology (PCB) antenna is presented in this paper. An approach was developed to enhance the bandwidth of a simple printed patch antenna. The proposed method is, step by step, detailed to discuss the evolution of the antenna geometry and depicts the contribution of the imported changes on the properties achieved each time. A 22% relative bandwidth in Ku-band was obtained for a footprint of $0.4\lambda_0 \times 0.6\lambda_0$ (λ_0 is the wavelength in the free space). A good agreement between the simulation and the measurement results of the wideband patch was observed, which proves the interest of this approach.

Index Terms — Antenna input impedance, antenna theory, Ku-band, linear polarization, polygonal antennas, wideband antenna.

I. INTRODUCTION

There is a growing interest in small, flat, discreet, efficient, and low-cost antenna design. In satellite application context, these antennas should have a broadband behavior covering all the Ku-band, a high directivity and a linear polarization. The reflector based antennas are commonly used because they satisfy all these requirements, but they are not practical due to their relatively big size and their 3D geometry. An interesting alternative of such antennas could be the grounded planar printed based antennas because of their low profile, cheap price and simple manufacturing [1,2]. Nevertheless, with such a technology for simple shape antenna, broadband behavior is limited to a few percent. To enhance the bandwidth, different techniques can be used. Some are based on the superposition of several layers of dielectrics and resonators known as the stacked antennas [3-7]. This technique implies a precise alignment of the resonators hard to achieve, especially at high

frequency like in Ku-band. Others use a co-planar arrangement of parasitic elements surrounding the driven resonator. These parasitic elements have almost the same size as the driven one which leads to a relatively large size of the patch. When high directivity has to be reached, antenna array is needed and therefore the patch size becomes a crucial criterion. In this case, if the basic element has more than a wavelength size, grating lobe problem arises. Coplanar multi-resonator solution is then irrelevant and incompatible with antenna array [8-11]. In [12] and [13], the authors explain that with some modifications of the geometry of the rectangular patch antenna, a relative bandwidth of 20% can be achieved just by coupling two different modes. The two chosen modes are orthogonal. It means that the polarization is unstable within the bandwidth. Therefore, the steady linear polarization criterion for satellite reception cannot be satisfied. In this paper, we propose to develop a new broadband single element printed antenna operating in Ku-band with compact size and stable linear polarization in order to be suitable with an antenna array configuration and achieve higher directivity. This article is organized as follows: In Section II, a rigorous theoretical approach is developed and validated according to simulations using CST Microwave Studio® software. A prototype of the proposed antenna is realized and measured. Measurement results, presented in Section III, are in good agreement compared to the simulations.

II. ANTENNA DESIGN

A. Rectangular patch antenna

Different kinds of planar antenna topologies exist: ungrounded and grounded ones. The first is interesting for its omnidirectional radiation pattern and an ultra-wideband behavior could be easily achieved. It is extensively used for applications like mobile communication systems. The second is more suitable for

point-to-point communication to avoid energy losses, except that the limited bandwidth is its handicap. As satellite services require point-to-point communication with direct link antennas, the grounded planar antenna technology is then more suitable, if solutions are found to maintain the linear polarization over a wide bandwidth. In this technology, the bandwidth usually depends on the thickness, the nature of the dielectric substrate, and the antenna's geometry. To broaden the bandwidth of a rectangular patch antenna, the most used techniques are based on decreasing the substrate relative permittivity ϵ_r , raising the dielectric thickness h and enlarging the patch width W [14]. However, the bandwidth of this simple shape printed antenna remains limited to about 10%. To highlight this issue, a probe-fed rectangular microstrip antenna printed on a 1.58 mm height Teflon-glass substrate of a relative permittivity 2.55 and $\tan\delta = 0.007$ operating at 11.7 GHz is firstly simulated with CST Microwave Studio®. Its dimensions are tuned in order to enlarge the bandwidth for this simple pattern. The optimized rectangular antenna's reflection coefficient S_{11} is represented in Fig. 1.

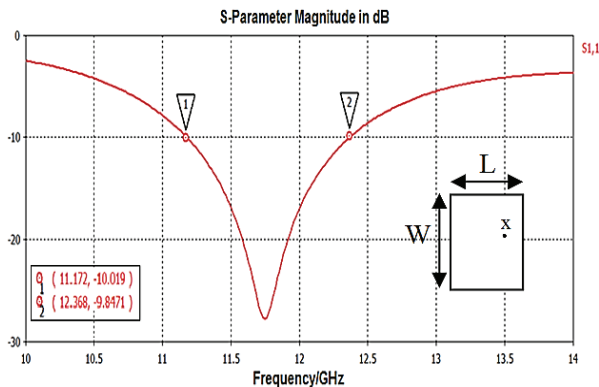


Fig. 1. Simulated reflection coefficient S_{11} of the rectangular patch antenna ($L = 7$ mm and $W = 10$ mm and $x = 2.7$ mm).

As previously mentioned, a relative bandwidth of 10% is observed in this figure, which is quite close to the maximum bandwidth for this kind of structure [14]. An idea to overcome this insufficiency consists in designing a simple patch antenna by exploring the rectangular patch characteristics and making some changes in its geometry to get an enlarged bandwidth of more than 10%, while maintaining the same linear polarization over the whole bandwidth. Therefore, a rectangular patch is introduced and analyzed. Its dimensions are calculated from the analytical expressions given in [15,16]. According to these expressions, the variation of the length L of a rectangular patch printed on a Teflon-glass substrate for fixed values of W (width of the patch), h (the substrate thickness), and ϵ_r (substrate relative permittivity) versus the frequency is represented in Fig. 2.

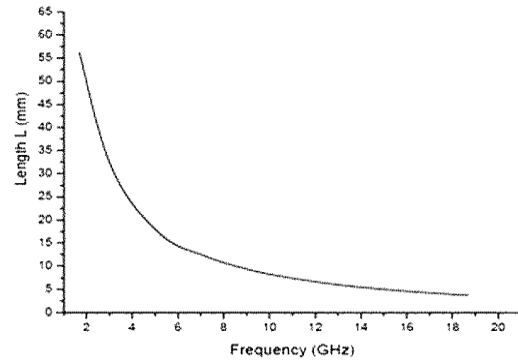


Fig. 2. Length of a rectangular patch versus frequency when $W = 13$ mm, $h = 1.58$ mm, $\epsilon_r = 2.55$ and $x = 2.7$ mm.

Internal for a rectangular patch antenna, fed by a coaxial cable at a distance x from the center of the rectangle patch, the input resistance R_i is defined in [16] by:

$$R_i = \frac{1}{2G} \sin^2\left(\frac{\pi x}{L}\right), \tag{1}$$

where

$$G = \frac{w}{120\lambda_0} \left[1 - \frac{(2\pi h/\lambda_0)^2}{24} \right], \tag{2}$$

is the radiation conductance and λ_0 is the wavelength.

According to equation (1), the value of the input resistance is related to the position x of the feed point from the center of the antenna. To get maximum power transfer, this position should be determined in a way that the input resistance R_i is equal to the source resistance (typically 50Ω). On the other hand, for a fixed distance x ; the input resistance will only depend on the frequency when W , h and ϵ_r have also fixed values as illustrated by Fig. 3 below.

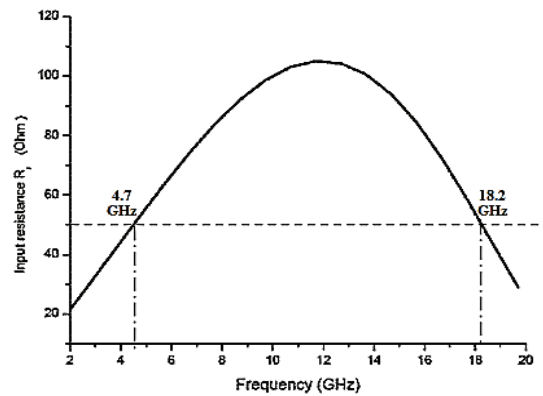


Fig. 3. Input resistance R_i (Ω) versus frequency when $W = 13$ mm, $h = 1.58$ mm, $\epsilon_r = 2.55$ and $x = 2.7$ mm.

According to Fig. 3, some same input resistance is met for two different frequencies. For example, $R_i = 50 \Omega$ is obtained at both 4.7 GHz and 18.2 GHz, which means that two collinear resonators can be optimally coupled to

the same feed point position.

B. Polygonal patch antenna

In accordance with Fig. 3, two resonators can be optimally coupled having the same feeding point; in this case, this is possible for coaxial feeding probe situated at $x = 2.7$ mm from the center of the resonators. Based on Fig. 2, the first resonator has 3.9 mm length for a frequency of 18.2 GHz and the second has 19.2 mm length for a frequency of 4.7 GHz. We should then present a geometry that has these two different lengths. One way consists in using the dimensions L and W of the patch antenna as L_1 and L_2 . But, in this case, two orthogonal modes are excited, which means that the radiated power has different polarizations. To ensure same polarizations over the two frequencies, L_1 and L_2 has to be carried on along only one axis. As illustrated in Fig. 4 (a), a polygonal design can be a possible candidate to meet the mentioned condition of the linear polarization using the two different lengths. From Fig. 3, the expected reflection coefficient S_{11} of this antenna should have the form given in Fig. 4 (b).

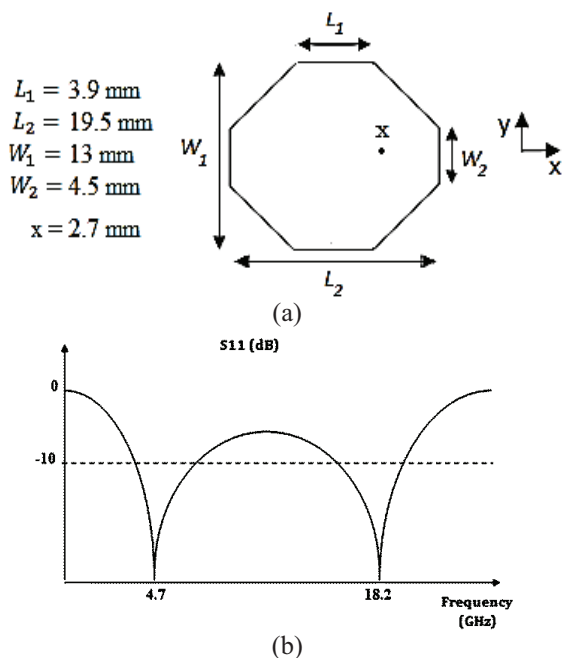


Fig. 4. Proposed antenna and its expected reflection coefficient: (a) polygonal patch antenna, and (b) S_{11} parameter of the polygonal antenna matched to 50Ω .

In order to reduce the size of the polygonal antenna, to widen the bandwidth of each resonant frequency and to have protection against the environment, a 3.175 mm thickness Nelco NY9220 substrate with a relative permittivity of 2.2 and $\tan \delta = 0.0009$ is used as a rodome. To take into account the rodome layer effect in the simulation, we need an optimization of the polygonal

antenna dimensions. Figure 5 shows the dimensions of the antenna with superstrate and the simulation result of its S_{11} parameter.

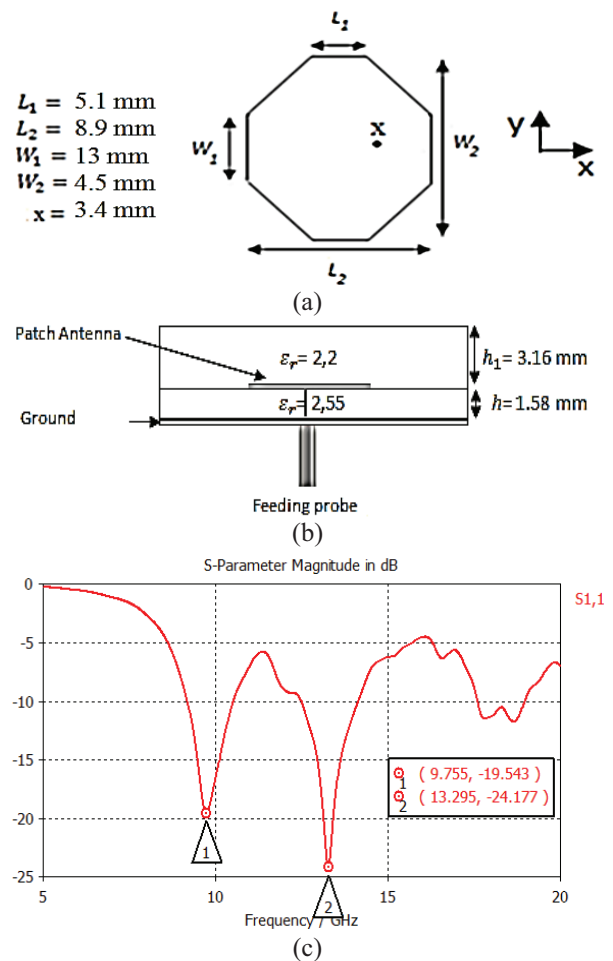
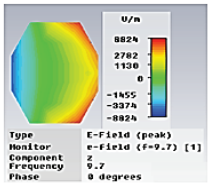
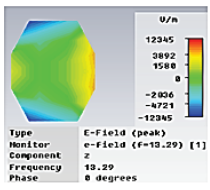
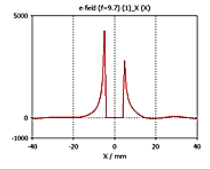
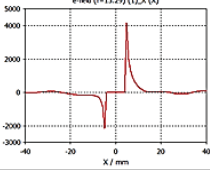
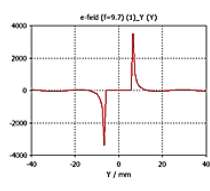
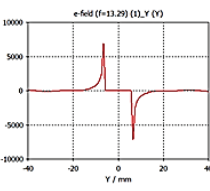


Fig. 5. (a) Dimensions of the polygonal antenna with rodome, (b) side view, and (c) simulated S_{11} parameter.

This figure confirms that the optimized antenna with rodome has a dual band behavior. Table 1 summarizes the electric field distribution for the two resonant frequencies to check their polarizations quality.

We notice that for all these two dips, the transverse fringing fields along Y-axis (E_y) on both sides of the antenna are in opposite phase with quite the same magnitude. In other words, the resulted vertical polarization radiation (cross-polarization) in the broadside direction is null for all frequencies, meaning that the polygonal shape of the patch does not introduce theoretically any cross-polarization. For the frequencies 9.75 and 13.29 GHz, the electric fields along X-axis are not in opposite phase, so the resulted radiation horizontal polarization (co-polarization) is maximal in the broadside direction.

Table 1: E-field of the polygonal antenna with rodome

| Frequency (GHz) | 9.75 | 13.29 | |
|-----------------|---|---|---|
| | I | II | |
| E_z |  |  | a |
| E_x |  |  | b |
| E_y |  |  | c |

C. Polygonal antenna with circular slot

The polygonal antenna depicted in Fig. 5 presents two separated bands corresponding to two distinct modal resonances. Nevertheless, wideband behavior is expected. From Fig. 3, the impedance plot presents a maximum for a frequency located between the two frequencies matched to 50 Ω, which explains the high reflection coefficient for this distinct frequency. The idea consists of reducing the reflection coefficient at this maximum without deteriorating the impedance matching of the existing two frequencies. It can be resolved by modifying the propagation conditions inside the resonator. Thus, follows a manner to enlarge the bandwidth by using a slot inside the polygonal patch is step by step detailed.

1) Influence of a slot inside the patch

First, it is important to review theoretically the effect of a simple slot inside a patch. Usually, a slot can be modeled as a capacitance whose value depends not only on the dimension of the slot, but also on its orientation and its position inside the patch. To evaluate the influence of the slot, the electric field distribution inside the substrate, under the patch, is studied. For the fundamental resonance of a rectangular patch antenna, the magnitude of the electric field is expressed in [16] as follows:

$$E = E_0 \sin \frac{\pi x}{L}, \tag{3}$$

where E_0 is the maximum electric field and x is between $-\frac{L}{2}$ and $\frac{L}{2}$.

The fringing field at the edge of the patch is the origin of its radiation. Its magnitude E_r can be determined

by the equivalent potential:

$$E_r = \frac{E_0 h}{\Delta}, \tag{4}$$

where h is the thickness of the substrate and Δ the line extension the resonators from both sides.

With a slot inside the antenna at a distance d from the center of the patch, an electric field \vec{E}_s appears inside the slot, Fig. 6.

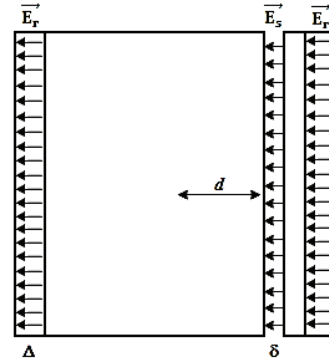


Fig. 6. Electric fields E_r and E_s .

The value of the magnitude of this electric field can be determined by calculating the potential difference between both sides of the slot:

$$E_s \delta = V_2 - V_1, \tag{5}$$

where δ is the slot width, V_1 is the potential at $y = d$ and V_2 is the potential at $y = d + \delta$.

Assuming that $d \gg \delta$ and $\delta \ll L$, then:

$$E_s = E_0 \frac{\pi h}{L} \cos \frac{\pi d}{L}. \tag{6}$$

From the expression of the electric field magnitude E_s , we deduce that E_s is much smaller than E_r because L is much bigger than Δ . Therefore, the slot does not have great influence on the radiation pattern of the antenna. Now, if the slot is oriented with an angle θ , Fig. 7, E_s can be written as follows:

$$E_s(y) = E_0 \left[\frac{\pi h \cos \theta}{L} \cos \frac{\pi d}{L} \right], \tag{7}$$

where d is the distance between the Y-axis of the patch and the slot location for a given value of y .

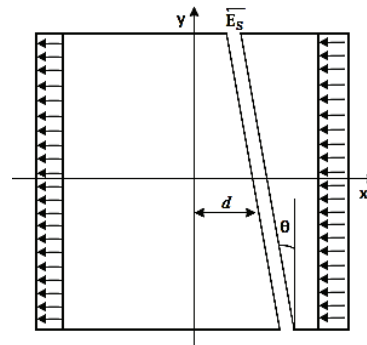


Fig. 7. Representation of the slot with an angle θ .

To maintain the symmetry of the structure, we propose to use a circular slot. In this case, the distance d will depend on the angle θ and the inner radius R of the circular slot and can be written as follows:

$$d = R \cos \theta, \quad (8)$$

where θ varies from 0° to 360° , Fig. 8.

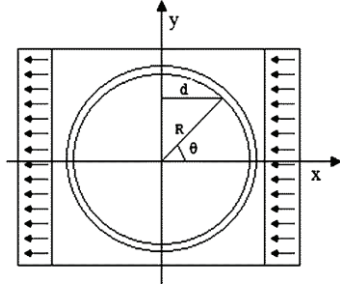


Fig. 8. Variation of the distance d in a circular slot.

Finally, the magnitude of the electric field inside the slot has the following expression:

$$E_s = E_0 \frac{\pi h}{L} \cos\left(\frac{\pi R \cos \theta}{L}\right) \cos \theta, \quad (9)$$

Fig. 9 represents the variation of E_s versus θ according to the equation (9).

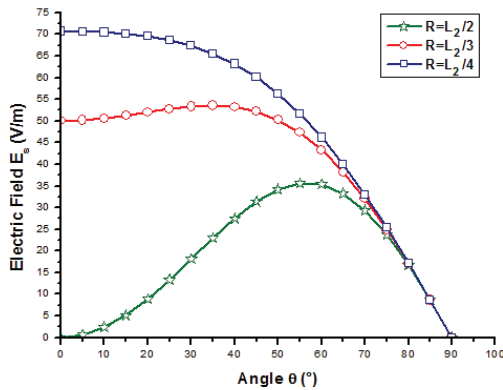


Fig. 9. Variation of the magnitude of the electric field inside the circular slot E_s versus theta (θ) for different values of the slot radius R when $E_0 \frac{\pi h}{L} = 100$.

To explain the circular slot influence, we consider the patch antenna as a transmission line [16]. From this model, the input impedance is related to the characteristic impedance of the line which is given by the following expression:

$$Z_c = \sqrt{\frac{L_0}{C_0}}, \quad (10)$$

where L_0 is the serial inductance per unit length and C_0 is the parallel capacitance per unit length.

When a slot is introduced inside the patch antenna, its equivalent capacitance C_s reduces the serial inductance L_0 and so the characteristic impedance of the line,

assuming that the phase velocity of the travelling wave remains unchanged. From Fig. 9, we notice that the value of the electric field E_s inside the circular slot is non-null, when theta (θ) is within the range $[0^\circ, 90^\circ]$ and it is null when $\theta = 0^\circ$ or $\theta = 90^\circ$ for $R \approx \frac{L}{2}$. In this case, the capacitance C_s is equal to zero when theta's value is equal to 0° or 90° , due to the absence of the electric field for these two values of theta. Therefore, the slotted patch characteristic impedance Z'_c at $\theta = 0^\circ$ and $\theta = 90^\circ$ is almost equal to the patch characteristic impedance Z_c without slot. But, its value decreases when θ is within the range of degrees from 0° to 90° .

In section I, we demonstrated that for a polygonal antenna, the lower resonant frequency is related to the largest length (L_2) and the higher one is related to the smallest length (L_1). Now, after the insertion of the circular slot, when $\theta = 0^\circ$, a portion of the slot is located on the largest length. But when $\theta = 90^\circ$, another portion is located on the smallest length. It is then expected, theoretically and based on the discussion following Fig. 9 that the circular slot will not impact the impedance matching for the two resonant frequencies of the antenna presented in Fig. 5. However, the frequencies between them undergo an input resistance reduction, which should improve the bandwidth of the antenna.

2) Simulation results

A polygonal antenna with a circular slot inside the patch [17] has been simulated and it is shown in Fig. 10. According to the previous theory, the value of the outer radius R_{out} is chosen close to $\frac{L_2}{2}$ ($R_{out} = 3.7$ mm). The slot width is equal to 0.3 mm. The feeding probe is located at a distance $x = 2.9$ mm from the center of the antenna. A small air gap of 0.1 mm needs to be taken into account in the simulation between the patch and the rodome. The simulation result of S_{11} parameter of the proposed antenna is given in Fig. 11.

According to the simulation result for the given value of the slot width (0.3 mm), this antenna has a bandwidth around 3 GHz (from 11.6 GHz to 14.8 GHz) at -10 dB. The simulation shows that due to the insertion of the circular slot, the dual band antenna was indeed transformed to a broadband antenna.

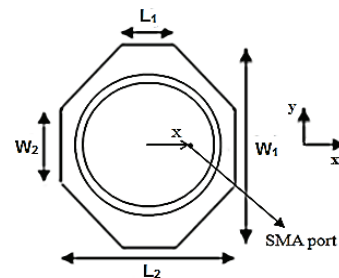


Fig. 10. Proposed polygonal antenna with a circular slot.

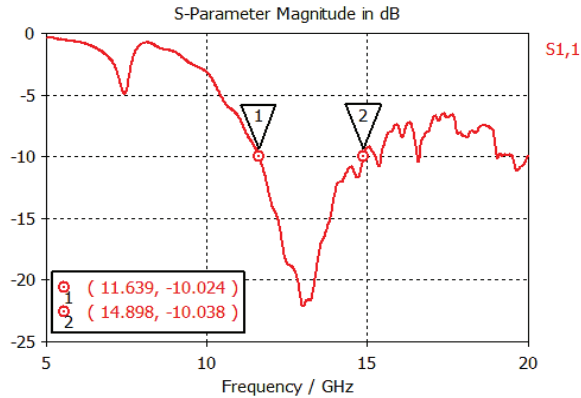


Fig. 11. Simulation result of the S_{11} parameter of the antenna patch with circular slot.

To show the influence of the slot width on the antenna reflection coefficient, a parametric study for different widths of the circular slot (quite small compared to the wavelength) is given in Fig. 12.

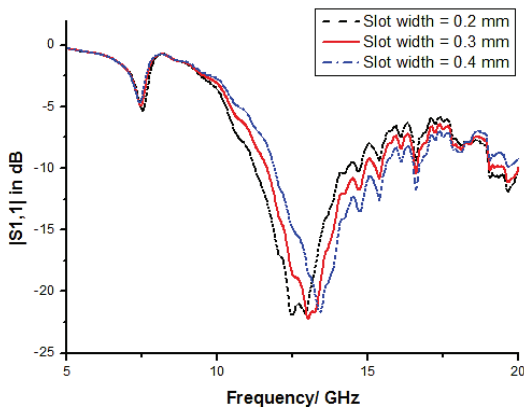


Fig. 12. Parametric study for different widths of the circular slot.

Table 2 shows that the relative bandwidth of the proposed antenna is not highly affected by the slot width which remains around 20%. Only the central frequency shifts towards higher frequencies as the slot width increases.

Table 2: Antenna relative bandwidth for different slot width

| Slot Width (mm) | Relative Bandwidth (%) | Central Frequency (GHz) |
|-----------------|------------------------|-------------------------|
| 0.2 | 21 | 12.75 |
| 0.3 | 21 | 13.2 |
| 0.4 | 22 | 13.7 |

This is mainly due to the changes in the phase velocity supposed to be constant in the theory. The E-fields of the circular slotted polygon at 11.63 GHz, 13 GHz, and at 14.8 GHz are provided in Table 3 below.

The electric field distribution symmetry observed for all frequencies within the bandwidth, shows that the resulted field is oriented along X-axis and that the cross-polarization theoretically is null due to its perfect symmetry.

Table 3: E-field of the polygonal antenna with circular slot

| Frequency (GHz) | 11.63 | 13 | 14.8 | |
|-----------------|-------|----|------|---|
| | I | II | III | |
| E_z | | | | a |
| E_x | | | | b |
| E_y | | | | c |

According to Table 3 comments, the simulated co/cross-polarization radiation pattern, given in Table 4, shows that the cross-polarization level is about 20 dB less than the main polarization, as expected. The same polarization is observed over the whole bandwidth.

Table 4: Co/Cross-polarization in the E-plane at different frequencies

| Frequency (GHz) | Co/Cross-polarization | | Co/Cross-polarization |
|-----------------|-----------------------|----|-----------------------|
| | 11.6 | 13 | |
| | | | |

III. PROTOTYPE AND MEASUREMENTS

A prototype of this antenna was manufactured and measured. The dimensions of this design are given in Table 5. The patch was printed on a Teflon-glass substrate of 1.58 mm thickness with a relative permittivity of 2.55 and $\tan\delta = 0.007$. Its dimensions are set to $50 \times 50 \text{ mm}^2$ ($2\lambda_0 \times 2\lambda_0$, where λ_0 is the wavelength at the lower frequency

10.7 GHz).

Table 5: Prototype antenna dimensions

| Parameter | Value (mm) |
|-----------------------------------|------------|
| L_1 | 5.1 |
| W_1 | 13 |
| L_2 | 8.9 |
| W_2 | 4.5 |
| R_{in} (the slot inner radius) | 3.41 |
| R_{out} (the slot outer radius) | 3.72 |
| Feeding probe at x | 2.9 |

The used rodome is a Nelco NY9220 substrate of a 3.175 mm thickness with a relative permittivity of 2.2 and $\tan\delta = 0.0009$. The total size of the antenna is near $0.4\lambda_0 \times 0.6\lambda_0$, compatible for the design of an antenna array. A photo of the proposed antenna is given in Fig. 13.



Fig. 13. Photo of the prototype antenna.

As shown in Fig. 14, a good agreement between simulations and measurements in terms of bandwidth is observed. It is around 3 GHz at -10 dB, which represents a relative bandwidth of 22%. The difference between the simulated and measured S_{11} is mainly due to the manual fabrication of the prototype, especially the feeding probe drilling (about few hundred μm).

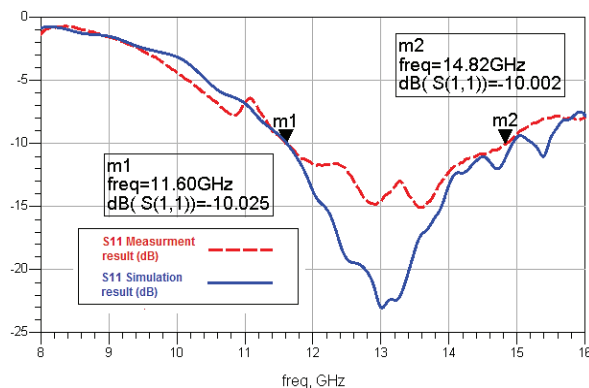


Fig. 14. Comparison of S_{11} parameter of the simulated and measured antenna.

Figure 15 below presents the measured radiation pattern of the antenna. The main and the cross-polarizations in E- and H-planes are given for three frequencies inside the band.

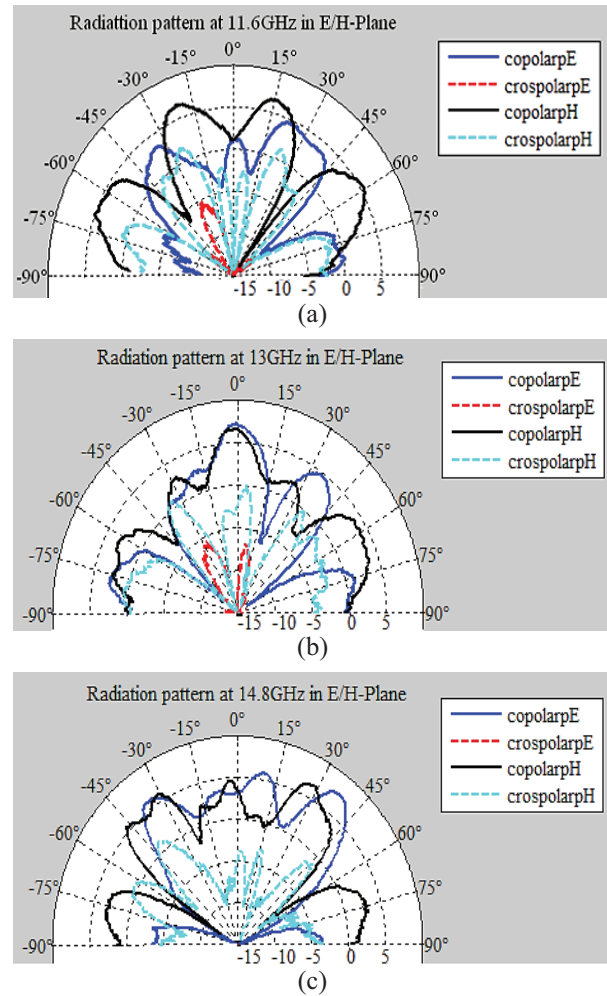


Fig. 15. Radiation pattern measurements within the bandwidth.

In the main radiation direction, the cross-polarization is about 10 dB lower than the main polarization. However, a slight degradation of the co/cross-polarization level is observed as we move away from broadside direction, particularly observed at lower frequencies of the bandwidth.

The reason behind this result could arise from the prototyping technology and maybe the zero-scale balance of the feeding probe problem due to the manual drilling. The observed ripples in the radiation pattern for all frequencies can be explained by the diffraction of the radiated field on the ground plane because of its limited dimensions. The maximum directivity observed is about 6.4 dBi.

IV. CONCLUSION

In this paper, a theoretical approach of an original broadband antenna design is presented. It consists of a polygonal antenna with a circular slot inside. A polygonal antenna presents initially a dual band behavior due to two different collinear resonant lengths. But, the insertion of a circular slot transforms it to a broadband behavior because this slot acts as an impedance regulator. The measurements agree well with the simulations and confirm the interesting properties of this design such as the wideband behavior (a relative bandwidth of 22% in the Ku-band is observed) and the guaranteed linear polarization over the entire bandwidth. With only a footprint of $0.4\lambda_0 \times 0.6\lambda_0$ and a 6.4 dBi gain, this design is a good candidate for antenna array configuration to achieve high gain like in satellite application services.

REFERENCES

- [1] V. Peshlov, R. Traykov, G. Bozmarova, M. Popova, D. Vasilev, and Z. Ivanov, "Low-cost scanning antenna for satellite reception," *IEEE International Symposium on Phased Array Systems and Technology*, Massachusetts, USA, pp. 441-445, 2003.
- [2] U. H. Park, K. H. Lee, and S. I. Jeon, "A novel mobile antenna for Ku-band satellite communications," *ETRI Journal*, vol. 27, no. 3, June 2005.
- [3] A. Sabban, "A new broadband stacked two-layer microstrip antenna," *Proc. IEEE Antennas Propagation Sympo. Dig.*, pp. 63-66, 1983.
- [4] W. Elhaji, F. Gallee, and C. Person, "Bi-access tri-band wideband antenna for an opportunistic communication between 4G terminals," *IEEE International Symposium on Antennas and Propagation*, Spokane, United States, 2011.
- [5] A. B. Nandgaonkar and S. B. Deosarkar, "Design of high gain two-layer electromagnetically coupled patch antenna in the ISM band," *International Conference on Electromagnetics in Advanced Applications*, Torino, Italy, pp. 547-550, 2007.
- [6] J. Granholm and K. Woelders, "Dual polarization stacked microstrip patch antenna array with very low cross-polarization," *IEEE Transactions on Antennas and Propagation*, vol. 49, no. 10, Oct. 2001.
- [7] R. Wansch, H. Adel, and H. Humpfer, "Mini-terminal - a small antenna for satellite reception," *INICA*, pp. 153-157, 2007.
- [8] F. F. Dubrovka and S. Y. Martynyuk, "Wideband dual polarized planar antenna arrays," *Int. Conference on Antenna Theory and Techniques, Dept. of Theoretical Fundamentals Radio Engineering, Kiev Polytechnic Institute*, National Technical University of Ukraine, Sevastopol, Ukraine, pp. 91-96, Sep. 9-12, 2003.
- [9] S. Bouaziz, A. Ali, S. Hebib, and H. Aubert, "Planar wideband microstrip antenna with inclined radiation pattern for C-band airborne applications," *The 4th European Conference on Antennas and Propagation (EuCAP)*, Barcelone-Spain, pp. 1-4, 2010.
- [10] K. Ito, K. Ohmaru, and Y. Konishi, "Planar antenna for satellite reception," *IEEE Transactions on Broadcasting*, vol. 34, no. 4, Dec. 1988.
- [11] Z. Haiyang, M. Yann, and R. Tchanguiz, "A novel wideband and dual-polarized cross-antenna for satellite communications," *Proceedings of the Progress in Electromagnetics Research Symposium*, Stockholm, Sweden, pp. 1425-1428, Aug. 2013.
- [12] M. Manzani, A. Alu, F. Bilotti, and L. Vegni, "Design of polygonal antennas with a broad-band behavior via a proper perturbation of conventional rectangular radiators," *IEEE Antennas and Propagation Society International Symposium*, vol. 2, pp. 268-271, 2003.
- [13] M. Manzini, A. Alu, F. Bilotti, and L. Vegni, "Polygonal patch antenna for wireless communications," *IEEE Transactions on Vehicular Technology*, vol. 53, no. 5, Sep. 2004.
- [14] C. A. Balanis, *Microstrip Antennas: in Antenna Theory Analysis and Design*, John Wiley & Sons, New York, Second Edition, 1997.
- [15] Z. N. Chen and M. Y. W. Chia, *Broadband Microstrip Patch Antenna: in Broadband Planar Antennas Design and Applications*, John Wiley & Sons, 2006.
- [16] CST Microwave Studio, Version 2008, Computer Simulation Technology, Framingham, MA, 2008.



Amal Harrabi was born in November 1986. She received the Ph.D. degree in Electrical Engineering jointly from the University of Nantes, France and the University of Tunis-El Manar, Tunisia in June 2015. Her research interests include antenna design, antenna miniaturization, antenna array design and RF circuits design.



Tchanguiz Razban was born in Tabriz, Iran, in 1956. He received the Engineering degree from University of Tehran, Iran, in 1980. He received the Ph.D. and Doctorat d'Etat from the Institut National Polytechnique de Grenoble (INPG), France, in 1983 and 1989, respectively. He is currently a Full Professor of Electrical Engineering at

Ecole Polytechnique de Nantes. Since 1999 he has been the Chief Manager of the Electrical Engineering Department, Deputy Director and finally Director of Ecole Polytechnique until January 2010. His research interests include MMIC's and printed circuits for wireless communications, smart antennas and optical-microwave interfaces



Yann Mahé was born on June 29, 1973. He received the Ph.D. degree in Electrical Engineering from the University of Nantes, Nantes, France, in 2001. He is now an Assistant Professor at the Polytechnic School of the University of Nantes, Nantes, France. He is also a Researcher with

Institut d'Electronique et Telecommunications de Rennes (IETR) of Nantes, France. His research interests include antenna design, development of miniaturized and tuneable antenna for MIMO systems, multi-function antennas and antenna array design



Lotfi Osman was born in 1958 in Mahdia, Tunisia. He received his Master's degree in Automation from Lille 1 University, Science and Technology, France in 1984 and his Ph.D. in Automation and Computer Engineering in 1987 at the same University. In June 2013, he obtained

the Habilitation Degree in Electronics and Microelectronics from INSAT, National Institute of Applied Sciences and Technology in Tunis, University of Carthage, Tunisia. He is currently Assistant Professor with the Department of Electronics, Physics and Propagation at Sup'Com, Higher School of Communication of Tunis. In 2004, he joined the Unit of Research in High Frequency Electronic Circuits and Systems at the Faculty of Sciences of Tunis, University of Tunis El Manar. His current research interests include antennas and modeling in microwave integrated circuits. He is also involved with experimental characterization and antenna measurement.



Ali Gharsallah was born in 1959 in Kerkenah, Tunisia. He is Professor at the Faculty of Sciences of Tunis and Head of Research Unit "CSEHF" (code 13ES37) at the Department of Physics of the Faculty of Sciences of Tunis - University of Tunis El Manar.

He now occupies the post of Director General of Technological Studies at the Ministry of Higher Education and Scientific Research. He received the Engineering's degree in Radio Electrical from the Higher School of Telecommunications of Tunis in 1986 and the Ph.D. degree in 1994 from the National Engineering School of Tunis. Since 1991, he was with the Department of Physics at the Faculty of Sciences of Tunis. His current research interests include antennas, multi-layered structures and microwave integrated circuits.

Two Element Dielectric Resonator Antenna with Beam Switching

M. Kamran Saleem, Majeed A. S. Alkanhal, and Abdel Fattah Sheta

Department of Electrical Engineering, College of Engineering
King Saud University, Riyadh, P. O. Box 800, 11421, Saudi Arabia
msaleem@ksu.edu.sa, majeed@ksu.edu.sa, asheta@ksu.edu.sa

Abstract— A wideband two element rectangular dielectric resonator antenna (DRA) is proposed in this paper. Each DRA element has two excitation strips and four parasitic patches. A wide impedance bandwidth of more than 37% at the center frequency of 1.6 GHz is achieved. The antenna radiation beam can be switched between two positions in elevation plane, i.e., $\theta = 45^\circ$ and $\theta = -45^\circ$. The measured antenna gain is found to be more than 6 dB in the whole frequency band of operation. The matching and the radiation characteristics of the designed switched beam antenna are studied and validated by measurements. A very good agreement between the measured and simulated results is observed.

Index Terms— Dielectric resonator antenna, parasitic patch, switched beam antenna, wideband antenna.

I. INTRODUCTION

The dielectric resonator antenna (DRA) was first introduced by Long in 1983 [1]. The DRA has many advantages such as low dissipation loss, high radiation efficiency and ease of excitation as well as wider impedance bandwidth [2-4]. Different shapes of DRAs such as rectangular, cylindrical, hemispherical, elliptical and perforated have been presented in the literature [5-9]. The DRA's having rectangular shape offer advantages over hemispherical and cylindrical shaped DRAs since they are easy to fabricate and have more design flexibility. There are many different schemes for exciting DRA such as probe feed, helical feed, slot feed and strip line feed [10-12].

The beam switching antenna finds many uses in applications requiring tracking or interference mitigation. The beam switching can be achieved by physical movement of antenna or by electronic control of some antenna parameters [13]. The mechanically steerable antennas [14] may be difficult to implement since they require a motor to rotate the antenna structure. One of possible solutions is to use multiple feeds [15-17] and radiation pattern can be switched using electronic switches, but this multiple feed antenna structure requires extra circuitry (phase shifters, power splitters/combiners) for feed selection and multiple antenna elements,

resulting in a more complex and a large antenna structure.

The work in this paper presents a two element small size DRA, which is investigated to achieve reconfigurable radiation patterns with high gain. The antenna impedance bandwidth is found to be 800 MHz (1.3 - 2.1 GHz). In addition, the antenna radiation pattern can be switched in two positions in elevation plan, i.e., at $\theta = 45^\circ$ and $\theta = -45^\circ$ from 1.3 to 1.9 GHz. The simulations are done using Ansys HFSS and a prototype is developed and tested to prove the design concept and to verify the simulation results.

II. THEORETICAL ANALYSIS

The analysis of operation of DRA is a complex electromagnetic field problem. The numerical techniques such as finite element method (FEM), finite-difference time domain (FDTD) and the method of moments (MoM) are usually employed to predict/compute the resonance frequency of DRA with specific dimensions. Since all these numerical techniques require intensive memory and processing, therefore, several simple models have been developed to estimate the resonance frequency of DRA. Utilizing the most commonly used the dielectric waveguide model (DWM), the TE_{mnl} resonance frequency (f_0) for rectangular DRA can be calculated as follows [18]:

$$f_0 = \frac{c}{2\pi\sqrt{\epsilon_r}} \sqrt{k_x^2 + k_y^2 + k_z^2}, \quad (1)$$

$$k_x = \frac{m\pi}{a}, \quad (2)$$

$$k_z = \frac{l\pi}{2d}, \quad (3)$$

$$k_y \tan\left(\frac{k_y b}{2}\right) = \sqrt{(\epsilon_r - 1)k_0^2 - k_x^2}, (n=1), \quad (4)$$

$$k_x^2 + k_y^2 + k_z^2 = \epsilon_r k_0^2, \quad (5)$$

where, k_0 is the free space wavenumber, c is the speed of light in vacuum and k_x , k_y and k_z are the wavenumber inside the DR in three directions. The ϵ_r is dielectric constant and a , b and d are length, width and height of DR respectively. The subscripts m , n and l of TE_{mnl}

denotes the number of extremes in the x , y and z directions respectively. Utilizing the above mentioned DWM the DR ($\epsilon_r = 10$) size is found to be $a = 32$ mm, $b = 29.6$ mm, and $d = 48.85$ mm, resulting in the dominant TE_{111} mode resonance frequency to be at 1.84 GHz.

Furthermore, the selection of suitable coupling/excitation scheme is one of the most crucial parts of DRA design. The type and location of coupling/excitation scheme very effectively effect the DRA performance. We know from the electromagnetic theory and the Lorentz theorem of reciprocity [19] that the amount of coupling between the sources (electric or magnetic) and the fields inside the DRA can be determined by:

$$k \propto \int (E \cdot J_e) dV, \quad (6)$$

$$k \propto \int (H \cdot J_m) dV, \quad (7)$$

where, \mathbf{E} and \mathbf{H} are the electric and magnetic field intensity vectors. \mathbf{J}_e and \mathbf{J}_m are the electric and magnetic currents. The above equations state that in order to achieve strong coupling between an electric or magnetic current source and the DRA, the excitation source should be placed in regime of strongest electric or magnetic field of the DRA. In proposed DRA structure, the vertical probe excitation scheme is employed, which is considered as vertical electric current source. The most suitable location for this excitation scheme is at the middle of DRA broad side wall, since the electric field is maximum in this location. As mentioned in our pervious communication [20], the dual excitation scheme is employed to split the broad side radiation pattern into two lobes, which plays an important role in DRA beam switching.

III. ANTENNA DESIGN AND CONFIGURATION

The proposed two element DRA configuration is shown in Fig. 1. The dielectric resonators (DRs) have dielectric constant and dielectric loss tangent of 10 and 0.0005, respectively. As mentioned earlier, the DR size is selected to be $a = 32$ mm, $b = 29.6$ mm, and $d = 48.85$ mm. The DRs are placed over FR4 substrate of thickness 1.575 mm. The bottom side of the substrate is fully copper plated and acts as an antenna ground plane. The DR is excited by means of dual excitation strips placed at the middle of two opposite side walls in the YZ -plane. The excitation strip lengths and widths are $L_E = 30$ mm and $W_E = 5.3$ mm, respectively. Furthermore, four parasitic patches are placed at the corner of each DR side wall in the XZ -plane having length $L_P = 22$ mm and width

$W_P = 1.5$ mm. Each parasitic patch is connected to the antenna ground plane through a metallic via hole in the FR4 substrate. To provide a short or open circuit between the parasitic patch and the antenna ground plane, a switch can be placed between them. All eight switches are shown in the top view of the proposed antenna structure as illustrated in Fig. 2. The optimum center to center distance between the two DR is found to be $S = 108$ mm ($0.6\lambda_0$, at center frequency of 1.6 GHz). The four excitation strips are connected together by means of a microstrip feed network and a coaxial probe is placed at the center of microstrip line of length $L_3 = 109.48$ mm and width $T_2 = 1.48$ mm. The microstrip feed network is optimized to mitigate the degradation caused in antenna return loss by the microstrip line in close proximity of DR [11]. The optimized dimensions shown in Fig. 2 are as follows: $L_1 = 15$ mm, $L_2 = 45$ mm, $L_4 = 21.48$ mm, $T_1 = 0.74$ mm, $L = 235.6$ mm and $W = 144$ mm.

The DRAs excited by a single feed usually has a maximum at broad side direction [18,21]. However, with the proposed dual strip excitation scheme the radiation pattern is altered such that a null in broadside direction is created and the main lobe is splitted into two lobes with maxima at approximately $\pm 45^\circ$ in elevation plane. Readers are referred to [20] to have a better understanding of DRA excitation utilizing dual excitation strips. The two parasitic patches on one side having connections with antenna ground plane through switches are utilized to suppress one of the lobes created, and thus provide pattern reconfigurability. Moreover, the dimensions of the parasitic patch also control the impedance bandwidth [20]. The antenna radiation pattern is found to be linearly polarized with the proposed arrangement of dual excitation strips and parasitic patches.

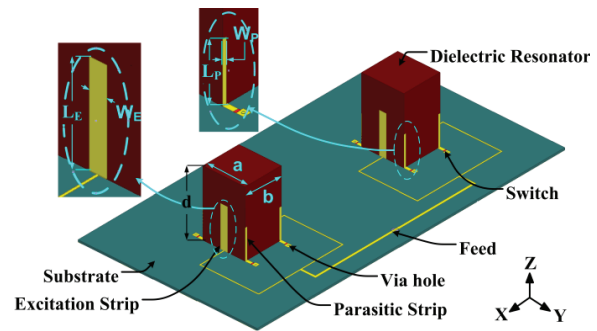


Fig. 1. The proposed two element DRA configuration. Each DRA has two excitation strips (YZ -plane) and four parasitic patches (XZ -plane).

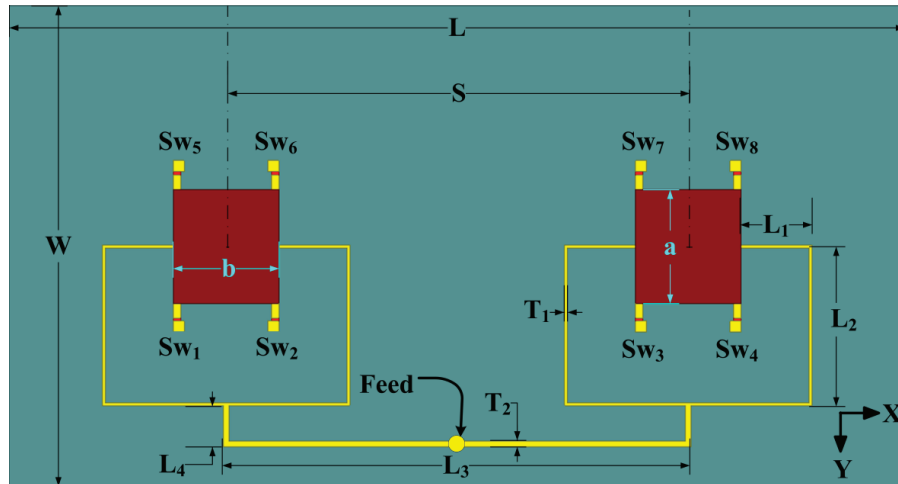


Fig. 2. Top view of two element DRA, with $a = 32$ mm, $b = 29.6$ mm, $d = 48.85$ mm, $S = 108$ mm, $L_E = 30$ mm, $W_E = 5.3$ mm, $L_P = 22$ mm, $W_P = 1.5$ mm, $L_1 = 15$ mm, $L_2 = 45$ mm, $L_3 = 109.48$ mm, $L_4 = 21.48$ mm, $T_1 = 0.74$ mm, $T_2 = 0.74$ mm $L = 235.6$ mm and $W = 144$ mm.

A prototype is fabricated to prove the design concept and to verify the simulations. The photograph of the fabricated antenna is shown in Fig. 3. The two DRs are glued over the FR4 substrate with a dielectric adhesive having dielectric constant of 10. The excitation strips and parasitic patches are cut from the conducting tap having thickness of 0.035 mm and positioned over the DR at appropriate locations as shown in Fig. 1. The utilization of eight switches ($Sw_1 - Sw_8$) in the proposed DRA configuration plays an important role to switch antenna radiation pattern in two directions in elevation plane (i.e., at $\theta = 45^\circ$ and $\theta = -45^\circ$). Although there are many possible switching combinations, but only two cases are discussed, which are summarized in Table 1. The antenna radiation pattern is not controllable with cases other than mentioned in Table 1, where “OFF” state refers to an open circuit between corresponding parasitic patch and antenna ground plane, and “ON” state refers to a short circuit between corresponding parasitic patch and antenna ground plane. For the proof of concept the switches are hard wired on the prototype (i.e., a small piece of conducting copper tap is utilized to provide a short circuit between the parasitic patch and the antenna ground plane). Subsequently, the return loss and radiation pattern measurements are taken for the fabricated DRA antenna structure as revealed in the subsequent sections.

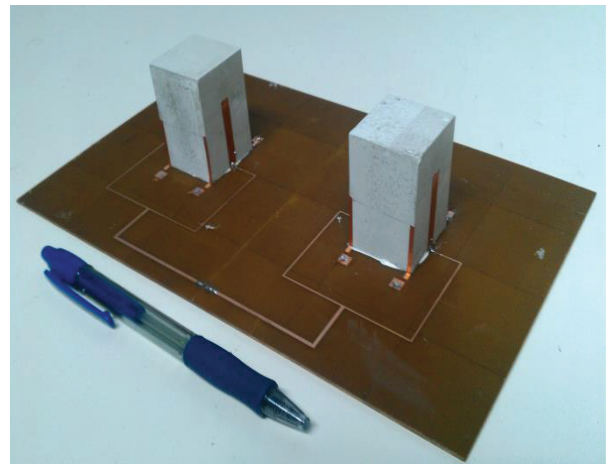


Fig. 3. Photograph of the developed two element DRA.

IV. SIMULATION AND MEASURED RESULTS

The DRA presented in Section II is simulated in Ansys HFSS. The simulated and measured return loss for the two cases mentioned in Table 1 are shown in Fig. 4. The overall antenna impedance bandwidth is found to be 800 MHz (1.3 - 2.1 GHz). The resonance of TE_{111} mode is found theoretically by DWM to be at 1.84 GHz. Experimentally, it is found at 1.78 GHz and corresponds to the strip loaded DR mode [21]. Furthermore, the resonance seen around 1.35 GHz is highly influenced by the length of the parasitic patch [20] and corresponds to the patch loaded DR mode [21]. The optimum length of the parasitic patch is found to be $L_P = 22$ mm. The field pattern inside DR is investigated and it is found that the antenna operates in a perturbed type TE_{111} from 1.3 - 1.9 GHz.

Table 1: Switch configuration for switching antenna radiation pattern in elevation plane

| | ON | OFF |
|---------|--------------------------|--------------------------|
| CASE-I | Sw_1, Sw_2, Sw_3, Sw_4 | Sw_5, Sw_6, Sw_7, Sw_8 |
| CASE-II | Sw_5, Sw_6, Sw_7, Sw_8 | Sw_1, Sw_2, Sw_3, Sw_4 |

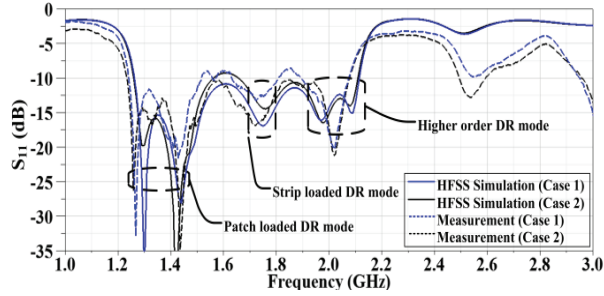


Fig. 4. Simulated and measured return loss (S_{11}) for two cases mentioned in Table 1.

The simulated 3D radiation patterns for both cases, i.e., Case-I and Case-II of Table 1 are shown in Fig. 5 for a better illustration of antenna beam switching. The comparison of measured and simulated radiation patterns at $\phi = 90^\circ$ (YZ-plane) at various frequencies for Case-I and Case-II, mentioned in Table 1, are shown in Fig. 6 and Fig. 7, respectively. It is found that after 1.9 GHz the antenna radiation pattern cannot be switched efficiently. This may be attributed to the excitation of higher order modes such as TE_{112} and TE_{113} . Theoretically, these two modes are found to be at 2.05 GHz and 2.34 GHz, respectively. Therefore, the actual antenna bandwidth in which antenna radiation pattern can be switched is from 1.3 to 1.9 GHz. The measured gain at center frequency of 1.6 GHz is found to be 6.92 dB at $\theta = -45^\circ$ for Case-I and 6.71 dB at $\theta = 45^\circ$ for Case-II respectively. The measured gain of the two-element DRA for both cases remains above 6 dB in whole frequency band of operation and is shown in Fig. 8.

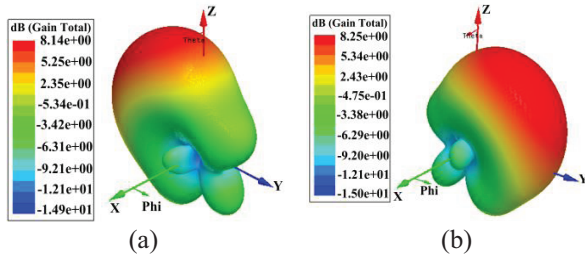


Fig. 5. 3D radiation pattern at 1.6 GHz for Case-I and Case-II given in Table 1: (a) Case-I, and (b) Case-II.

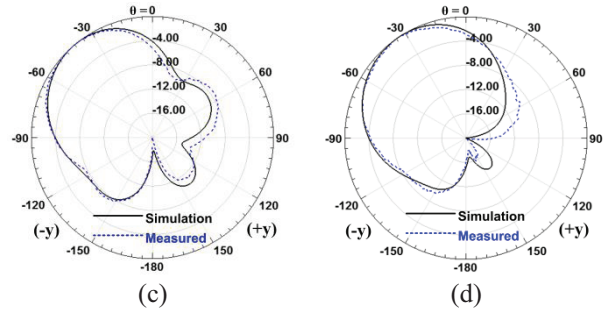
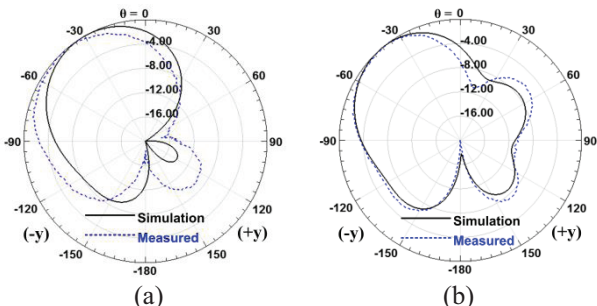


Fig. 6. Simulation and measured radiation patterns for Case-I given in Table 1: (a) 1.3 GHz, (b) 1.5 GHz, (c) 1.7 GHz, and (d) 1.9 GHz.

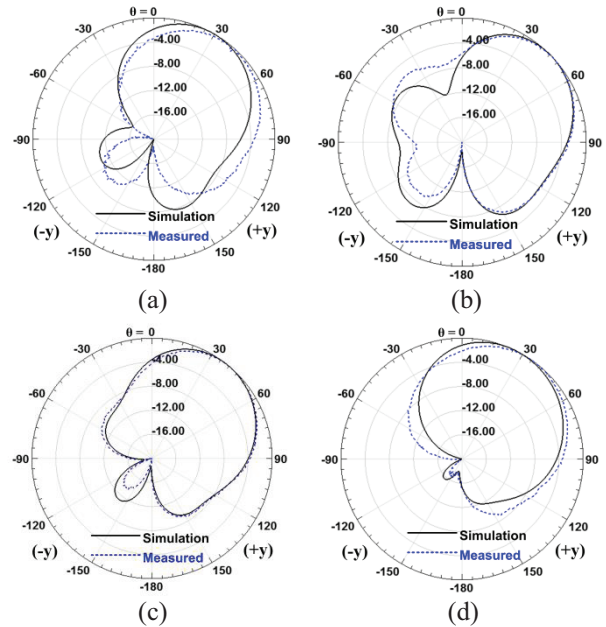


Fig. 7. Simulation and measured radiation patterns for Case-II given in Table 1: (a) 1.3 GHz, (b) 1.5 GHz, (c) 1.7 GHz, and (d) 1.9 GHz.

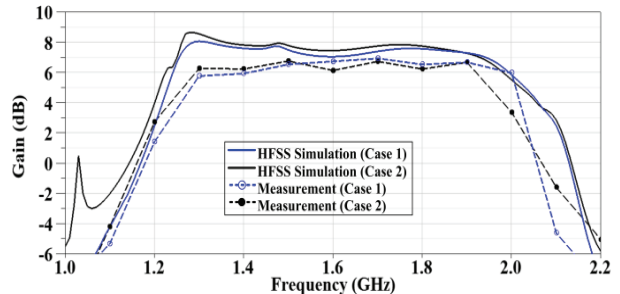


Fig. 8. A comparison of simulation and measured antenna gain for both cases mentioned in Table 1.

In Table 2, the proposed two-element switched beam DRA structure is compared with other switched

beam DRA structures found in literature. The proposed DRA structure includes only one coaxial feed and does not require any phase shifters or power splitter/combiners.

The gain and overall size of proposed DRA structure is also found to be better than other reported DRA structures.

Table 2: Comparison between the proposed and other published switched beam DRAs

| | No. of DRA Feeds | No. of Switchable Radiation Patterns | Impedance Bandwidth | Gain in Operating Bandwidth (dB) | Overall Size (L × W × H) |
|--------------|------------------|--------------------------------------|-------------------------|----------------------------------|--|
| [15] | 5 | 4 (requires power splitter/combiner) | 1 MHz (58.9 - 59.8 MHz) | Not mentioned | 800 × 800 × 200 mm 0.16λ ₀ × 0.16λ ₀ × 0.05λ ₀ |
| [16] | 4 | 4 (requires phase shifters) | 3.5 GHz (9.5 - 13 GHz) | Min: 1.5 Max: 3.0 | 55 × 55 × 6.8 mm 2λ ₀ × 2λ ₀ × 0.25λ ₀ |
| [17] | 4 | 4 (requires power splitter) | 900 MHz (1 - 1.9 GHz) | Min: 4.5 Max: 6.5 | 350 × 350 × 70 mm 1.8λ ₀ × 1.8λ ₀ × 0.36λ ₀ |
| Proposed DRA | 1 | 2 (RF switches) | 600 MHz (1.3 - 1.9 GHz) | Min: 6.0 Max: 7.0 | 235.6 × 144 × 49 mm 1.2λ ₀ × 0.74λ ₀ × 0.25λ ₀ |

λ₀ is the free space wavelength at the center frequency

V. CONCLUSION

Two elements small size wideband DRA in array configuration is proposed for beam switching applications. Dual excitation strips are utilized to excite each DRA element. Four parasitic patches associated with each DRA are utilized to increase the antenna impedance bandwidth as well as to switch antenna radiation pattern in elevation plane. Wide impedance bandwidth of approximately 37% (1.3 - 1.9 GHz) is achieved with similar radiation pattern characteristics. The antenna gain is found to be above 6 dB in the whole frequency band of operation. The proposed design based on two DRAs and a single coaxial feed network can be extended to more sophisticated antenna structures with higher gain and antenna radiation pattern reconfigurability.

ACKNOWLEDGMENT

The authors would like to extend their sincere appreciation to the Deanship of Scientific Research (DSR) at King Saud University for its funding of this research through the Research-Group Project No. RG-1436-001.

REFERENCES

- [1] S. A. Long, M. W. McAllister, and L. C. Shen, "The resonant cylindrical dielectric cavity antenna," *IEEE Trans. Antennas Propagat.*, vol. 31, no. 5, pp. 406-412, May 1983.
- [2] R. K. Mongia, A. Ittipiboon, and M. Cuhaci, "Measurement of radiation efficiency of dielectric resonator antennas," *IEEE Microwave and Guided Letters*, vol. 4, no. 3, pp. 80-82, 1994.
- [3] A. A. Kishk, "Dielectric resonator antenna, a candidate for radar applications," *Proceedings of 2003 IEEE Radar Conference*, pp. 258-264, May 2003.
- [4] I. A. Eshrah, A. A. Kishk, A. B. Yakovlev, and A. W. Glisson, "Theory and implementation of dielectric resonator antenna excited by a waveguide slot," *IEEE Trans. Antennas Propagat.*, vol. 44, no. 53, pp. 483-494, Jan. 2005.
- [5] M. Khalily, M. K. A. Rahim, and A. Kishk, "Bandwidth enhancement and radiation characteristics improvement of rectangular dielectric resonator antenna," *IEEE Antennas and Wireless Propagation Letters*, vol. 10, pp. 393-395, 2011.
- [6] Z. Deen, H. Saber, H. A. Malhat, and K. H. Awadalla, "8×8 near-field focused circularly polarized cylindrical DRA array for RFID applications," *Applied Computational Electromagnetics Society Journal (ACES)*, vol. 27, no. 1, 2012.
- [7] A. Tadjalli, A. R. Sebak, T. A. Denidni, and A. A. Kishk, "Spheroidal dielectric resonator antenna," *URSI Digist, USNC/URSI National Radio Science Meeting*, pp. 184, 2004.
- [8] A. Tadjalli, A. Sebak, T. Denidni, and I. Ahadi-Akhlghi, "Design of elliptical dielectric resonator antennas using genetic algorithm and Rayleigh-Ritz technique," *Applied Computational Electromagnetics Society Journal (ACES)*, vol. 24, no. 1, pp. 37-44, 2009.
- [9] Z. Deen, S. H. S. M. Gaber, A. M. Abd-Elhady, K. H. Awadalla, and A. Kishk, "Perforated dielectric resonator antenna reflectarray," *Applied Computational Electromagnetics Society Journal (ACES)*, vol. 26, no. 10, 2011.
- [10] G. Almpanis, C. Fumeaux, and R. Vahldieck, "Novel broadband dielectric resonator antennas fed through double-bowtie-slot excitation scheme," *Applied Computational Electromagnetics Society Journal (ACES)*, vol. 22, no. 1, 2007.
- [11] A. Petosa, *Dielectric Resonator Antenna Handbook*, Artech House Publishing, ISBN: 978-1-59693-206-7, 2007.
- [12] A. Motevasselian, A. Ellgardt, and B. L. G.

- Jonsson, "A circularly polarized cylindrical dielectric resonator antenna using a helical exciter," *IEEE Trans. Antennas Propagat.*, vol. 61, no. 3, Mar. 2013.
- [13] A. Petosa and A. Ittipiboon, "Dielectric resonator antenna: a historical review and the current state of the art," *IEEE Antennas Propagat. Mag.*, vol. 52, pp. 91-116, Oct. 2010.
- [14] H. Fayad and P. Record, "Experimental investigation on new steerable dielectric resonator antenna," *IET Electronics Letters*, vol. 43, no. 19, pp. 1009-1010, Sep. 2007.
- [15] S. P. Kingsley and S. G. O'Keefe, "Beam steering and monopulse processing of probe-fed dielectric resonator antennas," *IEE Proceedings-Radar, Sonar and Navigation*, vol. 146, no. 3, pp. 121-125, 1999.
- [16] H. Fayad and P. Record, "Multi-feed dielectric resonator antenna with reconfigurable radiation pattern," *Progress in Electromagnetics Research*, vol. 76, pp. 341-356, 2007.
- [17] M. Grag and S. K. Sharma, "Wide-bandwidth dielectric resonator antenna with omni-directional radiation patterns for beam focusing properties in a circular array," *International Journal of RF and Microwave Computer-Aided Engineering*, vol. 24, no. 1, pp. 92-101, 2014.
- [18] R. K. Mongia and A. Ittipiboon, "Theoretical and experimental investigations on rectangular dielectric resonator antennas," *IEEE Trans. Antennas Propagat.*, vol. 45, no. 9, pp. 1348-1356, Sep. 1997.
- [19] R. E. Collin and F. J. Zucker, *Antenna Theory, Part 1*, Inter-University Electronics Series, 1969.
- [20] M. K. Saleem, M. A. S. Alkanhal, and A. F. Sheta, "Dual strip-excited dielectric resonator antenna with parasitic strips for radiation pattern reconfigurability," *International Journal of Antennas and Propagation*, vol. 2014, Jan. 2014.
- [21] B. Li and K. W. Leung, "Strip-fed rectangular dielectric resonator antennas with/without a parasitic patch," *IEEE Trans. Antennas Propagat.*, vol. 53, iss. 7, pp. 2200-2207, July 2005.

A Transparent UWB Antenna with a 5 to 6 GHz Band Notch Using Two Split Ring Resonators

M. S. A. Rani¹, S. K. A. Rahim¹, P. J. Soh², B. M. Saad¹, M. I. Sabran¹,
and M. F. M. Yusoff¹

¹ Wireless Communication Center (WCC)
Universiti Teknologi Malaysia, 81310 UTM Skudai, Johor, Malaysia
msubri2@gmail.com, sharulkamal@fke.utm.my, engrbash@yahoo.co.uk, mursyid@fkegraduate.utm.my,
fairus@fke.utm.my

² Advanced Communication Engineering (ACE) CoE, The School of Computer and Communication Engineering
Universiti Malaysia Perlis (UniMAP), Pauh Putra Campus, 02600 Arau, Perlis, Malaysia
pjsoh@unimap.edu.my

Abstract — A miniaturized thin film transparent ultra-wideband (UWB) antenna design with a band notch is presented. A pair of split-ring resonators (SRRs) is placed besides the radiating element to realize the band notch centered at 5.5 GHz. The proposed transparent antenna covers the whole 3.1 to 10.6 GHz UWB frequency band with a notch from 5 to 6 GHz to isolate interferences from wireless local area network (WLAN) and dedicated short-range communication (DSRC) applications. The transparency of this antenna of up to 80% is enabled by the fabrication on a conductive silver coated thin film (AgHT-8). Hence, the proposed transparent antenna is a suitable for UWB home entertainment network (IEEE 1394 over UWB network) for green building applications, where high data rates are required for multimedia transfer. Implementation of the proposed transparent antenna will reduce the space consumption due to its very low thickness and low profile, while at the same time increasing the aesthetic values of the installed wireless system due to its high transparency.

Index Terms — AgHT-8, band notch, split ring resonator, transparent antenna, UWB.

I. INTRODUCTION

Ultra wideband (UWB) antenna covers the 3.1 to 10.6 GHz frequency range, as approved by the Federal Communication Commission (FCC) for unlicensed radio frequency applications. A frequency notch is needed to eliminate the possibilities of interferences between this application and other wireless services. Narrow bands wireless services such as IEEE 802.a (5.15 GHz - 5.825 GHz) for WLAN and IEEE 802.11p (5.50 GHz - 5.925 GHz) for dedicated short-range communication (DSRC) frequency band are included within the UWB frequencies [1]. Hence, it is highly desirable that the frequency bands for these

applications be segregated from the UWB receiver.

Several techniques have been reported recently for realizing band notches in UWB antennas [2-4], which mainly comprises of various slot configurations. The implementation of split ring resonators (SRR) to introduce an antenna band notch is one of the best techniques for realizing band notches as it does not consume a large area in the antenna topology [5]. SRRs are commonly placed in the radiating element, near the transmission line to maximize the coupling effect, as in [6-8]. However, slot placement on these locations results in gain degradation due to the partial removal of the radiating element. Several other SRR positioning techniques have been reported in previous works [9-12] to address this issue, where the SRRs are placed outside the radiating element but in close vicinity of the transmission line. Most of these topologies are implemented on non-transparent substrates such as Rogers, Taconic, and Fire Retardant-4 (FR-4).

Due to the use of conventional, non-transparent materials, the antenna loses its aesthetic values and this becomes apparent to the users when they are installed in public areas. Several previous investigations on transparent antenna have also been performed to overcome this issue. An example is the optically transparent UWB antenna [13] using conductive silver coated thin film (AgHT-4/8), with Perspex substrate. Another transparent UWB antenna with tunable notch reported in [14], consists of a simple rectangular radiating element with vertical slots for band notching. However, the resulting resonant frequency is dependent on the length of the vertical slots. This complicates its implementation at the lower frequency, as long slots are needed, thus requiring a larger radiator footprint. Several disadvantages of the transparent materials have been reported in [15-16], where it is highlighted that the high material losses and consequently, feeding line losses has limited the usage

of such materials. Table 1 summarizes a comparison of the proposed band notch transparent antenna against other recent transparent UWB antennas in term of.

Despite these investigations, the implementation of SRRs on a transparent antenna patch has yet to be reported. In this paper, a transparent UWB antenna with SRRs outside the radiating element [10] using conductive silver coated thin film (AgHT-8) is proposed. The design concept and the resulting performance of the transparent antenna are analyzed and thoroughly discussed. Its structure is potentially suitable for UWB home entertainment network (IEEE 1394 over UWB network) [17].

Table 1: Transparent UWB antennas comparison

| Ref. | Description* | | | |
|-------------|---|----------------------|------------------------------|---------------------|
| | Notch Freq. (GHz) | Min RL at Notch (dB) | Max Gain (dBi) @ Freq. (GHz) | Gain at Notch (dBi) |
| [13] | *Transparent antenna using Perspex | | | |
| | - | - | -5 @ 6 | - |
| [14] | *Tunable transparent UWB antenna with vertical slot | | | |
| | 5 | -10 | -2 @ 15 | -7 |
| This design | *Notched transparent UWB antenna using SRR | | | |
| | 5.8 | -10 | -5 @ 9.5 | -9.5 |

II. MATERIALS AND ANTENNA DESIGN

A. Split ring resonator and UWB antenna

The proposed antenna is implemented on a conductive silver coated thin film (AgHT-8) as the conductor. Its estimated conductivity, σ is 1.25×10^5 S/m. A thin polyethylene terephthalate polymer with permittivity of $\epsilon_r = 3.228$ is used as the substrate. Both materials are optically transparent with a total thickness, h , of, 0.175 mm.

SRR consist of a pair of concentric metallic rings, etched on a dielectric substrate. The SRR structure is introduced onto the antenna topology to create a band notch. Split ring resonators are formed using two concentric metallic rings with a split on opposite sides, see Fig. 3. This structure behaves similarly to an LC resonant circuit driven by an external electromotive force. The resonant frequency of the of the SRR can be expressed as [11-12]:

$$\omega_0 = \sqrt{\frac{2}{\pi r_0 LC}}, \quad (1)$$

where L is the total inductance of the circular SRR, C is the capacitance per unit length between the rings and r_0 is the average radius of the rings. Therefore, the SRR resonant frequency can be easily tuned by optimizing its parameters shown in Fig. 1.

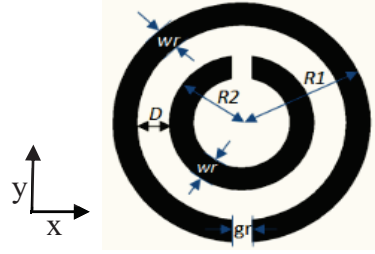


Fig. 1. Geometry of the split ring resonator.

A two port network for the thin film transmission line was constructed to analyze the insertion loss. Figure 2 shows a high insertion loss is evident in this transmission line caused by the high AgHT-8 losses. Moreover, the insertion loss increases as the frequency increases. The implementation of the SRR inside the transmission line interrupts the current flowing on the transmission line causing further insertion losses. This indicates that a good band notch with high insertion losses can be potentially created using an optimized SRR.

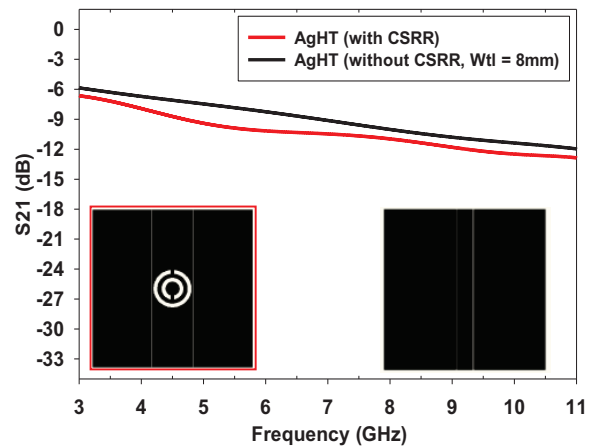


Fig. 2. Simulated insertion loss for two port network using AgHT (with and without SRR).

The transparent UWB antenna consists of a coplanar waveguide (CPW) feed attached to a circular radiating element, as shown in Fig. 3. The optimized parameters of the proposed UWB antenna and SRR are listed in Table 2.

The gap between the ground and the transmission line, g , is optimized to $g = 0.15$ mm to achieve the 50- Ω impedance matching. Simulations and optimizations were performed using Computer Simulation Technology (CST) Microwave Studio. Figure 4 shows the effect of the size variation of the circular radiating element on the antenna reflection coefficient. The minimum radius for the

circular radiating element to exhibit UWB characteristics is at least 8 mm.

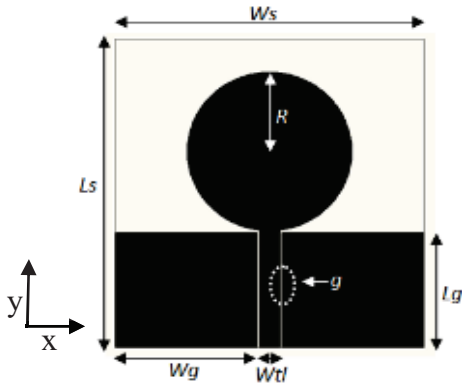


Fig. 3. Geometry of the proposed transparent UWB antenna.

Table 2: Optimized geometries of the proposed UWB antenna with SRRs

| Symbols | Parameter | Dimensions (mm) |
|----------|-------------------------|-----------------|
| W_s | Substrate width | 30.0 |
| L_s | Substrate length | 30.0 |
| W_g | Ground width | 13.85 |
| L_g | Ground length | 11.5 |
| R | Patch radius | 8.0 |
| g | CPW gap | 0.15 |
| W_{tl} | Transmission line width | 2.0 |
| R_1 | Outer SRR radius | 3.2 |
| R_2 | Inner SRR radius | 1.8 |
| w_r | Width of resonators | 0.6 |
| D | Separation of SRR | 0.8 |
| gr | Gap of resonators | 0.5 |

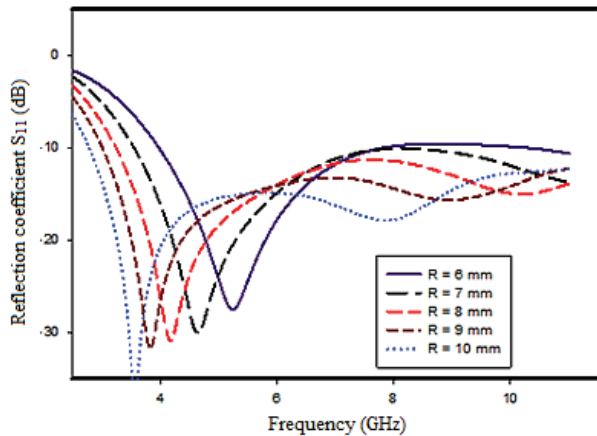


Fig. 4. Antenna reflection coefficient due to different radiating element radius “R”.

B. Integration of the SRR into UWB antenna

It is important to determine the optimum SRR location for maximum coupling between the SRR and the antenna to properly enable the desired band notch characteristics. Two SRRs are used to increase the notch bandwidth and ensure a symmetrical radiation pattern. Figure 5 shows the proposed SRRs locations; they are placed on each side of the radiating element.

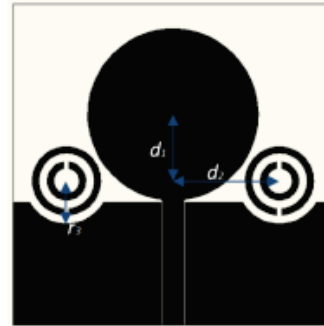
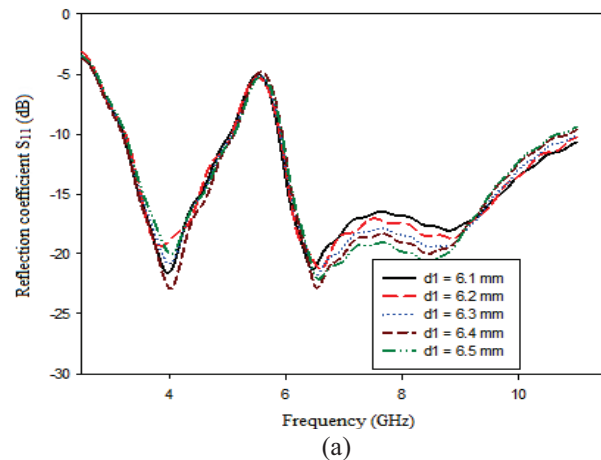


Fig. 5. Proposed SRRs location.

The optimal SRR locations are determined via a series of parametric studies. The first study concerns the location of the SRRs. Figure 6 (a) shows the reflection coefficient (S_{11}) of the proposed antenna when the distance between the SRRs and the center of the radiating element along the transmission line (y-axis), d_1 , is increased. It can be observed that this change has a minimal effect on the S_{11} . On the contrary, increasing the distance between the SRRs and the radiating element in x-axis, d_2 , shows a significant S_{11} degradation, see Fig. 6 (b). The optimum distance for the d_1 and d_2 are 6.2 mm and 10 mm, respectively. Areas where the SRR structures are overlapping with the antenna ground are removed using a semi-circular slot with a radius of $r_3 = 3.7$ mm from the center of SRRs. This ensures that the SRRs are not grounded.



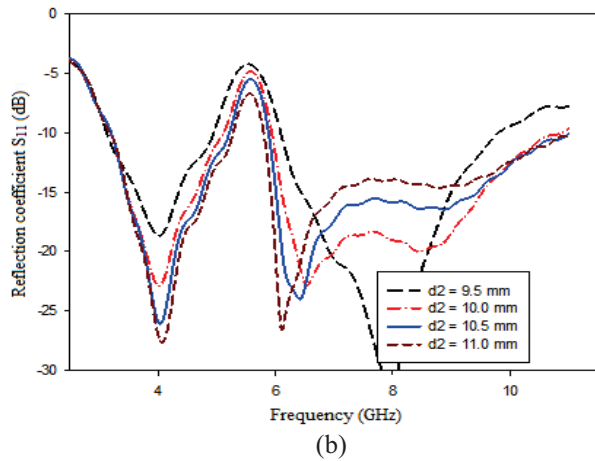


Fig. 6. Reflection coefficients: (a) due to the different distances of SRR in the y-axis “d1”, and (b) due to different distance of SRR in the x-axis “d2”.

The final antenna is then fabricated using a transparent conductive silver coated thin film (AgHT-8), as shown in Fig. 7 (a). Figure 7 (b) depicts the oxidation effect when the antenna is exposed to a high humid environment, which can be avoided by an additional tint film on top of the conductive layer.

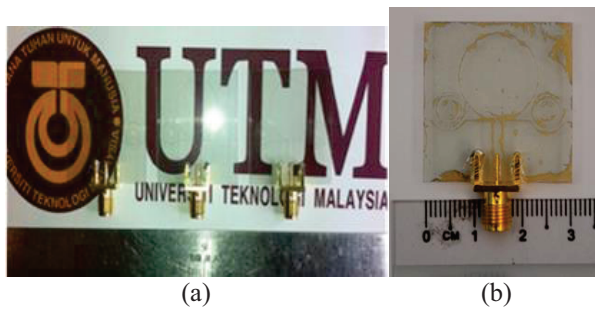


Fig. 7. Transparent UWB antenna with SRRs: (a) fabrication with low humidity environment exposure, and (b) after exposure to high humidity environment.

III. RESULTS AND DISCUSSION

Figure 8 shows the surface current distribution of the proposed antenna at 5.5 GHz. An evenly distributed surface current is observed at the circular edges of the radiating element when the SRRs are yet to be introduced (Fig. 8 (a)). The addition of the SRRs resulted in the high surface current concentration on the structures at 5.5 GHz, thus creating the reject band centered at this frequency.

Figure 9 shows the comparison between simulated and measured S_{11} for the antenna with and without the SRRs. The simulations indicated an operating frequency between 3.1 to 10.6 GHz, whereas the measurements are slightly shifted upwards, starting from 3.7 to more than 10.6 GHz. Simulations show that the antenna with SRRs

generated a notch band centered at 5.5 GHz with $S_{11} = -4.5$ dB, which attenuated signal reception/transmission by nearly 60%. Meanwhile, measurements performed on the same structure resulted in a band notch S_{11} of only -9 dB. These discrepancies may be caused by the high sheet resistance of the material, which restricted the current from properly exciting the SRRs, coherent with the report in [15-16]. Moreover, the narrow dimensions of the slots and rings may have also caused fabrication discrepancies [14].

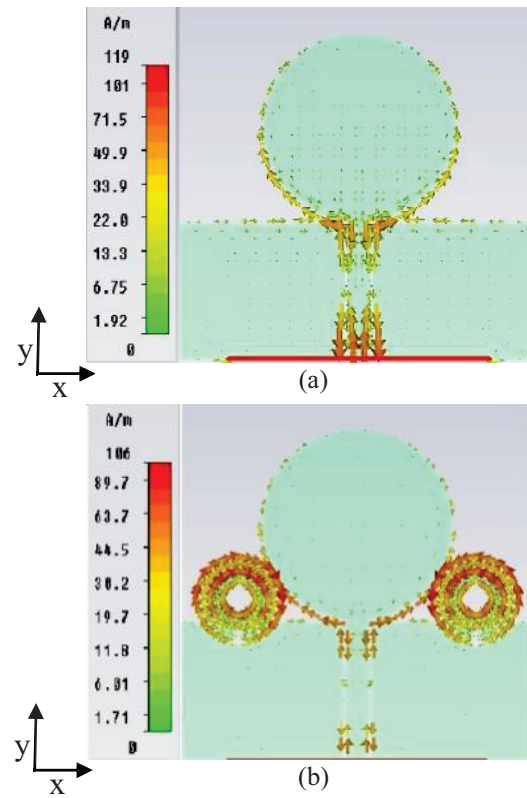


Fig. 8. Simulated surface currents at 5.5 GHz for the: (a) UWB antenna, and (b) UWB antenna with SRRs.

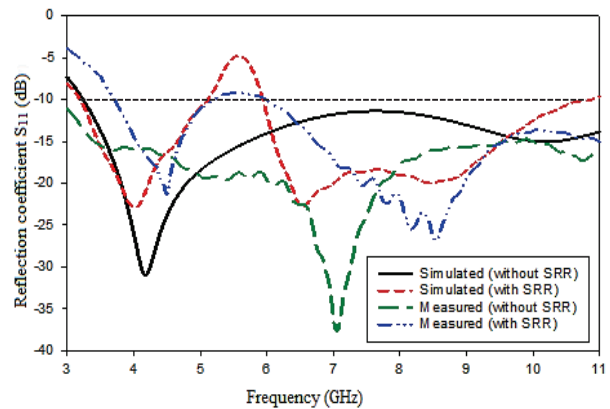
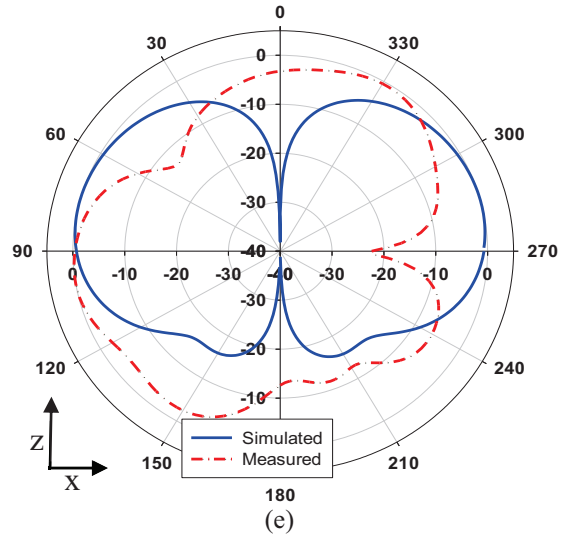
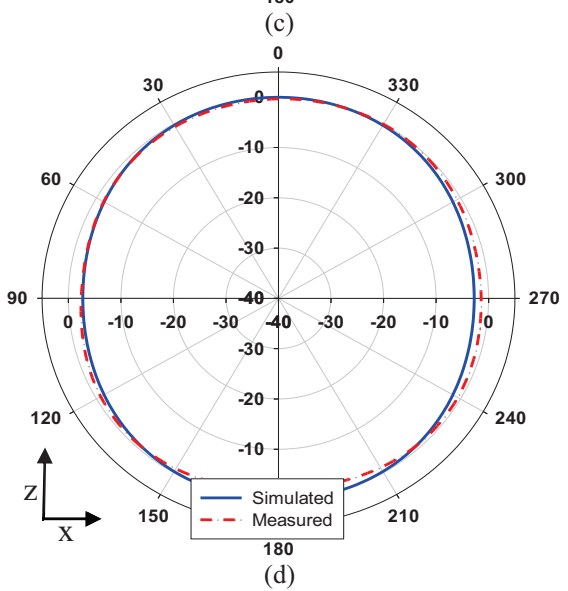
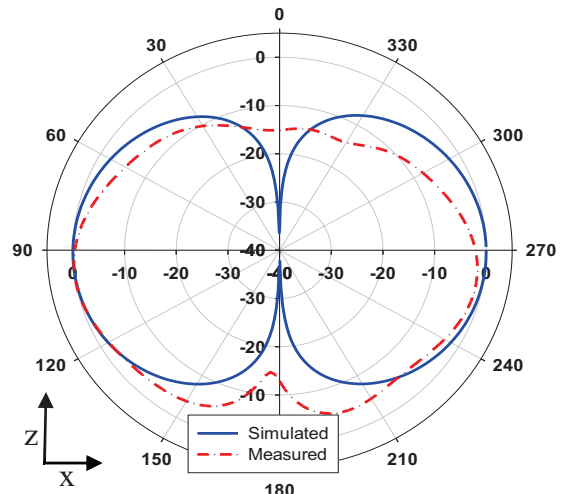
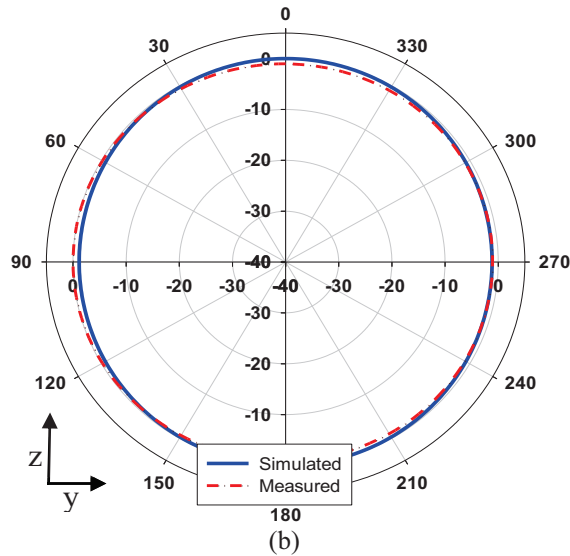
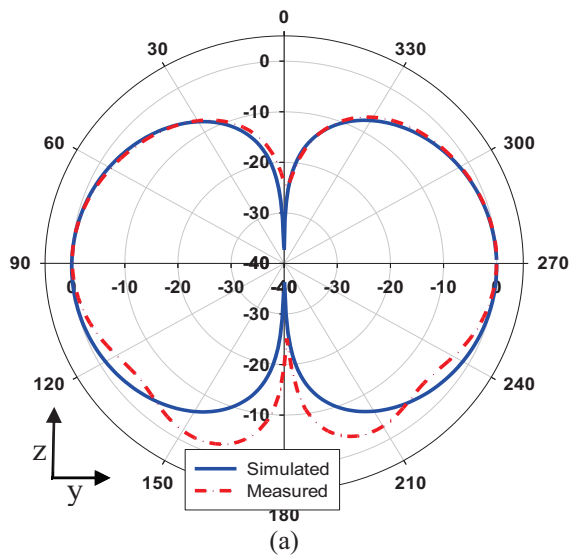


Fig. 9. Simulated and measured reflection coefficients.

Figure 10 illustrates the simulated and measured radiation patterns of the proposed antenna at 4, 7 and 10 GHz. The proposed antenna has a bi-directional radiation pattern at 4 GHz in the E-plane, and an omnidirectional pattern in the H-plane, see Figs. 10 (a) and 10 (b). The symmetrical radiation pattern is produced due to the implementation of two SRRs instead of a single SRR in comparison to [10]. At higher frequencies, the antenna produced slightly unsymmetrical and more directive radiation patterns, see Figs. 10 (c), 10 (d), 10 (e) and 10 (f). For instance, the antenna is pointing towards $\theta = 330^\circ$ in the y-z plane at 10 GHz, resulting in a gain increase towards this direction. Due to the high conductor losses at higher frequencies [14], a maximum gain of -5.0 dBi is obtained at 9.5 GHz.



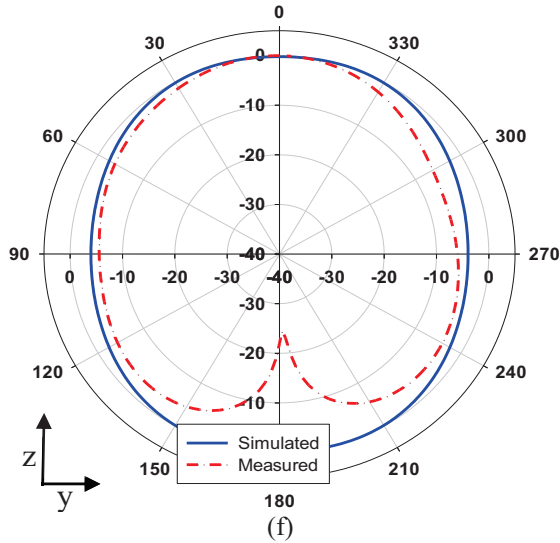


Fig. 10. Simulated and measured radiation patterns at: (a) 4 GHz (E-plane), (b) 4 GHz (H-plane), (c) 7 GHz (E-plane), (d) 7 GHz (H-plane), (e) 10 GHz (E-plane), and (f) 10 GHz (H-plane).

Figure 11 shows the measured gain of each antenna, where it can be seen that the highest gain achieved is only -5 dBi, which is comparable to [14]. There are 1.6 dB gain drops at 5.8 due to the implementation of the SRRs. This gain values are expected when using the thin film material because of its low conductivity, low electrical properties and the high losses of the conductive surface. The thin transmission line that has been used in this proposed design has the tendency to have higher losses according to [15]-[16]. However, this antenna is designed for UWB applications which only support short distance and high data rate transmission/reception such as near field communication; the gain of this antenna is still acceptable for practical implementation. The maximum efficiency of this antenna is 18%, which is comparable to the same notched transparent antenna designed in [14].

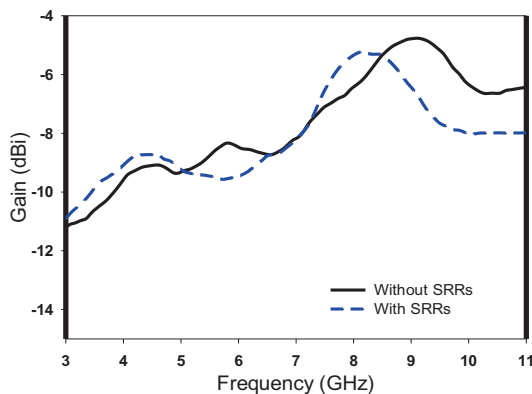


Fig. 11. Measured gain of proposed antenna with and without SRRs.

IV. CONCLUSION

A new optically transparent UWB antenna with band notch at 5.5 GHz is presented in this paper. Optical transparency is achieved by using conductive silver coated thin film (AgHT-8) and a polyethylene terephthalate (PET) substrate. The proposed antenna exhibits a band notch at 5.5 GHz by introducing a pair of SRR at both the sides of the radiating element. The proposed antenna operates with S_{11} better than -10 dB impedance bandwidth and bi-directional radiation pattern throughout the whole UWB band, except in the 5 to 6 GHz notch band. The antenna shows satisfactory agreement between simulated and measured results. The proposed transparent antenna is applicable for UWB home network (IEEE 1394) for green building applications. It enables high data rate multimedia transfer and simultaneously reduces space consumption due to its low profile and size. Moreover, due to its transparent property, it can also be deployed without compromising aesthetic values or users' noticing, especially for covert operations. Since this is a pulsed system, the lower gains in a limited higher frequency band will not severely affect its overall performance in real applications.

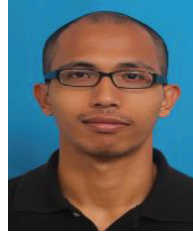
ACKNOWLEDGMENT

The authors would like to acknowledge and express sincere appreciation to the Ministry of Higher Education (MOHE) Malaysia for financing this project.

REFERENCES

- [1] R. Azim and M. T. Islam, "Compact planar UWB antenna with band notch characteristics for WLAN and DSRC," *Progress In Electromagnetics Research*, vol. 133, pp. 391-406, Nov. 2013.
- [2] F. D. Dahalan, S. K. B. A. Rahim, M. R. Hamid, M. Z. B. M. Nor, M. S. B. A. Rani, and P. S. Hall, "Archimedean spiral antenna with band-notched characteristics," *Progress In Electromagnetics Research C*, vol. 37, pp. 83-94, Jan. 2013.
- [3] S. R. Emadian, C. Ghobadi, and J. Nourinia, "A novel compact dual band-notched slot antenna for ultrawideband applications," *Microwave and Optical Technology Letter*, vol. 54, no. 6, pp. 1365-1368, June 2012.
- [4] M. Naser-Moghadasi, L. Asadpor, and B. S. Virdee, "Compact ultra-wideband slot antenna with band-notch property," *Microwave and Optical Technology Letter*, vol. 54, no. 8, pp. 1829-1832, Aug. 2012.
- [5] M. C. Tang, S. Xiao, T. Deng, D. Wang, J. Guan, B. Wang, and G. D. Ge, "Compact UWB antenna with multiple band-notches for WiMAX and WLAN," *IEEE Transactions on Antennas and Propagation*, vol. 59, no. 4, pp. 1372-1376, Apr. 2001.
- [6] X-J. Liao, H-C. Yang, N. Han, and Y. Li, "A semi-

- circle-shaped aperture UWB antenna with triple band-notched character,” *Journal of Electromagnetic Waves and Applications*, vol. 25, no. 2-3, pp. 257-266, 2011.
- [7] T-N. Chang and M-C. Wu, “Band-notched design for UWB antennas,” *IEEE Antennas Wireless Propagation Letters*, vol. 7, pp. 636-640, 2008.
- [8] J. Y. Deng, Y. Z. Yin, X. S. Ren, and Q. Z. Liu, “Study on a dual-band notched aperture UWB antenna using resonant strip and CSRR,” *Journal of Electromagnetic Waves and Applications*, vol. 23, no. 5-6, pp. 627-634, 2009.
- [9] J. Montero-de-Paz, E. Ugarte-Muñoz, F. J. Herraiz-Martínez, V. González-Posadas, L. E. García-Muñoz, and D. Segovia-Vargas, “Multifrequency self-diplexed single patch antennas loaded with split-ring-resonators,” *Progress in Electromagnetics Research*, vol. 113, pp. 47-66, 2011.
- [10] M. S. A. Rani, S. K. A. Rahim, H. Rezaie, F. D. Dahalan, M. I. Sabran, M. Z. M. Nor, and A. Zainal, “Directional UWB antenna with a parabolic ground structure and split ring resonator for a 5.8 GHz band notch,” *Journal of Electromagnetic Waves and Applications*, vol. 27, no. 1, Jan. 2013.
- [11] D-O. Kim, N-I. Jo, D-M. Choi, and C-Y. Kim, “Design of the ultra-wideband antenna with 5.2 GHz/5.8 GHz band rejection using rectangular split-ring resonators (SRRS) loading,” *Journal of Electromagnetic Waves and Applications*, vol. 23, no. 17-18, pp. 2503-2512, Apr. 2009.
- [12] R. Marques, F. Mesa, J. Martel, and F. Medina, “Comparative analysis of edge- and broadside-coupled split ring resonators for metamaterial design-theory and experiments,” *IEEE Transactions on Antennas and Propagation*, vol. 51, no. 10, pp. 2572-2581, Oct. 2003.
- [13] A. Katsounaros, Y. Hao, N. Collings, and W. A. Crossland, “Optically transparent antenna for ultra wide-band applications,” *3rd European Conference on Antennas and Propagation*, Berlin, Germany, pp. 1918-1921, 2009.
- [14] T. Peter, Y. Y. Sun, T. I. Yuk, H. F. AbuTarboush, R. Nilavalan, and S. W. Cheung, “Miniature transparent UWB antenna with tunable notch for green wireless applications,” *2011 International Workshop on Antenna Technology (iWAT)*, pp. 259-262, Mar. 7-9, 2011.
- [15] B. M. Levin, “Transparent antennas,” *2011 XVth International Seminar/Workshop on Direct and Inverse Problems of Electromagnetic and Acoustic Wave Theory (DIPED)*, pp. 101-104, Sep. 26-29, 2011.
- [16] B. Levin and M. Haridim, “Conical feed transparent antenna,” *2012 IEEE 27th Convention of Electrical & Electronics Engineers*, pp. 1-5, Nov. 14-17, 2012.
- [17] S. Ullah, M. Ali, M. A. Hussain, and K. S. Kwak, “Applications of UWB Technology,” *The 5th Annual International New Exploratory Technologies Conference 2008 (NEXT 2008)*, Turki, pp. 225-232, Aug. 2008.



Mohd Subri received his B.Eng. and Master degrees from Universiti Teknologi Malaysia (UTM). His research interests include antenna design, radio frequency and microwave devices.



Sharul Kamal Abdul Rahim received his first degree from University of Tennessee, USA majoring in Electrical Engineering, graduating in 1996, M.Sc. in Engineering (Communication Engineering) from Universiti Teknologi Malaysia (UTM) in 2001, and Ph.D. in Wireless Communication System from University of Birmingham, UK in 2007. Currently, he is an Associate Professor at Wireless Communication Centre, Faculty of Electrical Engineering, UTM. His research interest is Smart Antenna on Communication System.



Ping Jack Soh was born in Sabah, Malaysia. He received the B.Eng. and M.Eng. degrees in Electrical Engineering (Telecommunication) from Universiti Teknologi Malaysia (UTM) in 2002 and 2005, respectively, and the Ph.D. degree in Electrical Engineering from KU Leuven, Belgium in 2013. He is currently a Senior Lecturer at the School of Computer and Communication Engineering, and a Researcher in the Advanced Communication Engineering (ACE) CoE, Universiti Malaysia Perlis (UniMAP).



Bashir M. Saad received the B.S. degree in Electrical Engineering (with honors) from ATBU Bauchi in 2002, M.S. degree from BUK Kano in 2010 and is currently working toward the Ph.D. degree at the Universiti Teknologi Malaysia (UTM) under Assoc. Prof. Ir. Dr. Rahim. His research interests include microwave components

for beam forming networks and antenna design.



Mursyidul Idzam Sabran was born in Selangor, Malaysia. He obtained his degree in Electrical Engineering (Telecommunication) in 2009 and M.Sc. in Master of Engineering (Electrical) in 2012 from UTM Skudai, Johor Malaysia. He is currently a full-time Ph.D. Research

Student at the Wireless Communication Centre (WCC), Faculty of Electrical Engineering, Universiti Teknologi Malaysia (UTM), Johor, Malaysia.



Mohd Fairus Mohd Yusoff is a graduate faculty member of the Faculty of Electrical Engineering, University Technology Malaysia (UTM). He joined UTM in 2002 as a Tutor. He received his Bachelor in Engineering (Electrical-Telecommunication) in 2002 and Master of Electrical Engineering (Electrical - Electronics

and Telecommunications) in 2005 from University Technology Malaysia. He obtained his Ph.D. in 2012 from the University of Rennes 1, France in area of Signal Processing and Telecommunication. His main research interests and areas are antenna design, millimetre waves and microwave devices. To date he has written more than 20 papers, which have been published in national and international journals and conferences.

Transient Current Distribution and Force Analysis of Three Phase Enclosure Type GIB Based on Field-Circuit Coupling FEM Method

Xiangyu Guan *ACES Member*, Bing Kang, Naiqiu Shu, Qiangqiang Yan, and Zipin Li

Department of Electrical Engineering
Wuhan University, Wuhan, 430072, China
Lzpwu@163.com

Abstract — On the purpose of optimal design and online monitoring of three phase enclosure gas insulated bus (GIB), a 3-D circuit-field coupling FEM model has been developed. The current constriction effects in plug-in connectors are simulated by modeling contact bridges between contact surfaces and the influence of conductor gravity on contact resistance has been taken into account. The distributions of current which is constrained by external circuit are obtained from field-circuit coupling calculation and electromagnetic force, which is derived from electromagnetic field calculation, is used as load inputs in mechanical field analysis. The validity of calculation model is demonstrated by comparing with vibration experiments. The dynamic current distribution and electromagnetic force behaviors of three phase enclosure GIB under steady state and different short circuit conditions have been analyzed using the calculation model. Analysis results show that the uneven heating of contact fingers due to current distributions under steady state and contact fingers with smaller contact forces are seriously ablated by large short currents under short circuit conditions, and are the main contact degradation mechanism of plug-in connector. Conductor electromagnetic forces under single phase short circuit condition are larger than those of two phase and three phase short circuit conditions and the electromagnetic force peak moments under different fault conditions are not the same.

Index Terms — Current distribution, electromagnetic force, field-circuit coupling, finite element method (FEM), GIB, plug-in connector, short circuit.

I. INTRODUCTION

The three-phase enclosure type gas insulate bus (GIB) with the compact design by sealing the three phase conductors in a single metal tank filled with SF₆ gas has the advantages of land saving and high reliability [1]. During equipment operation, eddy currents in tank are induced by the alternating electromagnetic field which is induced by the conductor currents, and uneven electromagnetic forces are produced by the

interaction between current carriers and alternating electromagnetic field. The current distributions will cause uneven heating sources especially on plug-in connectors due to the existence of contact resistance and overheating fault may happen [2]. The electromagnetic forces can cause mechanical vibration of conductors and tank, and the contact force of connectors will decrease because of the existence of electromagnetic repulsion force between contact surfaces. Inadequate short-circuit strength may lead to a mechanical collapse of connectors and a damage of insulators when the large short circuit current flows through the device. So current distributions and electromagnetic force of GIB under normal and short circuit currents are key problems in equipment design and maintenance [3].

The image current method [4] is used to calculate the short circuit electromagnetic force in three phase enclosure type GIB [5], and the vibration of GIB is analyzed by assuming metal tank as thin cylindrical shell and the conductors as a transverse beam [6-7]. These methods are easy to formulate and fast to solve, however, the distributions of current and electromagnetic force of GIB are not uniform due to skin effect and proximity effect; these complex field patterns cannot be captured by using lumped parameter models, and numerical modeling techniques are established to represent these important phenomena occurring inside GIB [8-10]. There are two following main deficiencies existing in current numerical models of GIB. First, plug-in connectors are not included so the electro repulsion force [11-12] and current distributions in plug-in connector cannot be considered. Second, nonlinear transient current and electromagnetic field of GIB are constrained by external circuit, thus belonging to the typical field-circuit coupling problem [13-17].

The time-varying electromagnetic force of three phase enclosure GIS based on contact bridge model has been introduced in our previous work [18]. Focus on the current and force distributions in GIB under normal and short circuit conditions, a 3-D field-circuit coupling FEM model of three phase enclosure type GIB is developed. The structure of the GIB is shown in Fig. 1.

Three phase conductors are fixed with disc-type insulators, the plug-in connectors containing 16 contact fingers arranged clockwise around the center conductor axis are used to eliminate the influence of thermal stress on insulators. An acceleration sensor (A1) placed on tank is used to measure the vibration of tank. Assumptions about the calculation model are as follows:

- The working current frequency is 50 Hz, so the electromagnetic field calculation model is based on the quasi-static approximation.
- The variation in electric field cannot influence magnetic field. To be clear, some parts chamfers which are used to improve electric field have been neglected for the simplicity of calculation.
- The influence of conductor and tank deformation on the electromagnetic field distribution is neglected.
- Though there is a difference between mechanical and electrical contact area, only mechanical contact area is considered for the chemical stability of SF₆ gas.
- The springs of connector are neglected.
- The nonlinearity of the material and the displacement current are neglected.

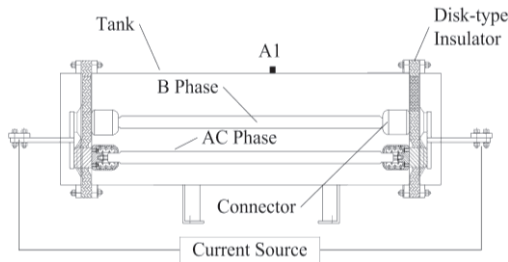


Fig. 1. Schematic structure of three phase enclosure type GIB.

II. ANALYSIS METHOD

A. Solution regions and boundary conditions

The solution region and boundary conditions of the field-circuit coupling model are shown in Fig. 2. The solution region contains circuit region which is excited by three-phase voltage source, and FEM region which is connected with extern circuit by coupling node voltage sources. The tank surrounded by air is filled with SF₆ gas and the eddy currents which are induced by the time-varying conductor currents flowing through it.

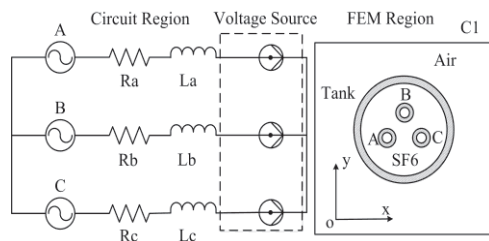


Fig. 2. Solution regions and boundary conditions.

B. Contact bridge model

The contact resistance and the electromagnetic repulsion force exist between bus connectors and contact fingers due to current constriction effect in the contact interface. A contact bridge model which takes into account the influence of conductor gravity has been developed (Fig. 3). The height of contact bridge is 0.2 mm and the radius of contact bridge can be calculated as the Hertz formula [19]:

$$a = (3F_j R^* / 4E^*)^{1/3}, \quad (1)$$

where a is the contact bridge radius, F_j is the contact force of one contact finger which is influenced by the spring holding force and the normal component of conductor gravity.

The equivalent contact radius R^* is illustrated in Fig. 3, and the equivalent Young's modulus E^* of plug-in connector can be described as:

$$1/E^* = [(1-\nu_1^2)/E_1 + (1-\nu_2^2)/E_2], \quad (2)$$

where E_1 , E_2 are Young's modulus of conductor and contact finger, ν_1 , ν_2 are Poisson's ratio of conductor and contact finger. All these parameters can be obtained from special GIS bus bar capsule design.

The one finger contact force of plug-in connector exerted by three circular holding springs and the normal component of conductor gravity can be calculated as:

$$F_j = 3K\pi^2(D_1 - D_0)/n - G_n, \quad (3)$$

where K is the spring stiffness coefficient, π is the circular constant, n is the number of fingers and $n=16$, D_0 and D_1 are the diameters of the spring center line before and after loading respectively. G_n is the normal component of conductor gravity exerting on one contact finger.

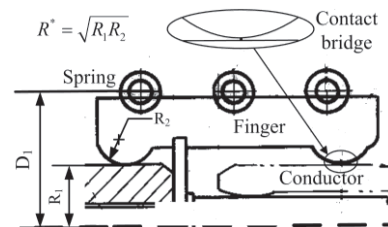


Fig. 3. Contact bridge between plug-in connector and conductor.

C. Calculation method

The flow chart for solving the coupled fields of GIB is shown in Fig. 4. The electromagnetic field of GIB and extern circuit are connected to each other by the coupling node voltage sources. A sequentially coupling method is used to simulate the interactions between electromagnetic and mechanical fields. The initial conditions such as contact forces and contact bridge radiuses are calculated from single mechanical analysis without load currents. New contact force can be obtained from mechanical field analysis which uses

nodal electromagnetic forces as load inputs and the contact radius should be changed. Such process is conducted until the contact radius converged.

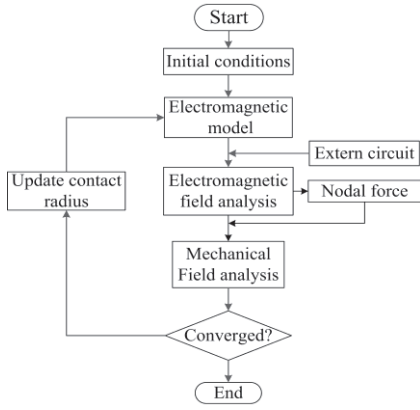


Fig. 4. Flow chart of field-circuit coupling calculation process.

III. FIELD-CIRCUIT COUPLING ANALYSIS

A. Electromagnetic field analysis

The quasi-static approximation can be used since steady state AC flows in the bus conductor.

With the magnetic vector potential \mathbf{A} , the Maxwell's equations can be rewritten as:

$$\left. \begin{aligned} \nabla \times \mathbf{H} &= \mathbf{J} \\ \nabla \times \mathbf{E} &= -\frac{\partial \mathbf{B}}{\partial t} \\ \mathbf{B} &= \nabla \times \mathbf{A} \end{aligned} \right\} \quad (4)$$

The governing equation of electromagnetic field (4) can be derived as:

$$\nabla \times \mu(\nabla \times \mathbf{A}) = \mathbf{J}, \quad (5)$$

where μ is magnetic permeability.

The governing Equation (5) can be rewritten as the form of Poisson's Equation (8) by using the vector Equation (6) and the Coulomb's gauge (7):

$$\nabla \times (\nabla \times \mathbf{A}) = \nabla(\nabla \cdot \mathbf{A}) - \nabla^2 \mathbf{A}, \quad (6)$$

$$\nabla \cdot \mathbf{A} = 0, \quad (7)$$

$$\nabla^2 \mathbf{A} = -\mu \mathbf{J}, \quad (8)$$

where the total current \mathbf{J} consists of the source current \mathbf{J}_s and the eddy current \mathbf{J}_e , that is:

$$\mathbf{J} = \mathbf{J}_s + \mathbf{J}_e. \quad (9)$$

The voltage drop of conductor (coupling node voltage source) which is the key to combining the extern circuit with FEM model can be calculated:

$$V_{drop} = \int_V c_i \left(-\frac{\partial \mathbf{A}}{\partial t}\right) dV, \quad (10)$$

where V is the conductor volume, c_i is the loop coefficient, $c_i=1$ if conductor inside loop i , otherwise $c_i=0$.

The eddy current in the conducting material is:

$$\mathbf{J}_e = \sigma \mathbf{E} = -\sigma \frac{\partial \mathbf{A}}{\partial t}, \quad (11)$$

where σ is electrical conductivity.

The boundary conditions of electromagnetic field are as follows:

$$\mathbf{A}|_{C_1} = 0, \quad (12)$$

$$\left. \begin{aligned} \mathbf{A}_1 &= \mathbf{A}_2 \\ \mu_1 \nabla \times \mathbf{A}_1 \cdot \mathbf{n}_{12} &= \mu_2 \nabla \times \mathbf{A}_2 \cdot \mathbf{n}_{12} \\ n \cdot (-j\omega \varepsilon \mathbf{A} - \varepsilon \nabla \phi) &= 0 \end{aligned} \right\} \text{ in } S, \quad (13)$$

where C_1 is the boundary of FEM region, S is the boundary of conductor material and no current regions (gas), ε is dielectric constant of conductor material.

B. Extern circuit analysis

According to the Kirchoff's voltage law (KVL), the extern circuit equation can be expressed as:

$$U = RI + L \frac{dI}{dt} + G \frac{d\mathbf{A}}{dt}, \quad (14)$$

where R is the total resistance which consists of line resistance and load resistance, L is the total inductance, G is a matrix which depends on the geometrical features of the GIB. I is the node current matrix, \mathbf{A} is the node magnetic vector matrix, U is the external voltage matrix. Three-phase voltage under symmetric power frequency can be represented as follows:

$$\left. \begin{aligned} u_A &= \sqrt{2}U \cos(\omega t + 0^\circ) \\ u_B &= \sqrt{2}U \cos(\omega t - 120^\circ) \\ u_C &= \sqrt{2}U \cos(\omega t + 120^\circ) \end{aligned} \right\} \quad (15)$$

C. Electromagnetic field-circuit coupling analysis

The global field-circuit coupling equations can be written as:

$$\begin{bmatrix} 0 & 0 \\ G & L \end{bmatrix} \frac{\partial}{\partial t} \begin{Bmatrix} \mathbf{A} \\ \mathbf{I} \end{Bmatrix} + \begin{bmatrix} K_e & D \\ 0 & R \end{bmatrix} \begin{Bmatrix} \mathbf{A} \\ \mathbf{I} \end{Bmatrix} = \begin{Bmatrix} 0 \\ U \end{Bmatrix}, \quad (16)$$

where K_e is the stiffness matrix of magnetic vector potential, D is the loading matrix. K_e and D can be obtained by the finite element analysis.

A backward time stepping scheme is used for the time discretization and the minimum time step is set to 0.3ms in order to simulate the transient process of alternating electromagnetic field:

$$\left\{ \frac{\partial \mathbf{A}}{\partial t} \right\}^{t+\Delta t} = \frac{\mathbf{A}^{t+\Delta t} - \mathbf{A}^t}{\Delta t}, \quad (17)$$

$$\left\{ \frac{\partial \mathbf{I}}{\partial t} \right\}^{t+\Delta t} = \frac{\mathbf{I}^{t+\Delta t} - \mathbf{I}^t}{\Delta t}. \quad (18)$$

D. Electromagnetic forces

The electromagnetic forces of three phase enclosure type GIB which induced by the interaction between

current carriers and alternating magnetic field caused by current carriers can be expressed as:

$$\mathbf{F} = \int_V \mathbf{J} \times \mathbf{B} dV. \quad (19)$$

IV. MECHANICAL ANALYSIS

The mechanical vibration of three phase enclosed type GIB during operation can be induced by the altering electromagnetic force. The mechanical governing equation coupled with electromagnetic force can be written as:

$$[M][\ddot{\mathbf{u}}] + [K][\mathbf{u}] = [\mathbf{F}_e], \quad (20)$$

where M is the mass matrix, K is the stiffness matrix, \mathbf{u} is the nodal displacement vector matrix and $\ddot{\mathbf{u}}$ is the nodal acceleration vector matrix. \mathbf{F}_e is the nodal force vector matrix which includes electromagnetic force and conductor gravity.

The boundary conditions of mechanical field can be expressed as follows.

Conductors are supported by the two ending plug-in connectors and the aluminum alloy tank is fixed on the ground through the bracket.

In order to resist the impact of short circuit current, plug-in connectors of GIB have positioning design which allows the contact fingers referring only to radial freedom (direction of contact force) and without axial freedom.

V. CALCULATION MODEL

A 3-D FEM model of three phase enclosure GIB has been developed for the multi-physics calculation. The material and geometrical properties are shown in Table 1. The line inductance (67 mH) and the line resistance (1.5 Ω) which get from one 220 kV gas insulated substation in China Southern Power Grid Company.

16 pieces of contact fingers are arranged clockwise in the xoy coordinate plane, and the gravity acceleration is along the $-y$ direction. Using the mechanical analysis, the initial contact forces between each contact spot deriving from the contact spring and the gravity of conductors are shown in Fig. 5 (a), and the contact bridge radiuses of each contact fingers can also be calculated (Fig. 5 (b)), which indicates that the contact forces and the contact radiuses increase from upper contact fingers to lower ones for the action of conductor gravity.

Table 1: Simulation model parameters

| | |
|--------------------|------------------------|
| Tank Material | Aluminum alloy 6063-T6 |
| Finger Material | Copper T2Y |
| Finger Number | 16 |
| Shield Material | Aluminum alloy 6063-T6 |
| Bus Material | Aluminum alloy 6063-T6 |
| Insulator Material | Epoxy resin |
| Tank Size | $\Phi 596/\Phi 580$ |
| Bus Size | $\Phi 90/\Phi 60$ |
| Span | 2300 mm |

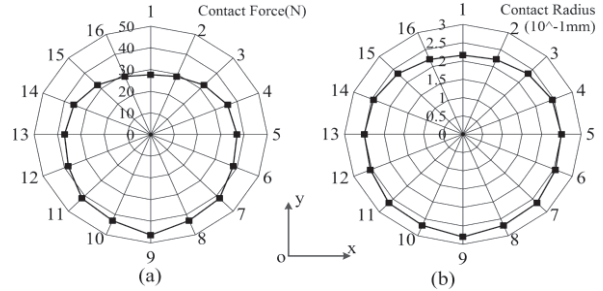


Fig. 5. Initial conditions of contact force and contact bridge radius versus contact fingers: (a) contact force, and (b) contact bridge radius.

VI. STEADY-STATE FIELD ANALYSIS

Using the field-circuit coupling FEM calculation model, the current density, electromagnetic force and tank vibration characters under steady-state are calculated. The validity of calculation model is demonstrated by vibration experiments.

A. Field distributions

The current density distributions of conductors and tank at $t=5$ ms (peak time of A phase current) under normal load current (1000A) are shown in Fig. 6 (a). It can be seen from current distribution results that the current densities in conductors and tank are not uniform due to proximity effect and eddy effect. Current distributions of different contact fingers are strongly influenced by the interactions between different phase conductor currents (Fig. 6 (b) and Fig. 6 (c)). From calculation results we can deduce one contact failure mechanism of three phase enclosure type GIB under steady state is that the contact finger fevers vary each other due to the uneven current distributions between different contact fingers; some contact fingers where larger currents flow through may cause overheating and failure first, other contact fingers then overheating due to the load current increasing with fewer contact fingers and eventually caused the whole connector failure.

The nodal electromagnetic forces of conductors and tank at $t=5$ ms (peak time of A phase current) under normal load current (1000A) are shown in Fig. 6 (d). Distributions of electromagnetic forces in conductors and tank are influenced by the distributions of currents and the nodal electromagnetic forces of A phase conductor and corresponding tank part are larger than other parts of GIB. The distributions of electromagnetic forces in different contact fingers are similar to current distributions (Fig. 6 (e) and Fig. 6 (f)) and the electromagnetic force of individual contact finger under normal load current is rather small compared with contact force (about 37N). So the main factor affecting the stability of GIB connector under normal operation conditions refers to the uneven heating of contact fingers rather than the action of electromagnetic force.

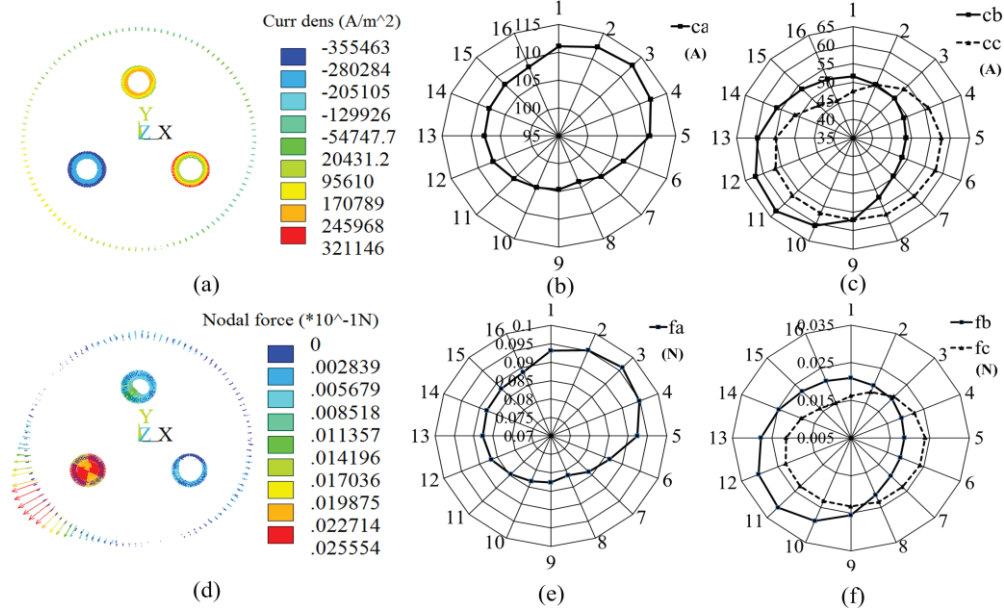


Fig. 6. Electromagnetic field distribution at $t=5\text{ms}$: (a) current density distributions, (b,c) absolute values of contact finger currents, (d) electromagnetic force distributions, and (e,f) contact finger electromagnetic forces.

B. Tank vibration under normal operation

In order to qualitatively validate the numerical results, vibration tests have been performed on a three phase enclosure type GIB capsule (Fig. 1). Tank vibration results obtained from calculation model and vibration test under AC steady state (1000A) show good agreement in Fig. 7. It can be seen from the results that vibration of tank under AC steady state mainly consists of electromagnetic vibration with 2 times of power frequency and the vibration amplitude is small (0.2 mm).

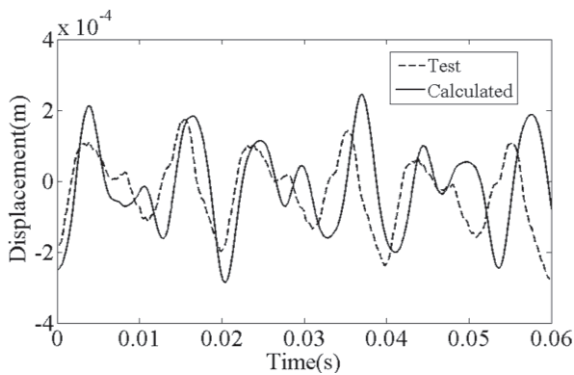


Fig. 7. Time varying curve of tank vibration under AC steady state.

VII. ELECTROMAGNETIC FORCE UNDER SHORT CIRCUIT CONDITIONS

The three phase enclosure type GIB will carry full short-circuit currents of the power system since it is a

series device. Larger power losses and electromagnetic forces may be induced by considerable short circuit currents. The short electromagnetic forces under different short circuit conditions are essential for analyzing the short circuit withstand capability of GIB. The line resistance and line inductance of external circuit are used to simulate the short circuit fault and the distributions of electromagnetic force are computed at the first peak of the B phase short-circuit current (6.7ms).

A. Distributions of short circuit electromagnetic force of conductors and tank

The electromagnetic force distributions of conductors and tank at $t=6.7\text{ms}$ (first peak time of B phase short current) under different short circuit conditions are shown in Fig. 8. It can be seen from the results that the electromagnetic force in conductors where short circuit fault happened is larger than other conductors. The distributions of electromagnetic force are influenced by the short circuit fault types and conductor space arrangement of GIB. During single B short circuit fault, the x-direction force component of B phase conductor is very small and the conductor vibration mainly along the vertical y-direction, the direction of short circuit electromagnetic force and vibration of tank are opposite to the conductor. During BC short circuit fault the short circuit electromagnetic forces are mainly distributed in the BC phase conductor and the tank short circuit electromagnetic force appears on the right half part which direction to BC phase conductors. During three-phase short circuit fault the short circuit electromagnetic force distributions of the conductor are the same as the

steady state condition which depend on the instantaneous values of short currents, and the short circuit electromagnetic force of tank rightly direct to the three phase conductors. Therefore 3 acceleration sensors

which are arranged on the tank of three phase conductors direction can be used for short circuit location of three phase enclosure GIB according to our analysis.

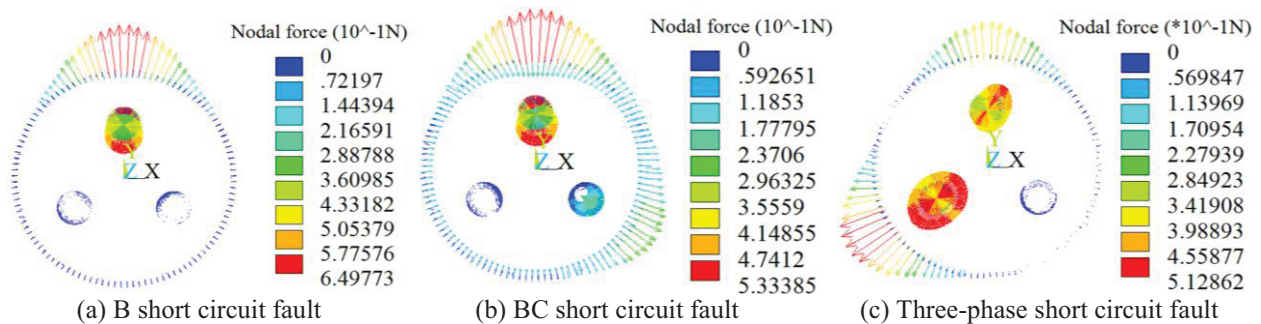


Fig. 8. Electromagnetic force of conductors and tank under different short circuit conditions at t=6.7ms.

B. Distributions of short circuit electromagnetic force of plug-in connector

The electromagnetic force distributions of contact fingers at t=6.7ms (peak time of B phase short current) under different short circuit conditions are shown in Fig. 9. Electromagnetic forces of A phase contact fingers and C phase contact fingers are influenced by the B phase conductor where short circuit current flows and the force amplitudes are rather small during single B phase short circuit fault, and the electromagnetic forces of B phase contact fingers are mainly influenced by the contact finger current distributions which are caused by conductor gravity. During BC short circuit fault the electromagnetic forces of B phase contact fingers and C phase contact fingers are strongly interacted with each other, whereas the conductor gravities have little influence on electromagnetic force distributions and the force amplitudes of B phase contact fingers are smaller than those of single phase short circuit fault. During three-phase short circuit fault the distributions of electromagnetic forces in different contact fingers are influenced by the instantaneous values of short currents which strongly interact with each other, and the force amplitudes of B contact fingers are smaller than those of single phase and BC short faults; the conductor gravities also have little influence on electromagnetic force distributions as BC short condition. Electromagnetic forces in contact fingers can reduce the contact force which is exerted by the holding springs and cause the transient contact degradation as mentioned in our previous work [18]. From analysis results in this work, it can be seen that the distributions of electromagnetic force in individual contact finger are influenced by the short circuit conditions, and some contact fingers with smaller contact forces may be seriously ablated by large short currents.

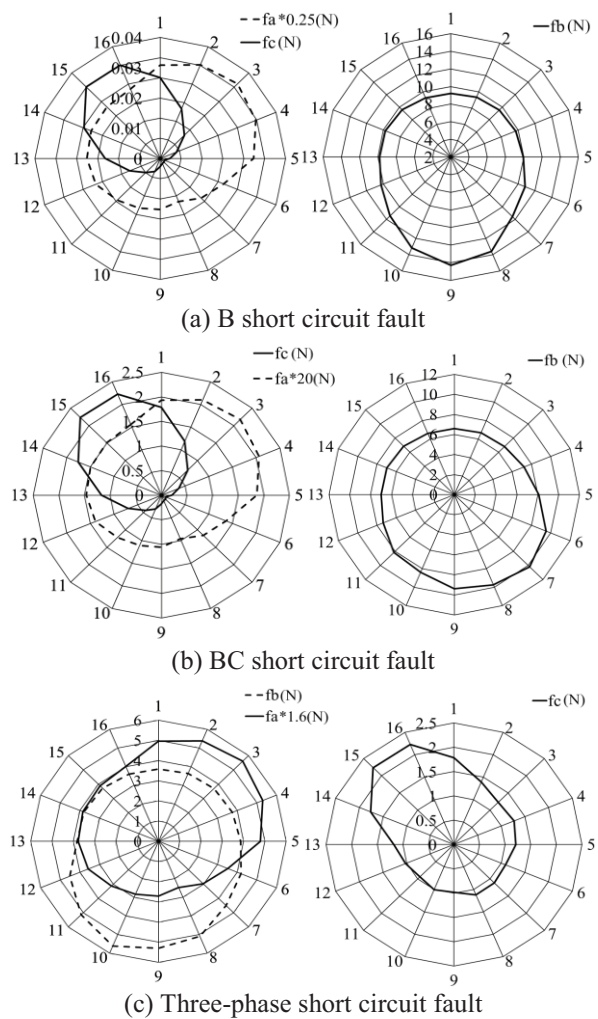


Fig. 9. Electromagnetic forces of plug-in connectors under different short circuit conditions at time=6.7ms.

C. Transient short circuit electromagnetic forces characters of conductor and tank

The transient electromagnetic force characteristics of B phase conductor and tank under different short circuit fault conditions are shown in Fig. 10 - Fig. 12. Transient short circuit electromagnetic forces of conductor and tank present space asymmetric vibration characteristics with fault time. Electromagnetic force amplitudes of B phase conductor and tank under single B phase short circuit fault are larger than those of two phase and three-phase short circuit faults according with the results described in [5]. The peak electromagnetic force moments under different short circuit conditions are not the same, and the moments of single B phase short circuit fault are earlier than those of BC short circuit and three short circuit faults.

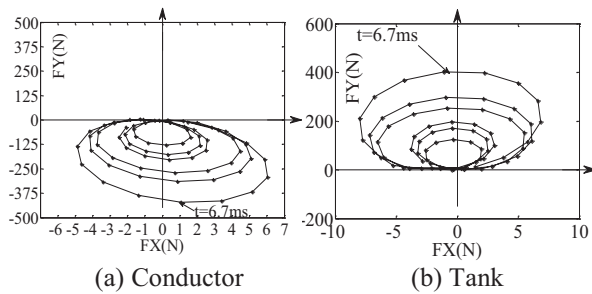


Fig. 10. Transient electromagnetic forces of B phase conductor and tank under B short circuit fault.

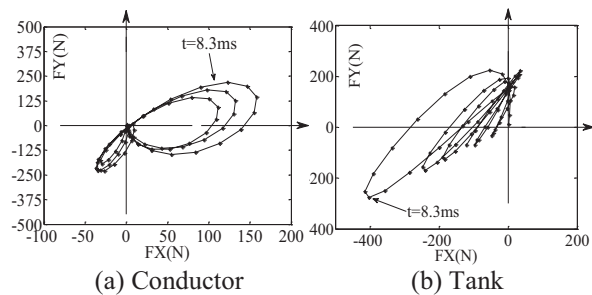


Fig. 11. Transient electromagnetic forces of B phase conductor and tank under BC short circuit fault.

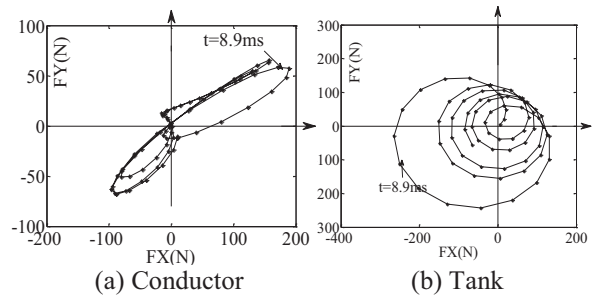


Fig. 12. Transient electromagnetic forces of B phase conductor and tank under three-short circuit fault.

The contact stability of three phase enclosure GIB capsule in which the conductors are supported only by two end plug-in connectors under short conditions must be taken into account seriously for the reason that large conductor electromagnetic forces (nearly 400N) together with repulsive forces between contact fingers will directly act on the plug-in connectors, which could cause serious contact degradation, even some contact fingers will lose contact and the whole connector may be damaged. Reliable contact finger positioning design which can withstand the short circuit impact is very important.

VIII. CONCLUSION

The current distribution and electromagnetic force calculation are essential for analyzing the contact degradation mechanism and the short circuit withstand capability of three phase enclosure type GIB capsule. Taking into account the distributions of contact force and the current constriction effect on the plug-in connectors, a 3-D circuit-field coupling FEM model has been developed for analyzing the dynamic current distributions and electromagnetic forces behaviors of three phase enclosure type GIB under steady state and different short circuit conditions. The validity of calculation model is demonstrated by vibration experiments and the following findings can be derived from this study.

The current distributions in the conductors and tank are not uniform because of skin effect and proximity effect. The current distributions in plug-in connectors are strongly influenced by the interactions between different phase conductor currents. Uneven temperature rise will be induced by the current distributions and some contact fingers can be overheating, leading to contact degradation.

The electromagnetic force and mechanical vibration of three phase enclosure GIB are relative small under steady state. However relatively large electromagnetic force can be exerted on them due to sharp increase of short circuit current and the distributions of electromagnetic force are directly influenced by the current distributions and conductor gravity. Electromagnetic force of individual contact finger is influenced by the short circuit conditions, contact forces of some contact fingers may decrease, even lost by the action of repulsive force and conductor electromagnetic force, some contact fingers with smaller contact force may be seriously ablated by large short currents. Electromagnetic forces of conductor and tank under single phase short circuit fault are larger than those of two phase and three-phase short circuit faults and the peak electromagnetic moments under different fault conditions are not the same. The results obtained by field-circuit coupling analysis can be used to optimal design and online monitoring of three phase

enclosure type GIB.

ACKNOWLEDGEMENT

This work was supported by the Fundamental Research Funds for the China Central Universities (2012207020208).

REFERENCES

- [1] A. H. Cookson and C. S. Cleale, "Three-conductor compressed gas cable optimization," *EPRI Project 7840 Final Report*, Feb. 1979.
- [2] Y. Mukaiyama, I. Takagi, K. Izumi, T. Sekiguch, A. Kobayashi, and T. Sumikawa. "Investigation on abnormal phenomena of contacts using disconnecting switch and detachable bus in 300kV GIS," *IEEE Trans. Power Delivery*, vol. 5, no. 1, pp. 189-195, 1990.
- [3] A. E. Emanuel, H. C. Doepken, and P. C. Bolin, "Design and test of a sliding plug-in conductor connector for compressed gas-insulated cables," *IEEE Trans. Power Apparatus and Systems*, vol. 95, no. 2, pp. 570-579, 1976.
- [4] A. G. Kladas, M. P. Papadopoulos, and J. A. Tegopoulos, "Leakage flux and force calculation on power transformer windings under short-circuit: 2D and 3D models based on the theory of images and the finite element method compared to measurements," *IEEE Trans. Magnetics*, vol. 36, no. 4, pp. 3487-3490, 1994.
- [5] H. Hama, T. Marutani, K. Takatsuka, T. Nitta, and T. Tanabe, "Characteristics of short circuit electromagnetic forces in three phase enclosure type gas insulated bus," *IEEE Trans. Power Delivery*, vol. PWRD-2, no. 2, pp. 367-373, 1987.
- [6] S. Tominaga, H. Mukae, S. Matsuda, N. Okutsu, and Y. Takahashi, "Dynamic behavior of metal enclosures for gas insulated substations during ground faults and their immediate location by mechanical means," *IEEE Trans. Power Apparatus and Systems*, vol. PAS-98, no. 4, pp. 1283-1290, 1979.
- [7] Y. Kanno, T. Amemiya, N. Takahashi, and N. Kobayahi, "The short circuit electromagnetic force of the three-phase encapsulated gas insulated busbar," *IEEE Trans. Power Apparatus and Systems*, vol. PAS-103, no. 6, pp. 1386-1393, 1984.
- [8] H-K. Kim, J-K. Jung, K-Y. Park, C-H. Im, and H-K. Jung, "Efficient technique for 3-D finite element analysis of skin effect in current-carrying conductors," *IEEE Trans. Magnetics*, vol. 40, no. 2, pp. 1326-1329, 2004.
- [9] T. Takeuchi, T. Yoshizawa, and Y. Kuse, "3-D nonlinear transient electromagnetic analysis of short circuit electromagnetic forces in a three-phase enclosure-type gas insulated bus," *IEEE Trans. Magnetics*, vol. 36, no. 4, pp. 1754-1757, 2000.
- [10] D. Labirdis and V. Hatzianthassiou, "Finite element computation of field, forces and inductances in underground SF6 insulated cables using a coupled magneto-thermal formulation," *IEEE Trans. Magnetics*, vol. 30, no. 4, pp. 1407-1415, 1994.
- [11] S. Ito, Y. Takato, Y. Kawase, and T. Ota, "Numerical analysis of electromagnetic forces in low voltage ac circuit breakers using 3-D finite element method taking into account eddy currents," *IEEE Trans. Magnetics*, vol. 34, no. 5, pp. 2597-2600, 1998.
- [12] K. Yoshihiro, M. Hiroyuki, and I. Shokichi, "3-D finite element analysis of electro-dynamic repulsion forces in stationary electric contacts taking into account asymmetric shape," *IEEE Trans. Magnetics*, vol. 33, no. 2, pp. 1994-1999, 1997.
- [13] G. Bedrosian, "A new method for coupling finite element field solutions with external circuits and kinematics," *IEEE Trans. Magnetics*, vol. 29, no. 2, pp. 1664-1668, 1993.
- [14] M. R. Shah, G. Bedrosian, and J. Joseph, "Steady-state loss and short-circuit force analysis of a three-phase bus using a coupled finite element + circuit approach," *IEEE Trans. Energy Conversion*, vol. 14, no. 4, pp. 1485-1489, 1999.
- [15] J. Weiss and V. K. Jarg, "Steady state eddy current analysis in multiply-excited magnetic systems with arbitrary terminal conditions," *IEEE Trans. Magnetics*, vol. 24, no. 6, pp. 2676-2678, 1988.
- [16] G. B. Kumbhar and S. V. Kulkarni, "Analysis of short-circuit performance of split-winding transformer using coupled field-circuit approach," *IEEE Trans. Power Delivery*, vol. 22, no. 2, pp. 936-943, 2007.
- [17] M. van der Giet, E. Lange, D. A. P. Corrêa, I. E. Chabu, S. I. Nabeta, and K. Hameyer, "Acoustic simulation of a special switched reluctance drive by means of field-circuit coupling and multi-physics simulation," *IEEE Trans. Industrial Electronics*, vol. 57, no. 9, pp. 2946-2953, 2010.
- [18] X. Guan and N. Shu, "Electromagnetic field and force analysis of three-phase enclosure type GIS bus capsule," *Applied Computational Electromagnetics Society Journal*, vol. 29, no. 8, pp. 582-589, 2014.
- [19] R. Holm, *Electric Contacts: Theory and Applications*, Springer, New York, 1979.



Xiangyu Guan received the B.S. degree in Environmental Science from Xinjiang Normal University, China, in 2010 and the M.S. degree in Power Electronics from Wuhan University, Hubei, China, in 2012. He is a Ph.D. candidate in Electrical Engineering College Wuhan University. He is Members of ACES and ICS, his research interests mainly focus on numerical methods of field calculation and condition monitoring of electrical equipment.

Bing Kang received the B.S. degree in Electrical Engineering from Beijing Institute of Petrochemical Technology, China, in 2010 and the M.S. degree in Electrical Engineering from Wuhan University, Hubei, China, in 2012. He is currently a Ph.D. candidate in School of Electrical Engineering Wuhan University. His research interest includes transient overvoltage and electromagnetic transient in power system.

Naiqiu Shu is a Professor in Electrical Engineering College Wuhan University. He received his M.S. and Ph.D. degrees in Electrical Engineering College Wuhan University. His research interests mainly focus on sensor technology and condition monitoring of electrical equipment.

Qiangqiang Yan received the B.E. degree in Electrical Engineering and Automation from China University of Mining and Technology, in 2013. He is now currently pursuing his M.S. degree in Electrical Engineering and its Automation from Wuhan University, Hubei, China. His primary research interests include numerical methods of field calculation and condition monitoring of electrical equipment.

Zipin Li is an Associate Professor in Electrical Engineering College Wuhan University. He received his M.S. and Ph.D. degrees in Electrical Engineering College Wuhan University. His research interests mainly focus on condition monitoring of electrical equipment.

Highly Efficient Technique for the Full-Wave Analysis of Circular Waveguide Filters Including Off-Centered Irises

Ángel A. San-Blas and José M. Roca

Department of Communications Engineering
Miguel Hernández University of Elche, Elche, Spain
aasanblas@umh.es, jose.roca01@alu.umh.es

Abstract — A rigorous method for the full-wave analysis and design of waveguide filters implemented in circular waveguide technology, and including off-centered circular irises, is presented. The implemented tool is based on an integral equation technique, which provides a full-wave representation of the elementary blocks of the analyzed components in terms of generalized impedance matrices. With the aim of improving the efficiency of the developed tool, the radial variation of the modal solutions of the circular waveguides has been expressed in terms of sinusoidal functions, thus avoiding the use of the more cumbersome Bessel's functions employed in the classical formulation. Furthermore, line integrals have been used (instead of surface integrals) to compute the modal coupling coefficients of the planar waveguide junctions involved in the considered filters, thus drastically reducing the CPU effort related to the implemented tool. New designs concerning band-pass filters including off-centered circular irises are also provided. The obtained results show that the relative position of the considered circular irises can be considered as a new design parameter with a noteworthy influence on the electrical response of the investigated components. The accuracy of the proposed method has been successfully validated by comparing the obtained results with data extracted from both the technical literature and a commercial software based on the finite-element method.

Index Terms — Circular waveguide filters, integral equation technique, multimode equivalent network, off-centered irises.

I. INTRODUCTION

Circular waveguides are widely used in the fabrication of many passive and active components (such as waveguide filters [1], traveling-wave tubes [2], orthomode transducers [3] and turnstile junctions [4]), and they can be considered as key elements of current space communications devices in both microwave and millimeter-wave range [5-8]. Furthermore, the consideration of off-centered irises in circular waveguide filters is an

important topic in the design of a great variety of microwave components, since off-centered irises can provide a new design parameter (i.e., the relative position of the iris), thus allowing a more flexible computer-aided design process. The main motivation of this work is that, to the authors' knowledge, very few works concerning the full-wave analysis of circular waveguide filters, including off-centered circular irises, can be found in the technical literature. Besides, a common feature of such technical contributions is that they are not focused on developing efficient analysis tools from a computational point of view. For instance, the analysis method proposed in [9-10] is based on the conservation of the complex power technique, which employs the more cumbersome Bessel's functions to express the modal solutions of the circular waveguides, and also to compute the modal coupling coefficients of the analyzed planar junctions. Moreover, in contrast to the procedure used in the present work, such modal coupling coefficients are computed in [9-10] by using surface integrals instead of line integrals. Therefore, an increased CPU-effort may be expected in the solutions proposed in the aforementioned contributions. In addition, the modal method used in [9-10] assumed that no propagation modes exist in the smaller circular waveguide, thus limiting the validity of such model to a narrow frequency range.

Another contribution based on the least-squares boundary residual method was proposed in [11] to analyze thick eccentric circular irises in circular waveguides. However, the technique used in such work also resorts to computing surface integrals in order to analyze the planar junction, and the convergence of the obtained results depends on selecting very large dimensions for the computed matrices. Moreover, the authors of [11] reported a loss of accuracy at high frequencies values. A very recent work has been presented in [12], where complex discontinuities in circular waveguides are analyzed. Nevertheless, such work is based on a hybrid approach combining the finite-element method and a multimode variational technique, thus requiring higher CPU resources than the

approach proposed in the present work. In fact, the authors of [12] state that the simulation of a single circular discontinuity needs “few minutes” ([12], p. 103) using a CPU very similar to the one employed in this work. For comparison purposes, it is worth mentioning that the simulation tool developed in the present work is able to perform the overall analysis of a circular waveguide filter (composed of several discontinuities) in just few seconds.

Although other analysis methods based on numerical techniques (as the finite-element method) can be employed to analyze circular waveguide filters, such techniques typically use high CPU resources (both time and memory), since the whole analyzed structure needs to be meshed to achieve an electromagnetic characterization of the component.

In order to overcome all cited drawbacks of the aforementioned contributions, the main objective of this work is to present a novel and very efficient approach for the rigorous full-wave analysis of waveguide filters composed of the cascade connection of circular waveguides of different radii, and considering the inclusion of off-centered circular irises (see Fig. 1). The influence of the off-centered circular irises in the electrical response of different waveguide filters is investigated, and some useful guidelines for microwave designers are provided (i.e., the relative position of the circular irises can be considered as an important new design parameter). The implemented tool is based on an integral equation technique, which provides a full-wave representation of a planar junction between two off-centered circular waveguides in terms of a generalized impedance matrix [13]. This technique is very efficient from a computational point of view and provides a wide-band characterization of the waveguide planar junctions present in the considered device.

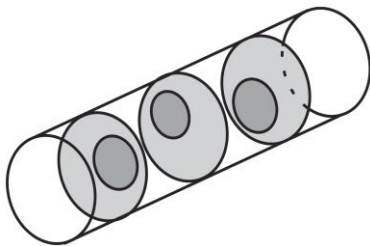


Fig. 1. Waveguide filter composed of the cascade connection of 7 circular waveguides. Note that the circular waveguides of smaller cross-section represent the waveguide irises of the filter and they are off-centered with respect to the axis of the filter. The length of the waveguide irises is small compared to the length of the resonators.

With the aim of optimizing the computational efficiency of the implemented tool, we follow a new

procedure in which the radial variation of the modal solutions of the circular waveguides is expressed in terms of sinusoidal functions, thus avoiding the use of the more cumbersome Bessel’s functions employed in the classical formulation. Furthermore, the surface integrals that must be calculated to compute the modal coupling coefficients between the two circular waveguides involved in the considered planar junctions are transformed into line integrals, thus reducing even more the CPU effort of the method. Additionally, the solution of the banded linear system obtained after performing the cascade connection of the derived wide-band matrices has been carried out by means of an iterative technique very efficient from a computational point of view. As a result, this novel approach produces a substantial improvement in terms of reduction of the computational effort with respect to previous works on the same subject.

In order to validate the proposed method, several band-pass circular waveguide filters including off-centered irises are analyzed and designed. The obtained simulated results are successfully compared to numerical data extracted from both the technical literature and a commercial tool based on the finite-element method, thus demonstrating the accuracy of the implemented software tool.

II. FULL-WAVE ANALYSIS OF CIRCULAR WAVEGUIDE FILTERS INCLUDING OFF-CENTERED IRISES

Waveguide filters based on off-centered circular irises can be readily analyzed by means of the so-called segmentation technique [14], which consists of decomposing the analysis of a complete waveguide structure into the characterization of its elementary key building blocks. In our particular case, a waveguide filter can be described as the cascade connection of planar junctions between off-centered circular waveguides, and uniform sections of circular waveguides, as it is shown in Fig. 1.

Both types of the aforementioned key building blocks can be characterized in terms of equivalent wide-band matrices. On the one hand, the electromagnetic characterization of a planar junction between two off-centered circular waveguides has been carried out by implementing the integral equation technique described in [13], which provides a full-wave characterization of the discontinuity in terms of an equivalent generalized impedance matrix (GIM) in the form:

$$Z_{(m,n)}^{(\xi,\gamma)} = \begin{cases} \sum_{q=1}^Q \alpha_q^{(n,\gamma)} A_{m,q}^*, & \text{if } \xi = 1 \\ \alpha_m^{(n,\gamma)} & \text{if } \xi = 2 \end{cases}, \quad (1)$$

where $(\xi, \gamma) = 1, 2$ denotes the two ports of the junction; $A_{m,q}$ represents the modal coupling coefficients

between two modes (m -th and q -th) of the circular waveguides involved in the junction; $\alpha_q^{(n,\gamma)}$ is a set of expansion coefficients used to represent the transversal magnetic field in the plane of the junction, and Q is the number of the considered expansion coefficients (the details of this formulation can be found in [13]). The multimode equivalent representation of the planar waveguide junction in terms of the GIM derived in (1) has been depicted in Fig. 2. In this figure, $I_i^{(\xi)}$ and $V_i^{(\xi)}$ (with $\xi=1,2$) are the corresponding modal currents and modal voltages, respectively; $\bar{I}_i^{(\xi)}$ represents a set of auxiliary modal currents; $N^{(\xi)}$ is the number of considered accessible modes, and $\hat{Y}_i^{(\xi)}$ are the so-called asymptotic admittances, which represent the modal admittance of high-order modes and are defined as follows:

$$\hat{Y}_i^{(\xi)} = \begin{cases} -j \frac{k_{t,i}^{(\xi)}}{\omega\mu}, & \text{if } i \text{ is a TE mode} \\ j \frac{\omega\epsilon}{k_{t,i}^{(\xi)}}, & \text{if } i \text{ is a TM mode} \end{cases}, \quad (2)$$

where $\omega = 2\pi f$, and $k_{t,i}^{(\xi)}$ is the cut-off wavenumber related to the i -th mode of the circular waveguide considered at port (ξ).

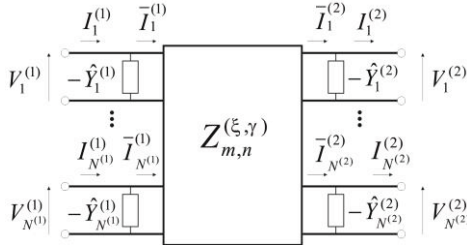


Fig. 2. Multimode equivalent representation of a planar waveguide junction in terms of a generalized impedance matrix.

The main advantage of this technique lies in its high computational efficiency, due to the fact that the size of the obtained GIM only depends on the number of the so-called accessible modes ($N^{(1)}$ and $N^{(2)}$ in Fig. 2), which is usually low to reach convergent results (10-20 modes in most cases). Moreover, since the frequency dependence of the obtained integral equation can be extracted from the kernel of such equation, the efficiency of the technique gets increased [13].

In order to obtain the elements of the GIM related to each planar junction, the modal coupling coefficients between the two circular waveguides involved in the discontinuity must be calculated first as follows:

$$A_{m,q} = \iint_S \mathbf{h}_m^{(1)}(\rho, \phi) \cdot \mathbf{h}_q^{(2)}(\rho, \phi) dS, \quad (3)$$

where $\mathbf{h}_\delta^{(i)}(\rho, \phi)$ with ($\delta = m, q$) is the magnetic vector mode function related to the δ -th mode of the i -th waveguide ($i=1,2$), and ρ and ϕ are the classical cylindrical coordinates. It is important to emphasize that the calculation of the coupling integral $A_{m,q}$ constitutes the core of the method. In fact, once these coupling coefficients are calculated, the computation of the GIM related to the planar waveguide junction can be easily performed following the general method detailed in [13].

Furthermore, it is important to note that the previous Equation (3) entails a surface integral that must be evaluated in the cross-section of the smaller circular waveguide of the junction. However, in virtue of the theory developed in [15], such surface integral can be transformed into a line integral, thus improving the CPU effort of the implemented tool. This transformation is very important from a computational point of view, since all the calculations involved in the evaluation of the coupling integral (3) must be performed using numerical methods. Therefore, following the guidelines of the work presented in [15], the evaluation of the previous modal coupling coefficients can be expressed in terms of line integrals as follows:

$$A_{m_{TE},q_{TE}} = \frac{k_{t,q}^2}{k_{t,q}^2 - k_{t,m}^2} \oint_c \frac{\partial \psi_m^{TE}(\rho, \phi)}{\partial \rho} \chi_q^{TE}(\rho, \phi) \rho d\phi, \quad (4)$$

$$A_{m_{TE},q_{TM}} = 0, \quad (5)$$

$$A_{m_{TM},q_{TE}} = \oint_c \frac{\partial \psi_m^{TM}(\rho, \phi)}{\partial \phi} \chi_q^{TE}(\rho, \phi) d\phi, \quad (6)$$

$$A_{m_{TM},q_{TM}} = -\frac{k_{t,m}^2}{k_{t,q}^2 - k_{t,m}^2} \oint_c \frac{\partial \chi_q^{TM}(\rho, \phi)}{\partial \rho} \psi_m^{TM}(\rho, \phi) \rho d\phi, \quad (7)$$

where $k_{t,m}$ represents the cut-off wavenumber related to the m -th mode of the bigger circular waveguide of the junction; $k_{t,q}$ is the corresponding cut-off wavenumber associated to the q -th mode of the smaller circular waveguide; $\psi_m(\rho, \phi)$ is the normalized scalar potential related to the m -th mode of the bigger circular waveguide, and $\chi_q(\rho, \phi)$ is the normalized scalar potential related to the q -th mode of the smaller circular waveguide. Note that the previous expressions derived in (4)-(7) for the calculation of the coupling integral (3) depend on the type of the involved modes (i.e., TE or TM modes).

To evaluate the modal coupling coefficients using line integrals, the TE and TM normalized scalar potentials of a circular waveguide are, therefore, needed. To this aim, in this work we follow a new procedure based on expressing the radial variation of the modal solutions in terms of sinusoidal functions [16]. Proceeding in this way, the CPU effort related to

the calculation of the modal coupling coefficients is substantially reduced, since we do not need to deal with the more cumbersome Bessel's functions employed in the classical formulation. The expressions of the normalized modal potentials (TE and TM) can be obtained as:

$$\psi_m^{\text{TE}}(\rho, \phi) = N_m^{\text{TE}} \left\{ \sum_{n=0}^P d_m^{(n)} \sin\left(\pi(n+0.5)\frac{\rho}{R}\right) \right\} \Phi_s(\phi), \quad (8)$$

$$\psi_m^{\text{TM}}(\rho, \phi) = N_m^{\text{TM}} \left\{ \sum_{n=1}^P d_m^{(n)} \sin\left(n\pi\frac{\rho}{R}\right) \right\} \Phi_s(\phi), \quad (9)$$

where R is the radius of the considered circular waveguide; N_m is the normalization factor related to the m -th mode; $d_m^{(n)}$ is the set of eigenvectors that describe the radial variation of the m -th mode; s is the angular modal index related to the m -th mode; $\Phi_s(\phi) = \cos(s\phi)$ or $\sin(s\phi)$ depending on the parity of the mode, and P is the number of terms considered in the radial expansion. If the angular modal index s is equal to zero, the following expressions must be used:

$$\psi_{m,(s=0)}^{\text{TE}}(\rho) = N_{m,(s=0)}^{\text{TE}} \sum_{n=0}^P d_m^{(n)} \cos\left(n\pi\frac{\rho}{R}\right), \quad (10)$$

$$\psi_{m,(s=0)}^{\text{TM}}(\rho) = N_{m,(s=0)}^{\text{TM}} \sum_{n=0}^P d_m^{(n)} \cos\left(\pi(n+0.5)\frac{\rho}{R}\right), \quad (11)$$

where $N_{m,(s=0)}$ is the corresponding normalization factor.

Next, we need to define a common reference system in order to carry out the computation of the modal coupling coefficients. To this end, the axis system depicted in Fig. 3 has been used. In such figure, the coordinates (ρ_0, ϕ_0) are used to express the offset of the center of the smaller waveguide with respect to the center of the bigger waveguide, while (ρ, ϕ) and (ρ_1, ϕ_1) are the local reference systems used in the bigger and smaller circular waveguides, respectively.

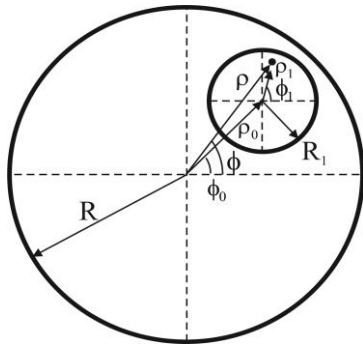


Fig. 3. Reference system used for the analysis of a planar junction between two off-centered circular waveguides.

Since the line integrations (4)-(7) have to be performed over the contour of the smaller circular waveguide, we are interested in expressing the local coordinates (ρ, ϕ) of the bigger waveguide in terms of the local coordinates (ρ_1, ϕ_1) of the smaller waveguide. Therefore, starting from Fig. 3, it is possible to state:

$$\rho = \sqrt{\rho_0^2 + \rho_1^2 + 2\rho_0\rho_1 \cos(\phi_1 - \phi_0)}, \quad (12)$$

$$\phi = \arctan\left(\frac{\rho_0 \sin(\phi_0) + \rho_1 \sin(\phi_1)}{\rho_0 \cos(\phi_0) + \rho_1 \cos(\phi_1)}\right). \quad (13)$$

Afterwards, we can use the transformations derived in (12)-(13) to update the expressions (8)-(11) related to the normalized modal potentials of the bigger circular waveguide. The normalized modal potentials of the smaller waveguide can be readily obtained starting from Equations (8)-(11), by using the local coordinates (ρ_1, ϕ_1) and denoting as R_1 the radius of the waveguide. In the end, the required modal coupling coefficients derived in (4)-(7) can be computed using classical numerical techniques, and the corresponding GIM of the planar junction can be finally calculated by means of expression (1).

Once the expressions of the wide-band matrices related to the planar waveguide junctions have been derived using the proposed technique, next step consists of characterizing the uniform waveguide sections present in the component. To this aim, let us consider the structure represented in Fig. 4, where we have illustrated a section of an arbitrary filter composed of the cascade connection of 3 circular waveguides of different radii. Note that the different planar waveguide junctions have been highlighted using dashed lines on the upper side of Fig. 4. In this figure, we have represented the multimode equivalent representation of such structure in terms of the computed GIMs $Z_{m,n}^{\text{PWJ1}}$ and $Z_{m,n}^{\text{PWJ2}}$, which are both associated to the planar waveguide junctions. We have also included in Fig. 4 the corresponding uniform waveguide section of length l used to interconnect the circular waveguides of greater radius.

Our objective is to obtain a multimode equivalent representation ($Z_{m,n}^{\text{UWS}}$ in Fig. 4) of the uniform waveguide section of length l , while also taking into account the asymptotic admittances introduced by the integral equation technique (see the dashed lines on the lower side of Fig. 4). To this aim, we should first obtain an equivalent lumped pi-network representation for the uniform waveguide section of length l and, afterwards, take into consideration the asymptotic admittances represented in Fig. 4. Proceeding in this way, the following generalized impedance matrix can be readily computed:

$$Z_{m,n}^{UWS} = \begin{pmatrix} Y^{(a)} & Y^{(b)} \\ Y^{(b)} & Y^{(c)} \end{pmatrix}^{-1}, \quad (14)$$

where $Y^{(a)}$, $Y^{(b)}$ and $Y^{(c)}$ are diagonal matrices whose non-zero elements can be written as:

$$Y_i^{(a)} = jY_{0,i} (\tan(\beta_i l / 2) - \csc(\beta_i l)) - \hat{Y}_{i,PWJ1}^{(2)}, \quad (15)$$

$$Y_i^{(b)} = -jY_{0,i} \csc(\beta_i l), \quad (16)$$

$$Y_i^{(c)} = jY_{0,i} (\tan(\beta_i l / 2) - \csc(\beta_i l)) - \hat{Y}_{i,PWJ2}^{(1)}, \quad (17)$$

with $i=1,2,\dots,N$, being N the number of considered accessible modes. In the previous Equations (15)-(17), $Y_{0,i}$ is the modal characteristic admittance related to the i -th mode of the considered waveguide section, and β_i is the corresponding propagation constant.

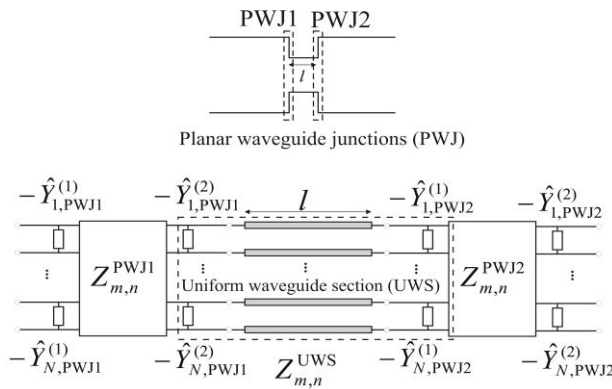


Fig. 4. Section of an arbitrary circular waveguide filter. Multimode equivalent network representation in terms of the obtained generalized impedance matrices (GIM). Note that N accessible modes are considered, and a uniform circular waveguide section of length l is included between the two GIMs.

Once the expressions for the wide-band matrices of all the elementary blocks of the structure (i.e., planar waveguide junctions and uniform waveguide sections) have been derived using the proposed techniques, the cascade connection of the obtained generalized impedance matrices must be performed in order to compute the electrical response of the whole filter. In relation to this, a very important advantage derived from expressing the GIM related to the uniform waveguide sections in the way we have previously described, is that the cascade connection of the obtained wide-band matrices produces a banded linear system (the non-zero coefficients of the matrix are distributed

over its main diagonals), which can be efficiently solved by means of an iterative technique. In fact, the banded configuration of such linear system can be exploited to perform an efficient inversion of the coefficients matrix following the guidelines proposed in [17] (although the procedure described in [17] is applied for the connection of generalized admittance matrices, it has been properly extended to cope with the cascade connection of generalized impedance matrices).

III. RESULTS AND DISCUSSION

The objective of this section is to validate the implemented tool for the full-wave analysis of waveguide filters based on off-centered circular irises. In order to obtain convergent results in the performed simulations, only 15 accessible modes have been used in all circular waveguides, and $P=150$ terms have been required in the radial expansions of the expressions (8)-(11). In addition, it is important to point out that the implemented tool is able to detect the presence of identical planar junctions in the filter to avoid unnecessary calculations (such detection is specially important in the case of symmetrical filters). Furthermore, if the circular irises of the filter are all in a centered position, note that only $TE_{1,r}$ and $TM_{1,r}$ modes are excited, and the developed tool is able to exploit this fact to reduce the overall CPU effort.

Firstly, we proceed to validate the proposed tool by analyzing a band-pass waveguide filter designed in [1], which makes use of centered circular irises (note that the method proposed in [1] can deal only with filters including centered irises). In this particular case, since the component does not include off-centered irises, the offset value is $\rho_0 = \phi_0 = 0$ (see Fig. 3). The analyzed filter is composed of the cascade connection of 7 circular waveguides, and its geometry and dimensions can be found in [1] (page 1140, Fig. 1). The radii (mm) of the waveguides are (numbered from left to right, according to Fig. 1): $R_1 = R_7 = 6.985$ (input and output waveguides), $R_3 = R_5 = 6.985$ (resonators), $R_2 = R_6 = 4.34$ and $R_4 = 3.51$ (irises). The length of the two resonators is 18.7 mm, and the thickness of the irises is 0.1 mm. This filter has been simulated using the implemented tool and the obtained scattering parameters are presented in Fig. 5. In this figure, our results are successfully compared with the data presented in the technical literature [1]. With regard to the computational efficiency of the developed tool, it is worth mentioning that the electrical response was computed in just 0.06 seconds per frequency point (Intel Core i3@3.1 GHz - 4 GB RAM).

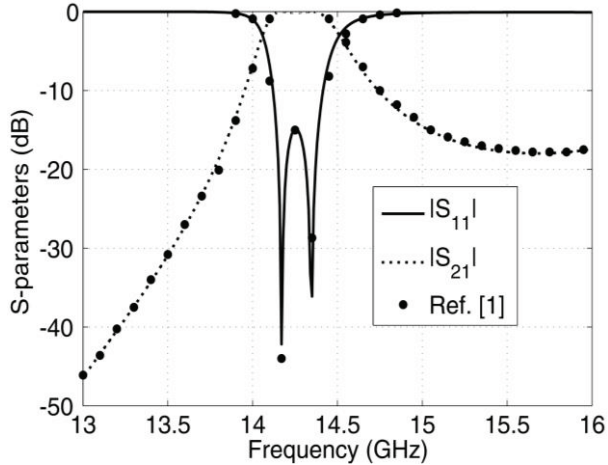


Fig. 5. S-parameters (dB) of a circular waveguide filter composed of 7 waveguides. The circular irises are all in a centered position. The obtained results are compared with the data extracted from the technical literature [1].

Next, we investigate the effect of considering off-centered circular irises in the structure. To this aim, we start from the filter analyzed in Fig. 5, and we proceed to off-center the circular irises of the component in order to study the influence of such variation on the electrical response of the device. Although, in this case, the three irises of the filter have been off-centered in the same magnitude, note that the implemented tool can deal with arbitrary off-centered irises, so there is no restriction in assigning a different offset to each circular iris. Figure 6 shows the electrical response of the filter for different values of the considered offset ρ_0 (mm), ϕ_0 (rad). The electrical response of the filter with centered irises (blue solid curve) has also been included in Fig. 6. Moreover, we have successfully compared the results of our simulation tool for the general case $\rho_0 = 2.343$ mm, $\phi_0 = 0.876$ rad (grey solid curve) with the simulated data provided by a commercial simulation tool (Ansoft HFSS 12) based on the finite-element method (FEM), thus fully validating the accuracy of the proposed technique. The results presented in Fig. 6 have been calculated in just 0.09 seconds per frequency point.

With regard to the parametric study performed in Fig. 6, it is important to point out that, compared to the filter with centered irises (blue solid curve), the electrical response of the component hardly change when different values of ρ_0 are considered along the line $\phi_0 = \pi/2$ rad (vertical displacement of the center of the iris). In fact, we observe that the electrical response for the case $\rho_0 = 2.25$ mm, $\phi_0 = \pi/2$ rad,

only has experienced a frequency shift, preserving both a good reflection level and the original relative bandwidth. As a consequence, these results show that the relative position of the circular iris can be considered as an additional design parameter to easily achieve a frequency shift of the electrical response of the device.

However, when different values of ρ_0 are considered along the line $\phi_0 = 0$ rad (horizontal displacement of the center of the iris), a severe degradation of the passband of the filter may be expected, specially when high values of ρ_0 are considered (see, for instance, the red solid curve in Fig. 6). The same behavior can be observed for a general displacement of the center of the circular iris (see grey solid curve in Fig. 6). Therefore, in general terms, we conclude that a degradation of the electrical response of the filter may be expected when it has been specifically designed with centered circular irises.

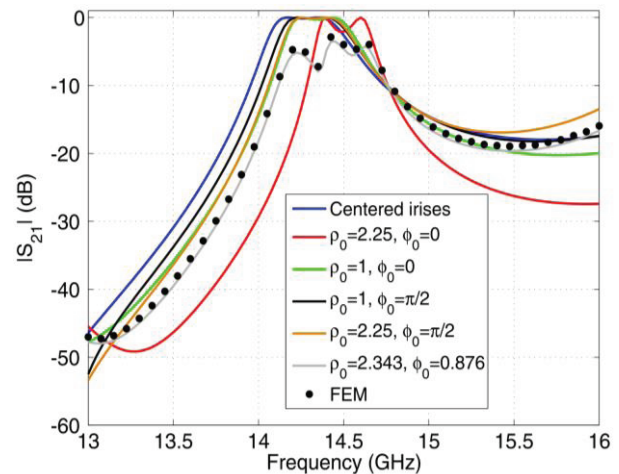


Fig. 6. Transmission parameters (dB) of the waveguide filter analyzed in Fig. 5 considering off-centered circular irises.

Finally, we present in Fig. 7 a new design of a Ku-band band-pass filter implemented in circular waveguide technology (composed of the cascade connection of 7 waveguides), including off-centered circular irises. A simple custom code based on the minimization of the average return losses has been developed in order to design the filter. In this design, the three irises of the structure have been off-centered using different offset values. The considered offsets have been listed in Table 1, while the radii and lengths of the circular waveguides are shown in Table 2 (the waveguides and irises have been numbered from left to right, according to Fig. 1).

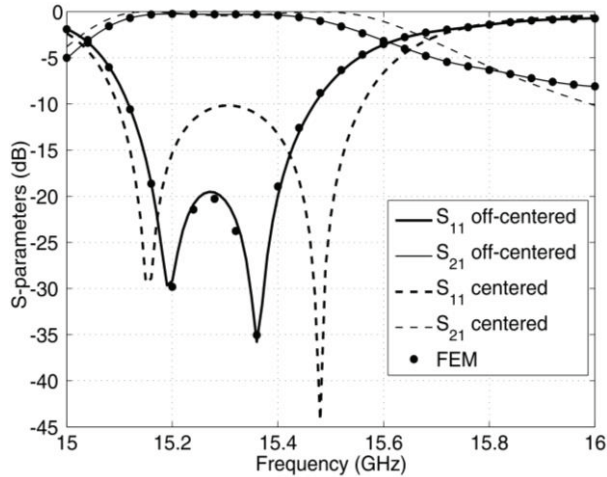


Fig. 7. Design of a band-pass filter including off-centered circular irises. The electrical performance of the designed filter (solid curves) is compared with the case where centered circular irises are used (dashed curves). Simulated data obtained using a commercial software based on the finite-element method (FEM) are also included to validate the proposed method.

Table 1: Offsets of the irises considered in the band-pass filter designed in Fig. 7

| Irish | ρ_0 (mm) | ϕ_0 (rad) |
|-------|---------------|----------------|
| 1 | 2.485 | 1.367 |
| 2 | 2.711 | 1.549 |
| 3 | 2.208 | 1.311 |

Table 2: Radii and lengths of the circular waveguides of the band-pass filter designed in Fig. 7

| Waveguide | Radius (mm) | Length (mm) |
|-----------|-------------|-------------|
| 1 | 6.985 | 10.0 |
| 2 | 3.946 | 0.1 |
| 3 | 6.985 | 14.541 |
| 4 | 3.208 | 0.1 |
| 5 | 6.985 | 14.525 |
| 6 | 3.968 | 0.1 |
| 7 | 6.985 | 10.0 |

It is worth noting that the band-pass filter designed in Fig. 7 presents an improved electrical response with respect to the filter designed in [1] (see Fig. 5), which operates at the same frequency band and makes use of the same number of circular waveguides (employing centered irises). In this case where off-centered irises have been employed, we have achieved a reflection level under -20 dB in the whole passband (about 250 MHz) of the filter, thus proving that the relative position of the iris can be considered as a new design parameter. We have also compared the results of our simulation

tool (off-centered case) with the simulated data provided by Ansoft HFSS, and an excellent agreement can be observed, thus fully validating the accuracy of the proposed modal technique.

Moreover, we have also included in Fig. 7 (using dashed lines) the electrical response of the new designed filter, but this time considering centered irises. It can be observed that the filter based on off-centered irises provides an improved electrical performance compared to the filter based on centered irises, thus demonstrating that the relative position of the iris has a noteworthy influence on the design process.

It is important to mention that the overall analysis of the new designed filter (off-centered case) only needed 0.12 seconds per frequency point. In contrast, the simulation performed using the commercial tool based on the finite-element method needed 2.3 seconds per frequency point (almost 20 times slower). Moreover, the hybrid analysis method presented in [12] needs few minutes to analyze just one planar junction between two circular waveguides. Therefore, the developed software achieves a substantial improvement in terms of reduction of the computational effort with respect to other analysis techniques, so it can be employed for design purposes employing very low CPU resources.

IV. CONCLUSION

A rigorous method for the full-wave analysis of circular waveguide filters including off-centered irises has been proposed. The implemented tool is based on an integral equation technique, and makes use of the segmentation method to provide a rigorous electromagnetic characterization of all the elementary blocks involved in the analyzed filters in terms of generalized impedance matrices. The presented technique, which is very efficient from a computational point of view compared to other technical contributions on the same subject, has been successfully validated through the analysis and design of different band-pass waveguide filters with centered and off-centered circular irises. The obtained results show that the relative position of the circular waveguide irises can be considered as a new design parameter having a noteworthy influence on the electrical response of the analyzed waveguide filters.

ACKNOWLEDGMENT

This work was supported by the Ministerio de Economía y Competitividad, Spanish Government, under the Research Project TEC2013-47037-C5-4-R.

REFERENCES

- [1] U. Balaji, "CAD of resonant circular iris waveguide filter with dielectric filled cavities," *Progress in Electromagnetics Research Symposium Proceedings*, pp. 1139-1141, 1993.

- [2] V. Kesari, "Analysis of alternate dielectric and metal vane loaded circular waveguide for a wideband gyro-TWT," *IEEE Transactions on Electron Devices*, vol. 61, no. 3, pp. 915-920, 2014.
- [3] A. Tribak, J. L. Cano, A. Mediavilla, and M. Boussois, "Octave bandwidth compact turnstile-based orthomode transducer," *IEEE Microwave and Wireless Components Letters*, vol. 20, no. 10, pp. 539-541, 2010.
- [4] A. A. San Blas, F. J. Pérez, J. Gil, F. Mira, V. E. Boria, and B. Gimeno, "Full-wave analysis and design of broadband turnstile junctions," *Progress In Electromagnetics Research Letters*, vol. 24, pp. 149-158, 2011.
- [5] J. Uher, J. Bornemann, and U. Rosenberg, *Waveguide Components for Antenna Feed Systems: Theory and CAD*, Artech House, Norwood, 1993.
- [6] G. Conciauro, M. Guglielmi, and R. Sorrentino, *Advanced Modal Analysis: CAD Techniques for Waveguides Components and Filters*, Wiley, Chichester, 2000.
- [7] M. Qudrat-E-Maula, L. Shafai, and Z. A. Pour, "Dielectric loaded circular waveguide feeds," *16th International Symposium on Antenna Technology and Applied Electromagnetics*, pp. 1-2, 2014.
- [8] J. Li, H. Huang, Z. Zhang, W. Song, H. Shao, C. Chen, and W. Huang, "A novel X-band diplexer based on overmoded circular waveguides for high-power microwaves," *IEEE Transactions on Plasma Science*, vol. 41, no. 10, pp. 2724-2728, 2013.
- [9] Z. Shen and R. H. MacPhie, "Scattering by a thick off-centered circular iris in circular waveguide," *IEEE Transactions on Microwave Theory and Techniques*, vol. 43, no. 11, pp. 2639-2642, 1995.
- [10] K. Wu, "An optimal circular-waveguide dual-mode filter without tuning screws," *IEEE Transactions on Microwave Theory and Techniques*, vol. 47, no. 3, pp. 271-276, 1999.
- [11] S. P. Yeo and S. G. Teo, "Thick eccentric circular iris in circular waveguide," *IEEE Transactions on Microwave Theory and Techniques*, vol. 46, no. 8, pp. 1177-1180, 1998.
- [12] M. Yahia, J. W. Tao, and H. Sakli, "Analysis of complex discontinuities in circular waveguides using hybrid finite element method and multimodal variational method," *Progress In Electromagnetics Research Letters*, vol. 51, pp. 101-107, 2015.
- [13] G. Gerini, M. Guglielmi, and G. Lastoria, "Efficient integral equation formulations for the computation of the multimode admittance or impedance matrix of planar waveguide junctions," *IEEE MTT-S International Microwave Symposium Digest*, pp. 1747-1750, 1998.
- [14] R. R. Mansour and R. H. MacPhie, "An improved transmission matrix formulation of cascaded discontinuities and its application to E-plane circuits," *IEEE Transactions on Microwave Theory and Techniques*, vol. 34, no. 12, pp. 1490-1498, 1986.
- [15] G. G. Gentili, "Properties of TE-TM mode-matching techniques," *IEEE Transactions on Microwave Theory and Techniques*, vol. 39, no. 9, pp. 1669-1673, 1991.
- [16] B. Gimeno and M. Guglielmi, "Multimode equivalent network representation for junctions between coaxial and circular waveguides," *International Journal of Microwave and Millimeter-Wave Computer-Aided Engineering*, vol. 7, no. 2, pp. 180-194, 1997.
- [17] V. E. Boria, G. Gerini, and M. Guglielmi, "An efficient inversion technique for banded linear systems," *IEEE MTT-S International Microwave Symposium Digest*, pp. 1567-1570, 1997.



Ángel A. San-Blas received a M.S. degree and a Ph.D. degree in Telecommunications Engineering, both from the Polytechnic University of Valencia, Valencia (Spain), in 2000 and 2008, respectively. In 2001, he became a Researcher with the Department of Communications, Polytechnic University of Valencia, where he was involved in the development of simulation tools for the full-wave analysis and design of passive waveguide devices. From November 2001 to March 2002, he was a Researcher at Department of Electronics, University of Pavia, Pavia (Italy), in the framework of the European Network MMCODEF (Millimeter-wave and Microwave Components Design Framework for Ground and Space Multimedia Network, V European Framework Programme). Since 2003, he has been an Associate Professor with the Department of Communications Engineering, Miguel Hernández University of Elche, Elche (Spain). His current research interests include numerical methods for the efficient analysis and design of passive and active waveguide components.



José M. Roca received a Telecommunications Engineering degree from the Miguel Hernández University of Elche, Elche (Spain) in 2014. He then joined the Department of Communications Engineering, Miguel Hernández University of Elche, to work on the

development of efficient simulation tools for the analysis and design of microwave and millimeter-wave devices making use of full-wave analysis methods.

Effect of Plasma on Electromagnetic Wave Propagation and THz Communications for Reentry Flight

L. Zheng, Q. Zhao, and X. J. Xing

School of Physical Electronics
University of Electronic Science and Technology of China, Chengdu, 0086, 610054, China
zlhengling@163.com, zqzhaoq@sohu.com, xingxj@yahoo.com.cn

Abstract—The spacecraft will experience the well-known “blackout” problem when it re-enters into the Earth’s atmosphere, which results in communication failures between the spacecraft and the ground control center. It is important to study the effect of the plasma on electromagnetic wave (EMW) propagation. The properties of EMW propagation in plasma based on theoretical analysis have been studied in this paper, which indicate that communications using terahertz (THz) wave is an alternative method for solving the blackout problem. The properties of 0.22 THz EMW propagation in plasma have been studied experimentally with shock tube, and the experimental results are in good agreement with the theoretical ones. Both the theoretical and experimental results indicate that communications using THz wave is an alternative and effective way to solve the blackout problem.

Index Terms — Blackout, EMW propagation, plasma, THz.

I. INTRODUCTION

The spacecraft will experience the well-known “blackout” problem [1-3] when it re-enters into the Earth’s atmosphere, which results in communication failures between the spacecraft and the ground control center. This phenomenon has attracted more and more attention recently [4-8].

A number of approaches have been proposed to solve the blackout problem, such as aerodynamic shape modification, quenchant injection, magnetic window and so on; however, the true technological breakthrough has not been achieved.

One of the major reasons for communication failures is that the plasma frequency is greater than the EMW frequency. The plasma density may reach $10^{21}/\text{m}^3$ and the corresponding plasma frequency is 0.284 THz, which are typical data of the RAM C (Radio Attenuation Measurement C) flight [9]. Besides, 0.2 THz has been specified for the next intersatellite communications by the International Telecommunication Union. For these

reasons, communications using THz wave is an alternative method for solving the blackout problem and the great advance in THz source technology recently provides a great opportunity for this issue [10-14]. Moreover, it is possible to solve the blackout problem using THz wave with the development of THz technology.

Therefore, it is important to study the properties of THz wave propagation in plasma. However, most published works were limited in microwave frequency (<100 GHz) and focus on theory and numerical simulations [15-19].

The effect of plasma on EMW propagation has been studied theoretically and the properties of 0.22 THz EMW propagation in plasma have been studied experimentally with shock tube in this paper.

II. PHYSICAL MODEL

The physical model used in this paper is as follows: the EMW incident vertically into the plasma along the z -axis, which is depicted in Fig. 1. The plasma is assumed to be homogeneous and unmagnetized. The electric field is parallel to the x -axis and the magnetic field is parallel to the y -axis. The thickness of plasma is d .

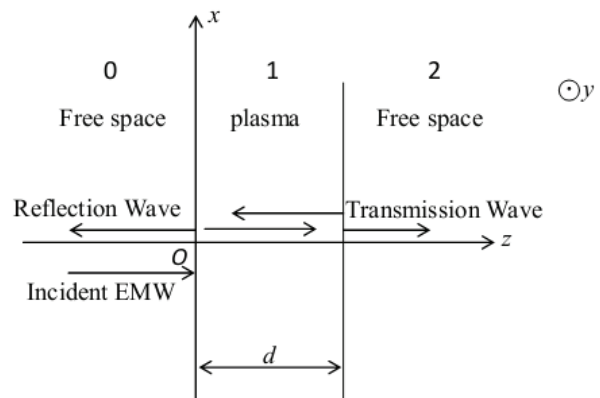


Fig. 1. The physical model of EMW propagation in plasma.

The Maxwell’s equations are the following [20-24]:

$$\left\{ \begin{array}{l} \nabla \times \vec{E} = -j\omega\mu_0 \vec{H} \\ \nabla \times \vec{H} = j\omega\varepsilon \vec{E} \\ \nabla \cdot (\varepsilon \vec{E}) = 0 \\ \nabla \cdot \vec{B} = 0 \end{array} \right. , \quad (1)$$

where \vec{E} and \vec{H} are the electric field and magnetic field, respectively, μ_0 is the permeability of vacuum, ε is the permittivity, $\omega = 2\pi f$, and f is the frequency of the incident EMW.

The electric field of the incident EMW can be expressed as: $E_x = E_0 e^{-jk_0 z}$, where E_0 is the amplitude of the incident electric field and k_0 is the wave number in free space.

From the Maxwell's equations, we can obtain the magnetic field of the incident EMW: $H_y = -\frac{1}{j\omega\mu_0} \frac{\partial E_x}{\partial z}$.

Then the electric field and magnetic field in medium 0 can be expressed as:

$$\begin{aligned} E_{0x} &= E_0 (e^{-jk_0 z} + r e^{jk_0 z}) \\ H_{0y} &= \frac{k_0}{\omega\mu_0} E_0 (e^{-jk_0 z} - r e^{jk_0 z}) \end{aligned} , \quad (2)$$

where r is the reflection coefficient.

Similarly, the electric and magnetic fields in medium 1 can be expressed as:

$$\begin{aligned} E_{1x} &= E_{PT} e^{-jk_p z} + E_{PR} e^{jk_p z} \\ H_{1y} &= \frac{k_p}{\omega\mu_0} (E_{PT} e^{-jk_p z} - E_{PR} e^{jk_p z}) \end{aligned} , \quad (3)$$

where E_{PT} and E_{PR} are the amplitudes of the transmission and reflection electric fields in medium 1, and k_p is the wave number in plasma.

The electric field and magnetic field in medium 2 are presented as the following:

$$\begin{aligned} E_{2y} &= E_T e^{-jk_0 z} \\ H_{2x} &= \frac{k_0}{\omega\mu_0} E_T e^{-jk_0 z} \end{aligned} , \quad (4)$$

where E_T is the amplitude of the transmission electric field in medium 2.

The continuity boundary conditions of the electric and magnetic fields can be described as:

$$\begin{aligned} E_{0x} \Big|_{z=0} &= E_{1x} \Big|_{z=0} \\ H_{0y} \Big|_{z=0} &= H_{1y} \Big|_{z=0} \\ E_{1x} \Big|_{z=d} &= E_{2x} \Big|_{z=d} \\ H_{1y} \Big|_{z=d} &= H_{2y} \Big|_{z=d} \end{aligned} , \quad (5)$$

i.e.,

$$\begin{aligned} E_0 (1+r) &= E_{PT} + E_{PR} \\ \frac{k_0}{\omega\mu_0} E_0 (1-r) &= \frac{k_p}{\omega\mu_0} (E_{PT} - E_{PR}) \\ E_{PT} e^{-jk_p d} + E_{PR} e^{jk_p d} &= E_T e^{-jk_0 d} \\ \frac{k_p}{\omega\mu_0} (E_{PT} e^{-jk_p d} - E_{PR} e^{jk_p d}) &= \frac{k_0}{\omega\mu_0} E_T e^{-jk_0 d} \end{aligned} . \quad (6)$$

The reflection coefficient r and transmission coefficient t can be obtained from equation (6):

$$\begin{aligned} r &= \frac{1 - \varepsilon_r}{2\sqrt{\varepsilon_r} \coth(jk_p d) + \varepsilon_r + 1} \\ t &= \frac{E_T}{E_0} = \frac{2\sqrt{\varepsilon_r} e^{jk_0 d}}{2\sqrt{\varepsilon_r} \cosh(jk_p d) + (\varepsilon_r + 1) \sinh(jk_p d)} \end{aligned} , \quad (7)$$

where ε_r is the relative permittivity of plasma.

Then the reflectance, transmission and attenuation of the EMW, i.e., R , T and Att can be expressed as the following:

$$\begin{aligned} R &= |r|^2 \\ T &= |t|^2 \\ Att &= -10 \log_{10} T \end{aligned} . \quad (8)$$

III. NUMERICAL SIMULATION RESULTS

The attenuation of the EMW versus plasma density and collision frequency at different EMW frequency are calculated and illustrated in Fig. 2, in which the thickness of the plasma d is 0.08 m.

As shown in Fig. 2, the attenuation decrease with EMW frequency for identical plasma density and collision frequency. The mechanism responsible for this phenomenon can be explained through the electrons' response to the electric field: the electrons will no longer be able to response to the electric field as the EMW frequency increases; hence, the EMW energy absorbed by electrons decrease and then the attenuation is decreased.

The maximum attenuation for $f=1.5$ GHz, $f=0.1$ THz and $f=0.22$ THz are 1100 dB, 350 dB and 100 dB, respectively, which can be seen from Fig. 2. The EMW attenuation is less than 30 dB for 0.22 THz EMW at most region when $n_e = 10^{12}/\text{cm}^3 \sim 10^{14}/\text{cm}^3$, $f_{en} = 10^9 \text{Hz} \sim 10^{11} \text{Hz}$. For this reason, communications using THz wave can be considered for solving the blackout problem.

From Fig. 2, we can also see that the attenuation increase with plasma density, which is because there are more electrons in plasma with higher plasma density, and then more EMW energy is absorbed by electrons and passed to neutral particles through collisions, i.e., the EMW attenuation is increased.

Figure 2 also shows that the attenuation decreases with plasma collision frequency when $f < f_p$ while increases

with plasma collision frequency when $f > f_p$. The reason is that the electrons are oscillating at EMW frequency when $f < f_p$, the acceleration time of electrons before collision with neutral particles is so short that there is little time for the electrons to receive energy from the electric field with increasing plasma collision frequency, so the attenuation is decreased. However, the electrons are oscillating at the inherent frequency when $f > f_p$, and the collision probability between the electrons and neutral particles increases and the energy passed to neutral particles is increased for higher plasma collision frequency, then the attenuation is increased.

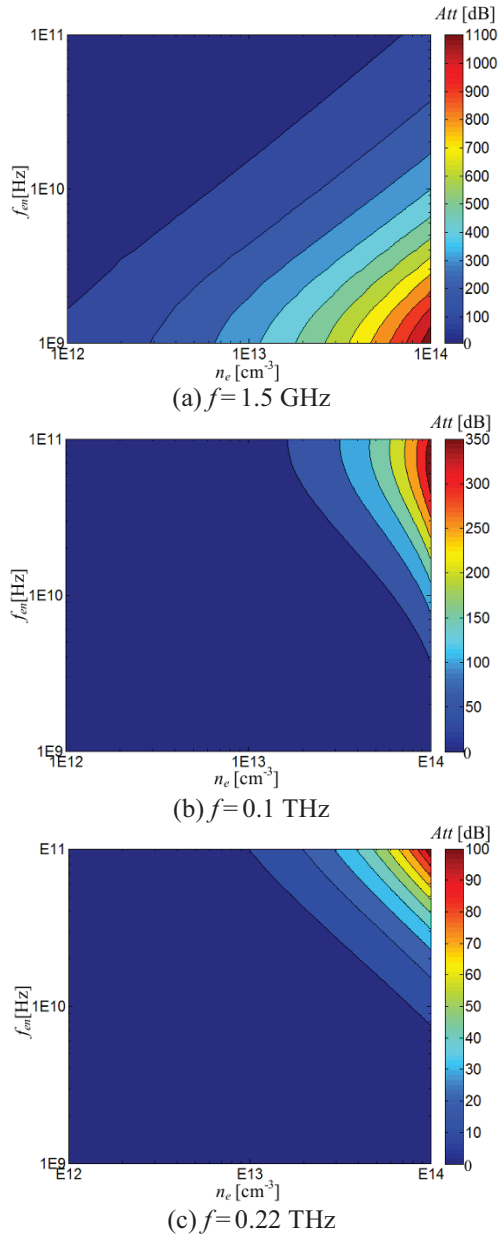


Fig. 2. The attenuation of EMW versus plasma density and collision frequency for various EMW frequency.

IV. EXPERIMENTAL RESULTS

The 0.22 THz EMW propagation properties in the plasma are studied experimentally with shock tube. The shock tube is a cylindrical device and it can produce approximate uniform plasma, which are usually used to simulate the plasma near the aircrafts [25,26]. The schematic diagram of the experimental setup is illustrated in Fig. 3. The diameter of the shock tube is 0.08 m. The original wall of the shock tube was replaced by Teflon in order to reduce the reflection. A total of five effective experiments were carried out and we denoted the experiments by numbers: 1, 2, 3, 4 and 5.

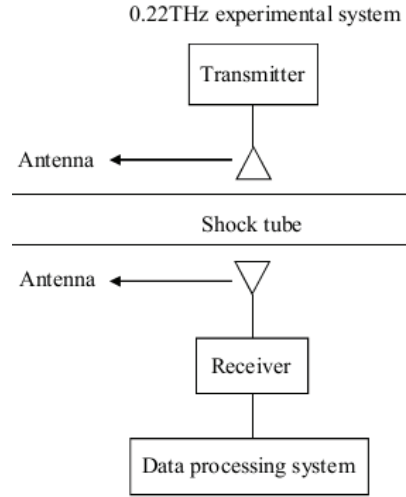
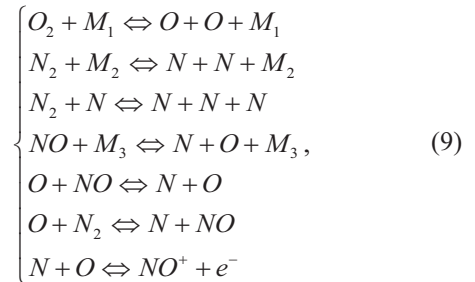


Fig. 3. The experimental setup of the 0.22 THz EMW propagation in the plasma.

The plasma densities and collision frequencies used in the experiments are presented in Table 1, which are calculated based on the physical states of the shock tube in the experiments.

A chemical reaction model consisting of 7 chemical reactions among 7 compounds was used in the calculation, which includes the reactions as follows:



where M is the collider in the reactions, and the reaction rate is presented in reference [27,28]. The theoretical plasma density n_e can be obtained from these reactions.

The collision frequency of the plasma f_{en} was acquired from equation (10):

$$f_{en} = 3.67 \times 10^{-15} \omega_p^2 T, \quad (10)$$

where $\omega_p = \sqrt{n_e e^2 / \varepsilon_0 m_e}$, e is the charge of the electron, ε_0 is the vacuum permittivity, m_e is electron mass, and T is the temperature of the plasma which was measured in the experiments.

The experimental EMW attenuation is acquired from the power of the receiver, which is proceeded by the "data processing system".

Table 1: The plasma densities and collision frequencies used in the experiments

| Number of the Experiments | n_e (m ⁻³) | f_{en} (Hz) |
|---------------------------|--------------------------|----------------------|
| 1 | 9.0×10^{17} | 8.2×10^{10} |
| 2 | 3.0×10^{18} | 9.2×10^{10} |
| 3 | 3.2×10^{18} | 9.7×10^{10} |
| 4 | 7.3×10^{18} | 1.0×10^{11} |
| 5 | 2.4×10^{19} | 1.2×10^{11} |

Figure 4 shows the comparison of the experimental results and theoretical ones of the 0.22 THz EMW attenuation. The experimental results match well with the theoretical ones, which can be seen from Fig. 4. However, there are some differences between the experimental results and theoretical ones, which may be attributed to the errors of the experimental systems and the calculation errors of plasma densities and collision frequencies. The theoretical and experimental results are both smaller than 30 dB even if the plasma density reach as high as $2.4 \times 10^{19}/\text{m}^3$ and the plasma collision frequency is 1.2×10^{11} Hz. According to these results, it can be deduced that communications using THz wave is an effective way to solve the reentry blackout problems.

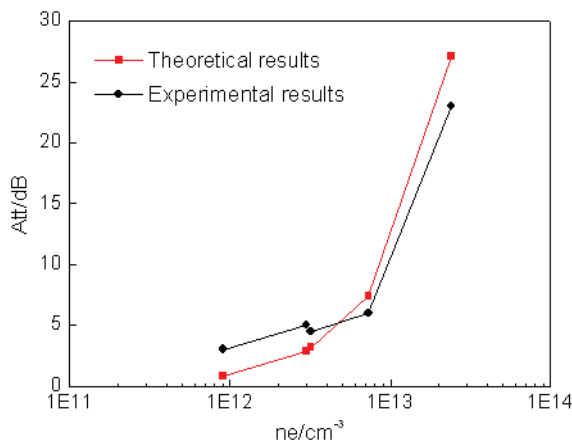


Fig. 4. The comparison of the experimental and theoretical results of 0.22 THz EMW attenuation.

V. CONCLUSIONS

The effect of plasma on EMW propagation have been studied theoretically in this paper, which indicate that communications using THz wave is an alternative

method for solving the blackout problem. The 0.22 THz EMW propagation properties in the plasma have been studied experimentally with shock tube and the experimental results match well with the theoretical ones. Both the theoretical and experimental results indicate that communications using THz wave is an alternative and effective way to solve the reentry blackout problems.

ACKNOWLEDGMENT

This work was supported by the National High Technology Research and Development Program of China (Grant No. 2011AA7022016) and the National Natural Science Foundation of China (Grant No. 11275045).

REFERENCES

- [1] F. H. Mitchell, "Communication-system blackout during reentry of large vehicles," *Proc. IEEE*, vol. 55, pp. 619-626, 1967.
- [2] J. P. Rybak and R. J. Churchill, "Progress in reentry communications," *IEEE Trans. Aerospace Electron. Syst.*, vol. 7, pp. 879-894, 1971.
- [3] X. J. Zeng, Z. F. Yu, S. Q. Bu, S. Liu, P. Ma, A. H. Shi, and S. C. Liang, "Research on the RCS of hypervelocity model and its plasma sheath," *Acta Aerodyn. Sin.*, vol. 28, pp. 645-649, 2010.
- [4] M. Keidar, M. Kim, and I. D. Boyd, "Electromagnetic reduction of plasma density during atmospheric reentry and hypersonic flights," *J. Spacecraft Rockets*, vol. 45, pp. 445-453, 2008.
- [5] J. F. Liu, X. L. Xi, G. B. Wan, and L. L. Wang, "Simulation of electromagnetic wave propagation through plasma sheath using the moving-window finite-difference time-domain method," *IEEE Tran. Plasma Sci.*, vol. 39, pp. 852-855, 2011.
- [6] M. Kim, M. Keidar, and I. D. Boyd, "Analysis of an electromagnetic mitigation scheme for reentry telemetry through plasma," *J. Spacecraft Rockets*, vol. 45, pp. 1223-1229, 2008.
- [7] C. Thoma, D. V. Rose, C. L. Miller, R. E. Clark, and T. P. Hughes, "Electromagnetic wave propagation through an overdense magnetized collisional plasma layer," *J. Appl. Phys.*, vol. 106, pp. 043301, 2009.
- [8] M. Kim, M. Keidar, and I. D. Boyd, "Electrostatic manipulation of a hypersonic plasma layer-images of the two-dimensional sheath," *IEEE Tran. Plasma Sci.*, vol. 36, pp. 1198-1199, 2008.
- [9] C. J. Schexnayder, J. S. Evans, and P. W. Huber, "Comparison of theoretical and experimental electron density for RAM C flights," *NASA*, vol. 252, pp. 277-303, 1970.
- [10] J. E. Shen, J. Rong, and W. X. Liu, "Progress of terahertz in communication technology," *Infrared Laser Eng.*, vol. 35, pp. 342-347, 2006.
- [11] M. Martl, J. Darmo, D. Dietze, K. Unterrainer, and E. Gomik, "Terahertz waveguide emitter with sub-wavelength confinement," *J. Appl. Phys.*, vol. 107,

- pp. 013110, 2010.
- [12] M. Koch, *Terahertz Frequency Detection and Identification of Materials and Object*, Braunschweig, 2007.
- [13] D. M. Vavriv, V. A. Volkov, and V. G. Churmak, "Clinotron tubes: high-power THz sources," *Proceedings of the 37th European Microwave Conference*, Kharkov, Ukraine, Oct. 2007.
- [14] Y. J. Ding, "Novel approaches to THz sources and detectors at room temperature," *The 18th Annual Meeting of the IEEE Lasers and Electro-Optics Society*, Bethlehem, Palestine, Oct. 2005.
- [15] C. X. Yuan, Z. X. Zhou, X. L. Xiang, H. G. Sun, and S. Z. Pu, "Propagation of broadband terahertz pulses through a dense-magnetized-collisional-bounded plasma layer," *Phys. Plasmas*, vol. 17, pp. 113304, 2010.
- [16] C. X. Yuan, Z. X. Zhou, X. L. Xiang, H. G. Sun, H. Wang, M. D. Xing, and Z. J. Luo, "Propagation properties of broadband terahertz pulses through a bounded magnetized thermal plasma," *Nucl. Instrum. Methods Phys. Res. B*, vol. 269, pp. 23-29, 2011.
- [17] C. X. Yuan, Z. X. Zhou, J. W. Zhang, X. L. Xiang, F. Yue, and H. G. Sun, "FDTD analysis of terahertz wave propagation in a high-temperature unmagnetized plasma slab," *IEEE Tran. Plasma Sci.*, vol. 39, pp. 1577-1584, 2011.
- [18] S. B. Liu, T. Zhou, M. L. Liu, and W. Hong, "Wentzel-Kramer-Brillouin and finite-difference time-domain analysis of terahertz band electromagnetic characteristics of target coated with unmagnetized plasma," *J. Syst. Eng. Electron.*, vol. 19, pp. 15-20, 2008.
- [19] Z. Tosun, D. Akbar, and H. Altan, "The interaction of terahertz pulses with dc glow discharge plasma," *34th International Conference on Infrared, Millimeter, and Terhertz Waves*, Busan, Korea, Sep. 2009.
- [20] T. S. Hector, R. Norma, and H. S. Paulo, "Electromagnetic properties of a chiral-plasma medium," *Appl. Comput. Electrom.*, vol. 12, no. 1, pp. 731-442, 1997.
- [21] B. Tissafi, F. Aniel, L. Pichon, B. Essakhi, C. Guiffaut, and S. Lepaul, "Comparative study of three wave propagation software programs for the modeling of coupled Maxwell and Boltzmann equations at THz frequency," *Appl. Comput. Electrom.*, vol. 24, no. 4, pp. 382-390, 2009.
- [22] F. Seydou, R. Duraiswami, N. A. Gumerov, and T. Seppanen, "TM electromagnetic scattering form 2D multilayered dielectric bodies-numerical solution," *Appl. Comput. Electrom.*, vol. 19, no. 2, pp. 100-107, 2004.
- [23] L. Zheng, Q. Zhao, S. Z. Liu, P. Ma, C. Huang, Y. F. Tang, X. L. Chen, X. J. Xing, C. Y. Zhang, and X. G. Luo, "Theoretical and experimental studies of 35 GHz and 96 GHz electromagnetic wave propagation in plasma," *Prog. Electromagn. Res. M*, vol. 24, pp. 179-192, 2012.
- [24] C. X. Yuan, Z. X. Zhou, and H. G. Sun, "Reflection properties of electromagnetic wave in a bounded plasma slab," *IEEE Tran. Plasma Sci.*, vol. 38, pp. 3348-3355, 2010.
- [25] J. Hilsenrath and M. Klein, *Tables of Thermodynamic Properties of Air in Chemical Equilibrium Including Second Virial Corrections from 1500K to 15000K*, Virginia, 1965.
- [26] M. Lamnaouer, *Numerical Modeling of the Shock Tube Flow Fields Before and During Ignition Delay Time Experiments at Practical Conditions*, Florida, 2004.
- [27] P. Ma, X. J. Zeng, A. H. Shi, S. Q. Bu, and Z. F. Yu, "Experimental investigation on electromagnetic wave transmission characteristic in the plasma high temperature gas," *J. Exp. Fluid Mechanics*, vol. 24, pp. 51-56, 2010.
- [28] Y. Chang, *Numerical Research on Supersonic/Hypersonic Plasma Flow and its Electromagnetic Characteristics*, Changsha, China, 2009.



Ling Zheng is a Ph.D. candidate in Computational Electromagnetics at School of Physical Electronics, University of Electronic Science and Technology of China. Zheng's research interests are computational electromagnetics, finite difference time method applied to electromagnetic wave propagation in medium.



Qing Zhao is a Professor in Computational Electromagnetics at School of Physical Electronics, University of Electronic Science and Technology of China. He got his Ph.D. in 2001 from Southwestern Institution of Physics. His research interests include the interaction between electromagnetic wave and medium, and scientific computing.



Xiaojun Xing is a Ph.D. candidate at School of Physical Electronics, University of Electronic Science and Technology of China. His research interests include scientific computing, plasma, and antenna.

